BIOMEDICAL APPLICATIONS OF PEPTIDE NANOSTRUCTURES

A DISSERTATION SUBMITTED TO

THE GRADUATE SCHOOL OF ENGINEERING AND SCIENCE

OF BILKENT UNIVERSITY

IN PARTIAL FULFILLMENT OF THE REQUIREMENTS FOR

THE DEGREE OF

DOCTOR OF PHILOSOPHY

IN

MATERIALS SCIENCE AND NANOTECHNOLOGY

By

MELİS ŞARDAN EKİZ

April 2016

BIOMEDICAL APPLICATIONS OF PEPTIDE NANOSTRUCTURES

By Melis Şardan Ekiz
April 2016

We certify that we have read this thesis and that in our opinion it is fully adequate, in scope and in quality, as a thesis for the degree of Doctor of Philosophy.

Mustafa Özgür Güler (Advisor)

Adil Denizli

Ayşe Begüm Tekinay

Bilge Baytekin

Erhan Bat

Approved for the Graduate School of Engineering and Science:

Levent Onural
Director of the Graduate School

ABSTRACT

BIOMEDICAL APPLICATIONS OF PEPTIDE NANOSTRUCTURES

Melis Şardan Ekiz

PhD in Materials Science and Nanotechnology

Advisor: Mustafa Özgür Güler

April, 2016

Nature as an important inspirational source for scientists presents complex and elegant examples for adaptive and intelligent systems created by self-assembly. There has been a great endeavour for understanding these sophisticated systems and self assembly gives us an opportunity to emulate these systems by customized molecular designs. In this thesis, next-generation biomaterials were developed by integrating peptide amphiphile molecules into sugar, lipid or inorganic based materials through covalent or noncovalent interactions and their biomedical applications were investigated. Peptide amphiphiles can form morphologically different supramolecular nanostructures based on the amino acid sequence they bear. Also, a bioactive amino acid sequence can be inserted into the peptide backbone not only to enhance the biocompatibility of the material but also to direct cellular responses. On the other hand, amphiphilic character of peptide amphiphiles enables to interact with other amphiphilic molecules or hydrophobic surfaces via hydrophobic interactions. In the scope of the present thesis, peptide based systems were utilized in three different biomedical applications: drug delivery, bioimaging and regenerative medicine. In the first chapter, the self-assembly as one of the

bottom-up approaches, peptide self-assembly, the forces and factors triggering the peptide assembly, the importance of peptide amphiphile design in the resulting nanostructure and the biomedical applications of peptide amphiphiles are shortly introduced. In the second chapter, a new drug delivery system is devised by incorporating peptide amphiphile molecules, which are synthesized using arginine residues that are known to enhance cell penetration, into the liposomal system. Beside the investigation of model dye and anticancer drug encapsulation capacities of the prepared formulation, cellular uptake profiles and therapeutic effects of liposomal systems are also examined. In the third chapter, mesoporous silica nanoparticles, which are anticipated to be used in drug delivery and theranostic applications, are individually functionalized with two distinct peptide amphiphile molecules with different overall charges and their biocompatibilities and cellular uptake profiles are examined. In the fourth chapter, superparamagnetic iron oxide nanoparticles that have also potential to be utilized in clinical applications are shown to be applicable as negative contrast agents in magnetic resonance imaging after coating with peptide amphiphiles. The last chapter covers the development of glycopeptides nanofibers that can mimic natural hyaluronic acid abundantly found in native cartilage tissue and its effect on the cartilage regeneration.

Keywords: Peptide amphiphiles, self-assembly strategy, liposomes, mesoporous silica nanoparticles, superparamagnetic iron oxide nanoparticles, glycopeptides, biomedical applications

ÖZET

PEPTİT NANOYAPILARIN BİYOMEDİKAL UYGULAMALARI

Melis Şardan Ekiz

Malzeme Bilimi ve Nanoteknoloji, Doktora

Tez Danışmanı: Mustafa Özgür Güler

Nisan, 2016

Bilim adamları için önemli bir ilham kaynağı olan doğa, kendiliğinden bir araya gelerek oluşan uyarlanabilir akıllı sistemler yaratabilmek için mükemmel ve kompleks örnekler sunmaktadır. Bu sofistike sistemleri anlamak için büyük çaba harcanmaktadır. Kendiliğinden bir araya gelme yaklaşımı farklı moleküler dizaynlar kullanarak bu sistemleri taklit etmemize olanak sağlamaktadır. Bu tez çalışmasında, peptit amfifil molekülleri şeker, lipit ya da inorganik içerikli yapılara kovalent ya da nonkovalent etkileşimler sayesinde entegre edilerek yeni nesil biyomalzemeler geliştirilmiştir ve bu malzemelerin biyomedikal uygulamaları test edilmiştir. Peptit amfifiller, içerdikleri farklı kimyasal özellikteki amino asitler sayesinde değişik morfolojilerde supramoleküler nanoyapılar oluşturabilmektedirler. Amaca uygun olarak eklenen biyoaktif amino asit dizileri malzemenin biyouyumluluğunu arttırırken aynı zamanda hücresel faaliyetleri de yönlendirme özelliğine sahiptir. Bunun yanısıra, amfifilik karakterleri hidrofobik etkileşimler sonucunda diğer amfifilik yapılarla ya da hidrofobik yüzeylerle etkileşime girmelerini mümkün kılar. Bu tez çalışması kapsamında üç uygulama alanı için farklı hibrit peptit amfifil sistemleri incelenmiştir. İlk bölümde aşağıdan yukarı fabrikasyon yaklaşımlarından

biri olan kendiliğinden bir araya gelme stratejisi, bu stratejinin genel olarak peptitlerde kullanımı, peptitlerin kendiliğinden birleşmelerini tetikleyen etkileşimler ve faktörler, oluşan yapılarda peptit amfifil dizaynının önemi ve geliştirilen peptit amfifil sistemlerin biyomedikal uygulamaları hakkında bilgiler verilmiştir. İkinci kısımda hücre penetrasyonunu arttırdığı bilinen arginine amino asitleri kullanılarak sentezlenen peptit amfifil molekülleri lipozomal sisteme dahil edilerek yeni bir ilaç taşıma sistemi geliştirilmiştir. Bu sistemin farklı model boya ve antikanser ilaçlarını enkapsüle etme kapasitesinin yanında yüklenen aktif moleküllerin hücreye alınma profilleri ve terapötik etkileri incelenmiştir. Üçüncü kısımda, ilaç taşıma ve teranostik amaçlar için kullanılması hedeflenen mezoporoz silika nanoparçacıklar farklı yüklerde sentezlenmiş peptit amfifiller ile fonksiyonelleştirilerek biyouyumlulukları ve hücreye alınma eğilimleri test edilmiştir. Dördüncü bölümde de klinik olarak da kullanılma potansiyeli olan süperparamanyetik demir oksit nanoparçacıkların peptit amfifil molekülleri ile kaplandıktan sonra manyetik rezonans görüntülemede negatif kontrast ajanı olarak kullanılabileceği gösterilmiştir. Son bölümde ise kıkırdak dokusunda yoğunlukla bulunan hyaluronik asit yapısını taklit edebilen ve doğal olarak kendiliğinden bir araya gelebilen glikopeptit nanofiber yapıları geliştirilerek kıkırdak rejenerasyonundaki etkisi hücre kültürü ve hayvan deneyleri ile incelenmiştir.

Anahtar kelimeler: Peptit amfifiller, kendiliğinden bir araya gelme stratejisi, lipozomlar, mezoporoz silika nanoparçacıklar, süperparamanyetik demir oksit nanoparçacıklar, glikopeptitler, biyomedikal uygulamalar

ACKNOWLEDGEMENT

I would like to express my deepest gratitude to my PhD advisor Prof. Mustafa Özgür Güler for his invaluable guidance, encouragement, knowledge, patience and support throughout my PhD thesis study. I am also sincerely grateful to Prof. Ayşe Begüm Tekinay for her knowledge, guidance and perpective. I would like to thank my jury members Prof. Dr. Adil Denizli, Prof. Bilge Baytekin and Prof. Erhan Bat for their contribution to my thesis. I would like to thank Prof. Dr. Semra İde for her scientific contribution to my thesis.

I would like to express my special thanks to Dr. Adem Yildirim, Dr. Seher Üstün Yaylacı, Elif Arslan, Ayşe Özdemir, Murat Kılınç, Didem Mumcuoğlu, Ilghar Orijalipoor, Alper Devrim Özkan, Egemen Deniz Eren, Gökhan Günay and Aygül Zengin for their fruitful collaboration. Another special thank to Dr. Rükan Genç and Dr. Ashif Shaikh who shared their knowledge and experience in liposome and carbohydrate chemistry, respectively.

I would also like to acknowledge my old and present lab and ofis members Gülistan Tansık, Gülcihan Gülseren, Melis Göktaş, Dr. Handan Acar, Dr. Hakan Ceylan, Dr. Ruslan Garifullah, M. Aref Khalily, Turan Selman Erkal, Hatice Kübra Kara, Melike Sever, Dr. Özlem Erol, Dr. Gözde Uzunallı, Meryem Hatip, Hepi Susapto, Begüm Dikeçoğlu, Oya İlke Şentürk, Samet Kocabey, Dr. Rashad Mammadov, Dr. Büşra Mammadov, Elif Arslan, Çağla Eren, Nuray Gündüz, Berna Şentürk, Aslı Çelebioğlu, Zeynep Aytaç, Yelda Ertaş, İrem Gürbüz, Seylan Ayan, Yasin Tümtaş, Öncay Yaşa, Ceren Garip, Ahmet Emin Topal, Mustafa Beter, Zeynep Orhan, Fatih Yergöz, Merve Şen, Canelif Yılmaz, İbrahim Çelik, Idil Uyan,

Şehmus Tohumeken, Nurcan Haştar, Oğuz Tuncay and Özge Uysal for creating such a warm working environement. My special thanks to Mrs. Zeynep Erdoğan, Mr. Mustafa Güler and Dr. Gökçe Çelik for their immense technical help.

I would like to acknowledge The Scientific and Technological Research Council of Turkey (TÜBİTAK BIDEB-2211A, 113T045 and 114S913) for funding my PhD research and financially supporting me in one international conference (in the form of 2224-A). In addition, I would like to thank to European Cooperation in Science and Technology (COST CM1102 Action) for giving me an opportunity to visit Prof. Bruce Turnbull's laboratory and be in their research environment.

I especially thank to my dearest friends Göksu Çinar, Bihter Dağlar, Fulya Karahan Dağ, Merve Kaplan, Sena Cüce Köse, Selen Güven, İnci Günler, Oya Ustahüseyin, Gülsu Şener, Başak Aysin, Adem Yildirim, Sinan Baysal, Burcu Barca, Cansu Beşiroğlu, Ongun Bilgin, Çağlar Beşiroğlu, Seren Hamsici, Özüm Şehnaz Günel and Barış Çiftçi for their endless support. Their friendship deserves all compliments. I am so lucky having you.

I wish to give special thanks to my family for their unquestionable belief in me. Without their love, support and trust, this thesis would not be done.

Last but not least, I owe my sincere gratitude to my life partner, Okan Öner Ekiz, who stood by me for all those times. None of this could have happened without his continuous support, patience and encouragement.

CONTENTS

LIST OF FIGURES

LIST OF TABLES

Abbreviations

A10	Vascular smooth muscle cell line
ANOVA	Analysis of variance
APTES	Aminopropyl triethoxysilane
ATRP	Atom transfer radical polymerization
Boc	*Tert*-butoxycarbonyl
CD	Circular dichroism
CPP	Critical packing parameter
CS	Chondroitin sulfate
CTAB	Cetyltriammoniumbromide
CTLP	Curvature tuned liposome preparation
DAB	Diaminobenzidine
DCM	Dichloromethane
DIEA	*N*,*N*-diisopropylethylamine
DMEM	Dulbecco's modified Eagle's medium
DMF	N,N-Dimethylformamide
DMMB	Dimethylmethylene blue
DMSO	Dimethyl sulfoxide
DOPG	1,2-dioleoyl-*sn*-glycero-3-[phosphor-*rac*-(1-glycerol)]
ECM	Extracellular matrix
FBS	Fetal bovine serum
FITC	Fluorescein isothiocyanate
Fmoc	9-Fluorenylmethoxycarbonyl
FTIR	Fourier transform infrared spectroscopy
GAG	Glycosaminoglycan
GAPDH	Glyceraldehyde 3-phosphate dehydrogenase
HAADF	High-angle annular dark field
HBTU	*N*,*N*,*N*′,*N*′-Tetramethyl-O-(1*H*-benzotriazole-1-yl) uronium hexafluorophosphate
HPLC	High pressure liquid chromatography
HR-TEM	High resolution transmission electron microscopy

HUVEC	Human umbilical vein endothelial cell
IC_{50}	Half maximal inhibitory concentration
ICP-MS	Inductively coupled plasma-mass spectrometry
LC-MS	Liquid chromatography-mass spectroscopy
MCF7	Michigan Cancer Foundation-7
mMSC	Mouse mesenchymal stem cells
MSN	Mesoporous silica nanoparticle
NCA	N-carboxyanhydrides
NCL	Native chemical ligation
NMR	Nuclear magnetic resonance
OD	Optical density
OMSN	Octyl modified mesoporous silica nanoparticle
OTS	Octyltriethoxysilane
PA	Peptide amphiphile
PBS	Phosphate buffered saline
PDD	Pair distance distributions
qRT-PCR	Quantitative real-time polymerase chain reaction
QTOF	Quadrapole time of flight
ROI	Region of interest
RT	Room temperature
SAXS	Small angle X-ray spectroscopy
SD	Standard deviation
SEM	Standard error of mean
SEM	Scanning electron microscopy
SI	Signal intensity
SPION	Superparamagnetic iron oxide nanoparticle
SPPS	Solid phase peptide synthesis
STEM	Scanning transmission electron microscopy
TCP	Tissue culture plate
TEM	Transmission electron microscopy
TEOS	Tetraetyl orthosilicate
TFA	Trifluoroacetic acid

TGA	Thermal gravimetric analysis
THF	Tetrahydrofuran
TIS	Triisopropyl silane
VSM	Vibrating sample magnetometer
XRD	X-ray diffraction

CHAPTER 1

INTRODUCTION

1.1 Self-Assembly

Molecular self-assembly, as one of the bottom-up approaches, is emerging powerful tool in the fabrication of functional nanoscale structures. It is defined as the spontaneous organization of molecules into stable, well-defined structures under equilibrium conditions through noncovalent interactions. The self-assembly is ubiquitous in many biological systems and results in the formation of a variety of complex biological structures found in Nature. These complex and elegant examples inspire scientists to create similar artificial systems by using building blocks of life such as peptides, lipids, nucleic acids, and saccharides. Naturally, many key developments in last century have paved the way for the progress of this sophisticated field such as the finding of close-packed form of amphiphilic molecules, the arrangement of monolayers by long chain hydrocarbon amines and the distribution of ordered monolayers of alkanethiolate molecules on gold substrate.[1]

In most cases, thermodynamically stable structures are formed from the assembling subunits utilized in biomaterials where both the molecular species and the solvent molecules contribute enthalpically and entropically. Since the mobility of the components involved in self-assembly is crucial, fluid phases or smooth surfaces are preferred for the assembly. In the case of the self-assembly of more complex systems yielding meso- or macroscopic structures, gravitational attraction, external electromagnetic fields, entropic interactions and magnetic capillary are also taken into consideration beside noncovalent or weak covalent interactions.[2]

The reason of the rapid growth of this field is that self-assembly allows seeking insight into the structural features of many important biological compounds and makes possible to synthesize larger structures (> 1000 atoms) that cannot be feasible with covalent bonds due to the poor stability.[3] Synthesized molecules can be organized on larger scales by means of self-assembly (Figure 1.1).[4]

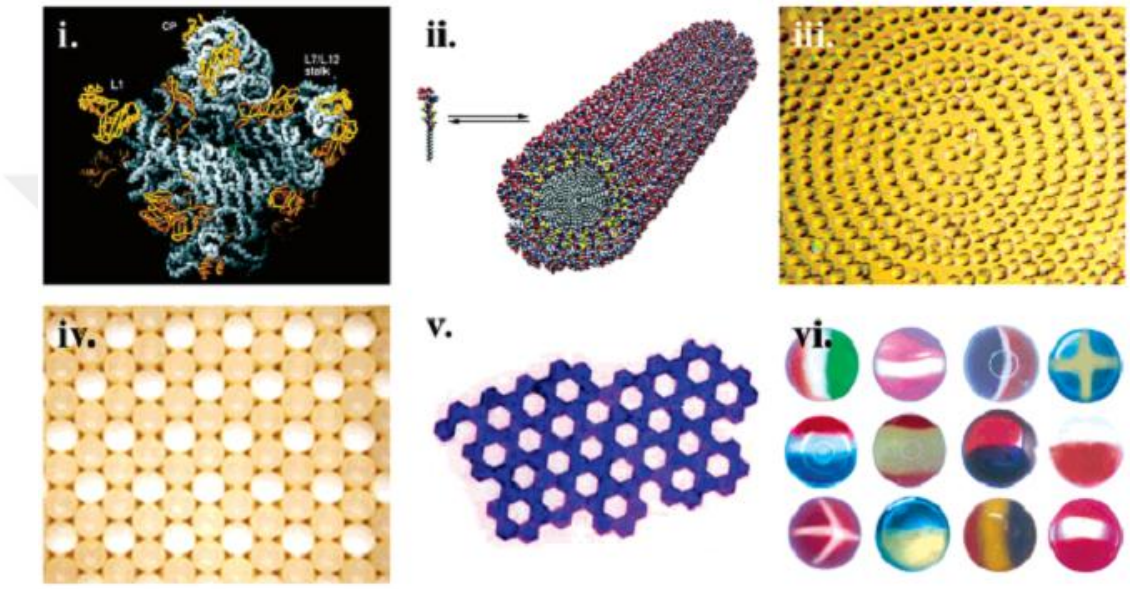

Figure 1.1 Examples of self-assembly. (i) Crystal structure of a ribosome. (ii) Selfassembled peptide-amphiphile nanofibers. (iii) Electrostatic self-assembly (ESA) of polymeric microspheres on a charge-exchanging substrate modified by wet stamping. (iv) ESA of macroscopic 2D crystals whose formation is mediated by charges developed by contact electrification. (v) Capillary SA of polymeric plates at an interface between two liquids. (vi) Self-assembled polymeric microspheres of complex internal structures. (Reproduced from Ref. 4 with permission from American Chemical Society)

1.2 Self-Assembly of Peptides

Amino acids serve a diverse pool for the construction of peptide-based materials through distinct physicochemical properties, regarding the charge, hydrophobicity,

size and polarity, of their side chains that increases the possibility of creating peptidic materials with different amino acid sequences and lengths. This diversity is further enriched by the introduction of non-proteinogenic groups into the peptide backbone. Since peptides are the biomolecules whose synthesis, structure and properties are well understood, significant effort is directed toward the research on self assemblies using peptide-based elements.[5] Peptide self assembly is mainly governed by noncovalent interactions. This type of interactions not only drive the self-assembly but also stabilize the secondary structure of peptides and proteins.[6]

1.2.1 Forces Driving the Peptide Self Assembly

Noncovalent interactions such as hydrogen bonding, hydrophobic, electrostatic, and van der Waals interactions, π-π stacking and coordination bonds are the main contributors of molecular self assembly (Figure 1.2).[7-8] While nonpolar amino acids, including aliphatic (eg. alanine, leucine, valine) and aromatic (eg. tyrosine, phenylalanine) amino acids, are mostly responsible for hydrophobic clustering through hydrophobic interactions and π-π stacking, respectively, polar amino acids result in either hydrogen bonding or electrostatic interactions depending on the fact that they have uncharged (eg. serine, asparagine) or charged (eg. lysine, histidine, glutamic acid) residues.[9] In addition to individual amino acids, the peptide backbone itself provides considerable stability through hydrogen bonds. Although these highly dynamic interactions are weak, when considered individually, compared to covalent interactions, concomitant interactions can elicit stable assemblies. Multiplicity in the noncovalent interactions leads to obtaining specificity in the self-assembling system.[10]

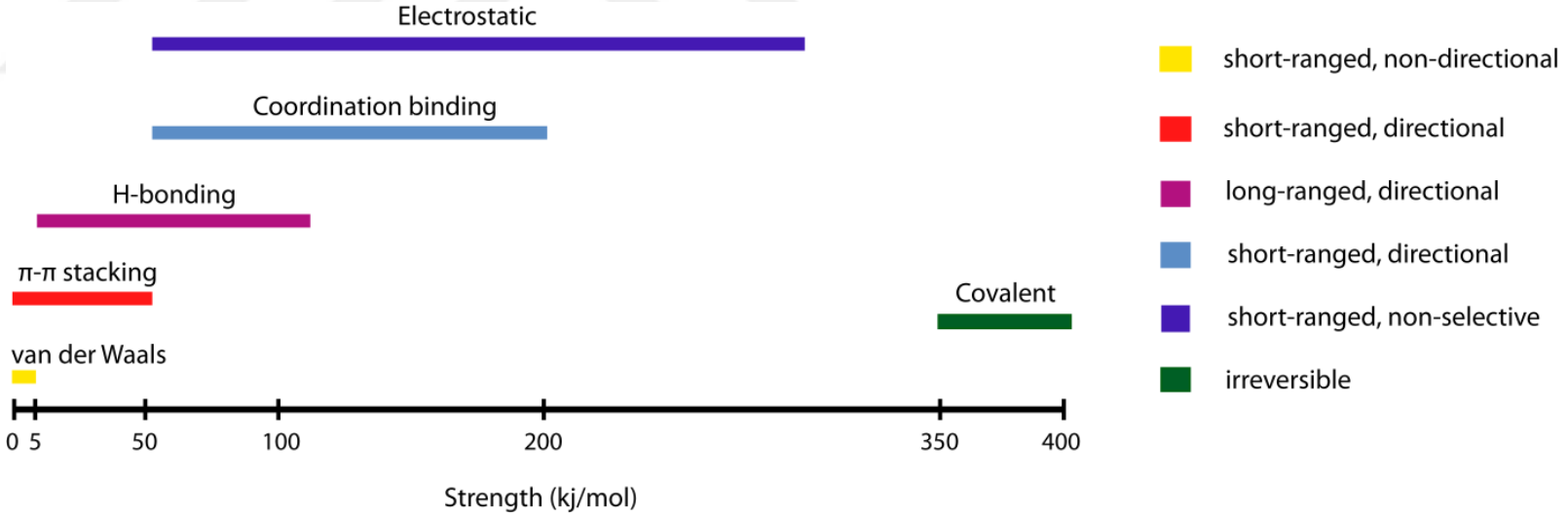

Figure 1.2 Strength and properties of noncovalent interactions involved in self-assembly

Naturally occurring hydrogen bonding patterns such as those found in β-sheet, α-helix, and coiled coils, are utilized in the design of a number of peptide sequences to form higher order structures as a result of self assembly (Figure 1.3).[11] The stabilization of the multiple peptide backbone arrangements by hydrogen bonding interactions between the backbone amide and carbonyls results in the formation of β-sheets. The sheet is either parallel or anti-parallel depending on the direction of the strands. Peptides composed of simple repeat sequences for hydrophobic and hydrophilic amino acids are organized in such a way that hydrophilic and hydrophobic faces are produced and hydrophobic face is buried while its hydrophilic face is exposed to aqueous environment.[12] Unlike β-sheets, the α-helices are formed by individual peptide chains where backbone amide components are intramolecularly hydrogen bonded. It leads to the presentation of the amino acid side chains on the surface of each helix and furtherly facilitates the accessibility of amino acid side chains to solvent. In some cases, these single α- helices can assembly by coiling together and form so called coiled coils. Peptide sequences responsible from coiled coil formation generally bear a repeat motif consisting of seven residues. This *heptad* motif is derived by utilizing from a wheel diagram labelled with specific letters (a-g). So far, the rules required to create coiled coil structure were well studied and conceived. In this section of the review, we give a relatively brief account for the H-bonding patterns exploited in peptide self-assembly; however, there are comprehensive reviews in the literature for more detailed information.[13-14]

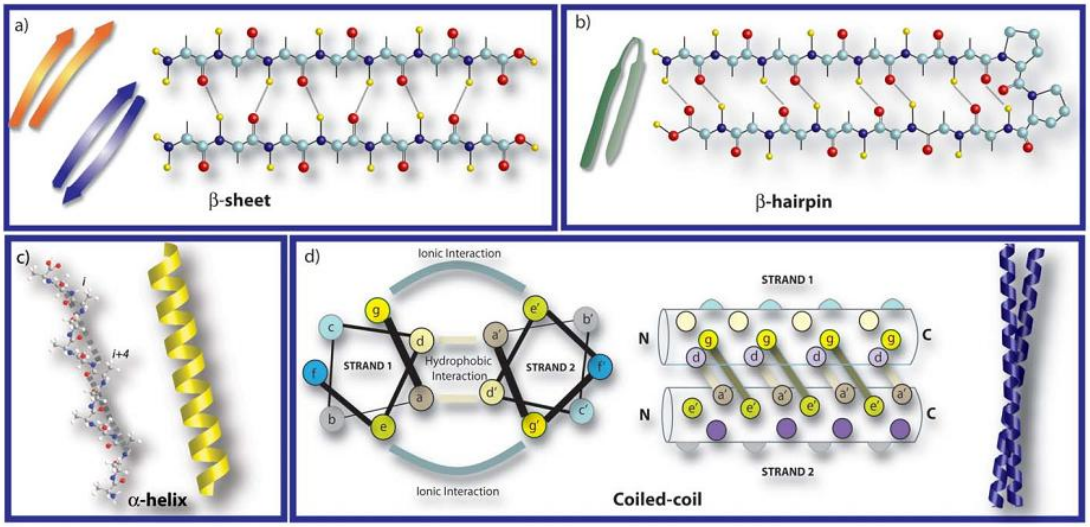

Figure 1.3 Schematic representation of the molecular self-assembly of peptides involved in the formation of different secondary structures (Reproduced from Ref. 11 with permission from Royal Society of Chemistry)

1.2.2 Factors Triggering the Peptide Self Assembly

There is a growing interest in creating systems that assemble and disassemble in response to the external cues. Since the noncovalent interactions are delicate interactions, they have great tendency to respond to the alterations in the environmental conditions such as pH, light, temperature, ionic strength, and solvent polarity (Figure 1.4).[15] Among them, pH switch is the most facile approach to control and direct the self-assembly.[16-20] A number of peptides are inherently sensitive to pH change due to the introduced charged amino acids, leading to a structural transformation. Apart from pH stimuli, light triggered systems designed by van Hest and Stupp groups were developed by using photocleavable group bearing peptide amphiphiles and morphological transitions were observed for both cases in response to light.[21-23] Furthermore, polymerizable diacetylene unit containing peptide molecules were shown to respond to UV light irradiation to acquire one dimensional

nanostructures by Tovar group.[24] On the other hand, thermally triggered peptide-based materials causing a change in the self-assembly of the nanostructure were reported by several groups.[25-30] Alternative to the thermal energy, Ulijn group demonstrated that ultrasound energy can assist the reorganization of supramolecular nanostructures due to the alteration in the contribution of noncovalent interactions, especially of H-bonding and π- stacking, to the resulting supramolecular assembly.[31] Differently, the effect of ionic strength and metal ions on the self-assembly mechanism of peptide molecules were examined by the addition of different type of cations into the peptide-based systems. While charged amino acids are mainly responsible for the salt-induced self-assembly as in the case of ionic-complementary peptides[32], beta-hairpin peptides[33], ultrashort peptides[34] and peptide amphiphiles[35-36], histidine residues have been predominantly used as metal-binding domain due to the affinity of imidazole ring to several coordination metal ions.[37-40] In addition to the above-mentioned external stimulus factors, solvent polarity can also exert a profound effect on the supramolecular nanostructures. Solvent controlled structural transition was observed for several peptides due to the changed interactions between the hydrophobic domain of peptide and solvent molecules.[41-44] Self assembly can be alternatively induced by enzyme catalyzed reactions. Structural switches can be employed in a controllable manner by using enzymes specific to peptide sequences.[45-49]

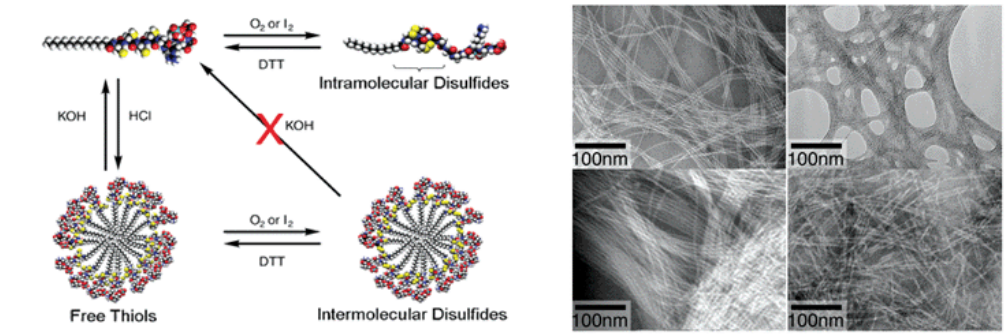

Oxidation of the assembled nanofibres improve their stability by the formation of intermolecular disulfide bridges. However, oxidation of monomers prevents self-assembly as the formation of intramolecular disulfide bridges disrupts the alignment of the amide backbone (above left).[40,41] Different self-assembly triggers result in different fibre networks visualised by TEM micrographs (above right). Figure adapted with permission from *Proc. Nat. Acad. Sci.*, 2002, **99**, 5133-5138. Copyright 2002 National Academy of Sciences, U.S.A.

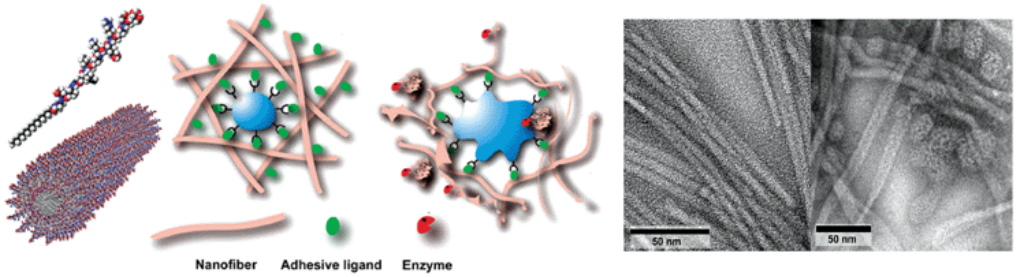

The self-assembly of matrix metalloprotease sensitive peptide monomers into nanofibres for use as cell culture results in a scaffold that degrades in response to extracellular matrix remodelling enzymes (above left). The TEM micrographs show the nanofibres before and after incubation with type IV collagenase (above right). Figure adapted with permission from *Adv. Mater.*, 2005, **17**, 2612-2617. Copyright 2005 Wiley Interscience.

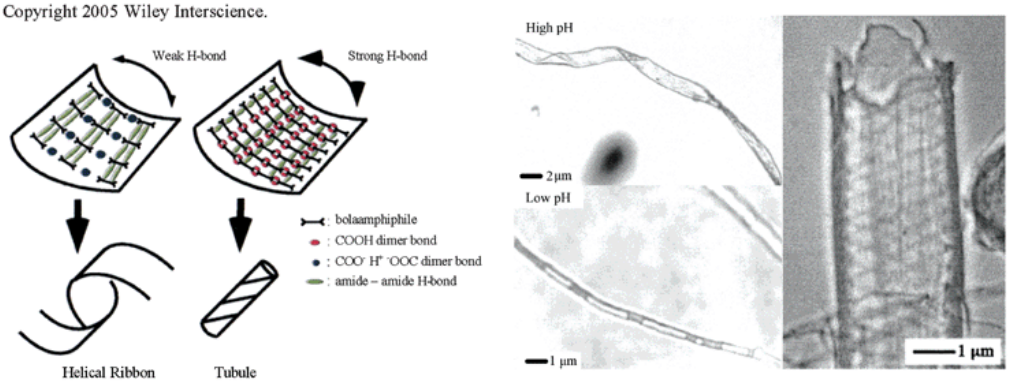

The pH responsiveness of bola-amphiphiles is proposed to arise from the difference in strength between an acid dimer hydrogen bond and a proton bridged acetate pair allowing for greater curvature of the resulting superstructure (above left). Micrographs show the tapes and tubules formed (above centre and right) Figure adapted with permission from *J. Phys. Chem. B*, 2000, **104**, 3383-3386. Copyright 2000, American Chemical Society.

Figure 1.4 Responsive self-assembled peptide systems (Reproduced from Ref. 15 with permission from Royal Society of Chemistry)

1.3 Synthetic Approaches for the Synthesis of Peptides

Peptides consisting of natural or synthetic amino acids are interesting building blocks for the construction of supramolecular assemblies. These simpler structures aid us to understand more complex systems present in nature. Scientists employ a variety of approaches in the synthesis of peptide building blocks and strive for the synthesis of the peptide of interest while minimizing or eliminating the other possible by-products. The synthetic approaches utilized to afford peptide can be classified in three main classes: solid-phase strategies, ring-opening polymerization techniques and genetic engineering.[50-51]

Most convenient methodology for the synthesis of small to medium-sized peptides is solid phase peptide synthesis (SPPS). In this technique, peptide is grown step by step on an insoluble polymeric resin as a result of iterative amino acid couplings where the deprotection of N-terminus of solid support bound amino acid is followed by the attachment of the subsequent amino acid to it after washing and filtering the unreacted reagents and by-products left from previous reaction (Figure 1.5).[52] Amino acids used for the couplings bear orthogonal protecting groups. Orthogonal chemistry approach enables two or more protecting groups to be used concurrently without affecting each other when one of the functional group requires manipulation. General features associated with these protecting groups can be considered as i) the ease of introduction into the functional group; ii) the stability in different reaction conditions; and iii) the safe removal at the end of the synthetic process.[53] Prior to the coupling, there is a need to activate the carboxylic group of amino acid by using phosphonium, aminium, uronium or carbodiimide-based reagents for the formation of amide bond. Although carbodiimide derivatives lead to an increase in the degree

of racemization during the activation of amino acids, it can be minimized by using additives, especially N-hydroxy derivatives, which suppress the formation of N-acylurea by shifting reaction towards the formation of active ester form of amino acid.[54] At the end of the synthesis, the peptide is easily cleaved from the resin with an acidic treatment.

Nowadays, microwave-assisted SPPS is another option to synthesize longer peptides with increased reaction rates and purities. Typically, coupling reagents and additives used in microwave-assisted SPPS are identical with those applied in conventional SPPS and peptide couplings are carried out at temperatures in the range 50-80°C unless amino acids carry a potential risk of epimerization.[55] Setbacks encountered in solution phase synthesis, such as time consuming isolation and purification of intermediate peptides are overcome with SPPS. With SPPS strategy, it is possible to control not only the amino acid sequence but also the C and N terminal functionality of the created peptide.[56] Therefore, this technique is eligible for the synthesis of linear, branched, dendritic or cyclic peptides.[57-58] In addition, different chemical moieties, such as fatty acids, lipids, saccharides, nucleotides, polymers, drugs, aromatic units, and dyes, can be incorporated into peptide backbone with proper linkage chemistry while peptide is still on the resin.

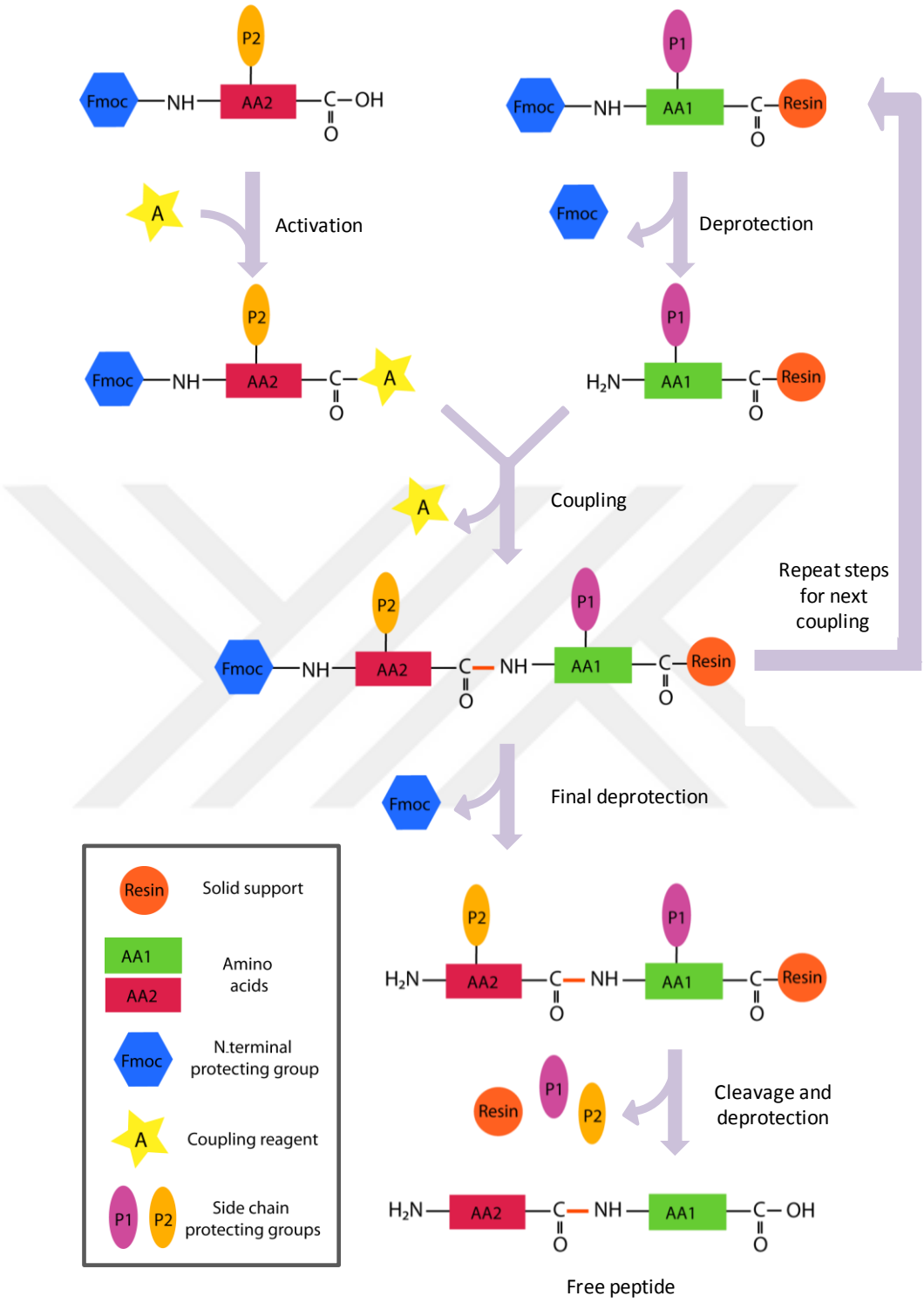

Figure 1.5 Schematic illustration of solid phase peptide synthesis

A further progress in peptide synthesis, which allows eliminating the limitations of SPPS with respect to the size and solubility of the peptides is the native chemical ligation (NCL) where two unprotected peptides, a α-thioester containing peptide and an N-terminal cysteine ended peptide, are chemoselectively conjugated through a thioester linkage. While individual peptides are synthesized using SPPS, they are linked to each other in solution phase to create large-sized peptides and even complex proteins.[59]

On the other hand, the preparation of high molecular weight monodisperse polypeptides with precisely defined primary structure can be achieved by protein engineering, also called as genetic engineering. This strategy allows to synthesize not only structural proteins but also de novo designed proteins as a result of the bacterial expression of artificial genes.[60] This technology can be considered as the molecular tool for the preparation of peptide-based materials which relies on the fact that the synthetically designed gene incorporated into the circular DNA plasmid encodes for a specific polypeptide or protein.[61] One of the advantages of this methodology is that broad range of nonproteogenic amino acids or functional groups can be also integrated for the preparation of the artificial proteins.[62]

Polypeptides with high molecular weight, narrow polydispersity and retained chiral integrity can be synthesized by the ring-opening polymerization of amino acid N-carboxyanhydrides (NCA) in a controlled manner. For the polymerization, there are two extensively accepted mechanisms, namely, normal amine (NAM) and the activated monomer (AMM) mechanisms. In both mechanisms, a range of nucleophiles and bases such as amines and metal alkoxides are used for the initiation of the polymerisation.[63] Although NCA polymerization has the lack of control over

the exact primary peptide sequence, in contrast to SPPS or genetic engineering, it allows to prepare polypeptides in high yield and large quantity.[64] In some cases, side reactions occurred during NCA polymerization may lead to the failure in the formation of homo and block polypeptides which have been mostly prevented by introducing various metal- and organo-catalysts.[65] In addition, some applications necessitate using high purity monomers to obtain optically pure polypeptides with predictable molecular weights and low polydispersities.

Several other chemical methodologies have been developed to synthesize peptide- and protein-based hybrids. Anchorage of two components has been achieved through thiol-maleimide or alkyne-azide couplings as well as by imine, hydrazone linkages, atom transfer radical polymerization (ATRP) and chemoselective peptide ligation methods.[51, 66-67] Although each strategy has its own limitations, with recent advances in synthetic strategies, sophisticated peptidic architectures can be created by using these versatile chemical tools.

1.4 Design-Nanostructure relation in peptide-based systems

The number, type, and sequence of amino acids can be manipulated to design self-assembled peptides. When amino acids are considered individually, they have their own specific characteristics. For instance, while glycine provides a high level of flexibility due to the absence of steric hindrance stemming from the side chains, locked conformation of proline results in a conformational rigidity.[68-69] Cysteine, on the other hand, can be chemically or intermolecularly modified via thiol-maleimide chemistry or disulphide bringing, respectively. Moreover, tyrosine, serine and threonine are utilized in further chemical and enzymatic modifications through their

hydroxyl groups. Depending upon the chemical modifications of C- or N-terminus, properties of peptide building blocks can also be modulated. There are two other major parameters affecting the structure of peptide-based systems, the secondary structure and noncovalent interactions, which were mentioned in the previous section. Peptides supported by α-helical or β-sheet features allow constructing various different nanostructures.[70-71] Apart from the secondary structure, to confer kinetically and thermodynamically stable structures, noncovalent interactions can also be enriched by conjugating functionalized organic linkers to peptide building blocks.[72] Figure 1.6 demonstrated examples of different nanostructures obtained as a result of peptide self-assembly.[73]

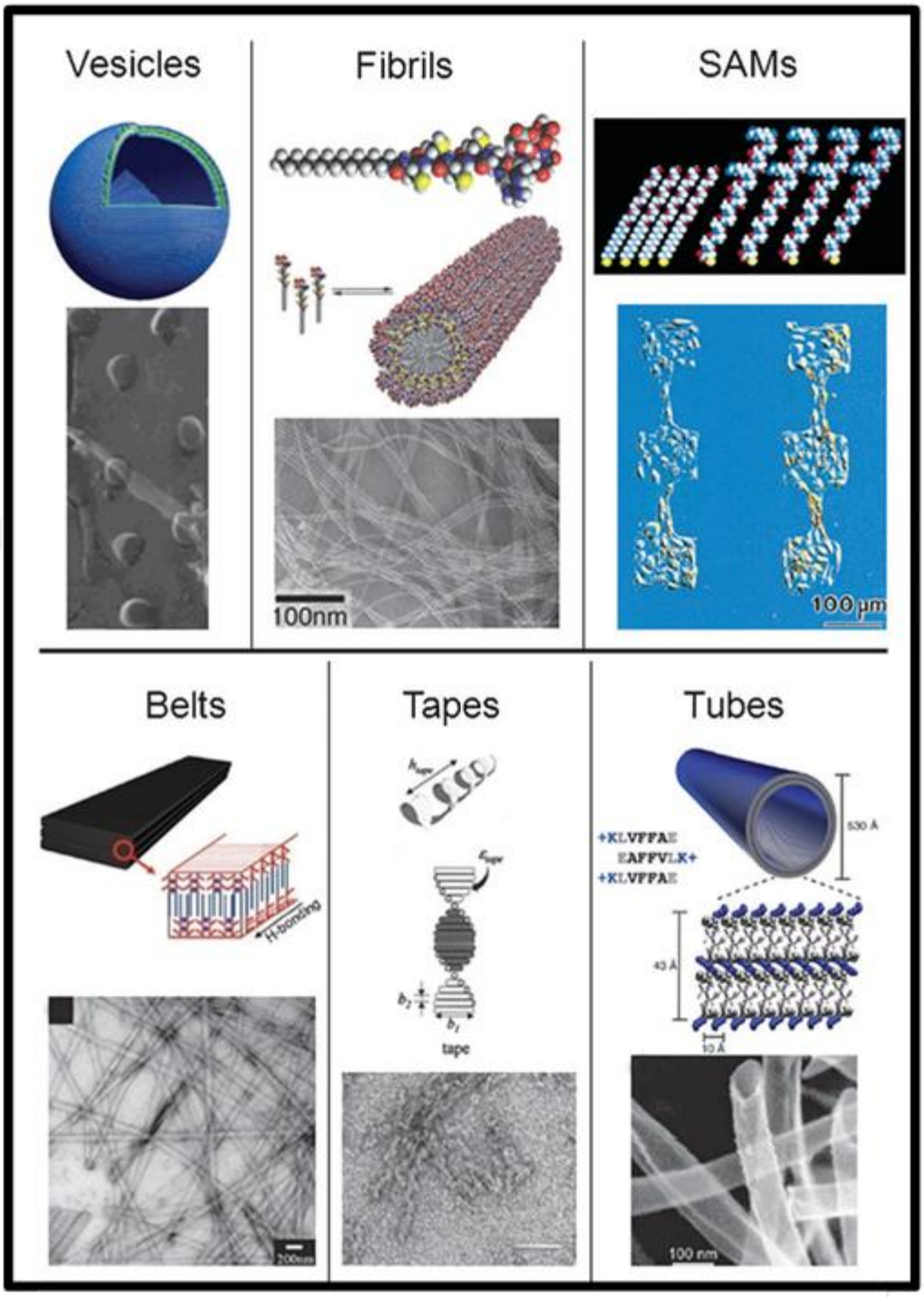

Figure 1.6 Examples of nanostructures achieved by peptide/protein self-assembly (Reproduced from Ref. 73 with permission from Royal Society of Chemistry)

1.5 Peptide Amphiphiles

Peptide amphiphiles (PAs), also called lipidated peptides or lipopeptides, are composed of two main regions, hydrophobic alkyl tail and hydrophilic peptide sequence. This type of molecules are naturally found in living organisms that have important roles especially as an initiator in the signal transduction pathways[74-75] and in the host defense mechanisms of bacteria.[76] The lipidic parts of these molecules are believed to take part in protein-protein and protein-lipid interactions and provide a linkage to the cellular membrane.[75]

Amphiphilicity is the main triggering factor for the self-assembly of PA monomers into well-defined supramolecular nanostructures and the stability of the resulting assemblies can be further improved by enhancing the amphiphaticity of PAs. The self-assembly is mediated by a variety of different noncovalent interactions such as electrostatic interactions between charged amino acids, hydrogen bonding, π-π stacking and hydrophobic interactions, leading to the formation of nanostructures with diverse morphologies (fibers, micelles, nanotapes, nanotubes, nanosheets).[69] As described by Israelachvili, the balance between hydrophobic and electrostatic interactions is needed to be taken into account while determining the geometry of amphiphiles with minimum free energy.[77] Since an alteration in the hydrophilic segment can lead to a change in the critical packing parameter (CPP)[78], it can affect the morphology of the overall assembly.[79-80] In addition, Velichko *et.al.* investigated the contribution of hydrophobic interactions and hydrogen bonding to the morphology of the resulting PA assemblies by molecular simulation techniques and created a phase diagram displaying distinct morphologies with respect to the corresponding variables.[81] Experimental results were also in good agreement with

those obtained by computational analysis. While high content of intermolecular hydrogen bonds between peptide blocks favored the formation of cylindrical PA nanofibers in solution, PA molecules lacking of hydrogen bonds had a tendency to form micellar structures.[82-83] Tsonchev *et.al* performed Monte Carlo simulations to demonstrate the role of electrostatic interactions in the self-assembly of PA nanofibers.[84] Later, their self-assembly mechanism was further studied by Lee *et.al.* and Fu. *et.al.* through molecular dynamic simulations and it was revealed that individual PAs initially formed spherical micelles and they transformed into long thin fibers by merging with one another due to hydrophobic interactions.[85-86] Considering the diversity in the molecular design, including the type of alkyl tail, the choice of amino acids and their order in the β-sheet domain, exploration of distinct PA assemblies is certainly fruitful and rewarding. Table 1.1 summarizes the sequences of the peptide amphiphiles discussed in this section, the resulting nanostructures and the additional information regarding the structural features.

Stupp and coworkers demonstrated that $C_{16}H_{31}O$-$V_3A_3E_3$ PA, in which hydrophilicity of the peptide domain increased towards the C-terminus, self-assembled into elongated fibers after neutralization by pH adjustment or by the salt-mediated screening of charged glutamic residues. Although both formulations exhibited similar morphologies, salt induced PA nanofibers formed stronger intra- and interfiber crosslinks through calcium mediated ionic bridges.[87]

Table 1.1 Recently published studies using peptide amphiphile architectures

Peptide amphiphile	Structure	Details	Refs
$C_{16}H_{31}O$-$V_3A_3E_3$	Nanofiber	Salt induced nanofiber formation	87-88
$C_{16}H_{31}O$-F_3E_3	Twisted/helical ribbon	Time/sequence dependent morphological transformation	89
$C_{16}H_{31}O$-$(VE)_2$, $C_{16}H_{31}O$-V_2E_2, $C_{16}H_{31}O$-$(EV)_2$, $C_{16}H_{31}O$-E_2V_2	Nanobelt/nanofiber/nanoribbon	Structural variation in isomeric peptide amphiphiles	90
$C_{16}H_{31}O$-$(VE)_n$ (n=2,4 and 6)	Nanobelt	Dimensions of belt structure vs. number of amino acid	91
$C_{16}H_{31}O$–$WA_4KA_4KA_4KA$	Wormlike micelle/Nanofibers	Time dependent morphological transition	92
$C_{16}H_{31}O$-A_4LSQETFSDLWKLLPEN	Wormlike micelle	Secondary structure-supramolecular structure relation	93
$C_{16}H_{31}O$-KTTKS	Flat tape-like/twisted structure/spherical micelle	pH tuned morphology	16
$C_{12}H_{23}O$-GAGAGAGY	Nanofiber/twisted nanoribbon	pH tuned morphology	94
$C_{16}H_{31}O$-IAAAEEEE-Am	Nanofiber	pH and concentration dependent self-assembly	95

$C_{16}H_{31}O$-KKFFVLK	Nanotube-helical ribbon/twisted tapes	Thermo-reversible transition	26
$C_{12}H_{23}O$-VFDNFVLK-Am and $C_{12}H_{23}O$-VVAGE (mixture)	Nanofiber	Nanofiber diameter ≈10-20 nm	96
$C_{12}H_{23}O$-P_4R_4-Am, $C_{12}H_{23}O$-$P_4K_2R_8$-Am	Nanosphere	Diameter ≈15-45 nm	97
KLWVLPKC$K_2A_2V_2$K(-$OC_{12}H_{23}$)-Am KLWVLPKCK_2K(-$OC_{22}H_{41}$)-Am	Nanofiber/nanosphere	Importance of β-sheet forming region on self-assembly	98
$C_nH_{(2n-1)}O$-VRGDV (n=10, 12, 14, 16)	Nanofiber	Tail length vs. self assembly at different pH	99
$C_{16}H_{31}O$-H_6-$(OEG)_4$-Am, $(OEG)_4$-H_6K(-$OC_{12}H_{23}$)-Am	Nanofiber/nanosphere	Position of aliphatic tail-control on morphology	20
$C_{24}H_{47}O$-GANPNAAG (diacetylene units on C_{24} chain)	Nanofiber	Temperature vs. fiber stability	100
di$C_{16}H_{31}O$-EQLESIINFEKLTWE-Am	Cylindrical micelle	8.0 ± 2.3 nm in diameter, polydisperse in length	101
qC_8-Tat, dC_8-Tat, mC_8-Tat	Nanofiber	Mean diameter of nanofiber≈15 nm	102

Additionally, highly aligned fibrils were obtained with the same design by either injecting heated PA solution into a saline solution or dragging the same solution through a film of calcium salt solution.[88] The lamellar plaque structure generated during the heat treatment transformed into bundles of nanofibers upon cooling. Same group also observed an unexpected morphological transformation from twisted ribbons into energetically more stable helical ribbons in $C_{16}H_{31}O$-F_3E_3 PAs after ageing them at room temperature for a month.[89] To clarify the reason behind this phenomenon, similar peptide was synthesized by replacing phenylalanine residues with alanine residues and it was observed that newly designed peptide formed 7-9 nm diameter of cylindrical fibrils and did not exhibit any change after being aged indicating that this conformational change is due to the aromatic stacking rearrangement and stems from the existence of the phenyalanine residues. Another critical parameter causing the morphological change in the nanostructure is the concentration. Cui *et al.* designed an alternating hydrophobic and hydrophilic amino acids containing PA, $C_{16}H_{31}O$-VEVE.[103] In the customized molecular design, laterally grown PAs self-assembled into one dimensional ultralong and wide nanobelts with widths on the order of 150 nm and heights between 10-20 nm presenting peptide epitopes at the surfaces. With a decrease in concentration, a morphological transition from large nanobelts to twisted nanoribbons was observed by TEM. Same peptide domain was also used in another study together with its isomeric counterparts to investigate the importance of peptide side chain interactions in the morphology of resulting supramolecular assembly.[90] Each peptide amphiphile isomer displayed different one-dimensional nanostructure such as nanobelts, nanofibers, twisted and helical ribbons, and nanotubes due to the switch in the amino

acid order. While alternating sequence bearing molecules, as in VEVE and EVEV, exhibited flat morphologies as nanobelts and twisted ribbons, respectively, VVEE and EEVV peptide segments led to the formation of two distinct types of nanofibers. In addition to the amino acid order, the effect of the number of valine-glutamic acid (VE) dimeric repeats on the shape and dimension of the supramolecular nanostructures was also systematically studied.[91] As the length of the peptide sequence increased, a shift from flat to cylindrical structures was observed due to the higher tendency of inducing twisting in β-sheets.

Apart from the discussed nanostructures, Tirrell group designed two different peptides self assembling into worm-like micelles due to their α-helix propensities.[92-93] In the first design, lysine residues were symmetrically distributed around the helical structure to provide individual helices in the micellar state.[92] The results acquired from cryo-TEM, IR and CD revealed that time dependent morphological transition from spherical to worm-like micelles was observed after days and eventually they were transformed into long nanofibrillar structures with outer diameter of ~10 nm. In the second one, they explored the influence of hydrophobic amino acid residues on the self-assembly of PA by inserting four alanine residues between the palmitic acid and oligopeptide sequence.[93] Interposing of hydrophobic alanine residues gave rise to a change in the morphology of corresponding PA from nanoribbons to worm-like micelles, further being confirmed by a secondary structural change from α-helices to β-sheets.

Nanostructural features of peptide amphiphiles can be manipulated by varying the external parameters such as pH, temperature or ionic strength. The effect of pH and temperature on the self-assembly behavior of $C_{16}H_{31}O$-KTTKS was investigated in

two separate studies.[16, 104] While an increase in the temperature gave rise to the formation of micellar structures rather than extended tape structure due to the disruption of hydrogen bonding, a gradual decrease in pH transformed nanotapes into twisted fibrils at pH 4 and spherical micelles at pH 2. Similarly, pH dependent morphological alteration was reported for $C_{12}H_{23}O$-GAGAGAGY PA.[94] Cylindrical nanofibers observed at pH 9 transformed into twisted ribbons at pH 4, most likely due to the neutralization of carboxylic acid and subsequently the weakening of electrostatic interactions, leading to the stacking of the beta sheet laminates. Furthermore, Ghosh *et al.* demonstrated that the tendency of PA to respond to pH change can be programmed by changing the position of single hydrophobic amino acid residue in a short amphiphilic peptide.[95] As isoleucine moved away from the alkyl tail, nanofiber formation was favored over spherical micelles due to the enhanced propensity for the beta sheet formation. In another study carried out by Hamley *et.al.*, thermo-responsive structural change was reported in PAs decorated with a KLVFF core motif that induced self-assembly through π-π stacking and hydrophobic interactions.[26] A reversible unwinding transition was observed between twisted tapes and nanotubes/ribbons in a temperature dependent manner.

Coassembly of two oppositely charged PAs can also lead to some modifications in the self-assembled nanostructures due to the electrostatic interactions occurring between charged amino acid residues. Cylindrical nanofibers were observed by Stupp group upon mixing of oppositely charged palmitoylated peptides.[105-106] Our group also reported that lauric acid anchored lysine and glutamic acid bearing peptides self-assembled into high aspect ratio, one dimensional fibrillar nanostructures.[35] Also, Guler group observed that short bioactive sequences

exploited in the PA design did not alter the shape of resulting supramolecular assemblies.[96, 107-108] Hamley group studied the co-assembly of oppositely charged PAs by mixing them at different ratios.[109] Coassembly driven mainly by electrostatic interactions brought about enhanced beta-sheet formation compared to samples prepared with a single component and resulted in the formation of nanotapes.

The shape of the nanostructure can be tuned by either varying or omitting the beta-sheet forming domain.[103, 110] Guler *et al.* examined the importance of hydrogen bonding among the peptide segment in supramolecular assemblies by replacing trileucine residues with triproline one.[110] Due to the beta sheet breaking nature of proline residues, spherical aggregates were observed instead of cylindrical nanofibers obtained with the former system. Mammadov[111] *et.al.* and Mumcuoglu[97] *et al.* also used proline residues to form micellar structures by disrupting beta sheet secondary structure to study the importance of nanostructural feature in tuning immune response and to develop an efficient delivery vehicle for the transfection of oligonucleotides, respectively. Recently, Moyer *et al.* demonstrated that nanofiber formation was disrupted when beta sheet forming region (A_2V_2) was removed from the peptide sequence and corresponding beta-sheet region removed sequence self-assembled into 5-10 nm diameter of nanospheres depending on the length of the tail.[98]

The insertion of an alkyl tail to a peptide segment was shown to enhance the thermal stability of the corresponding structure.[57, 75] The influence of alkyl tail length, its position and number on the self-assembly of PAs was investigated in detail by several research groups. The van Hest group examined the effect of alkyl tail length on the stability of β-sheet assemblies of GANPNAAG[112] and KTVIIE[113] peptides. As

the length of the tail increased, the thermal stability of the PAs improved and the transition from beta sheet to random coil was observed at higher temperatures. Furthermore, Xu *et al.* synthesized four peptide amphiphiles with different tail lengths by using VRGDV sequence as the peptide domain and showed that PAs with shorter tail lengths did not maintain the stability at higher pHs due to weaker hydrophobic interactions.[99] On the other hand, the relation between the site at which hydrophobic segment are attached to the peptide domain and the resulting nanostructure shape was investigated by incorporating an alkyl tail on either N- or C-terminus of an oligo-histidine peptide sequence and it was revealed that cylindrical and spherical morphologies were obtained at physiological conditions, respectively.[20] He *et al.* reported that while two aliphatic tails attached to one side of the peptide sequence formed long fibrils, peptide being conjugated from either side self-assembled into short twisted fibrils.[114] Differently, van del Heuvel *et al.* showed that stability of the self-assembled nanofibers can be controlled by changing the position of the diacetylene moiety on the hydrophobic tail without playing with the length of the tail.[100] Tirrell and colleagues introduced dialkyl chain containing peptides [115] and investigated the effect of the length of double tail on the thermal stability of collagen like structure in the peptide amphiphile.[116] They further studied the effects of both the number and the length of alkyl tail on the nanostructural feature of model collagen peptide amphiphiles by using the combination of small-angle neutron scattering and cryo-TEM.[117] In their recent design, dialkyl tail conjugated T-cell epitope bearing peptide self-assembled into 8 nm diameter of cylindrical micelles.[101] In addition to dialkyl tail bearing peptide amphiphiles, Cui group designed three Tat peptide conjugates with different numbers of octanoic acid tails.[102] It was reported

that while single and double tail containing peptides could not form any well-defined nanostructure, four aliphatic tails attached one self-assembled into fibrillar structure with diameter of 15 nm, most likely due to enhanced intermolecular hydrogen bonding.

1.6 Biomedical Applications of Peptide Amphiphiles

Peptide amphiphile molecules combining the structural features of amphiphilic surfactants with the bioactive peptides have gained immense interest not only due to their unique nanostructural features but also because they are biocompatible and biodegradable.[7, 83] Their self-assembly process is governed by various noncovalent interactions resulting in the generation of one-dimensional nanofibers under certain solution conditions.[118] Taken together, they are attractive candidates to be used in diverse biomedical applications as drug delivery and antimicrobial agents, tissue scaffolds for regenerative medicine, and imaging probes (Figure 1.7).[119-124]

PAs were shown to be used as local or systemic therapeutic delivery vehicles for the delivery of hydrophobic drugs to a target. While their hydrophobic tail facilitates the translocation through cell membrane and enhances bioavailability, the bioactive sequence specifically interacts with the cell of interest.[125] They can either carry the therapeutic agent or, in most cases, encapsulate it for sustained drug release. Since the self-assembly of PAs generally resulted in the formation of nanofibers, they formed hydrogels which is more suitable for sustained release applications. While Cui group designed hydrophobic drug camptothecin conjugated peptide amphiphile whose peptide segment was derived from tau protein,[126] Stupp group encapsulated the same drug into palmitoyl-$A_4G_3E_3$ peptide nanofibers to treat breast cancer.[127] Elsewhere, release of anticancer agent cisplatin from cell adhesive MMP-2 sensitive

PA nanofibrils was demonstrated through enzymatic degradation.[128] Moreover, anti-inflammatory drug, dexamethasone, conjugated palmitoyl-$V_2A_2E_2K$ nanofiber gel was administered into mice, exhibiting minimal burst release compared to drug-peptide mixture and leading to a remarkable decrease in the number of infiltrating inflammatory cells.[129] Alternatively, our group demonstrated that positively charged fibrillar and micellar peptide-based nanostructures are proper delivery vehicles for negatively charged antisense oligonucleotide drug.[97, 130]

Tirrell and coworkers reported that antimicrobial properties of peptides can be improved by the incorporation of a lipid tail into the peptide segment.[131] Antibacterial activities of several PAs were investigated against some clinical bacteria even though the exact mechanism of action is still contentious. The results revealed that cationic-rich peptide amphiphiles exhibited enhanced antimicrobial activities.[132-133]

Apart from biocompatible nature of PAs, the capability of forming three-dimensional nanofibrous network makes them proper candidates to be utilized in tissue engineering and regenerative medicine as cell culture matrices or scaffolds. Peptide scaffolds exhibited superior adaptabilities to cellular environment compared to polymeric alternatives due to their ability to present bioactive signals and to mimic native extracellular matrix (ECM). Different bioactive domains resulting in specific binding to, such as TGFβ-1, VEGF, heparin, BMP-2 or integrin, were incorporated into peptide amphiphiles to develop scaffolds for articular cartilage regeneration,[120] angiogenesis,[122, 134] bone[135] and spinal cord[136] regeneration. Unlike linear peptide amphiphiles, branched RGDS containing peptide amphiphiles were also reported as suitable scaffolds to grow human bladder smooth muscle cells.[137]

Finally, PAs were also shown to be used as magnetic resonance imaging contrast agents. To obtain positive contrast in MRI, Gd(III) chelation was achieved by the integration of 1,4,7,10-tetraazacyclododecane-1,4,7,10 tetraacetic acid (DOTA) moiety into peptide backbone.[138] On the other hand, iron oxide nanoparticles were decorated with lauryl-VVAGE and lauryl-VVAGK PAs to give negative contrast in MRI.[139]

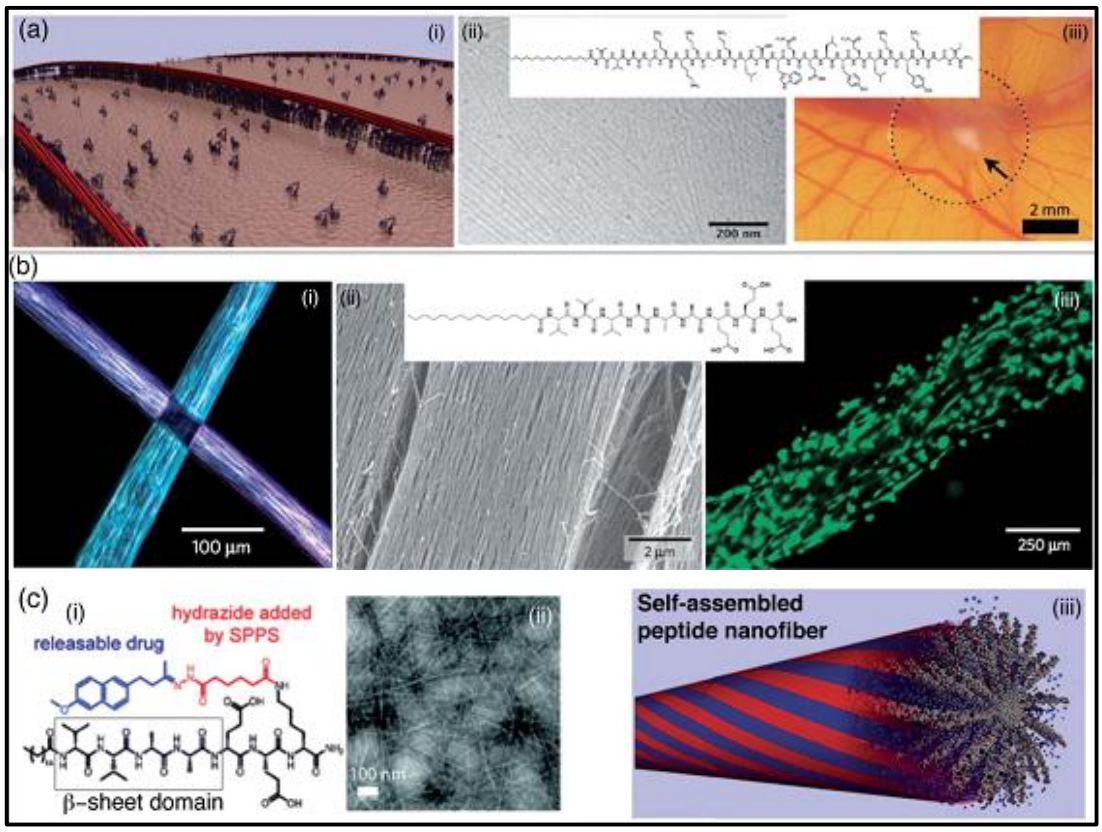

Figure 1.7 Self assembled peptide amphiphiles used in biomedical applications. a) VEGF-mimetic peptide amphiphile presenting high density of biological signals induces angiogenesis. b) Calcein-labeled cells are aligned on the peptide amphiphile nanofiber bundles. c) Peptide amphiphile is conjugated to a drug through reversible covalent bond. (Reproduced from Ref. 124 with permission from Royal Society of Chemistry)

CHAPTER 2

CELL PENETRATING PEPTIDE AMPHIPHILE INTEGRATED LIPOSOMAL SYSTEMS FOR ENHANCED DELIVERY OF ANTICANCER DRUGS TO TUMOR CELLS

Part of this chapter of thesis is published in the following article[140]; Reprinted from "Cell penetrating peptide amphiphile integrated liposomal systems for enhanced delivery of anticancer drugs to tumor cells"*;* Sardan, M., Kilinc, M., Genc, R., Tekinay, A. B., and Guler, M.O., *Faraday Discussions,* 2013, 166, 269-283, with permission from Royal Society of Chemistry

2.1 INTRODUCTION

Liposomes have attracted attention of researchers as potential drug delivery agents for several decades because of their non-toxic, biodegradable nature, as well as their resemblance to cell membrane.[141] The lipid molecules organized in such a way that bilayer structure forms spherical vesicles in aqueous environment due to the amphipathic character of lipids.[142] These artificial membranes are generally composed of phospholipids and their amphiphilic nature enables solubilising the lipids in either nonpolar or polar solvents due to their lipophilic and hydrophilic parts, respectively. Furthermore, liposomes with their amphiphilic feature can entrap both hydrophobic and hydrophilic drugs into their aqueous cavity or into the lipid bilayer.[143] Functional liposomal systems can be decorated with a wide range of bioactive molecules such as antibodies, viral proteins, carbohydrates, peptides, aptamers, and vitamins for therapeutic delivery.[144,145] Various strategies have been employed to functionalize liposomes including chemical anchorage of lipid molecules or ligand of interest before liposome formation, covalent conjugation of biologically active segments to the liposome surface and noncovalent incorporation of liposome constituents.[146, 147, 148] The applicability of the prepared liposomes to deliver antitumor agents, antimicrobial substances and immunological adjuvants have been extensively studied.[149-152]Apart from drugs, genes and DNA were also encapsulated into liposomal systems.[153-154] Several liposomal formulations have already in market and some of them have currently been in clinical trial phase.[155]

Peptide amphiphiles with their bioactive peptide sequence and lipidic tail are promising candidates for the functionalization of liposomal carriers. They can be

noncovalently incorporated into liposomes by means of their lipid-like amphipathic property with minimized activity loss or without compelling chemical functionalization steps.[156,157-159] Not only the ease of functionalization but also high encapsulation capacities make them attractive tools for the construction of carrier systems, which can deliver cargo to the target with improved *in vivo* stability and prolonged circulation time.[160] In addition to their simple integration, diversity in the biofunctionality of the liposomal carriers can be provided by utilizing distinct peptide sequences.

Membrane permeability is a critical issue for the translocation of the exogenous molecules in drug delivery applications. It was previously reported that cell penetrating peptides including human immunodeficiency virus type 1 (HIV-1), Tat and *Drosophila* Antennapedia derived peptides, oligoarginines, and chimeric cell penetrating peptides have been utilized in several studies as a component of a delivery vehicle carrying therapeutic agents to target cells.[161,162] They have ability to translocate through cell membrane and deliver the cargo to cytoplasm and nucleus.[163] Among these, a series of oligoarginine peptides with or without lipidic tail were synthesized and evaluated in terms of cellular uptake efficiencies, where it was revealed that the delivery efficiencies were improved by fatty acid integration.[164]

In this chapter, an arginine rich, cell penetrating amphiphilic peptide molecule was synthesized and its integration into liposomal formulation composed of negatively charged 1,2-dioleoyl-*sn*-glycero-3-[phosphor-*rac*-(1-glycerol)] (DOPG) phospholipid and cholesterol was analyzed with different techniques. Physical properties such as size, surface potential, and membrane polarity of

resulting PA free and PA integrated liposomes were examined by using TEM, DLS and spectroscopic methods. Hydrophilic and hydrophobic dyes, Rhodamine B and Nile Red, respectively, were encapsulated into the liposomal formulations and their encapsulation efficiencies were determined by employing specific equations after some theoretical assumptions. Optimization of the encapsulation efficiencies of dye loaded liposomes was followed by *in vitro* cytotoxicity and uptake experiments. For that purpose, two known cancer drugs, hydrophilic Doxorubicin-HCl and hydrophobic Paclitaxel, were entrapped into PA free and PA incorporated liposomes and the *in vitro* examination was carried out with human breast cancer cell line MCF7.

2.2 EXPERIMENTAL SECTION

2.2.1 Materials

9-Fluorenylmethoxycarbonyl (Fmoc) and *tert*-butoxycarbonyl (Boc) protected amino acids, [4-[α-(2',4'-dimethoxyphenyl) Fmoc-aminomethyl] phenoxy] acetamido norleucyl-MBHA resin (Rink amide MBHA resin), and 2-(1*H*-Benzotriazol-1-yl)-1,1,3,3 tetramethyluronium hexafluorophosphate (HBTU) were purchased from NovaBiochem and ABCR. Lauric acid was purchased from Merck. 1,2-dioleoyl-*sn*-glycero-3-[phosphor-*rac*-(1-glycerol)] (DOPG) was purchased from Avanti Polar Lipids. Other chemicals were purchased from Alfa Aesar, Sigma-Aldrich or Applichem and used without further purification.

2.2.2 Synthesis and Characterization of Peptide Amphiphile

Lauryl-PPPPRRRR-Am peptide amphiphile was constructed on MHBA Rink Amide resin (loading= 0.56 mmol/g). Amino acid couplings were performed with 2 equivalents of Fmoc protected amino acid, 1.95 equivalents of HBTU and 3 equivalents of N,N-diisopropylethylamine (DIEA) in DMF for 3 h. 20% piperidine/dimethylformamide (DMF) solution was administered for 20 min to cleave Fmoc protecting group. Resin bound peptide was cleaved from the solid support and other protecting groups residing in side chains of amino acids were cleaved by treating with a mixture of trifluoroacetic acid (TFA) : triisoproplysilane (TIS): water in the ratio of 95:2.5:2.5 for 2 h. Excess TFA was removed by rotary evaporation and remained viscous peptide solution was treated with ice-cold diethyl ether and the resulting white pellet was freeze-dried. The peptide amphiphiles were elucidated by reverse phase HPLC on an Agilent 6530 accurate-Mass Q-TOF LC/MS equipped with an ESI source. An Agilent Zorbax SB-C8 4.6 mm x 100 mm column as stationary phase and water/acetonitrile gradient with 0.1% volume of formic acid as mobile phase were used to identify peptide amphiphile molecule.

2.2.3 Liposome Preparation

Curvature tuned preparation method, reported previously,[165] was used for the preparation of the liposomes. Basically, rehydration of 50 mg of phospholipid formulation in PBS buffer (10 mM, pH 7.4, 3% glycerol, with and without encapsulated material) was performed at 65 °C under nitrogen supply while the mixture was continuously stirred, followed by treating the solution with a rapid pH jump (pH 7.4 to pH 11 and to pH 7.4) continuing with an equilibrium period

of 25 min, where lipid clusters transformed into encapsulating nanosized liposomes. G50 Sephadex column was used for the purification of resulting liposomes and stored at 4 °C.

2.2.4 Particle Size and Zeta-Potential by Dynamic Light Scattering

A Malvern ZetaSizer nano-ZS ZEN 3600 (Malvern Instruments, USA) instrument with detector angle of 173° was used to determine the mean diameter and zeta-potential of liposomes. Standard deviations were derived from the mean of the data from a series of experiments ($n \geq 3$). Also, zeta potential measurements were conducted by using a dip cell electrode in quartz cuvettes.

2.2.5 Transmission Electron Microscopy

Using a glass pipette, a drop of sample was placed on a 200 mesh formvar coated copper grid. While PA free liposomes were stained with 2% (w/w) of phosphotungstic acid, PA integrated liposomes were stained with 2% (w/w) of uranyl acetate. After removing excess dye, they were carefully dried under the fume hood. Sample was allowed to stay at room temperature to dry until a dried film was obtained. A TEM (FEI Tecnai G2 F30) operated at 100 keV was used to image the prepared liposome formulations.

2.2.6 Spectroscopic Analysis for the Determination of Nile Red Integration into Liposomes

1.5 mM of Nile Red was initially dissolved in ethanol and further diluted in water to 10 μM. Nile Red fluorescence intensity maxima shifts depending on the polarity of the environment and, accordingly, Nile Red dye solubility in different types of liposomes was analyzed and compared in between the formulations with

and without peptide amphiphile molecules. 1.05 ml of two times diluted liposome solutions (2.5 mg/mL) or PBS were mixed with 450 μL of Nile Red solution whose final dye concentration was set to 3 μM. Samples were incubated for 24 h at 4 °C. Micellar character was determined by measuring the fluorescence intensity of liposomes in PBS (λ_{exc}= 520 nm, λ_{em}= 525-700 nm) with a Varian Eclipse Fluorescence Spectrophotometer.

2.2.7 Quantification of the Amount of Integrated Peptide Amphiphile Molecules into Liposomal Membrane

Protein concentration determination procedure offered by Thermo Scientific was utilized to indirectly quantify the amount of peptide amphiphile molecules integrated into liposomal systems. The measurements were taken at 205 nm with extinction coefficient of 31 mg/mL at 1 cm path length. The peptide amphiphile solutions were prepared at different concentrations in the range of 0.6 mg/mL to 0 mg/mL by several dilutions. Firstly, liposomes were centrifuged and separated from free peptide amphiphile molecules by using Millipore Microcon Centrifugal Filter Units, with 50K MW cut-off, 3 to 4 times. The elutions were collected in each step and peptide amphiphile concentration was measured by NanoDrop 2000 (Thermo Scientific). The amount of integrated PA into liposomal system was then calculated by subtracting the amount of free PA from the initial PA concentration. Obtained results were further utilized in the calculation of the number of peptide amphiphile per liposome.

2.2.8 Encapsulation of Liposomes with Model Reagents and Anticancer Drugs

2.2.8.1 Hydrophilic Dye and Drug Encapsulation

Rhodamine B was used as a model hydrophilic dye molecule. Two initial concentrations (10 μM and 100 μM) were selected for the liposome encapsulation, as described in the liposome preparation procedure. Millipore Microcon Centrifugal Filter Units, with 50K MW cut-off (3 to 4 times), were used to discard free Rhodamine B molecules from liposome solution. The integrity of the purified liposomes were destructed in the presence of ethanol (100 μL liposome in 1900 μL ethanol) to release the loaded dye and encapsulated Rhodamine B amount was determined by a Varian Eclipse Fluorescence Spectrophotometer (λ_{exc}= 540 nm, λ_{em}= 575 nm). Total encapsulated and % encapsulated Rhodamine B concentration was then calculated by E (%) = (measured intensity/initial dye intensity) x 100. Standard curve was plotted with the solutions prepared from known amount of Rhodamine B solutions which were serially diluted and used for the determination of encapsulated dye concentration.

Same procedure was carried out for the determination of encapsulated hydrophilic drug (Doxorubicin-HCl) which was encapsulated with an initial concentration of 0.2 mg/mL. Similarly, standard curve was also obtained for Doxorubicin-HCl by fluorescence measurements (λ_{exc}= 480 nm and λ_{em}= 588 nm).

2.2.8.2 Hydrophobic Dye and Drug Encapsulation

Nile Red was used as a model dye for hydrophobic drug encapsulation. First, dye encapsulation was studied by measuring the increased emission (λ_{exc}= 476 nm,

λ_{em}= 633 nm) of dye dissolved in ethanol and then 0.53 μM of Nile Red was administered into previously prepared PA integrated and PA free liposomes. After 24 h, all samples reached to a maximum which means that all possible dye molecules integrated into liposomal membrane. At that point, the integrity of liposomal membranes were destructed by the addition of 1900 μL of ethanol into 100 μL of liposomes and encapsulated Nile Red concentration was calculated by using standard curve obtained from Nile Red with known concentrations. Same equation **(**E (%) = (measured intensity/initial dye intensity) x 100) was used to calculate the encapsulation efficiency.

Paclitaxel was chosen as the hydrophobic drug, encapsulated into prepared liposomal formulations. Encapsulation capacities and efficiencies of liposome formulations were calculated based on a HPLC procedure optimized by Wang *et al.*[166] Unlike the Nile Red extraction, acetonitrile was used instead of ethanol to extract Paclitaxel from the liposomes (100 μL of liposome in 900 μL acetonitrile). Sample was filtered with a 0.2 mm syringe filter prior to the injection into HPLC-1200S (Agilent) to quantify the encapsulated Paclitaxel amount. 10 μL sample solution was injected into Eclipse XDB-C18 (4.6 x 150 mm, 5 μm) column. Water and acetonitrile (53:47, v/v %) was used as mobile phase. Elution rate was adjusted to 1.0 mL/min and 229 nm was selected as the paclitaxel detection wavelength. The drug concentration of Paclitaxel was calculated from standard curves.

2.2.9 Release Study for Rhodamine B

The release of the hydrophilic Rhodamine B from liposomes was studied by using dialysis when liposomes were suspended in 10% FBS containing PBS medium.[166]

A dialysis bag (Spectra/Por membrane MWCO 500-1000 Da, 24 mm flat width, Spectrum Medical Industries, Los Angeles, CA) was used to place Rhodamine B encapsulated liposomes. The experiment was performed at two different pH conditions (pH 7.4 and pH 5.5) while Rhodamine B encapsulated liposomes were dialyzed against 50 mL of PBS at 37°C. At predetermined time points (0.5, 1, 2, 4, 18, 24, 48, 72 h), 1 mL aliquots of dialysis buffer were removed and replaced by equal volume of fresh buffer at 37 °C. The results were represented as the percentage of cumulative release, obtained by reading the fluorescence intensity of Rhodamine B at each time interval upto 72 h (λ_{exc}= 540 nm, λ_{em}= 575 nm).

2.2.10 *In Vitro* Studies

Cytotoxicity was assessed by using Alamar Blue™ assay. MCF7 cells were treated with 10% FBS and 1% penicillin/streptomycin containing DMEM under 5% CO_2 at 37 °C. 50 µL of liposome with or without peptide formulations were administered prepared at different PA concentrations (250, 25 and 12.5 µM, n=4 for all groups). After 4 h and 24 h of treatment, culture media was replaced with serum free DMEM supplemented with 1% penicillin/streptomycin and 10% Alamar Blue™ solutions and samples were incubated for an additional 4 h. Microplate reader (Molecular Devices Spectramax M5) was used for the quantification of cell viability.

Uptake profiles of PA integrated liposomes were examined with Rhodamine B and Nile Red loaded samples. Firstly, MCF7 cells were seeded at a density of 3 x 10^4 cells per well in 24 well plates. 4.5 µM of Rhodamine B and 10 µM of Nile Red were administered and plates were individually incubated for 3 h. Lysed cells were centrifuged and the supernatants were used conducted to measure the

Rhodamine B and Nile Red concentrations by Nanodrop 3300. (λ_{exc}= 540 nm, λ_{em}= 590 nm for Rhodamine B and λ_{exc}= 476 nm, λ_{em}= 633 nm for Nile Red.) The relative uptake values were obtained after measured values were normalized to protein concentrations. Bradford protein assay (Roche) was used to determine the protein concentration of lysates.

Fluorescence imaging of Nile Red encapsulated liposomes were performed with Zeiss AxioCam^{TM} fluorescence microscope. MCF7 cells were seeded at a density of 1 x 10^4 cells per well in 24 well plates. After 24 h of incubation and washing steps, they were visualized on glass slides.

For drug encapsulated liposomes, the cytotoxicity was assessed by Alamar Blue assay. MCF7 cells were cultured in 96-well plates at a cell density of 8 x 10^3 and 4 x 10^3 cells per well for Doxorubicin-HCl and Paclitaxel loaded liposomes, respectively. The cells were treated with drug loaded liposomes or soluble drugs for different period of time (1, 3 and 6 h), where 10 μM of Doxorubicin-HCl and 30 μM of Paclitaxel were selected as the final concentration of drugs for time response experiments. Also, cytotoxicity was evaluated by changing the drug concentrations (0.1 μM - 10 μM for Doxorubicin-HCl, 0.2 nM - 10 μM for Paclitaxel) while keeping time and liposome concentrations constant for dose response experiments. After 24 h of incubation, Alamar Blue assay was performed to assess the cytotoxicity.

2.2.11 Statistical Analysis

All data were presented as standard error of the mean (mean ± SEM). One-way or two-way analysis of variance (ANOVA) was used to determine the significance of differences between groups. Differences were considered significant when p

value is smaller than 0.05.

2.3 RESULTS AND DISCUSSION

2.3.1 Synthesis and Characterization of Liposomes

Cell penetrating arginine-rich peptide amphiphile integrated and non-integrated liposomes were prepared based on curvature tuned liposome preparation (CTLP) method, in which sudden pH jump and constant temperature were the triggering factors for phospholipid residues to be ordered in a nanostructure.[165] In this study, negatively charged phospholipid DOPG was used as one of the main components of the liposomes.[167] The fluidity and curvature of the membrane, as well as the physical properties of the resulting liposome such as particle size, zeta potential and morphology can be affected if an additional amphiphilic molecule is integrated into the liposomal membrane. Previously, it was observed that DOPG liposomes prepared by CTLP methodology with a size of 20 nm in diameter were not large enough to develop an efficient drug delivery system.[165, 168] Therefore, cholesterol was added into the formulation to decrease the curvature of the liposomal membrane leading to the formation of larger liposomes and to afford intermediate membrane fluidity and integrity, as well as enhanced circulation time.[169] As shown in Table 2.1, homogenously distributed liposomes with a size of 63.5±8.2 nm in diameter and a net negative charge of -41.4±3.9 mV were obtained when liposomal formulation was composed of negatively charged phospholipid DOPG and cholesterol at a molar ratio of 1:1. Unilamellarity of the resulting liposome membrane was confirmed by transmission electron microscopy (Figure 2.1).

Table 2.1 Physical properties of liposomes composed of DOPG:Chol

Liposome Formulation (molar ratio)	Size(nm)±SD	PDI	ζ-Pot (mV) ±SD
DOPG:Chol (1:1)	63.5±8.2	0.43	-41.4±3.9

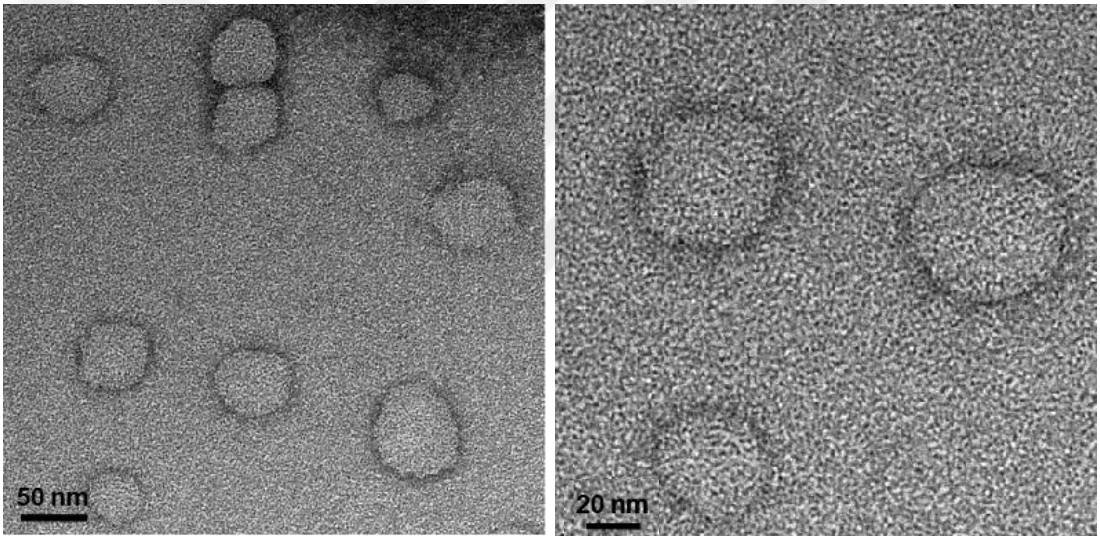

Figure 2.1 Transmission electron microscope images of liposomes composed of 1:1 molar ratio of DOPG:Chol (scale bars= 50 nm and 20 nm, respectively).

Liposome functionalization with cell penetrating peptides can be achieved by different strategies. Covalent attachment of a peptide to a lipid through different chemistries prior to the liposome formation or direct functionalization on the surface of already formed liposome is common strategies to afford peptide incorporated

liposomal systems. Both strategies not only require additional steps and lead to the reduction of the peptide integration efficiency but might also result in the loss of activity.[170] Thus, significant effort has been devoted to the development of noncovalent strategies to avoid problems associated with chemical modifications.[171] Due to the resemblance of peptide amphiphiles to phospholipids in terms of their amphiphatic nature, utilizing amphiphilic peptides in noncovalent liposome functionalization is a promising approach.[172,173] For this purpose, we designed and synthesized an arginine rich peptide amphiphile (PA) molecule composed of a lauryl group and arginine rich amino acid sequence, Lauryl-PPPPRRRR-Am (Figure 2.2). In the design, proline residues that impede the formation of hydrogen bonding as well as beta-sheet structure were used to enhance the integration of the PA into liposomal membrane.[110] In Figure 2.2, chemical structures of other two constituents of liposomal system were also illustrated. Corresponding PA was synthesized via solid phase peptide synthesis method and the chemical identity of the resulting PA was analyzed by liquid chromatography mass spectroscopy (Figure 2.3). Since the PA contained four positively charged arginine residues, we observed different masses corresponding to m/z values of same PA in the mass spectrum.

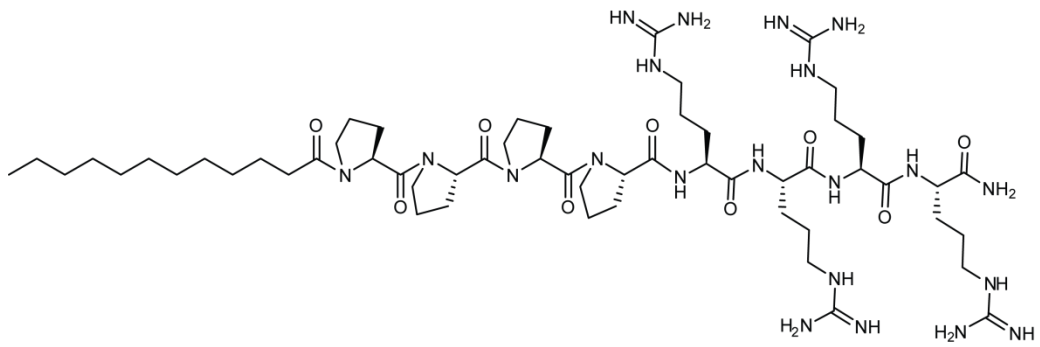

Lauryl-PPPPRRRR-Am

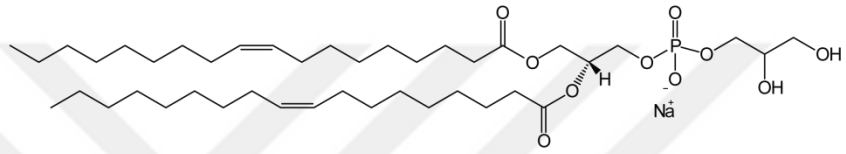

1,2-dioleoyl-sn-glycero-3-phospho-(1'-rac-glycerol) (DOPG)

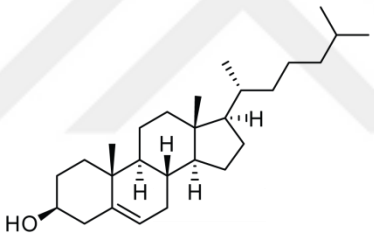

cholesterol

Figure 2.2 Chemical structures of peptide amphiphile (PA) Lauryl-PPPPRRRR-Am, negatively charged phospholipid 1,2-dioleoyl-*sn*-glycero-3-phospho-(1'-*rac*-glycerol) (DOPG) and cholesterol.

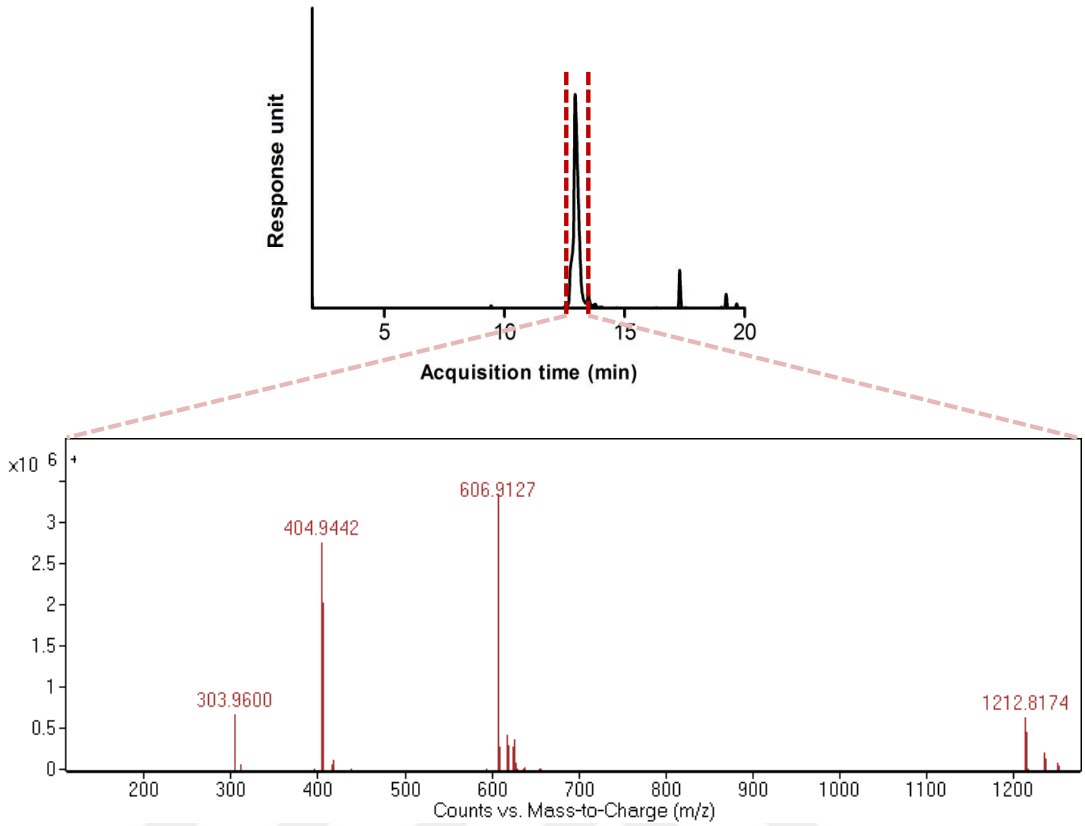

Figure 2.3 Liquid chromatogram of Lauryl-PPPPRRRR-Am and mass spectrum of corresponding peptide molecule. Mass data $[M+H]^+$ (calculated) = 1212.54, $[M+H]^+$ (observed) = 1212.82, (observed $[(M+2H)/2]^+$= 606.91, $[(M+3H)/3]^+$= 404.94, $[(M+4H)/4]^+$= 303.96).

In addition to DOPG and cholesterol, the arginine rich PA molecule was used as the third liposomal constituent of the formulation. Two different formulations in which PA amount showed variations were prepared at molar ratios of 7:8:1 and 7.5:8:0.5 (DOPG:Chol:PA) to investigate the effect of PA content in terms of cell penetration. PA integrated liposomes had similar hydrodynamic sizes and zeta potentials. While hydrodynamic sizes of higher dose PA containing liposomes were 95.26±7.03 nm, the diameters of lower dose PA containing liposomes were 98.49 ± 4.9 (Table 2.2 and Figure 2.4). Although zeta-potential values rose up to -30.4 mV and -33.2 mV

from -41.4 mV for higher and lower dose PA containing liposomes, respectively, due to the integration of positive net charge bearing guanidinium groups of arginine residues, PA integrated liposomal systems did not exhibit significant difference with respect to each other.

Table 2.2 Physical properties of PA integrated liposomes

Liposome Formulation (molar ratio)	Size(nm) ±SDV	PDI	ζ-Pot (mV) ±SDV	Peptide Integration (%)	Integrated PA/Liposome
DOPG:Chol:PA (7:8:1)	95.26±7.03	0.46	-30.4±2.57	75.40	4568
DOPG:Chol:PA (7.5:8:0.5)	98.49 ± 4.9	0.32	-33.2 ± 1.71	77.24	2706

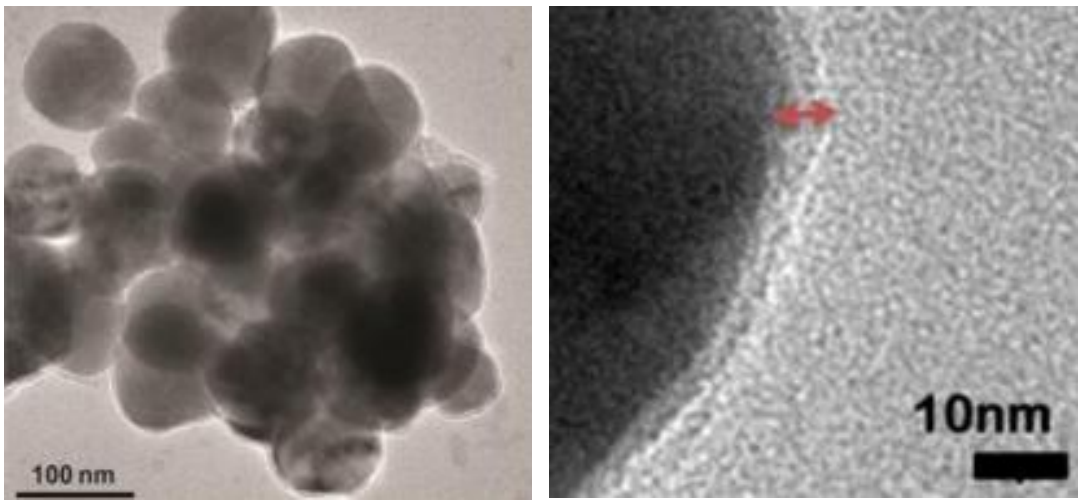

Figure 2.4 Transmission electron microscope images of liposomes composed of 7:8:1 molar ratio of DOPG:Chol:PA (scale bars= 100 nm and 10 nm, respectively).

The amount of the peptide molecules incorporated to the liposomal membrane was indirectly calculated by measuring the absorbance of unbound peptide molecules collected by ultrafiltration process at 205 nm.[173] As shown in Table 2.2, 4568 and 2706 peptide amphiphile molecules were estimated to be integrated per liposomal system for higher and lower amount of PA containing systems, respectively.

The number of membrane integrated peptide amphiphile per liposome was calculated according to the given equations.[174] Firstly, total number of lipid molecules per vesicle was estimated from Equation 1 shown below,

$$\mathbf{Ntot} = \frac{\left[4\pi\left(\frac{d}{2}\right)^2 + 4\pi\left(\frac{d}{2} - h\right)^2\right]}{a} \qquad \text{(Eq. 1)}$$

where lipid bilayer thickness was denoted as $\boldsymbol{h}$ and taken as 5 nm, $\boldsymbol{d}$ is the diameter of a unilamellar vesicle derived from dynamic light scattering measurements, and $\boldsymbol{a}$ is the average area of polar head group. Average area per lipid molecule ($\boldsymbol{a}$) was calculated as $\boldsymbol{a}=\boldsymbol{a}_1N_1+\boldsymbol{a}_2N_2+...+\boldsymbol{a}_nN_n$, where; N is the molar fraction of each component. $\boldsymbol{a}$ values for each amphipathic molecule used in liposomal formulations were 69 $Å^2$ for DOPG, 41 $Å^2$ for cholesterol and 75 $Å^2$ for PA .[175-176] The latter one was obtained by using ChemDraw Ultra 8.

Secondly, theoretical number of membrane integrated peptide amphiphiles was calculated by using total number of lipid molecules per liposome (Ntot) value estimated from previous equation and molar concentration of the membrane integrated peptide amphiphile (Mpep) value obtained from liposome preparation experiment and it was formulated in Equation 2 where NA is the Avogadro

number,

$$\mathbf{Npep} = \frac{\mathbf{Mpep\ x\ NA}}{\mathbf{Ntot}} \qquad \text{(Eq. 2)}$$

Peptide amphiphile integration was also confirmed by a fluorescence assay utilizing Nile Red molecule as a polarity sensitive probe.[177] Normally, Nile Red dispersion is transparent in aqueous conditions; however, changes in environment of this hydrophobic dye results in a switch from polar to nonpolar in the presence of phospholipid or any kind of amphiphilic molecule and give an increased fluorescence emission. In the case of peptide integrated liposomes, a blue shift was observed indicating a slight decrease in membrane polarity as expected (Figure 2.5). This data in conjunction with the results obtained from size and zeta-potential measurements confirmed that peptide amphiphiles were integrated into the liposomal membrane, and enhanced the nonpolar character of the membrane, which can be considered as an advantage for the encapsulation of hydrophobic molecules.

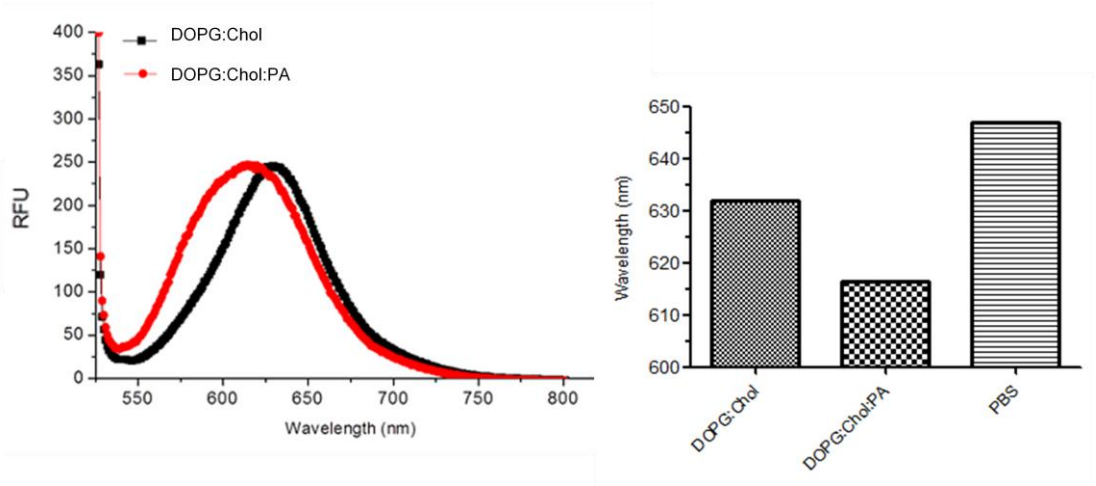

Figure 2.5 Fluorescence measurements performed with Nile Red for the investigation of PA integration into the liposomal membrane.

2.3.2 Encapsulation of Dyes and Anticancer Drugs

Since liposomes have ability to encapsulate both hydrophobic and hydrophilic molecules, we firstly investigated the encapsulation efficiencies of PA free and PA integrated liposomes by using fluorescent hydrophilic Rhodamine B and hydrophobic Nile Red molecules and then continued with cancer drugs, hydrophilic Doxorubicin-HCl and hydrophobic Paclitaxel (Figure 2.6 and 2.7).

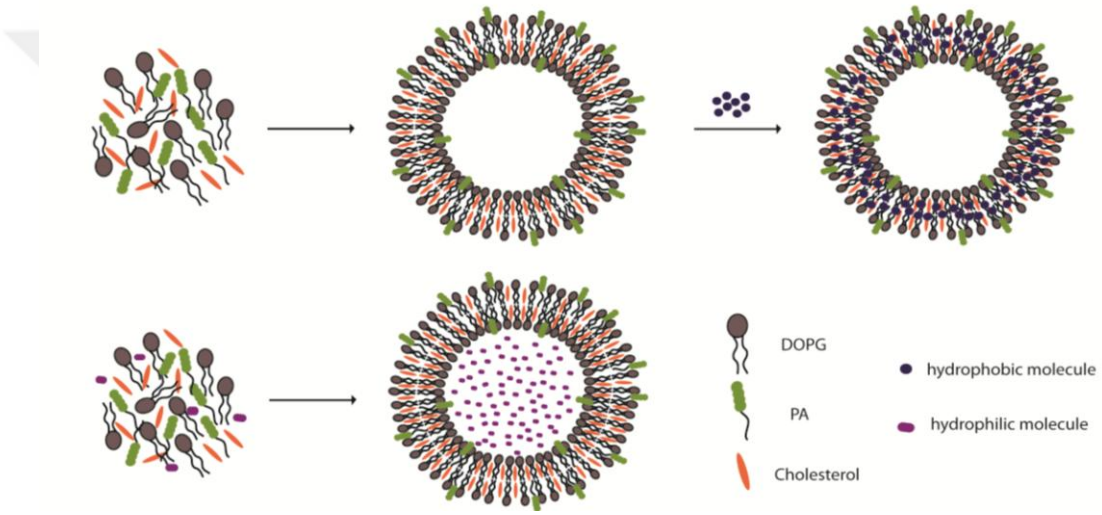

Figure 2.6 Schematic illustration for the preparation of PA integrated liposomes loaded with hydrophobic (Nile Red, Paclitaxel) or hydrophilic (Rhodamine B, Doxorubicin-HCl) molecules.

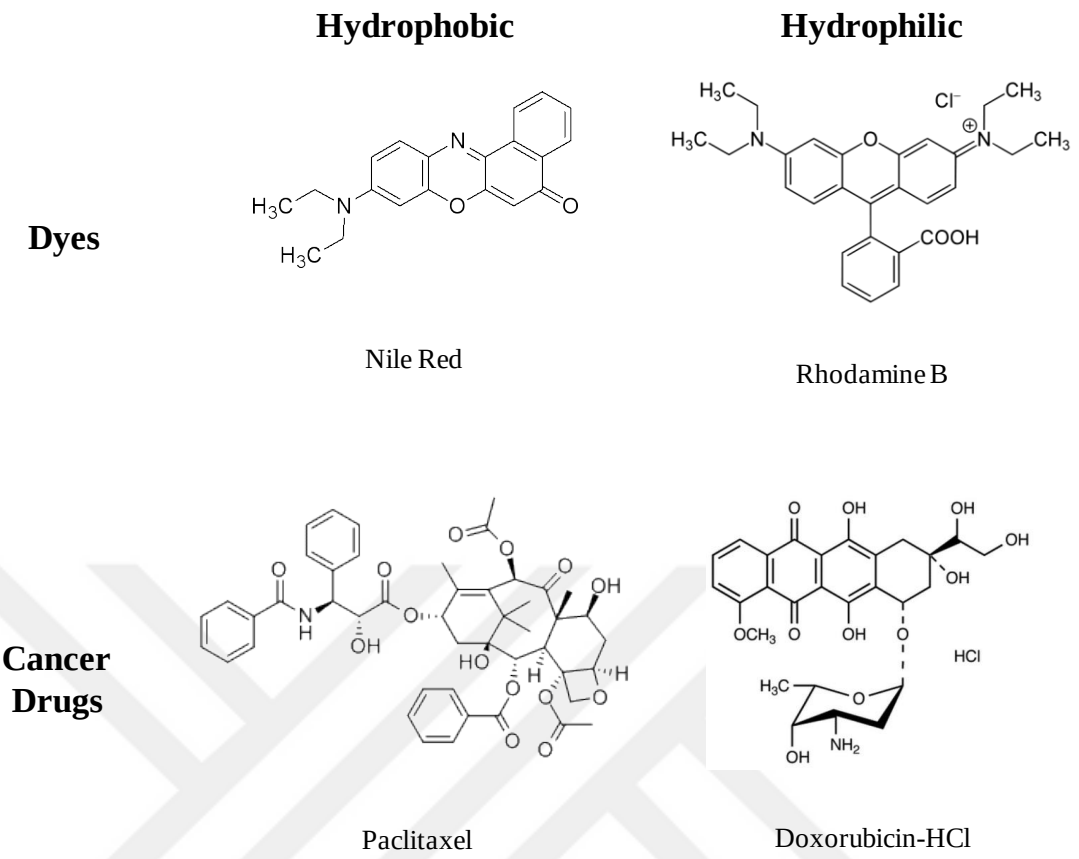

Figure 2.7 Chemical structures of hydrophobic and hydrophilic dyes and cancer drugs used for liposomal encapsulation.

2.3.2.1 Encapsulation of Dyes: Rhodamine B and Nile Red

Rhodamine B, a hydrophilic fluorescent dye, was used to probe the encapsulation capacities of both PA free and PA integrated liposomes. Rhodamine B was administrated into the solution during the liposome preparation at two different concentrations (10 μM and 100 μM) and it was observed that encapsulation capacities of both liposomal systems were affected from the initial dye concentration. Before determining the encapsulation efficiencies, calibration curves were derived by measuring the emission intensities of known concentration of Rhodamine B dissolved in PBS or ethanol (Figure 2.8). Although a slight decrease was observed in

the encapsulation efficiency of liposomes from 36% to 30% after PA integration, their encapsulation capacities increased three-fold compared to PA free liposomes due to their larger internal volume (Table 2.3).

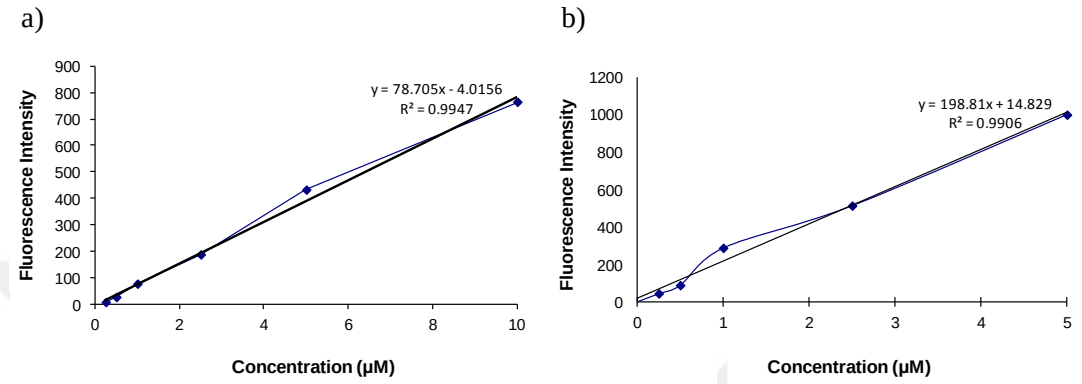

Figure 2.8 Rhodamine B calibration in (a) PBS and (b) ethanol (λ_{ex}= 540 nm, λ_{em} = 575 nm).

Table 2.3 Encapsulation of Rhodamine B by PA free and PA integrated liposomes

Liposome Formulation	**Encapsulated Rhodamine B (μM) ±SD**		**Number of Rhodamine B/ Liposome**	
	Initial Rhodamine B Concentration		Initial Rhodamine B Concentration	
	10 μM	100 μM	10 μM	100 μM
DOPG:Chol	7.90±0.8	36.3±3.9	4.15 x10^4	19.1 x10^4
DOPG:Chol:PA	7.00±0.4	30.5±2.2	12.4 x10^4	54.0 x10^4

The number of encapsulated dye molecules by liposomal systems was calculated based on the given equations. Firstly, the number of liposome per mL (Nlip) was calculated for known amount of liposomes by using Equation 3, which is quite similar to the calculation of the number of membrane integrated peptide amphiphile molecules.

$$\mathbf{Nlip} = \frac{\mathrm{M(lipid)\ x\ NA}}{\mathrm{Ntot\ x\ 1000}} \qquad \text{(Eq. 3)}$$

where NA is the Avogadro number, M(lipid) is the average molar concentration of lipidic region containing molecules, and Ntot is the total number of lipids per liposome, which was previously shown how to be calculated. Finally, number of encapsulated material (N(Enc)) can be calculated by using Equation 4. M(Enc) is the molar concentration of encapsulated material per mL of the sample.

$$\mathbf{N(Enc)} = \frac{\mathrm{M(Enc)\ x\ NA}}{\mathrm{Nlip}} \qquad \text{(Eq. 4)}$$

On the other hand, Nile Red was used as a hydrophobic model molecule to observe the encapsulation capacities of PA integrated and PA free liposomes**.** Since the hydrophobic dye encapsulation was performed after liposomes were prepared, free Nile Red was firstly removed and dye encapsulated liposomes were dissolved in ethanol to destruct the liposomal membrane and subsequently release the dye. Firstly, a calibration curve was plotted for Nile Red dissolved in ethanol (Figure 2.9). By this way, it was possible to quantify the amount of encapsulated hydrophobic dye molecule. Due to slightly lower polarity and larger lipophilic surface area, an increase in the encapsulated Nile Red molecule was observed for PA integrated

liposomes compared to the PA free liposomes (Table 2.4). The results can also be represented in terms of number of encapsulated dye per liposome as $7.9x10^5$ and $31.3x10^5$ for native and PA integrated liposomes, respectively. When the results were represented in terms of number of encapsulated dye per liposome, four-fold increase in the number of encapsulated hydrophobic dye molecule was seen in PA decorated liposomes with respect to PA free liposomes due to the larger surface area and larger vesicle size of PA integrated liposomes.

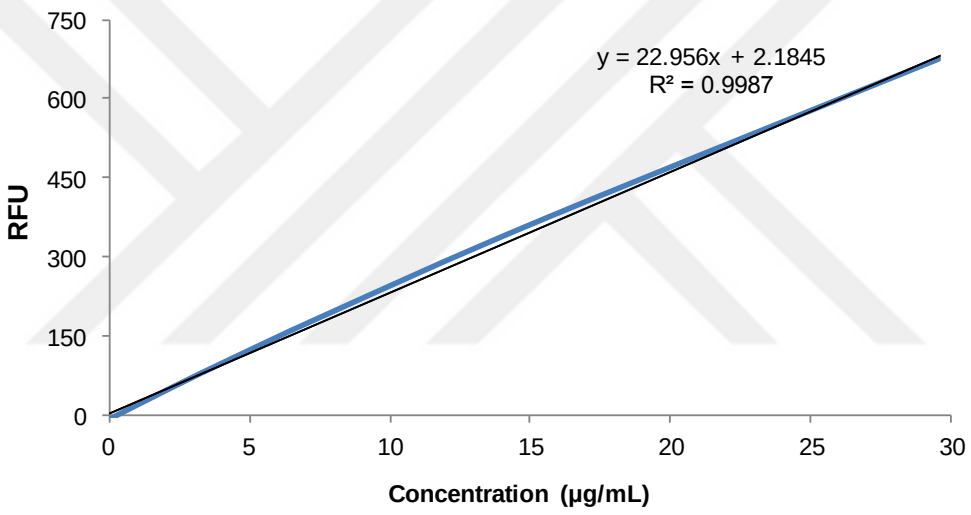

Figure 2.9 Nile Red calibration in ethanol (λ_{ex}= 474 nm, λ_{em}= 633 nm).

Table 2.4 Encapsulation of Nile Red by PA free and PA integrated liposomes

Liposome Formulation	**Encapsulated Nile Red (µM)±SD***	**Number of Nile Red/ Liposome**
DOPG:Chol	150.4±5.2	$7.90\ x10^5$
DOPG:Chol:PA	176.7±6.7	$31.3\ x10^5$

*Initial Nile Red concentration was 0.53 mM.

2.3.2.2 Encapsulation of Anticancer Drugs: Doxorubicin-HCl and Paclitaxel

The effect of arginine-rich cell penetrating peptide integration on liposomal delivery was examined by using two well-studied cancer drugs, hydrophilic Doxorubicin-HCl and hydrophobic Paclitaxel (Figure 2.7). For Doxorubicin-HCl and Paclitaxel encapsulations, liposomal content to drug ratio (w/w) were adjusted to 1:25 and 1:15, respectively. Not only the liposome formulation but also the liposome preparation methods are important parameters affecting the encapsulation capacity.[178] Therefore, influence of peptide integration on encapsulated cancer drugs were systematically studied. While Doxorubicin-HCl amount was estimated by using fluorescence spectroscopy (Figure 2.10), HPLC was utilized to determine the quantity of encapsulated Paclitaxel (Figure 2.11). Similar to the estimation of the concentration of encapsulated dyes, calibration curves for both drugs were provided. The concentration of encapsulated drugs, the number of drug per liposome and corresponding encapsulation efficiencies for both liposomal systems were determined and presented in Table 2.5 and 2.6. The obtained results were correlated with the studies carried out with model dyes.

For hydrophilic drug, encapsulated Doxorubicin-HCl was calculated as 0.26 mM and 0.23 mM for native and PA integrated liposomes, respectively. Encapsulation efficiency was 75% in PA free liposomes and this value was 66% in PA integrated liposomes, which is still higher than acceptable (Table 2.5). Since Doxorubicin entrapment was achieved by pH gradient method after liposome preparation in most of the studies, lower encapsulation efficiencies in between 5-30% were reported.[178-179] Thus, pH jump method that we have exploited during both PA free and integrated liposome preparations significantly improved Doxorubicin-HCl encapsulation.

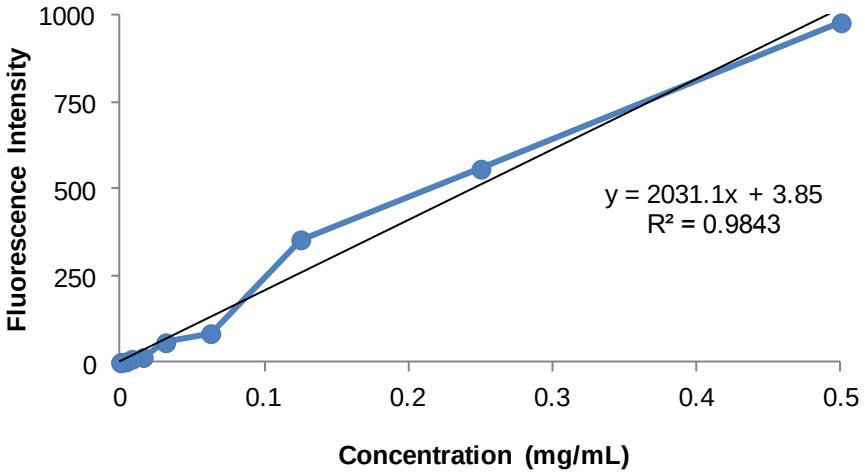

Figure 2.10 Doxorubicin-HCl calibration in ethanol (λ_{ex}= 480 nm, λ_{em}= 588 nm).

Table 2.5 Doxorubicin-HCl encapsulation capacities of two liposomal formulations

Liposome Formulation	Encapsulated Doxorubicin-HCl (mM)±SD*	Number of Doxorubicin-HCl/ Liposome	Encapsulation Efficiency (%)
DOPG:Chol	0.258± 2.6×10^{-4}	1.36×10^{3}	75.0
DOPG:Chol:PA	0.227±1.2×10^{-3}	4.03×10^{3}	65.9

*Initial Doxorubicin-HCl concentration of this sample was 0.344 mM.

Paclitaxel is a known hydrophobic drug, which is currently used in 50:50 (v/v) mixture of Cremophor® and ethanol. Serious side effects associated with Cremophor® and possible precipitation of Paclitaxel in aqueous media were considered as the drawbacks of current formulation; thus, development of new carrier materials with high entrapment efficiency have garnered great deal of interest.[180] Similar to Nile Red encapsulation results, PA integrated liposomes

showed higher encapsulation efficiency compared to PA free liposomes stemming from more nonpolar membrane of PA integrated liposomes compared to PA free liposomes. The concentration of encapsulated Paclitaxel was 92 µM in native liposomes and it increased to 117 µM in PA integrated liposomes (Table 2.6). When the number of entrapped molecules per liposome was estimated for individual drugs, PA integrated liposomes showed superior encapsulation efficiency over PA free liposomes (Table 2.5 and 2.6).

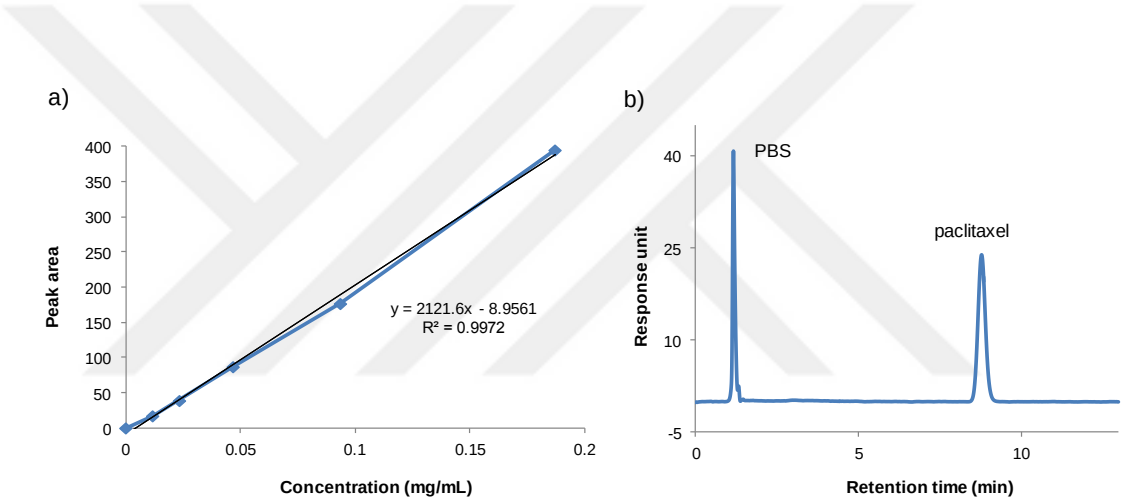

Figure 2.11 a) Calibration curve of Paclitaxel plotted from HPLC results, b) HPLC chromatogram of 0.16 mg/mL Paclitaxel in PBS.

Table 2.6 Paclitaxel encapsulation capacities of two liposomal formulations

Liposome Formulation	Encapsulated Paclitaxel (mM)*	Number of Paclitaxel/ Liposome	Encapsulation Efficiency (%)
DOPG:Chol	0.092	4.85×10^5	49.33
DOPG:Chol:PA	0.117	20.7×10^5	62.6

*Initial Paclitaxel concentration of this sample was 0.187 mM

2.3.3 Release of Rhodamine B

To estimate the effect of PA integration on the release of the entrapped dye, liposomes suspended in 10% FBS containing PBS medium were dialyzed at pH 5.5 and pH 7.4 against PBS at 37 °C. For the determination of the percentage release, it was needed to quantify total amount of encapsulated dye molecules inside the liposomes. Therefore, ethanol was added into serum containing liposome solutions at the end of the experiment to disrupt the membrane and subsequently to transfer dye molecules into ethanol solution. In order to obtain the release profiles of liposomes, first of all, calibration curve was derived for Rhodamine B molecule dissolved in 10% FBS containing PBS and ethanol (Figure 2.12). As shown in Figure 2.13, DOPG:Chol:PA liposomes were stable for over 72 h with no apparent release (< 2%), while DOPG:Chol liposomes released 7.5% of the encapsulated Rhodamine B at physiological pH. On the other hand, no significant difference was observed between two liposomal formulations in terms of the released dye amount at acidic pH. These results indicated that both formulations showed stability at two different pHs and in serum containing PBS medium.

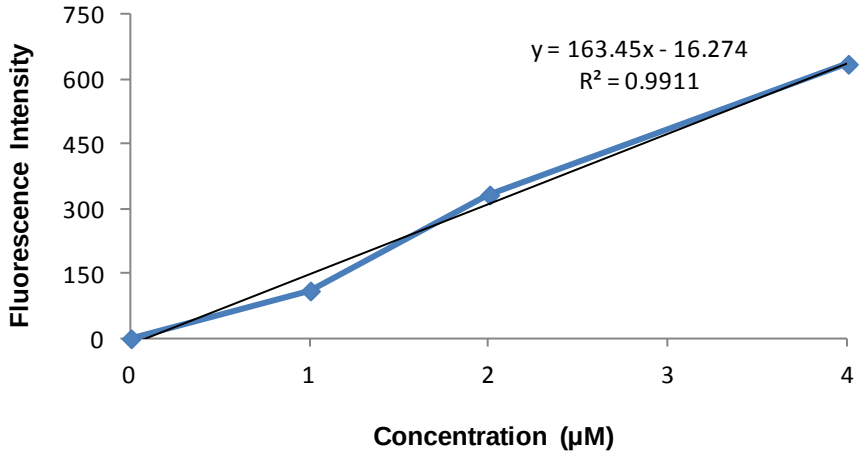

Figure 2.12 Rhodamine B calibration in 10% FBS containing PBS and ethanol (λ_{ex}= 540 nm, λ_{em}: 575nm).

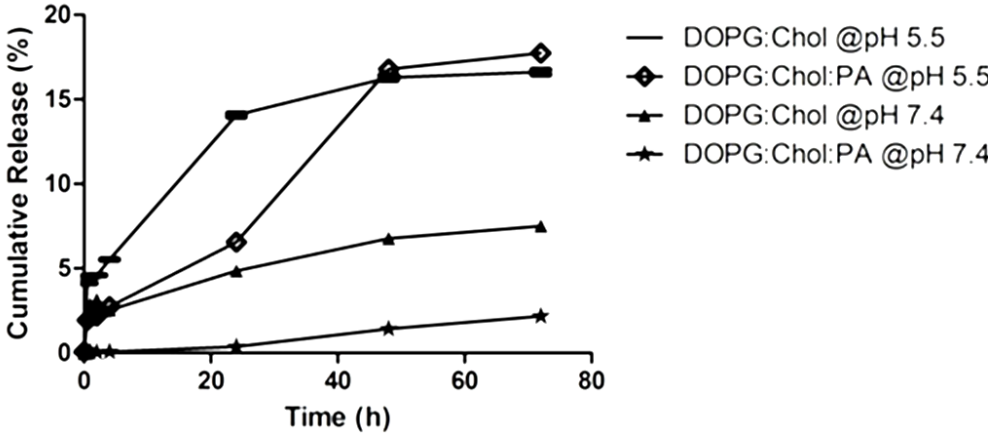

Figure 2.13 Release profile of DOPG:Chol and DOPG:Chol:PA liposomes at pH 7.4 and pH 5.5 for Rhodamine B**.** Both liposome formulations are stable at physiological condition while they both show slow release slightly triggered by acidic pH.

2.3.4. Uptake of Dye Encapsulated Liposomes by MCF7 cells

In the beginning of the uptake study, the biocompatibility of liposomal formulations were evaluated by treating MCF7 cells with bare liposomes, PA integrated liposomes

and PA molecules alone. None of them exhibited any significant change in cell viability after 4 h and 24 h of treatment (Figure 2.14).

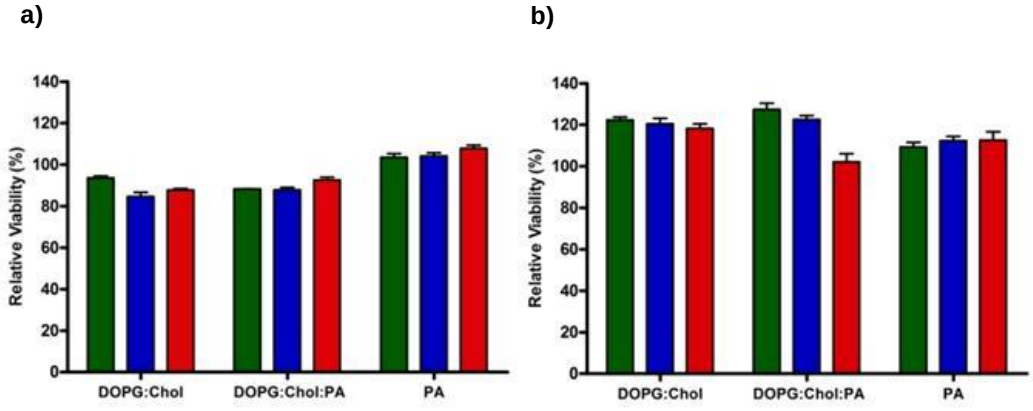

Figure 2.14 Cellular viability of MCF7 cells after a) 4 h and b) 24 h. Colours of the bars represent the final peptide concentration, green: 250 µM, blue: 25 µM and red: 12.5 µM. Results were normalized to cells treated with PBS, (n=4).

Delivery efficiency of liposomes was tested by assessing the amount of uptaken dye molecules, Rhodamine B and Nile Red, by MCF7 cells *via* fluorescence measurements.[181-182] Upon 3 h of treatment of Rhodamine B, five-folds more dye uptake was observed in PA integrated liposomes compared to both native liposomes and free dye ($p < 0.001$) (Figure 2.15a). Although it was previously reported that there is a inverse proportion between the liposome size and its *in vitro* uptake rate,[183] PA integrated liposomes, larger than bare liposomes, exhibited improved delivery of hydrophilic dye into MCF7 cells which indicated that cell penetrating PAs integrated into liposomes facilitated the internalization rate of liposomes. From the literature, the guanidinium group of arginine residues are known with their membrane translocation properties,[184] which might result in enhanced internalization of PA functionalized liposomes.

Similar to Rhodamine B, hydrophobic Nile Red alone, Nile Red encapsulated PA free and PA integrated liposomes were administered to MCF7 cells and incubated for 3 h. The results revealed that the uptake level of free Nile Red was significantly lower than that of both PA free and PA integrated liposomes and PA modified DOPG:Chol liposomes exhibited 30% increase in uptake ($p < 0.001$) compared to PA free liposomes (Figure 2.15b). Same experiment was performed with liposomes containing lower content of PA (in DOPG:Chol:PA (7.5:8:0.5)) and their relative uptake was found in between bare liposomes and high content PA integrated liposomes. Higher encapsulation capacity of PA integrated liposomes enables administration of less amount of liposome compared to bare liposomes for delivering equal concentration of Nile Red when the number of Nile Red per liposome values was considered (Table 2.4). Fluorescent images indicated that DOPG:Chol liposomes facilitated internalization of hydrophobic cargo upon PA modification in contrast to unmodified liposome (Figure 2.15c). Overall, enhanced encapsulation capacity of PA integrated DOPG:Chol liposomes together with their increased liposomal internalization facilitated the hydrophobic Nile Red uptake by MCF7 cells.

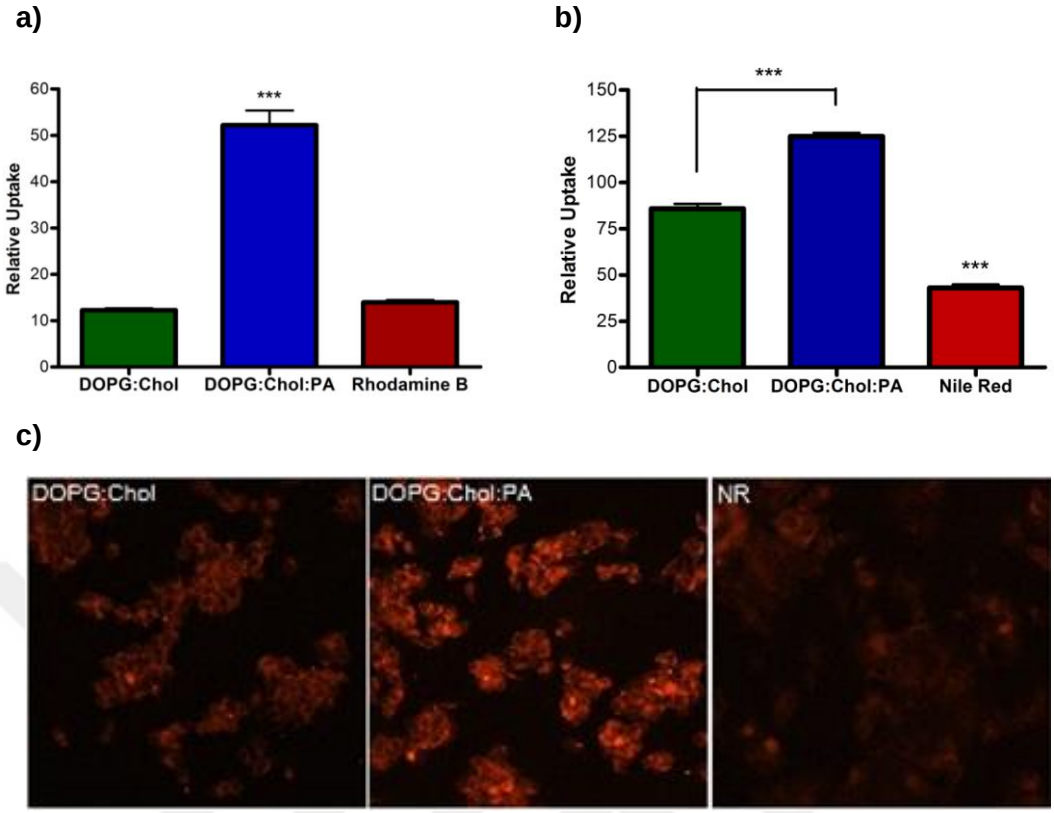

Figure 2.15 Analyses of uptaken model dyes by MCF7 breast cancer cells. a) Uptake of 4.5 μM Rhodamine B alone or within DOPG:Chol and DOPG:Chol:PA liposomes by cells. The results were normalized to the protein concentration of samples for estimating relative uptake value. (*** stands for $p < 0.0001$) (n=4), b) Uptake of 10 μM Nile Red alone or within DOPG:Chol and DOPG:Chol:PA liposomes by cells. Results were normalized to protein concentration of samples. (*** stands for $p < 0.001$) (n=4), c) Fluorescent microscopy images of cells treated with liposomal DOPG:Chol, DOPG:Chol:PA and free Nile Red.

2.3.5 Therapeutic Effects of Anticancer Drug Encapsulated Liposomes on MCF7 cells

In vitro therapeutic effects of anticancer drug loaded PA integrated and PA free DOPG:Chol liposomes were investigated via cytotoxicity assays and corresponding cell proliferation rates were determined by using MCF7 breast cancer cell line. As

previously mentioned, two anticancer drugs were chosen depending on their hydrophobic and hydrophilic natures. During the evaluation of the therapeutic effects of the prepared liposomes, Doxorubicin-HCl and Paclitaxel were utilized as encapsulating agents. While the former one causes oxidative DNA damage and topoisomerase II inhibition in the nucleus of cancer cells,[185] Paclitaxel mainly serves as G2/M cell cycle inhibitor and hinders cell proliferation by inhibiting microtubule dynamics.[186]

Doxorubicin-HCl was used as a hydrophilic cancer drug to be encapsulated inside the vesicular cavities due to its water-soluble characteristic. Dose and time response of breast cancer cells to the treatment of drug loaded liposomal formulations or free drug were investigated (Figure 2.16). Dose response of Doxorubicin-HCl loaded DOPG:Chol liposomes and free Doxorubicin-HCl were evaluated by the quantification of total metabolic activity after 24 h of exposure (Figure 2.16a). Accordingly, half maximal inhibitory concentration (IC_{50}) values were estimated as 2.58 μM, 2.48 μM and 0.88 μM for Doxorubicin-HCl loaded DOPG:Chol, DOPG:Chol:PA liposomes and free drug, respectively. It was previously reported, liposomal Doxorubicin-HCl had lower toxicity compared to free Doxorubicin when administered at low concentrations.[187] The results revealed that increasing the concentration of Doxorubicin-HCl enhanced the effectiveness of liposomal Doxorubicin-HCl systems.

Following dose response studies, time dependent response of MCF7 cells to Doxorubicin-HCl treatment was evaluated at 1, 3 and 6 h exposure times (Figure 2.16b).

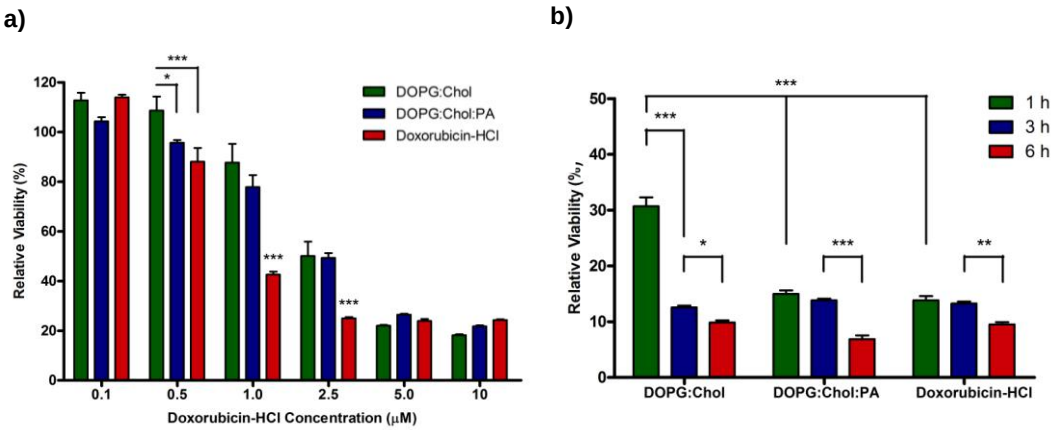

Figure 2.16 a) Dose and b) time response of MCF7 cells to the treatment of Doxorubicin-HCl loaded liposomes or free drug. a) Viability of cells was assessed by Alamar Blue assay and results were normalized to untreated cells in PBS. b) After 1, 3 and 6 h of 10 μM free or liposomal Doxorubicin-HCl treatment, cells were incubated in fresh media for further 24 h and viability of cells was measured. (*** stands for $p < 0.001$, ** stands for $p < 0.01$, * stands for $p < 0.05$) (n=4).

For free and liposomal Doxorubicin-HCl systems, viability decreased with increasing exposure time. After 1 h of treatment, we observed that PA modified DOPG:Chol liposomes and free Doxorubicin-HCl had almost two fold lower viability with respect to PA free DOPG:Chol liposomes ($p < 0.001$). Higher cytotoxicity of PA integrated liposomal Doxorubicin-HCl demonstrated improvement in delivery efficiency caused by arginine-rich cell penetrating peptide incorporation into native liposomes. While bare liposomes showed a sharp decrease in cell viability after 3h treatment ($p < 0.001$), there was significant decrease in cell viability for PA integrated liposomal Doxorubicin-HCl and free Doxorubicin-HCl ($p < 0.001$ for DOPG:Chol:PA and $p < 0.01$ for free Doxorubicin-HCl) after 6 h drug exposure.

On the other hand, Paclitaxel was used as a hydrophobic cancer drug to examine the cytotoxic effect of drug loaded liposomes and free form of drug on MCF7 cells. The

dose and time responses were compared with respect to each other by evaluating the inhibition of cell proliferations. Dose dependent cytotoxicity studies demonstrated that PA integrated liposomes resulted in enhanced therapeutic effect at all doses from 0.2 nM to 2 μM of Paclitaxel ($p < 0.001$) compared to free Paclitaxel (Figure 2.17a). At the highest concentration, inhibitory effect of both DOPG:Chol and DOPG:Chol:PA liposomes was two-folds higher than that of free Paclitaxel. The results indicated that both liposomes caused proliferation inhibition since average doubling time of MCF7 cells are 24 h and untreated cell number (control group) was doubled at given time.[188] These results showed that enhanced cell growth inhibition through PA incorporated liposomes was observed for Paclitaxel treatment with various concentrations.

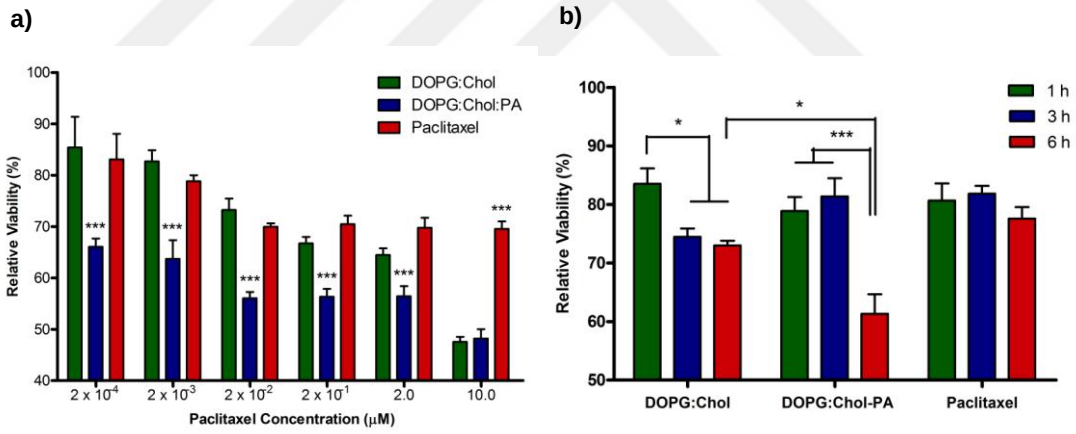

Figure 2.17 a) Dose and b) time response of MCF cells to the treatment of Paclitaxel loaded liposomes or free drug. a) Viability of cells was assessed by Alamar Blue assay and results were normalized to untreated cells b) After 1, 3 and 6 h of 30 μM free or liposomal Paclitaxel treatment, cells were incubated in fresh media for further 24 h and viability of cells was measured. (*** stands for $p < 0.001$, ** stands for $p < 0.01$, * stands for $p < 0.05$) (n=4).

In addition, response of MCF7 cells was evaluated by administering 30 μM of Paclitaxel at different time points (1 h, 3 h and 6 h). Time dependent cytotoxic response was observed for both PA integrated and PA free liposomes (Figure 2.17b). At longer liposomal Paclitaxel exposure, cell viability decreased by 25% in PA integrated liposomes while it did not change and remained at 75% in PA free liposomes. Free form of Paclitaxel did not exhibit a significant change in terms of therapeutic effect at any exposure time and the cell viability was close to that of PA free liposomes. Overall, a more efficient delivery system for Paclitaxel was developed by using PA integrated DOPG:Chol liposomes.

2.4 CONCLUSION

In the present study, a liposomal carrier system decorated with cell penetrating arginine-rich peptide amphiphile molecules was demonstrated. A noncovalent functionalization strategy was employed as an alternative to covalent linkage approach to develop multicomponent liposome system. The amphiphilic nature of both peptide and phospholipid was utilized for the formation of vesicular structures. The resulting liposomes were found to be biocompatible and had high encapsulation capacities both for hydrophobic (Nile Red and Paclitaxel) and hydrophilic (Rhodamine B and Doxorubicin HCl) model dyes and cancer drugs with very slow release kinetics. Fluorescence measurements indicated that integration of cell penetrating peptide amphiphiles to liposomes enhanced the uptake of model dyes by MCF7 breast cancer cells with respect to native liposomes as well as free dyes. According to the *in vitro* experiments carried out to understand the therapeutic effects of cancer drugs, Doxorubicin-HCl and Paclitaxel, encapsulated into the

liposomal systems, corresponding liposomes exhibited a concentration dependent cytotoxicity. PA integration was shown to improve the liposomal delivery and enhance the therapeutic effect of both hydrophilic (Doxorubicin-HCl) and hydrophobic (Paclitaxel) anticancer agents on MCF7 breast cancer cells based on time response studies. By use of this functionalization technique, different liposomal formulations can be prepared by simply changing the peptide sequence with bioactive epitopes to improve the therapeutic effect of the cargo.

CHAPTER 3

NONCOVALENT FUNCTIONALIZATION OF MESOPOROUS SILICA NANOPARTICLES WITH AMPHIPHILIC PEPTIDES

Part of this thesis is published in the following article[189]; Reprinted from "Noncovalent functionalization of mesoporous silica nanoparticles with amphiphilic peptides"; Sardan, M., Yildirim, A., Mumcuoglu, D., Tekinay, A.B., and Guler, M.O., *J. Mater. Chem. B,* 2014, 2, 2168-2174, with permission from Royal Society of Chemistry

3.1 INTRODUCTION

Mesoporous silica nanoparticles (MSNs) with their high specific surface area, large pore volume, controlled particle size and morphology are considered as promising platforms for theranostics applications.[190-192] Previously, *in vitro* studies conducted with MSNs revealed that these materials can be effective as drug delivery and cell marking agents.[193-195] Its unique mesoporous structure leading to high loading capacity enables MSNs being applicable in bone/tendon tissue engineering, diabetes, inflammation, and cancer.[196] However, reactive silanol group presenting bare silica surfaces were shown to induce aggregation of particles and opsonization in biological environment. Moreover, they nonspecifically interact with the membrane of several cell types, causing poor biocompatibility and pharmacokinetics for *in vivo* applications.[197-201] Abovementioned problems restricting the *in vivo* applications of MSNs can be overcome by modifying the reactive MSN surface with polymers[202-205] (e.g. PEG and zwitterionic copolymers), small molecules[200, 206] (e.g. phosphonate) or biomolecules[207-209] (e.g. antibodies, peptides, lipid bilayers, DNA and aptamers). In particular, recently, there has been a surge of interest in the use of short peptide chains due to their tunable functionality, biodegradability, and comparably facile synthesis.[210-212] Previously, short peptide sequences such as RGD and IL-13 were utilized to target nanoparticles to specific cancer cell lines.[185, 212-215] Apart from the targeting properties, cell penetrating and endosomal escape properties of some peptide sequences (e.g. TAT peptide) were reported in recent years.[216-218] In addition, biodegradable nature of peptides makes them appropriate molecules as stimuli responsive gatekeepers in controlled

drug release[219-220] and linkers in FRET based diagnostics.[221-223] In literature, peptides are generally covalently bound to the silica surface in the presence of additional cross-linking reagents; nevertheless, it yielded poor surface grafting density and led to costly synthesis of functionalized materials.[214, 219, 224]

In this chapter, a simple and cost-effective self-assembly approach was demonstrated as a promising alternative method to covalent attachment methods to develop hybrid peptide functionalized MSNs.[203] Hydrophobic interactions between octyl groups of MSNs and alkyl chains of PAs led to the integration of peptide molecules into the octyl modified MSN surfaces in aqueous media (Figure 3.1a). Two model PA molecules were selected based on the total charge of the system to modify MSNs. The glutamic acid and lysine residues on the PAs present negative and positive charges to the hybrid system, respectively (Figure 3.1b). The unmodified MSN was synthesized and used to make comparison with peptide functionalized MSNs. Peptide functionalization was studied in terms of its effect on cell viability and uptake by using human umbilical vein endothelial cells (HUVECs) and a vascular smooth muscle cell line (A10). Good cyto-compatibility was assessed with both cell lines treated with all type of MSNs up to a concentration of 200 $\mu g\ mL^{-1}$. Interestingly, a significant increase (1.8 to 6.3 fold) was observed in the cellular uptake of peptide functionalized MSNs compared to bare MSNs.

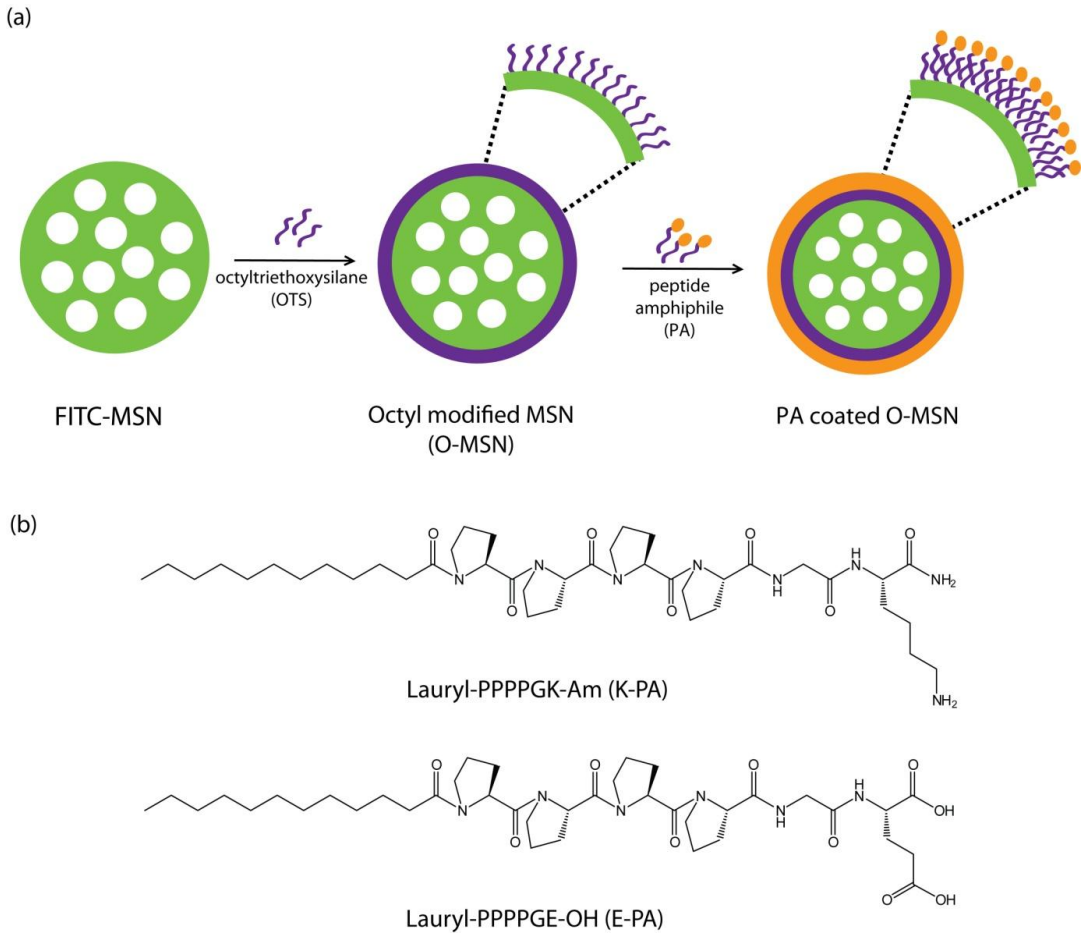

Figure 3.1 a) Schematic illustration for the preparation of fluorescent peptide functionalized MSNs, b) Chemical structures of the peptide amphiphile molecules used in this study.

3.2 EXPERIMENTAL SECTION

3.2.1 Materials

9-Fluorenylmethoxycarbonyl (Fmoc) and *tert*-butoxycarbonyl (Boc) protected L-amino acids, [4-[α-(2',4'-dimethoxyphenyl) Fmoc aminomethyl] phenoxy] acetamidonorleucyl-MBHA resin (Rink amide MBHA resin), and 2-(1*H*-Benzotriazol-1-yl)-1,1,3,3 tetramethyluronium hexafluorophosphate (HBTU) were purchased from NovaBiochem and ABCR. Tetraetyl orthosilicate (TEOS),

octyltriethoxysilane (OTS), aminopropyl triethoxysilane (APTES), sodium hydroxide, lauric acid were purchased from Merck. Fluorescein isothiocyanate (FITC), and cetyltriammoniumbromide (CTAB) and ethanol were purchased from Sigma-Aldrich. Methanol was purchased from Carlo-Erba. Tetrahydrofuran (THF) was purchased from Labkim. All reagents and solvents were used as provided. Cell culture chemicals were purchased from Gibco, Life Technologies.

3.2.2 Synthesis of MSN and OMSN

FITC labelled OMSNs was synthesized as described: 2 mg of FITC was conjugated to 10 μL of APTES in 1 mL of ethanol and stirred for 24 h. Then, 200 mg of CTAB and 6 mg of F127 were dissolved in 96 mL of deionized water and 0.7 mL of 2 M NaOH was added. The solution was heated to 80 °C under vigorous stirring (600 rpm). After the temperature of the reaction mixture was stabilized at 80 °C, 1 mL of TEOS and FITC solution were rapidly added. After 75 min, octyl-containing shell was formed by slowly adding 0.2 mL of OTS dissolved in 10 mL THF to the reaction mixture. The mixture was stirred for additional 90 min. Finally, particles were centrifuged at 9000 rpm, precipitate was collected and washed with methanol twice. The particles were stirred in 50 mL of 20 g L^{-1} ethanolic ammonium nitrate at 60 °C for 1 h for surfactant extraction. This treatment was repeated twice to ensure complete surfactant removal. Particles were washed with ethanol twice and dried at 50 °C overnight. Same parameters were used to synthesize MSN was synthesized except OTS addition.

3.2.3 Synthesis and Characterization of Peptide Amphiphile Molecules

Two different solid supports were used to synthesize peptide amphiphiles depending on the type of functional group in the C-terminus. While the positively charged peptide amphiphile (K-PA) was constructed on MHBA Rink Amide (0.59 mmol/g loading) resin, negatively charged peptide amphiphile (E-PA) was constructed on Fmoc-Glu-Wang (0.64 mmol/g loading) resin to introduce amide and carboxylic acid groups, respectively. All amino acid couplings were performed with 2 equivalents of Fmoc protected amino acid, 1.95 equivalents of HBTU and 3 equivalents of N,N-diisopropylethylamine (DIEA) in DMF for 2 h. Fmoc deprotection was carried out by treating solid beads with 20% piperidine/dimethylformamide (DMF) solution for 20 min. Cleavage of the peptides from the resin and removal of side chain protecting groups were performed by the addition of a mixture of trifluoroacetic acid (TFA) : triisoproplysilane (TIS) : water in the ratio of 95 : 2.5 : 2.5 for 2 h. Excess TFA was discarded by rotary evaporation. The remaining viscous peptide solution was treated with ice-cold diethyl ether and the remaining white precipitate was freeze-dried. The peptide amphiphiles were identified and analyzed by reverse phase HPLC on an Agilent 6530 accurate-Mass Q-TOF LC/MS equipped with an Agilent 1200 HPLC. An phenomenex Luna 3µ C8 100A (50 x 3.00 mm) column was used as stationary phase; whereas water/acetonitrile gradient with 0.1% volume of formic acid was used as mobile phase during the characterization of the positively charged peptide amphiphile. For negatively charged peptide amphiphile, an Agilent Zorbax Extend-C18 (2.1 x 50 mm) column as stationary phase and water/acetonitrile gradient with 0.1% volume of ammonium hydroxide

as mobile phase were used. The positively and negatively charged peptide amphiphiles were purified by using 1200 Agilent HPLC on Zorbax 300SB C8 (21.2 x 150 mm) PrepHT and Zorbax-Extend C18 (21.2 x 150 mm) PrepHT column, respectively.

3.2.4 Coating the OMSN with Peptide Amphiphiles

While 14 mg of each peptide amphiphile dissolved in 12 mL deionized water was sonicated, 2 mg of OMSN powder was slowly added to the solution. The weight ratio of peptide amphiphiles to OMSN was adjusted to 1:7. After repeated sonication and vortex steps for 3 h at room temperature, solution was centrifuged at 5500 rpm. Dispersions concentrated by centrifugation were rinsed with water and centrifuged twice to obtain resulting water dispersible peptide modified MSNs.

3.2.5 Characterization of the Particles

Hydrodynamic size and zeta potential of the bare and PA functionalized MSNs were measured by zetasizer. A Malvern Nanosizer/Zetasizer nano-ZS ZEN 3600 (Malvern Instruments, USA) instrument was exploited for the analysis. Measurements were performed in glass cuvettes and repeated at least three times. TEM images were taken with FEI Tecnai G2 F30 TEM at 300 kV. Samples for imaging were prepared by diluting PA coated MSNs to 0.01% (w/v) on a 200-mesh cupper TEM grid for 5 min without staining and air dried. Fluorescence spectra of the particles were recorded by a Varian Eclipse spectrophotometer with an excitation wavelength of 488 nm. FTIR spectra of MSNs and PAs were collected by using a FTIR (Vertex 70, Bruker). Thermal gravimetric analyses

(TGA) were performed with Q500 (TA Instruments). The temperature was increased from room temperature to 800 °C with a rate of 20 °C min^{-1} under nitrogen gas.

3.2.6 *In Vitro* Studies

Human umbilical vein endothelial cells (HUVECs) and A10 rat aortic smooth muscle cells (ATCC® Cat# CRL-1476™) were used to assess the biocompatibility of the nanoparticles and investigate the uptake of nanoparticles by these cells. HUVECs were donated by Yeditepe University, Istanbul, Turkey. HUVECs were purified as described[225] and stained with CD34, CD31, and CD90 surface markers for further characterization. These cells were found to be positive for CD31 and CD34 but negative for CD90. A10 and HUVEC cells were cultured in 75 cm^2 polystyrene cell culture flasks with standard medium, containing Dulbecco's modified eagle medium (DMEM) with 10% fetal bovine serum (FBS), and 1% penicillin/streptomycin and passaged at cell confluency between 80 to 90% using trypsin/EDTA. In all experiments, particles were administered in serum free medium (1% penicillin/streptomycin containing DMEM) to avoid any influence of serum proteins on uptake mechanism.

Cellular viability experiment was carried out with Alamar Blue assay. 5000 cells/well (HUVEC or A10) were seeded on 96 well plate in 100 µL of standard medium and incubated for 24 h followed by the removal of medium and addition of 100 µL of serum free medium. Freshly prepared nanoparticle solutions (25 µL) were administered to have a final concentration in the range of 10-200 µg mL^{-1}. Cells were treated with particles for 4 h then medium was changed to standard medium and cells were further incubated for 20 h. Then, Alamar Blue reagent

diluted to 10% in DMEM was added. After 3 h, a microplate reader (SpectraMax, M5) was used to measure the fluorescence at 570/612 nm ($\lambda_{ex}/\lambda_{em}$).

For cellular uptake experiments, 13 mm glass coverslips were placed in 24 well plates, and 4 x 10^4 cells (HUVEC or A10) in standard medium were seeded in each well. After 24 h, medium was replaced with 400 µL of serum free medium. 100 µL of bare or functionalized MSN particles were administered to have a 200 µg mL^{-1} final concentration of MSN and medium was changed with standard medium after 4h incubation. Cells were incubated 20 h more, washed with PBS and fixed with 4% paraformaldehyde. Then, cells were permeabilized with 0.1% TritonX-100 (Sigma-Aldrich) and actin proteins were stained with Phalloidin-TRITC (Sigma-Aldrich). Images were taken with laser scanning confocal microscopy (Zeiss, LSM 510).

Quantitative analysis for the uptaken nanoparticles by cells was performed by flow cytometer (BD, FACS Aria III). 1 x 10^5 HUVEC or A10 cells/well were seeded in 6 well plates in standard medium. After 24 h incubation, medium was exchanged to 1600 µL of serum free medium. 400 µL of bare or functionalized MSN particles (200 µg mL^{-1}) were administered and medium was changed with standard medium after 4h incubation. Cells were incubated 20 h more, then washed with PBS and trypsinized. Cells were centrifuged, washed with PBS, resuspended in 1 mL PBS and kept on ice until the analysis. MSN particle uptake was analyzed with FITC channel of flow cytometer. Non-treated cells were used as control. Student's t-test was applied to all datasets and differences were considered significant when $p < 0.05$.

3.3 RESULTS and DISCUSSION

3.3.1 Synthesis and Characterization of Peptide Functionalized MSNs

Octyl modified water insoluble MSNs (OMSN) were synthesized *via* one-pot respective condensation method.[203, 226-227] The condensation of tetraethyl orthosilicate (TEOS) molecules in basic conditions resulted in the formation of initial MSNs which was followed by the addition of octyl triethoxysilane (OTS) molecules to the reaction mixture to obtain hydrophobic octyl layer on MSN surface. The fluorescein isothiocyanate (FITC) molecules were conjugated to the MSNs in first step of the synthesis to label and track the uptake by using confocal imaging and flow cytometry methods.[206] The anchorage of fluorescent moiety to silica network was confirmed by using fluorescence spectroscopy, where emission bands of FITC molecules were easily observed (Figure 3.2). Bare MSNs were synthesized and exploited for control experiments under the same experimental conditions without the OTS addition.

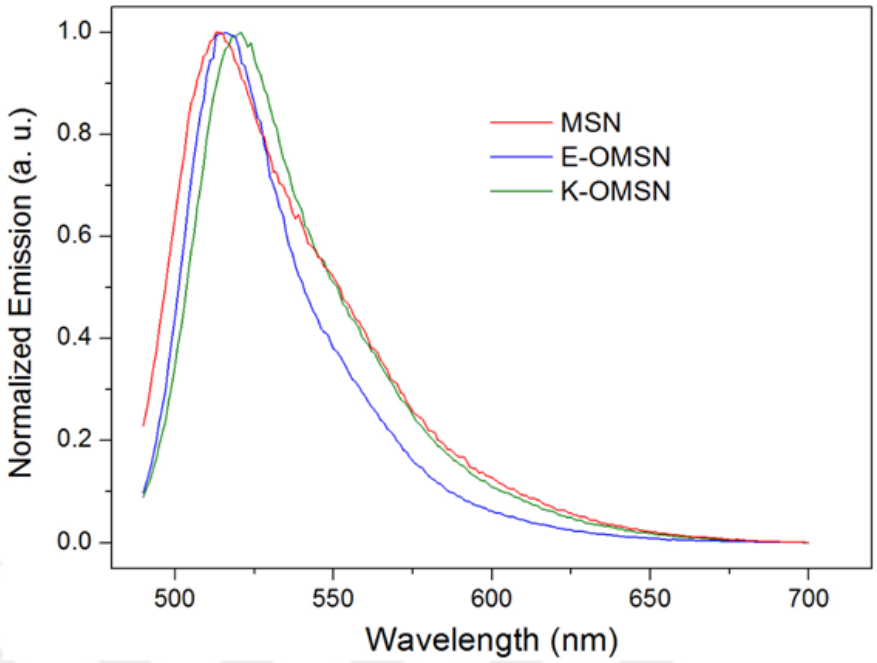

Figure 3.2 Fluorescence emission spectra of bare and modified MSNs

Peptide amphiphiles were synthesized by solid phase peptide synthesis method based on orthogonal protection and verified by liquid chromatography and mass spectrometry (Figure 3.3 and 3.4). Besides hydrocarbon tail and proline residues, glutamic acid or lysine residue were inserted into the sequence to present negative or positive charge in the molecule as well as to provide water dispersibility.

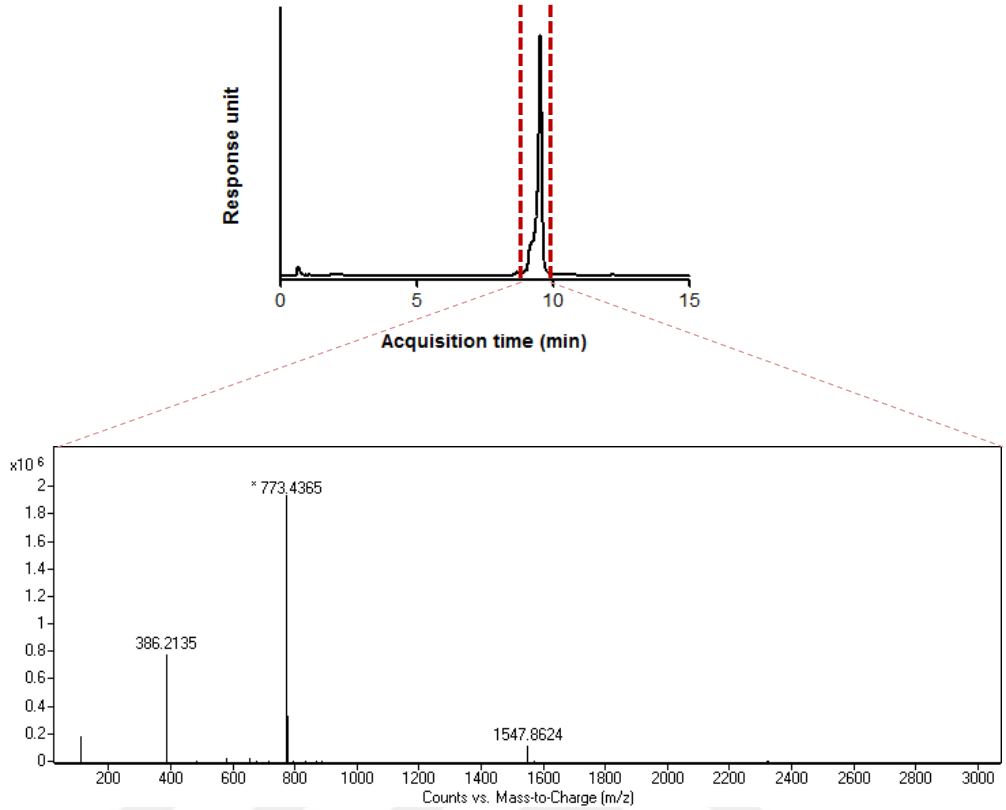

Figure 3.3 Liquid chromatogram of Lauryl-PPPPGE and mass spectrum of corresponding amphiphilic peptide molecule. Mass data $[M+H]^-$ (calculated) = 773.45, $[M+H]^-$ (observed) = 773.41, $[(M-2H)/2]^-$ (observed) = 386.20, $[2M-H]^-$ (observed) = 1547.86)

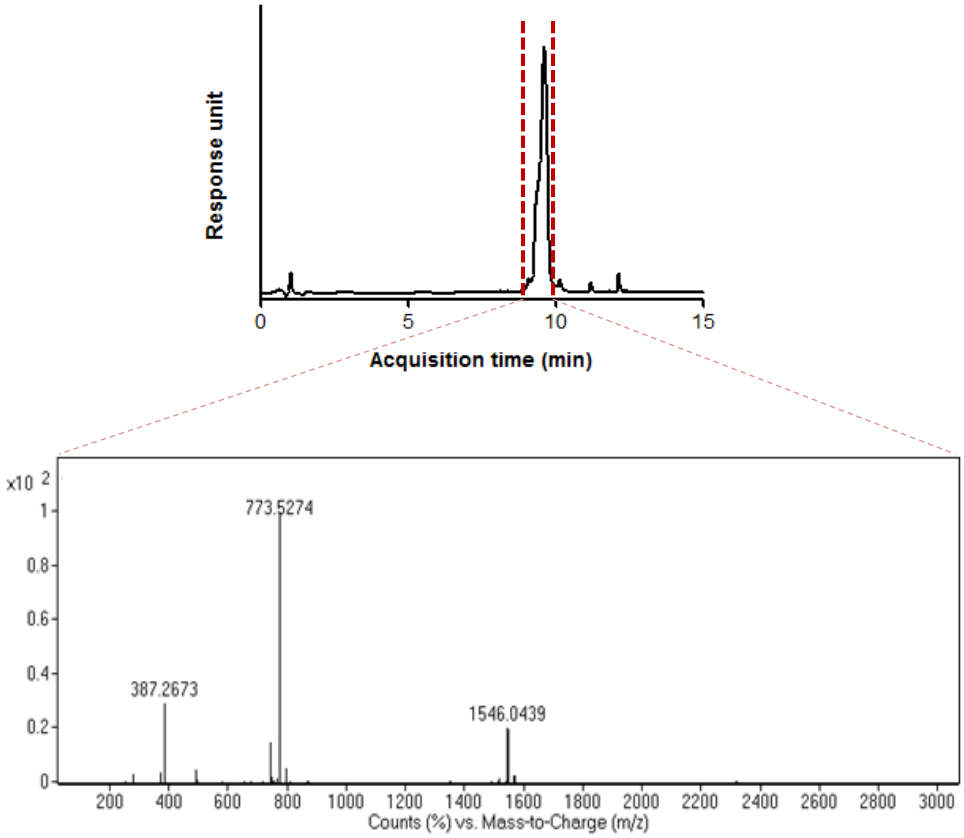

Figure 3.4 Liquid chromatogram of Lauryl-PPPPGK-Am and mass spectrum of corresponding amphiphilic peptide molecule. Mass data $[M+H]^+$ (calculated) = 773.52, $[M+H]^+$ (observed) = 773.53, $[(M+2H)/2]^+$ (observed) = 387.27, $[2M+H]^+$ (observed) = 1546.04)

Peptide amphiphile molecules were coated on OMSN surface by simply sonicating OMSN powder in aqueous E-PA or K-PA solutions (Figure 3.5a). Since the surface of as-prepared OMSNs was covered with hydrophobic octyl groups, nanoparticles became insoluble in water (Figure 3.5a left). After the addition into PA solution along with harsh ultrasonication, PA molecules incorporated into OMSN surface through hydrophobic interactions between alkyl chains of both OMSN and PA (Figure 3.1a). Decoration of the surface of MSN with peptide amphiphiles rendered particles water dispersible by providing either positively or negatively charged water soluble moieties. Additionally, photograph

of MSNs dispersed in water was demonstrated in Figure 3.5b. Both dispersions have light green colour due to the covalently attached fluorescent dye molecules.

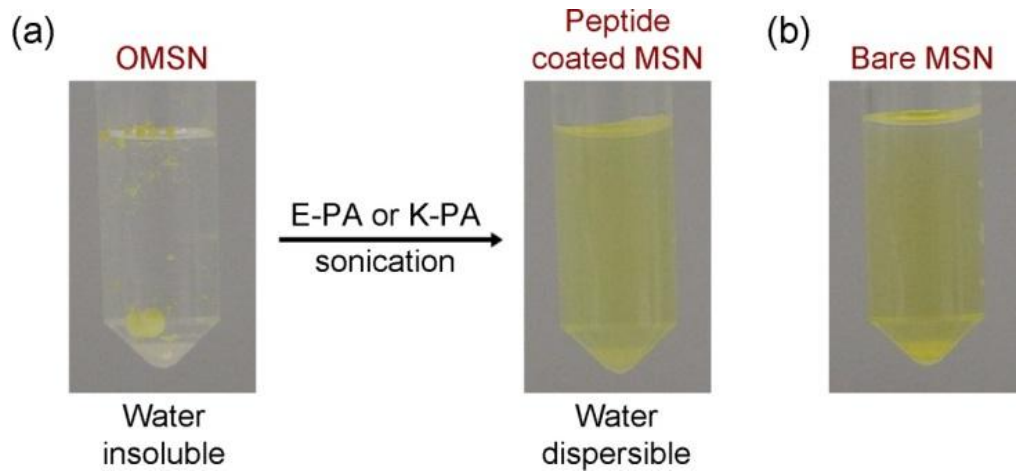

Figure 3.5 (a) Photographs of OMSNs before and after coating with peptide amphiphiles and (b) Photograph of MSN dispersion in water.

TEM images of the particles are shown in Figure 3.6. While bare MSNs exhibited MCM-41 type highly ordered hexagonal porous structure, a randomly porous thin shell was observed over a MCM-41 type porous core for OMSNs which is in accordance with our previous work.[203] After coating the OMSNs with corresponding PAs, E-PA and K-PA, the surface of the mesoporous particles were covered with a thin organic layer.

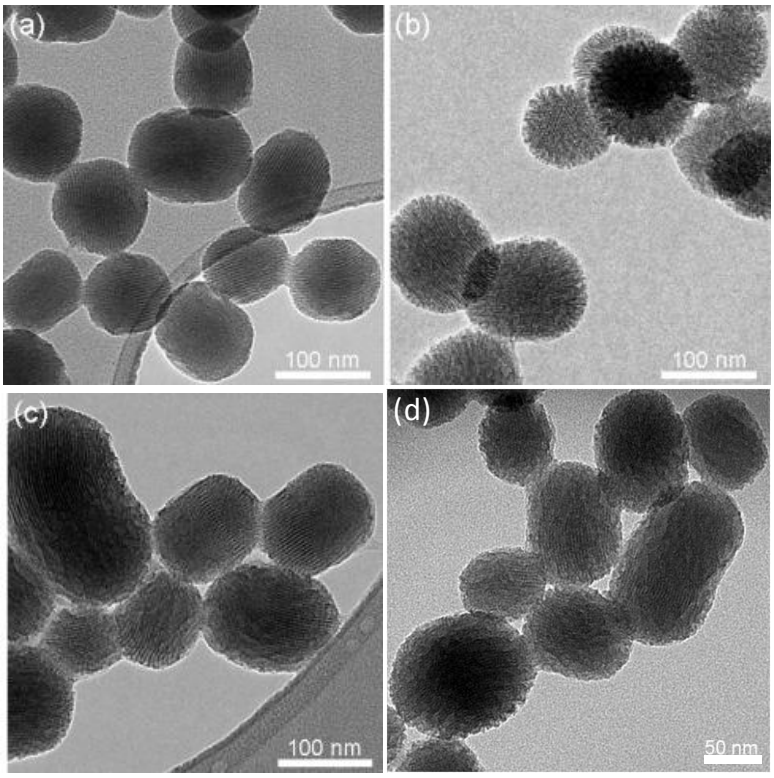

Figure 3.6 Morphological characterization of the mesoporous silica nanoparticles. TEM images of (a) MSN, (b) OMSN, (c) E-OMSN and (d) K-OMSN.

Formation of peptide coating over OMSNs was further confirmed by conducting FTIR and TGA analyses. Figure 3.7a exhibits the FTIR spectra of the particles. In the case of OMSN spectrum, the –CH peaks between 2800 cm^{-1} and 3000 cm^{-1} were observed indicating the successful octyl modification. Additional –CH bonds of PAs, especially residing in lipid tail, resulted in stronger absorption bands for PA modified particles (E-OMSN and K-OMSN). In addition, new absorption bands between 1400 cm^{-1} and 1800 cm^{-1} were appeared, which are in good agreement with FTIR spectra of individual PAs. In addition, Amide I (1600−1690 cm^{-1}, C=O stretching) and amide II (1480−1575 cm^{-1}, CN stretching, NH bending) bands of PAs were observed for PA functionalized MSNs. Moreover, additional C=O stretching vibration was observed for glutamic

acid containing particles at around 1725 cm^{-1} corresponding to the side chain of glutamic acid residue.

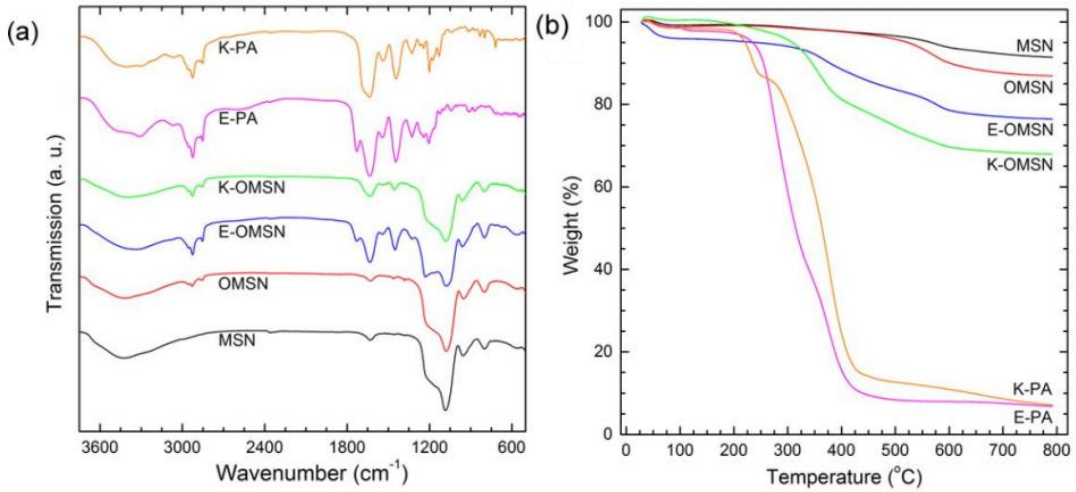

Figure 3.7 FTIR spectra (a) and TGA spectra (b) of particles and peptide amphiphiles.

The results of TGA analysis of the particles are demonstrated in Figure 3.7b. For MSNs, heating upto 800 °C caused a small weight loss of 7.8% because of the dehydroxylation of the silica surface.[228] Octyl modified MSNs lost their 11.9% weight content especially from 300 °C to 500 °C indicating the decomposition of octyl moieties.[203] The weight of E-OMSN and K-OMSN, having both organic and inorganic contents, decreased by 19.6 % and 32.5 %, respectively. Also, two sharp declines were observed in spectra of peptide coated particles around 400 °C and 500 °C, most likely due to the decomposition of PAs and octyl groups, respectively. For bare peptide amphiphiles, almost all weight was lost at 800 °C. By utilizing TGA and TEM results, grafting densities of PAs onto the OMSN surfaces were calculated.[229-230] How grafting densities were calculated is explained below.

Some assumptions were done for the calculations. For instance, OMSN was considered as spherical in shape and its average diameter was estimated as 100 nm based on the TEM images.

Volume of single OMSN = $\frac{4}{3}\pi r^3$ = 5.23x10^{-16} cm^3/ # of OMSN

Density of amorphous silicon is 2.65 g/cm^3 and pore volume of OMSN is 1 cm^3/g was previously calculated in another study.[3] Thus, number density of OMSN per gram (x) can be calculated by:

$$x = \frac{\left[\frac{1}{2.65}\left(\frac{cm^3}{g}\right) + 1\left(\frac{cm^3}{g}\right)\right]}{5.23x10^{-16}\left(\frac{cm^3}{\#\ of\ OMSN}\right)} = 2.63x10^{15}\left(\frac{\#\ of\ OMSN}{g}\right)$$

Amount of peptide amphiphile (PA) per gram of OMSN for both E-PA and K-PA coated particles were calculated based on TGA results. For MSN, OMSN, E-OMSN and K-OMSN, weight losses (wt %) at 800 ^{0}C are 7.8 %, 11.9 %, 19.6 % and 32.5 %, respectively. Calculation was made according to the following equation:

$$\frac{(W_{peptide\ OMSN} - W_{OMSN})}{100 - W_{MSN}}\ x\ \frac{100}{(100 - W_{MSN}) - (W_{peptide\ OMSN} - W_{OMSN})} =$$

$$x\ \left(\frac{g\ of\ peptide}{g\ of\ OMSN}\right)$$

where w is the weight loss in percentage of corresponding particle.

Accordingly, gram of peptides per gram of OMSN values were calculated as 0.099 and 0.312 for E-OMSN and K-OMSN, respectively. Since the molecular weights of E-PA and K-PA were known as 774 g/mol and 772 g/mol, respectively, number of peptides per OMSN can be calculated by using following equation:

$$\frac{\frac{g\ of\ peptide\ per g\ of\ OMSN}{Mw_{peptide}}\ x\ Avogadro\ number}{2.63x10^{15}}$$

Numbers of peptides per OMSN were found as 29,360 and 92,770 for E-OMSN and K-OMSN, respectively.

Surface area (SA) of single OMSN was calculated with the assumption of smooth particle surface which follows as:

$$SA_{OMSN} = 4\pi(50nm)^2 = 3.14\text{x}10^4\text{nm}^2$$

Finally, grafting densities (# of peptides/nm^2) were calculated as 0.94 and 2.95 for E-OMSN and K-OMSN, respectively.

The grating densities indicated that the surface of OMSNs was intensively covered by PAs. The higher grafting density calculated for K-OMSN might likely stem from the electrostatic interactions between positively charged K-PA and unreacted surface silanol groups of OMSNs. Table 3.1 listed the physical properties of bare and modified MSNs. Average particles sizes of the MSNs and OMSNs were estimated as 100 nm and 104 nm, respectively, based on the images taken by TEM. Octyl modification led to 4 nm of increase in the particle size, which was observed in TEM as ~2 nm shell formation around the particles. Hydrodynamic sizes of the MSN, E-MSN and K-MSN except OMSN were measured by using dynamic light scattering technique (Table 3.1 and Figure 3.8). Since OMSN is water insoluble, we unabled to measure its hydrodynamic size. Hydrodynamic sizes of the PA coated particles showed difference (around 40 nm) with respect to the sizes observed in TEM due to the slight aggregation in aqueous media for these particles during DLS measurements. On the other hand,

aggregation becomes more pronounced for bare MSNs with a 67 nm difference between hydrodynamic and primary particle sizes. This difference may stem from the fact that two different techniques, TEM and DLS, were used for the measurements. While hydrodynamic size of particles was measured with DLS in which interactions with solvent molecules are also taken into account during calculations, dried samples were used for TEM imaging.

Table 3.1 Physical properties of bare, octyl modified and PA functionalized MSNs

Sample	TEM Size (nm)	DLS Size (nm)	Zeta potential (mV)
MSN	99.8 ± 20.7	166.5 ± 8.0	-36.6 ± 1.1
OMSN	104.3 ± 21.5	N/A	N/A
E-OMSN	N/A	143.8 ± 19.8	-38.0 ± 0.8
K-OMSN	N/A	145.2 ± 1.6	-25.1 ± 0.7

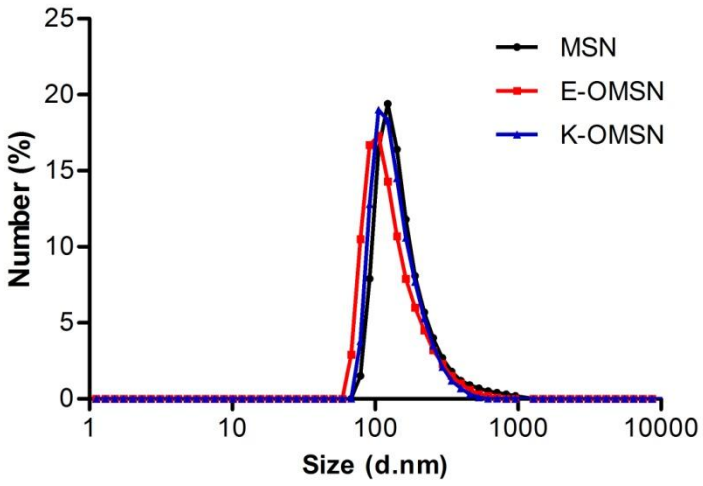

Figure 3.8 Number (%) distribution of MSN, E-OMSN and K-OMSN.

The surfaces of the particles were also examined by measuring their zeta potentials (Table 3.1). Bare MSN surface is negatively charged (-37 mV) due to the surface silanol groups.[200] Functionalization of the MSN surface with a negatively charged E-PA did not significantly change the zeta potential of the surface (-38 mV) since both silanol and E-PA groups possess negative charges. On the other hand, coating of MSN surface with positively charged K-PA led to a remarkable increase in the zeta potential (-25 mV).

3.3.2 *In Vitro* Cell Compatibility of MSNs

Good compatibility of therapeutic nanoparticles with biological organism is an essential issue to avoid possible side effects of these therapies. Accordingly, *in vitro* cytocompatibility of the peptide functionalized and bare MSNs were assessed by using HUVEC and A10 cell lines prior to uptake experiments. The viability of the cells treated with different particle concentrations (10 to 200 μg mL^{-1}) was tested by using Alamar blue assay. 4 h incubation of cells with particles was followed by additional 20 h incubation in particle free media. None of the particles exhibited decrease in viability of both cell lines even at very high particle concentration of 200 μg mL^{-1} (Figure 3.9 a, b).

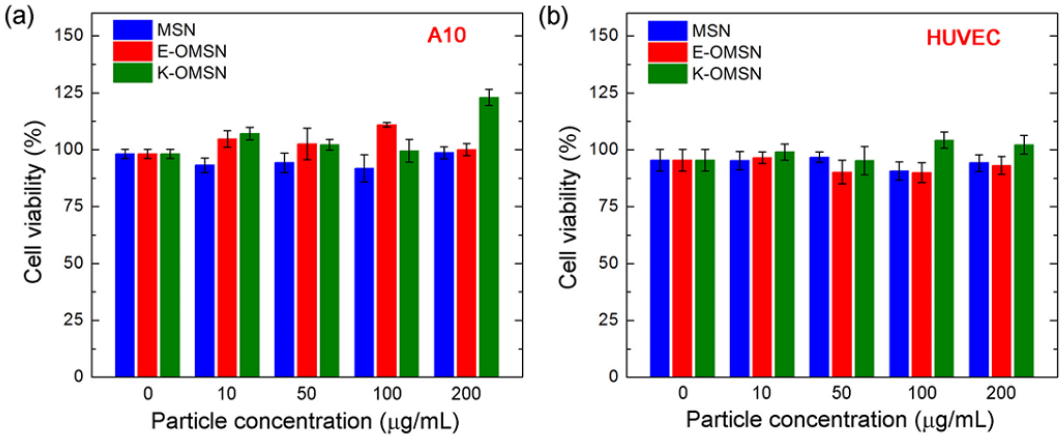

Figure 3.9 Cellular viability results of (a) A10 and (b) HUVECs treated with bare and peptide functionalized MSNs.

3.3.3 Cellular Uptake Studies

Improving cellular uptake of the therapeutic nanoparticles is crucial for enhancing their efficacy. Therefore, we examined the uptake of the particles by A10 and HUVEC cells by visualizing with confocal microscopy and quantifying with flow cytometry techniques. The concentration of particles to be administered into the cells was determined by the viability experiment and accordingly both A10 and HUVEC cells were treated with 200 μg mL^{-1} nanoparticles for 4 h and the cells were analyzed after 20 h of further incubation. As demonstrated in Figure 3.10a, confocal microscopy images showed that the peptide coated particles were uptaken remarkably more than the bare MSNs by A10 and HUVEC cells.

Since the particles are fluorescent, it is also possible to quantify the internalized particles by using flow cytometer to make comparison between groups in terms of the amount of uptaken particle by the cells. The highest uptake was observed for

K-OMSN in both cell lines. The amount of internalized fluorescent E-OMSNs was less than K-OMSNs; however, they were internalized more than bare particles. While the uptake of K-OMSN by A10 and HUVEC cells was 2.3 and 6.3 fold higher than the uptake of bare MSN, respectively, E-OMSN demonstrated 1.8 and 3.1 fold increased uptake by A10 and HUVEC cells compared to bare MSNs. Since positively charged surfaces can electrostatically interact with the slightly negatively charged cell membrane, highest cellular internalization was observed for positively charged K-OMSN.[231] Although, both MSN and E-OMSN have almost same zeta potential values, which are close to -40 mV, cellular uptake of E-OMSNs was significantly higher than MSNs. This observation stresses that the uptake rate and amount of nanoparticles cannot be directly related with net surface charge of the surface; instead, it is more related with the chemical structure of the surface functional groups and its presentation to the cells.

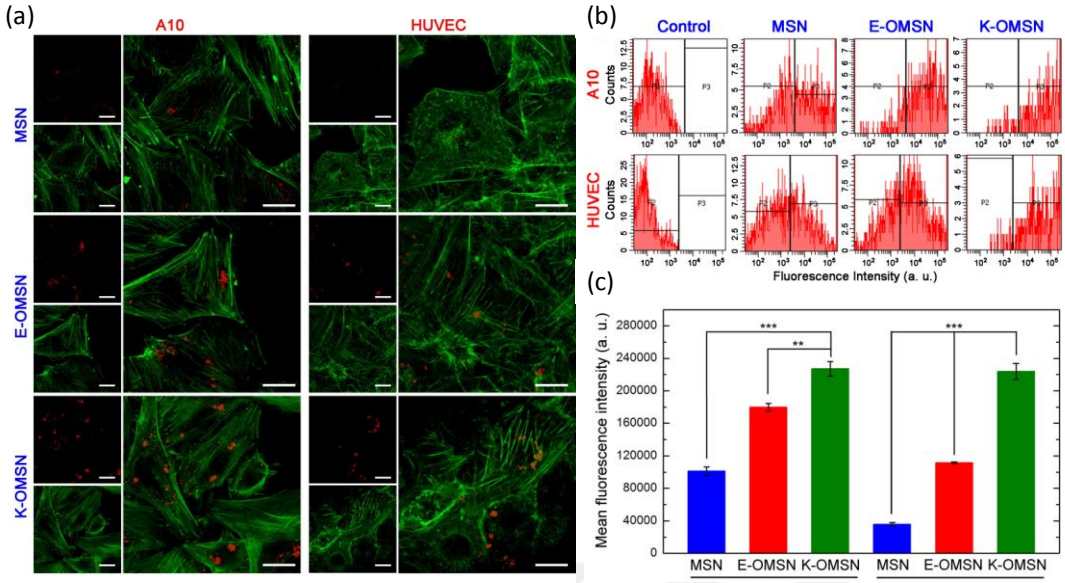

Figure 3.10 Uptake results of bare and peptide functionalized MSNs. (a) Confocal imaging of A10 and HUVEC cell lines when treated with bare and PA functionalized MSNs. Upper images at left shows the fluorescence of particles, lower images at left shows the fluorescence of actin filaments stained by Phalloidin-TRITC and panels at right shows the merge images. (b, c) Flow cytometry analysis of A10 and HUVECs treated with bare and PA functionalized MSNs. (b) Flow cytometry histograms of corresponding groups. (c) Mean fluorescence intensity of bare and PA modified MSNs. According to Student's t test, **$p < 0.001$ and ***$p < 0.0001$, n=3.

3.4 CONCLUSION

The surface of mesoporous silica nanoparticles (MSNs) have been modified for enhancing their cellular uptake, cell targeting, bioimaging, and controlled drug release. For this purpose, covalent anchorage on silica surface was predominantly exploited with a wide range of bioactive molecules. In this chapter, a facile self-assembly method was described to prepare a hybrid peptide silica system composed of octyl-modified mesoporous silica nanoparticles (MSNs) and peptide amphiphiles (PAs). Hydrophobic organosilane surface of mesoporous silica was coated with amphiphilic peptide molecules. Peptide functionalization rendered MSNs water soluble and dispersible. The peptide functionalized particles attained good biocompatibility with vascular smooth muscle and vascular endothelial cells. The peptide coating also improved the cellular uptake of particles up to 6.3 fold, which is promising for development of highly efficient MSN based theranostics agents. Moreover, this facile method demonstrated in this chapter can be applied to prepare MSNs with diverse functionalities including cancer cell targeting, cell penetrating properties and responsive drug release, by simply varying the peptide signal to achieve selective and specific bioactive properties.

CHAPTER 4

AMPHIPHILIC PEPTIDE COATED SUPERPARAMAGNETIC IRON OXIDE NANOPARTICLES FOR IN VIVO MR TUMOR IMAGING

Part of this thesis is published in the following book;[232] Reprinted from "Therapeutic Nanomaterials, Chapter 9. Advances in Nanoparticle-Based Medical Diagnostic and Therapeutic Techniques"; Sardan, M., Ozkan, A.D., Zengin, A., Tekinay, A.B., and Guler, M.O., *Wiley,* 2016, ISBN: 978-1-118-98745-2 with permission from John Wiley and Sons and the work presented in this chapter conducted by Sardan Ekiz, M.; Ozdemir A.; Dilli, A.; Guler, M.O. and Tekinay, A. B. is submitted to a journal as a research article. (equal contribution)

4.1 INTRODUCTION

Numerous modalities are currently used for non-invasive imaging in medicine and advanced research is still in progress for further enhancement. These modalities significantly improve the quality of diagnose and lead to more precise treatments. Although the techniques may show some variances in the electromagnetic region they use, basically an electromagnetic field is scanned or rotated over the target area to measure the response given either by the affected tissue or a specific tracer administered prior to imaging. It is obvious that the headway on biomedical imaging research has been made with the substantial progress in nanotechnology and there has been a surge of interest during the last few decades in producing nano-sized inorganic particles composed of semiconductors, noble metals and metal oxides for imaging and sensing applications.[233] In the light of the results acquired from a vast of research, it was revealed that nanoparticles showed superiority over the metal complexes not only because of their ease of functionalization and diminished toxicities but also due to their intrinsic optical and magnetic properties.

Among the non-invasive imaging modalities, magnetic resonance imaging (MRI) is a non-ionizing technique providing high spatial resolution and depth for *in vivo* imaging with pronounced soft-tissue contrast. This differential contrast between soft tissues can be adjusted by altering the data acquisition parameters. To generate a MRI signal, primarily water molecules but also lipids inside the body are used as the main source of protons.[234] Since the abnormal tissue and normal tissue may have different intrinsic relaxation times depending on the physiological environment,

specific contrast may be observed at a late stage of the disease.[235] In order to enhance the diagnostic value of MRI and detect the abnormality at an earlier stage, different type of contrast agents (CAs) have been designed which have the ability of shortening T_1 or T_2 relaxation times; in other words, increasing $r_1(1/T_1)$ or $r_2(1/T_2)$ relaxivities.[236] These contrast agents are promising candidates for highly effective molecular imaging due to their small size and versatile functionality. Positive and negative CAs comprise two classes of MRI agents. While positive CAs, mainly gadolinium and manganese containing agents, diminish relaxation time T_1 and bring about brighter contrast, negative CAs, primarily iron oxides, shortens relaxation time T_2 and give rise to darker contrast. Because of the detrimental effects associated with the dissociation and accumulation of gadolinium and manganese ions in the body[237], immense research has been focused on the preparation of non-toxic formulations of these metals, as well as on the preparation of non-toxic alternatives to traditional T1 contrast agents. Thus, iron-based CAs are considered as promising candidates in terms of enhanced biocompatibility due to the fact that iron atoms are naturally found in human blood and the excessive amount of them can be stored as ferritin in the body.

Superparamagnetic materials exhibit high susceptibility similar to ferromagnetic materials in external magnetic field and rapid demagnetization similar to paramagnetic molecules when magnetic field is removed.[5] The reduction in T2 relaxation time and obtaining darker images with low signal intensity are the consequences of two phenomena, microscopic field inhomogeneity and activation of proton dephasing, observed in T2 contrast agents, negative agents. The spin-spin relaxivity r2, which firmly depends on the magnetic moment and the relaxation

processes of the magnetic spin, is a key factor for determining the degree of T2 contrast effect of the nanoparticle and higher values of r2 bring about greater contrast effect. Although resulting darker signals, which resemble the signals stemming from bleeding, calcification or metal deposits, and susceptibility artifacts that alter the background image are considered as drawbacks of T2 MRI contrast agents, they still have potential to be used in clinical applications on account of their high r2, biocompatibility, and prolonged circulation time in the body.[21] It is exploited from pure iron and cobalt metals, alloys such as CoPt3, FePt, FeZn, and from iron oxides, including magnetite (Fe_3O_4) and maghemite (γ-Fe_2O_3) to develop T2 contrast agents. Unfortunately, problems associated with toxicity and susceptibility to oxidation restrain cobalt and nickel containing nanoparticles using in biomedical applications. On the other hand, +2 cations including Mn, Fe, Co or Ni can be used as dopant for iron oxides to improve magnetic properties of newly formed MFe_2O_4 structures.[22]

Among all types of iron oxide nanoparticles, that are maghemite, γ-Fe_2O_3, magnetite, Fe_3O_4, and haematite, α-Fe_2O_3, magnetites are potent CAs as next generation imaging agents due to their biocompatibility, biodegradability and low level of toxicity.[238-239] They can display superparamagnetic properties depending on the crystal structure, size and shape of the synthesized particle.[240] The synthetic approaches can be listed as i) co-precipitation of iron salt solutions, ii) thermal decomposition and/or reduction, iii) hydrothermal synthesis, iv) polyol synthesis.[25] Among all techniques, thermal decomposition is widely used method to produce nanoparticles with tunable size (4-50 nm) and narrow size distribution despite of large scale production limitations. Additionally, phase transfer into aqueous solution is required for these hydrophobic nanoparticles to be used in biomedical

applications.[26] Since the MRI contrast agents administrated intravenously, the solubility and dispersity of the particles in water are additional essential requirements to be fulfilled for the designed CAs to be used effectively for any clinical application.[241] Diverse surface modification strategies were developed, thereby gaining fundamental features including colloidal stability, facile ligand coupling and enhanced pharmacokinetic performance.[242] So far, ligands possessing anchor groups such as carboxylic acids, phosphines, amines, and catechol were generally utilized to modify the surface of the iron oxide nanoparticles *via* ligand exchange reaction and render them water-dispersible.[243] Depending on the availability of terminal functional groups in the ligand, bioactivity can also be imparted by decorating chemically active organic coating with different moieties such as cell penetrating or RGD peptides[244-245], antibodies[246], folic acid[247] and carbohydrates[248]. Alternatively, amphiphilic ligands such as PEGylated phospholipids, PEGylated and Pluronic polymers were exploited to form organic shell around the nanoparticle core by physical encapsulation or assembly through van der Waals interactions and/or electrostatic interactions.[243] Unfortunately, research conducted with iron oxide based CAs prepared according to the second approach is very limited in terms of *in vivo* studies.

In terms of MR contrast enhancement, size of the nanoparticles is the predominant parameter which should be taken into consideration. Jun *et al.* investigated the effect of size on spin-spin relaxivity r2 value and the results revealed that r2 gradually increases as the size of Fe_3O_4 nanoparticles enlarges due to enhanced magnetic moment.[29] Recently, Zhou *et al.* developed new strategy to increase r2 relaxivity by monitoring the morphology of iron oxide nanoparticles. Size-controllable octapod

iron oxide nanoparticles were synthesized, which had ultrahigh transverse relaxivity value (679.3±30 $mM^{-1}.s^{-1}$), and they were considered as promising candidates to be used for in vivo imaging and small tumor detection.[30] Additionally, surface hydrophilicity and coating thickness are known to contribute greatly to the resulted MR contrast effect by affecting proton relaxivities of iron oxide nanoparticles.[31]

In this chapter, the co-assembly of proline rich peptide amphiphiles and SPIONs through noncovalent interactions was demonstrated, leading to the formation of superparamagnetic, water dispersible hybrid system suitable for MR imaging. SPION/K-PA was further investigated by several different techniques. The utilization of co-assembled SPION/K-PA as a MRI contrast agent was assessed in both *in vitro* and *in vivo* experiments. While the cellular viability and uptake of these nanoparticles by human vascular endothelial cells (HUVECs) were evaluated with *in vitro* assays, the biodistribution and bioelimination of SPION/K-PA nanocomposite were investigated in MRI in an animal breast cancer model.

4.2 EXPERIMENTAL SECTION

4.2.1 Materials

1-Dodecylamine (98%) and iron(III) 2,4-pentanedionate (97%) ($Fe(acac)_3$) were ordered from Alfa Aesar. 1,2-Hexadecanediol was purchased from Sigma-Aldrich. Lauric acid and trifluoroacetic acid (TFA) were acquired from Merck. Chemical required for peptide synthesis such as 9-Fluorenylmethoxycarbonyl (Fmoc), tert-Butyloxycarbonyl (Boc) protected amino acids, [4-[α-(2',4'-dimethoxyphenyl)Fmoc-aminomethyl]phenoxy]acetamidonorleucyl-MBHA resin (Rink amide MBHA resin) and HBTU (2-(1H-Benzotriazol-1-yl)-1,1,3,3-tetramethyluronium

hexafluorophosphate) were purchased from NovaBiochem. All other reagents and solvents were used as received. Water used during the experiments was deionized by Millipore Milli-Q with a resistance of 18 MΩ.cm.

4.2.2 Synthesis of Superparamagnetic Iron Oxide Nanoparticles

The magnetite nanoparticles were synthesized according to the previously proposed procedure with some changes.[249] Briefly, 6 mmol (1.112 g) lauric acid, 6 mmol (1.2 g) laurylamine, and 10 mmol (2.584 g) 1,2-hexadecanediol were mixed in 20 mL of dibenzylether. When reaction medium reached to 200 °C, 2 mmol (0.706 g) $Fe(acac)_3$ was added and stirred for 1-1.5 hr at 200 °C under inert atmosphere. Condenser was added to the setup for reflux and system was moved to hot jacket heater to increase the temperature to 300 °C. The stirring continued 1h. After 1 h, the mixture was allowed to decrease its temperature to room temperature and 50 mL ethanol was added under air. The mixture was centrifuged at 8000 rpm for 15 min., the pellet was taken, 2-3 ml of hexane was added, it was sonicated for a minute and 20-30 mL ethanol was added. It was centrifuged again and brownish supernatant was discarded. Ethanol addition, centrifugation and decantation of supernatant steps were repeated until a clean color of supernatant was obtained. After observing colorless supernatant and discarding it, 6-7 mL hexane was added to the pellet. Superparamagnetic iron oxide nanoparticles were obtained by sonication for 5 min. followed by centrifugation for 10 min. at 6000 rpm and stored in the refrigerator.

4.2.3 Synthesis of peptide amphiphile (PA)

MBHA Rink Amide resin with loading 0.59 mmol/ g was selected as solid support to synthesize Lauryl-PPPGK-Am peptide amphiphile. Amino acid couplings were

carried out in DMF in the presence of 2 equivalents of Fmoc protected amino acid, 1.95 equivalents of HBTU and 3 equivalents of N,N-diisopropylethylamine (DIEA) for 2 h. Base labile Fmoc protecting groups were removed by treatment with 20% piperidine/dimethylformamide (DMF) solution for 20 min. Cleavage of both the acid labile protecting group on the side chain of amino acid and peptide itself from the resin was achieved by the addition of cleavage cocktail solution (trifluoroacetic acid (TFA) : triisoproplysilane (TIS) : water in the ratio of 95:2.5:2.5) into the beads and reaction was left for 2 h at room temperature. Excess TFA was removed by rotary evaporation. The remaining viscous peptide solution was treated with ice-cold diethyl ether and the resulting white pellet was freeze-dried. The chemical composition of the peptide amphiphile was elucidated with reverse phase HPLC on an Agilent 6530 Accurate-Mass Q-TOF LC/MS equipped with an Agilent 1200 HPLC. An phenomenex Luna 3μm C8 100A (50 x 3.00 mm) column and water (0.1 % formic acid)/acetonitrile (0.1 % formic acid) gradient were used as stationary phase and mobile phase, respectively. The peptide amphiphile was purified on an Agilent 1200 HPLC having Agilent Zorbax 300SB-C8 (21.2 x 150 mm) column with water (0.1% TFA)/acetonitrile (0.1% TFA) gradient.

4.2.4 Surface Coating of SPIO Nanoparticles

While 50 mg Lauryl-PPPGK-Am peptide amphiphile dissolved in deionized water (20 ml) was heated upto 55-65 °C and sonicated, 7 mg of SPION nanoparticles dissolved in hexane (2 ml) were added dropwise to the peptide solution. Peptide amphiphile molecules and SPIONs were mixed with a weight ratio of 7:1 and volume ratio of 10:1, respectively. After repeated sonication and vortex steps lasted one hour at indicated temperature range, solution was centrifuged at 6500 rpm for 5

min by using ultrafiltration tubes with 50 kDa cut-off membranes (Millipore Amicon Ultra-Regenerated Cellulose). This step was repeated at least 2 times.

4.2.5 Characterization of SPIO Nanoparticles and Hybrid SPION-PA System

4.2.5.1 Morphological Characterization

TEM was performed with FEI Tecnai G2 F30. 10 μL of 50 times diluted PA coated and uncoated SPION samples were placed on a carbon film (300 mesh) coated copper grid. They were left for 5 min and excess solution was removed by the pipette. Afterwards, the grids were dried under fume hood at room temperature over 2 h. Selected area electron diffraction (SAED) pattern of hydrophobic SPIONs was taken at an accelerating voltage at 200 kV by TEM. The diameter of the nanoparticles was determined by using Image J software from at least 100 nanoparticles.

4.2.5.2 X-Ray Diffractometry Analysis

Crystal structure of magnetite nanoparticles was investigated by a PANalytical X'Pert Powder Diffractometer operating at 45 kV and 40 mA. The analyses were performed under Cu Kα radiation ($\lambda = 0.15418$ nm) in the range of $2\theta = 10°\text{-}80°$. Lyophilized powders were grinded before the analysis and dispersed homogeneously into the holder. All XRD patterns were smoothed and the backgrounds were substracted by using instrument's software (X'Pert High Score) to show the diffraction peaks clearly.

4.2.5.3 Chemical Characterization by Infrared Spectroscopy

FTIR analysis was carried out using a Bruker VERTEX 70 with Hyperion scanning to confirm both organic coating layer and iron oxide nanoparticle existence. Prior to the pellet preparation, all samples were lyophilized or dried in a vacuum oven (Memmert GmbH + Co. KG, Germany). After mixing SPION, SPION/K-PA or K-PA with KBr (1:99 (w/w %)), brownish transparent pellet was obtained in case of iron containing samples. Their spectra were derived between 400 and 4000 cm^{-1}.

4.2.5.4 Thermogravimetric Analysis

Thermal gravimetric analyses (TGA) were performed using Perkin-Elmer TGA to analyze the organic/inorganic composition of SPION/K-PA samples. The temperature was increased from room temperature to 800 °C with a heating rate of 20 °C/min. 3-5 mg of lyohilized K-PA and SPION/K-PA samples were used for the analysis. Hydrophobic SPIONs dissolved in hexane solutions were dried in a vacuum oven (Memmert GmbH + Co. KG, Germany).

4.2.5.5 Particle Size and Zeta-Potential Analysis

Hydrodynamic size and zeta potential of the particles were measured by dynamic light scattering (DLS). A Malvern Nanosizer/Zetasizer nano-ZS ZEN 3600 (Malvern Instruments, USA) instrument with detector angle of 173° was used for DLS analysis. Hydrophobic particles and hydrophilic particles were diluted with hexane and water, respectively and measurements were performed in quartz cuvettes. Zeta measurement was carried out using a dip cell electrode in quartz cuvettes. The measurements were triplicated and standard deviations were calculated from the mean of the data. For the experiments conducted in 5% dextrose solution at 25 °C, refractive index, viscosity and dielectric constant values were selected as 1.34, 1.03

Pa.s and 77.37, respectively. The concentration of iron oxide nanoparticles was set to 250 μg/ml for all experiments and 2.42 were used as the refractive index of magnetite particles.

4.2.5.6 Iron Content Determination

Iron concentration was determined through inductively coupled plasma-mass spectrometry (ICP-MS, Thermo X Series II) and colorimetric Prussian Blue assay prior to PA coating step, *in vitro* and bioimaging experiments. In the former one, a standard curve was derived by dissolving and serially diluting iron plasma emission standard solution (1000 ppm, VWR-BDH Prolabo) in 2% nitric acid to obtain 500, 250, 100 and 50 ppb standard iron concentrations. SPION solutions were dissolved in concentrated nitric acid before dilution and heated upto 60 °C for the digestion. On the other hand, in Prussian Blue assay, a calibration curve was plotted by preparing serially diluted iron solutions (1000 ppm, VWR-BDH Prolabo) in 6 N HCl solution. All samples including standards and unknowns were digested at 65°C for an hour for the conversion of iron from nanoparticle form to ionic form. 160 mL of HCl was added samples (50:50, (v/v %)) were mixed with 40 μl of 5% $K_4Fe[CN]_6$. Samples for each concentration were prepared as triplicates in a 96 well-plate. HCl and 5% $K_4Fe[CN]_6$ added water was used as blank solution. They were allowed to interact for 20-25 min and color change was observed from yellow to blue for concentrated iron samples. UV intensities were measured at 690 nm by using Spectramax M5 (Molecular Devices).

4.2.5.7 PA Content Determination

PA coated SPIONs were purified from excess peptide amphiphile molecules by ultrafiltration using Millipore Microcon Centrifugal Filter Units, with 50K MW cut-off, 2 to 3 times at 6500 rpm for 5 minutes. The eluted parts were collected in each step and peptide amphiphile concentration was measured by NanoDrop 2000 (Thermo Scientific). The results were compared with the results obtained from samples prepared with known amount of PAs. Peptide quantification method offered by Thermo Scientific was utilized to measure the absorbance at analysis wavelength of 205 nm with extinction coefficient of 31 mg/mL at 1 cm path length.[250-251] The peptide amphiphile solutions were prepared at different concentrations in the range of 0.5 mg/mL to 0 mg/mL by several dilutions.

4.2.6 *In Vitro* Studies

In vitro studies were performed by using human vascular endothelial cells (HUVEC) donated by Yeditepe University, Istanbul, Turkey. Dulbecco's Modified Eagle's Medium (DMEM) supplemented with 10% FBS and 1% penicillin/streptomycin was used in cell culture experiments. Cells were cultured in standard humidified incubators with constant 5% CO_2 at 37 °C.

Biocompatibility of the samples on HUVECs was tested by live-dead assay (Invitrogen). They were seeded into 96-well plates at a density of 5×10^3 cell/well and treated with SPION/K-PA (75 μg/mL, based on iron content) and K-PA (214 μg/mL, 317 μM) for 24 h (n=3). HUVECs were then rinsed with PBS and stained with 1 μM calcein-AM. Fluorescence microscopy images (n=5) were quantified with Image J for each sample.

SPION internalization was monitored by Prussian blue staining, in which a bluish color is the indication of iron in the cell. They were seeded into 96-well plates at a density of 1 x 10^4 cells/ well and treated with SPION/K-PA (75 μg/mL, based on iron content). After cells were incubated for 6 hours, medium together with unbound particles were discarded and rinsed with PBS (10x) three times. The fixation process was done with 4% paraformaldehyde (100 μL) for 15 min. A mixture of 6 N HCl: 20% $K_4Fe[CN]_6$, 1:1 (v:v) was prepared and freshly used. 100 μL of solution was added to each well. After an hour of incubation, cells were washed with PBS and monitored under optical microscope at different magnifications. Experiments were performed two independent times in triplicate.

4.2.7 *In Vivo* Studies

Prior to *in vivo* study, Institutional Animal Care and Use Committee of Diskapi Yildirim Beyazit Training and Research Hospital approved the related protocols for animals. 36 Sprague-Dawley rats from ADACELL Laboratories (12-14 week old, weighing about 200-250 g) were used for MRI experiments. Animals randomly divided into two to create healthy and tumor-bearing groups were maintained at constant temperature and a relative humidity of 50−60% with 12 h light/dark cycles. Subcutaneous injection into the second right mammary pads of adult female rats was performed with single doses of 50 mg/kg body weight of DMBA dissolved in sesame oil to induce mammary carcinomas. Tumor formation was checked weekly and observed 3 months after the injection. It was waited until tumor volume reached 100 mm^3 to initiate MRI measurements. For the tumor volume calculations, the following formula was used: Tumor volume (mm^3) = (D x d^2)/2 (D: big diameter, d: small diameter of tumor).[252] Except non-treated control group, SPION/K-PA (5 mg Fe/kg

body weight in 5% dextrose solution) slowly injected through the tail vein and sacrificed at two different time points (after 4 hours or 15 days). During imaging, ketamycin (80 mg/kg) and xylazine (20 mg/kg) were intraperitoneally injected to anesthetize Spraque-Dawley rats prior to MR imaging. A 1.5 T clinical whole body MR scanner (Philips MR system intera) within a sense C3 small surface coil was used for MRI. Images of rats were obtained at different time intervals as just before SPION treatment, during nanoparticle injection, at 1 h, 4 h and 15 days after injection, with the following sequences and parameters: m-GRASE (gradient and spin-echo weighted imaging): act.TR (ms) 2126, active TE (ms) n* 18, field of view (cm) 160 x 200, min slice gap (mm) 0, thickness 2.2 mm, ACQ matrix Mxp (mm) 84 x 72. T2-weighted spin echo coronal: TR (ms) 3000, TE (ms) 80, field of view (cm) 160 x 200, slice gap (mm) 0, thickness 2.2 mm, ACQ matrix Mxp (mm) 388 x 270. T2-weighted fat sat: TR (ms) 3000, TE (ms) 80, field of view (cm) 160 x 200, slice gap (mm) 0, thickness 2.2 mm, ACQ matrix Mxp (mm) 388 x 270. The analysis of MRI data was conducted on a diagnostic workstation equipped with dedicated software (Philips extended MR workspace 2.6.3.4 2009). The image depth was kept constant during image collection to compare SPION-mediated darkening. Signal intensities (SI) of the regions of interest (ROI) were collected from circles of equivalent sizes (~ 5 mm diameter) drawn on the organs and relative signal enhancement was calculated from SI values obtained before (SI pre) and after (SI post) the injection of SPIONs: 1+ [(SI post − SI pre)/SI pre][253]

4.2.8 Statistical Analysis

All data were presented as ± standard error of mean (SEM) for all *in vitro* and *in vivo* results. One-way analysis of variance (ANOVA) with Tukey's test for group-wise

comparisons and two-way ANOVA test were used for viability and MRI experiments, respectively. Statistical significance was considered when p values were less than 0.05.

4.3 RESULTS AND DISCUSSION

4.3.1 Synthesis and Characterization of the Nanoparticles

Thermal decomposition method is an effective method for the production of iron oxide nanoparticles with a desired shape and size.[249] Although the method results in the formation of water insoluble nanoparticles and requires further modification for the efficient dispersion in the aqueous environment, it provides higher stability and significant control on the size and shape of the nanoparticle compared to one of the frequently used method, co-precipitation method.[254] Here, iron oxide (Fe_3O_4) nanocrystals were synthesized as a result of high temperature reaction of iron (III) acetylacetonate, $Fe(acac)_3$, in dibenzyl ether in the presence of 1,2-hexadecanediol, lauric acid and dodecylamine. Since the prepared nanoparticles were hydrophobic due to the lauric acid and dodecylamine capping, they were dispersed in a non-polar organic solvent, hexane. Subsequently, they were stored at 4°C and used for further modification in the course of six months. It was known that iron oxide nanoparticles having an average size of 4-16 nm, prepared via thermal decomposition method, displayed superparamagnetic characteristics.[255] In our previous study, this behavior was verified by vibrating sample magnetometer (VSM) measurements.[139] We furthermore observed that the synthesized superparamagnetic iron oxide

nanoparticles (SPIONs) possessed rapid magnetic responsivity to an applied external magnetic field (Figure 4.1).

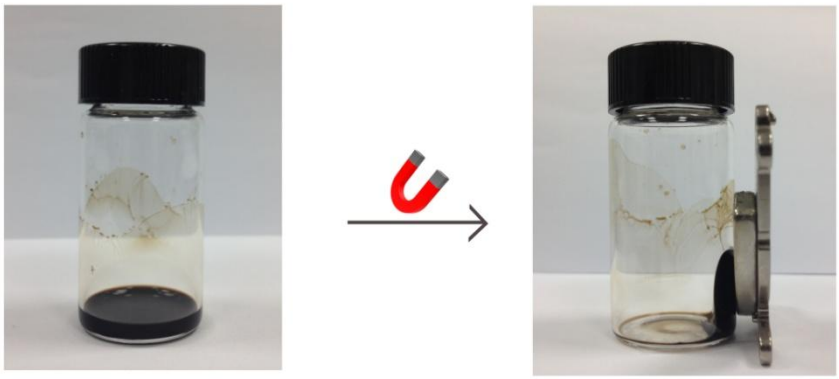

Figure 4.1 Images of hydrophobic iron oxide nanoparticles in the absence and presence of magnetic field when they are dispersed in hexane (10 mg/mL, concentration based on the iron amount).

TEM images, inserted in Figure 4.2c, exhibited that monodisperse SPIONs had narrow size distribution with uniform spherical morphologies. Their average diameter was found as 5.5 nm with a standard deviation of 0.6 nm. Dynamic light scattering (DLS) analysis of the nanoparticles dispersed in non-polar organic solvent were also performed and the diameter was found as 7.1±0.3 nm which is quite similar to the value obtained from TEM imaging (Figure 4.3). The lattice fringes can be observed in the high resolution transmission electron microscopy (HR-TEM) image of SPIONs (Figure 4.2 a, b), demonstrating the crystallinity of the respective nanoparticles.

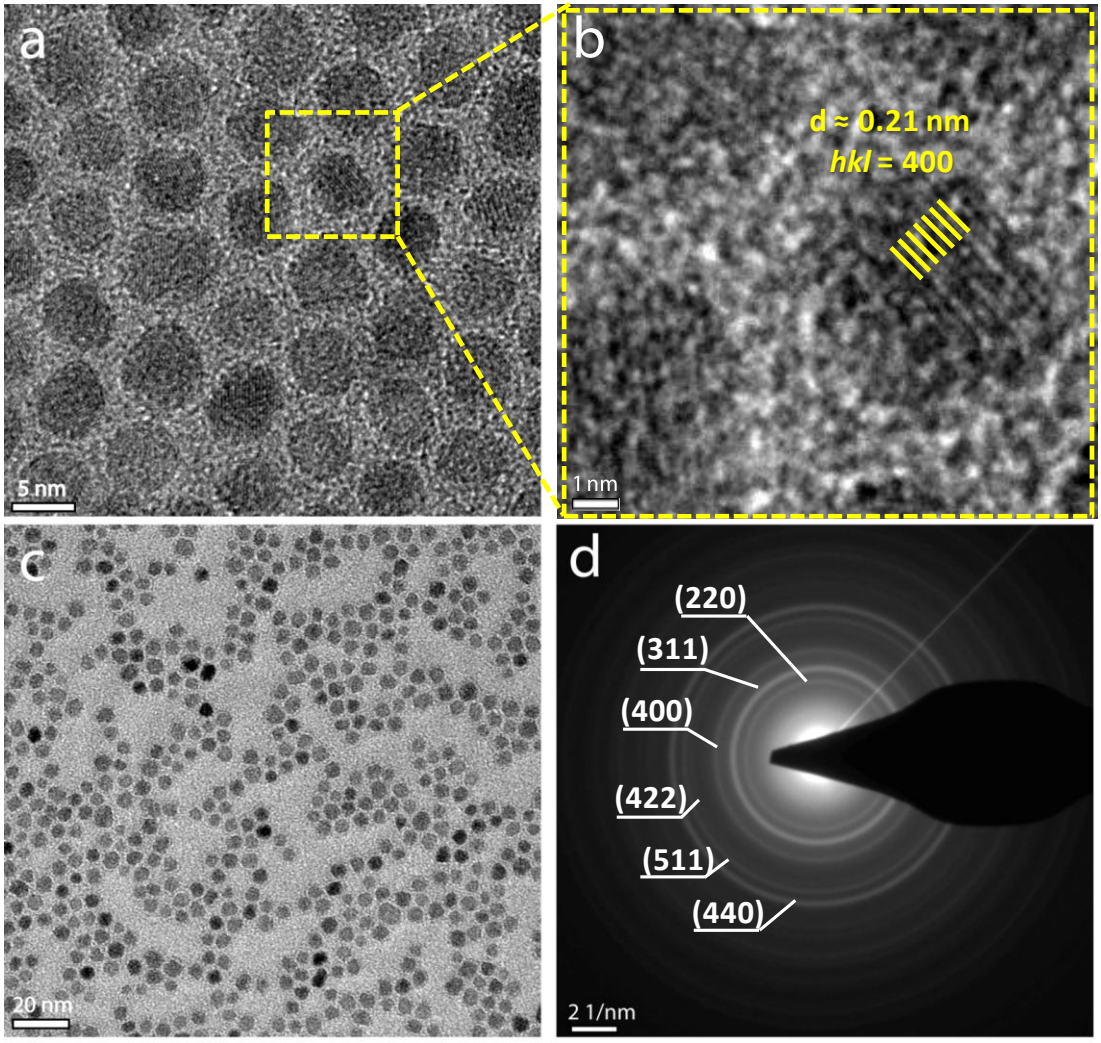

Figure 4.2 a) HR-TEM image of SPIONs, b) lattice fringe corresponds to the (400) lattice plane of magnetite nanoparticles, c) TEM image of SPIONs d) SAED pattern of SPIONs.

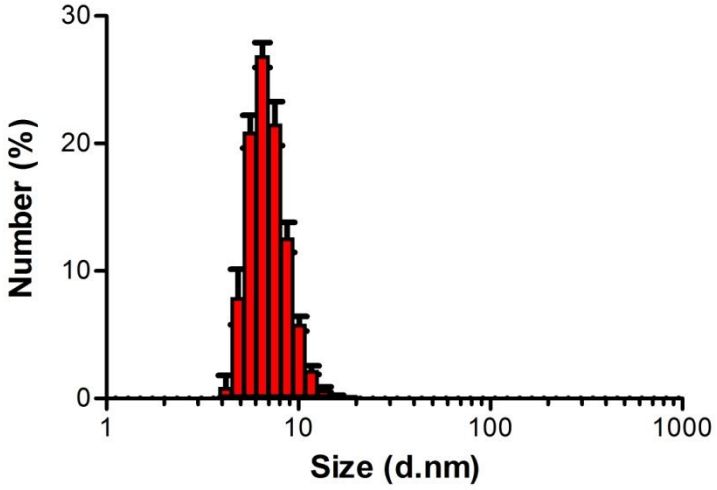

Figure 4.3 Number distribution of hydrodynamic diameter of SPIONs dispersed in hexane.

A specified area was magnified from the image to visualize the individual lattice plane more clear. The measured d-spacing of 2.12˚A corresponded to that for the (400) plane (2.09˚A) of magnetite.[256] Additionally, the circular rings appeared in electron diffraction pattern presented in Figure 4.3d confirmed the polycrystalline nature of the magnetite nanoparticles. Lattice spacings corresponded to each ring were calculated based on the diffraction patterns and showed good agreement with that for magnetite structure (JCPDS, No: 19-0629). XRD analysis result of SPIONs was also in consistent with that of obtained from SAED pattern and literature (Figure 4.4a).[257] The diffraction patterns demonstrated in Figure 4.4a were used to estimate the d-spacings of SPIONs by using Bragg's law. The calculated values along with the respective Miller indices values (*hkl*) and reference data were listed in Table 4.1. The results acquired from the different techniques supported each other and revealed that synthesized SPIONs have inverse spinel structure.[256]

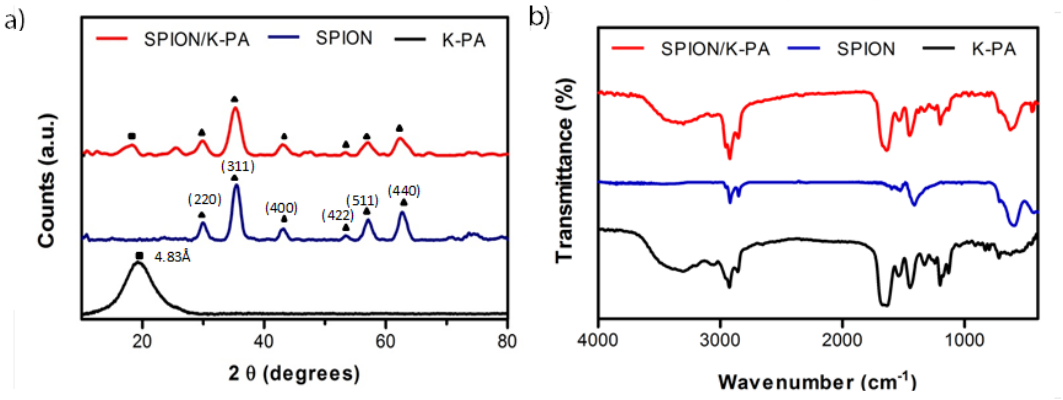

Figure 4.4 a) XRD patterns and b) FTIR spectra of bare and modified nanoparticles

Table 4.1 The d-spacing values (nm) calculated from peak positions in XRD pattern inserted in Figure 5.4 and standard atomic spacing for magnetite together with respective Miller indices (*hkl*) from the JCPDS card (19-0629)

2 θ (degrees)	**Calculated d-spacing (nm)**	**JCPDS data (nm)**	***hkl***
30.02	0.2961	0.2967	220
35.43	0.2524	0.2532	311
43.11	0.2096	0.2099	400
53.31	0.1740	0.1714	422
57.11	0.1610	0.1615	511
62.75	0.1479	0.1484	440

To render SPIONs water soluble and enhance the dispersion stability in physiological conditions, which are the indispensable prerequisites for the applicability of the nanoparticles, there are different strategies mainly achieved by the ligand addition or ligand exchange approaches.[258] In the former one, noncovalent interactions, such as electrostatic interactions, hydrophobic interactions and hydrogen bonding, are the

major driving forces for the physical adsorption of molecules to the surface of SPIONs. It was formerly reported that amphiphilic macromolecular ligands and liposomes were used for the preparation of water-dispersible SPIO nanocomposites.[243] To attain and improve the biocompatibility and biodegradability of the functionalized SPIONs, we previously demonstrated the utility of peptide amphiphile (PA) molecules in the production of SPION/PA coassembled nanocomposites.[139] In this study, we made an alteration in the design of PA molecule by replacing beta sheet forming sequence (-VVA) with proline-rich segment (-PPP) to avoid the nanofiber formation and improve the intermolecular cohesive interactions. It was known that proline rich sequence bearing PAs exhibited random coil conformation as analyzed by circular dichroism.[97, 110] PA was synthesized by solid phase peptide synthesis strategy based on orthogonal protection/deprotection chemistry and chemical structure was verified by liquid chromatography and mass spectroscopy (Figure 4.5). The change in the design led to an increase in the integration of lauryl group of the PAs into alkylated surface of SPIONs and resulted in more effective transfer into aqueous phase. Water stabilization of SPIONs was achieved by simply sonicating two immiscible solutions at the temperature range of 55-65°C below the boiling point of hexane. While SPIONs transferring into water phase, hexane slowly evaporated with time. After purification steps, they were concentrated *via* ultrafiltration method.

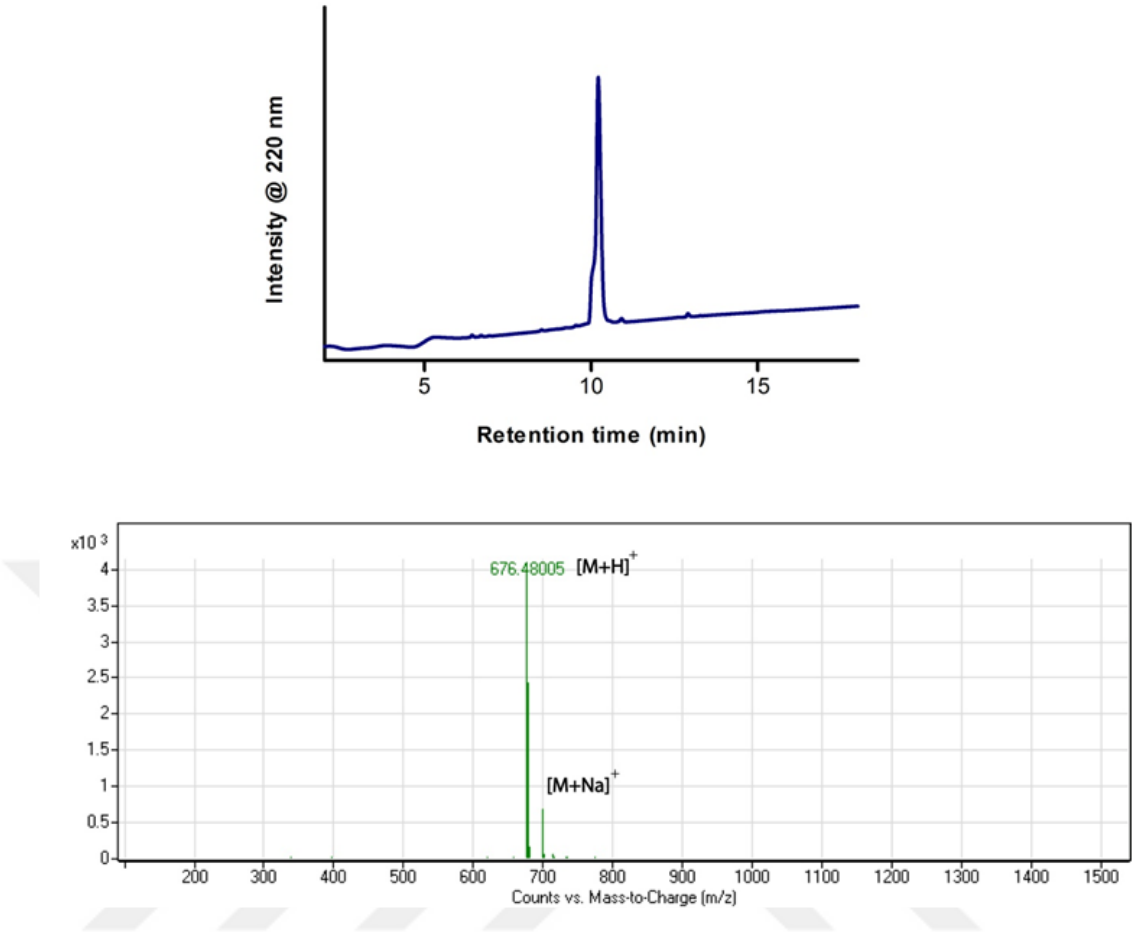

Figure 4.5 Liquid chromatogram of Lauryl-PPPGK-Am and mass spectrum of corresponding peptide amphiphile molecule. Mass data $[M-H]^+$ (calculated) = 676.47, $[M-H]^+$ (observed) = 676.48.

As depicted in Figure 4.6, SPIONs were successively transferred into aqueous environment with this method. The eluted parts were also collected to indirectly determine the amount of PA in the SPION/K-PA co-assembled system. Excess PA amount was calculated by measuring peptide bond absorption at 205 nm.[250] Since PA molecules were not purely composed of amino acids but also contained alkylated part, we primarily normalized the values by measuring known amount of PA samples prepared at different concentrations. After normalization, the value was substracted

from the initial PA amount used for the SPION functionalization. According to the calculations, nearly 35% of initial PA remained in the co-assembled system.

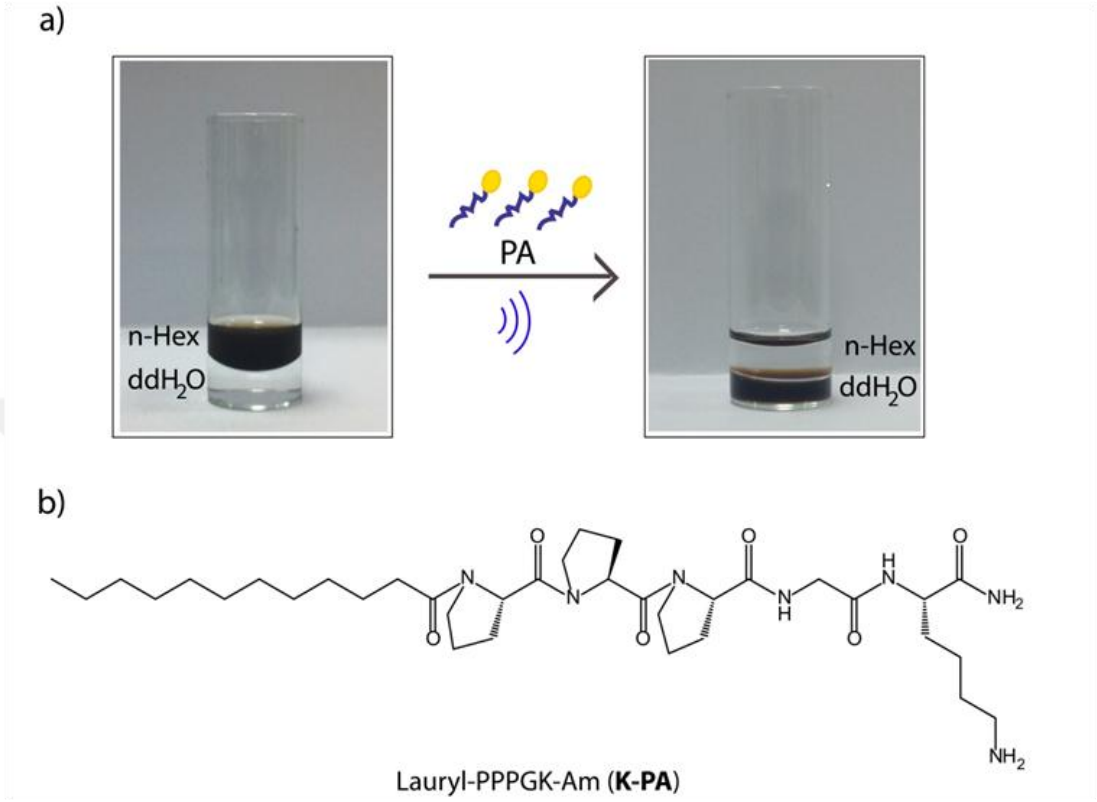

Figure 4.6 a) Photograph of modification of hydrophobic SPIONs with peptide amphiphile molecules, b) Chemical structure of peptide amphiphile molecule, K-PA.

Coassembled SPION/K-PA system was further examined by using diverse techniques. The XRD pattern of pure peptide amphiphiles showed a diffused halo peak registered between 10-30° (2θ), revealing the amorphous nature of PAs and confirming the disorganized structure of PAs (Figure 4.4a). SPION/PA nanocomposite also provided the same diffraction pattern as those obtained before PA functionalization, indicating that SPIONs retained their crystal structure after being assembled with PAs. FTIR spectra of sole PA and SPION along with their co-

assembled form are presented in Figure 4.4b. Hydrophobic SPIONs showed two prominent bands at 596 and 438 cm^{-1} which are the Fe–O vibrations related to the ferrite core.[259] The peaks appeared at 2926 and 2848 cm^{-1} were attributed to the asymmetric and symmetric stretching vibrations of $–CH_2$ groups present in lauric acid and dodecyl amine. Two peaks were observed at 1526 and 1413 cm^{-1} corresponding to two carboxylate stretches which implied the chemisorption of lauric acids on the surface of nanoparticles. In the case of PA molecules, characteristic peaks regarding the C=O stretching vibrations were observed between 1600 and 1700 cm^{-1}. N-H bending vibrations generate a broad band at 3200-3600 cm^{-1}. The IR spectrum of K-PA also exhibited C-N stretching and N-H bending vibration peaks at around 1534 cm^{-1} corresponding to the amide II band of PA. In the coassembled form, the identified peaks for both SPION and PA were still observed. Additionally, the strength of $–CH_2$ stretching peaked at 2926 and 2848 cm^{-1} increased with the integration of the alkyl tail of PA into the system. The TGA thermograms were also obtained to determine the organic/inorganic content of SPION/PA system and the corresponding decomposition temperatures. SPIONs before PA functionalization showed two major transitions due to the weight loses occuring between 200-450 °C and 600-750 °C which most likely result from the decomposition of organic coating and phase transition from Fe_3O_4 to FeO followed by deoxidation of FeO, respectively.[260] (Figure 4.7a) In case of K-PA, first pronounced mass loss was observed at 220 °C due to the decomposition of alkyl tail and a second marked one between 300 and 450°C was ascribed for the cleavage of side chain groups of amino acids and peptide bonds. After PA functionalization, similar decomposition processes were observed and found that nearly 52% mass loss stems from the PA. (Figure 4.7b)

Results acquired from TGA analysis also corroborated with the results obtained from the PA amount determination analysis.

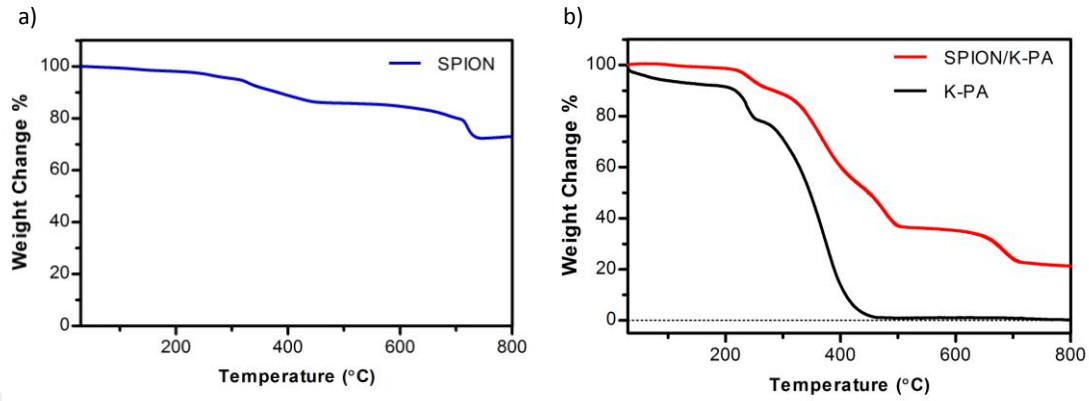

Figure 4.7 Gravimetric analysis of a) SPIONs before assembly with PA, b) SPION/K-PA nad PA samples.

As depicted in Figure 4.8, PA functionalization process did not change the shape of the nanoparticles and they were mostly randomly distributed on the TEM grid except very few overlapping areas. Since there was no staining on the samples, only the core was imaged and the mean diameter of the SPION/K-PA nanoparticles were estimated as 5.3 nm with a standard deviation of 0.7 nm, revealing that functionalization did not cause any change in the morphology of nanoparticle in terms of sphericity and size.

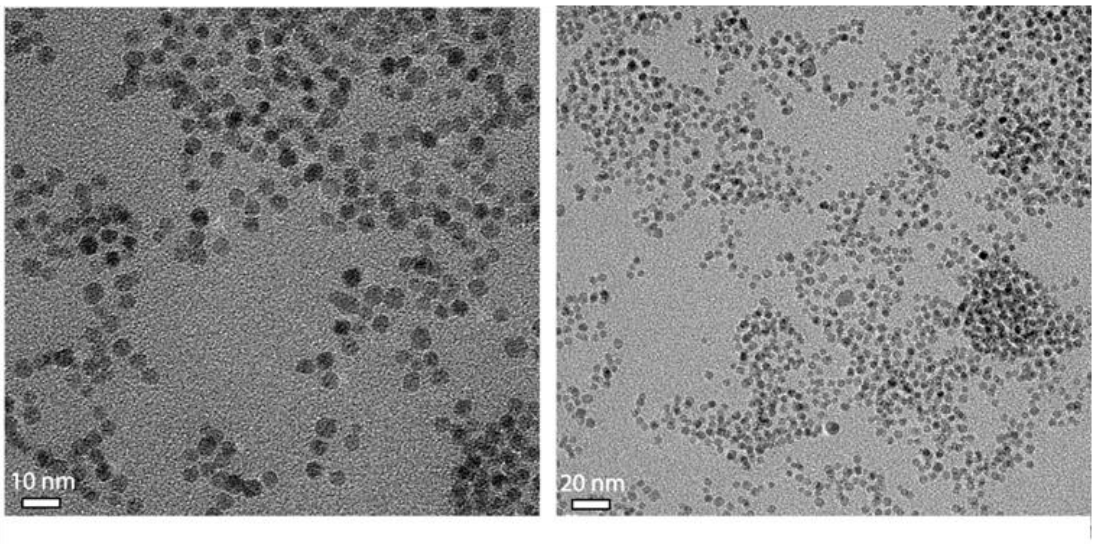

Figure 4.8 TEM images of PA coated SPIONs, scale bars = 10 nm and 20 nm, respectively.

On the other hand, hydrodynamic size of SPION/K-PA was determined in two different media, water and 5% dextrose solution. Nanoparticles with a core size of 5.3 nm had hydrodynamic sizes of 58.0 nm ± 0.7 and 58.6 nm ±0.1 in water and 5% dextrose, respectively, which are in the range of optimal values for long circulation times *in vivo* (Figure 4.9 and Table 4.2).[261] The hydrodynamic sizes did not significantly change over the measured period of time for both solutions and the photographs of nanoparticle dispersions indicated that they maintained the dispersion stabilities even after a week (Figure 4.9). Nanoparticles dispersed in 5% dextrose solution exhibited smaller changes in their hydrodynamic size compared to those dispersed in water which is suitable for the storage of these nanoparticles prior to any administration. Their zeta potentials were also measured and found that both solutions are positively charged due to the lysine residue present in the PA structure.

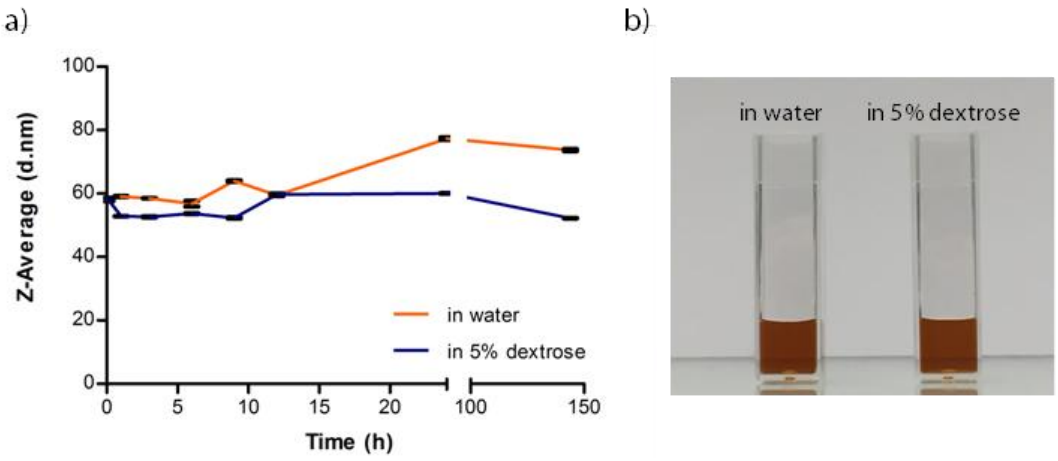

Figure 4.9 a) Dynamic light scattering (DLS) analysis to determine the dispersion stability of PA coated SPIONs prepared in two different media, b) photographs taken after a week dispersion in corresponding media.

Table 4.2 Physical properties of fatty acid/amine capped SPIONs and PA functionalized SPIONs (a: in water, b: in 5% dextrose, c: in hexane)

Sample	TEM size (nm)	DLS size (nm)	Zeta potential (mV)
SPION	5.5±0.6	7.1±0.3[c]	N/A
SPION/K-PA[a]	5.3±0.8	58.0±0.7	18.3±1.4
SPION/K-PA[b]	N/A	58.6±0.1	23.7±1.7

4.3.2 *In Vitro* Cytotoxicity and Uptake Studies

The biocompatibility of SPION/K-PA was assessed on vascular endothelial cells (HUVECs) by live-dead assay. Before starting cell experiments, iron concentration was determined by measuring iron content of the solutions *via* two different techniques, inductively coupled plasma-mass spectrometry (ICP-MS) and colorimetric Prussian blue assay. In the latter one, to colorimetrically determine iron

content, a calibration curve was plotted for solutions prepared from serially diluted reference solutions (Figure 4.10). As previously mentioned, PA amounts in corresponding SPION/PA solutions were also spectroscopically determined.

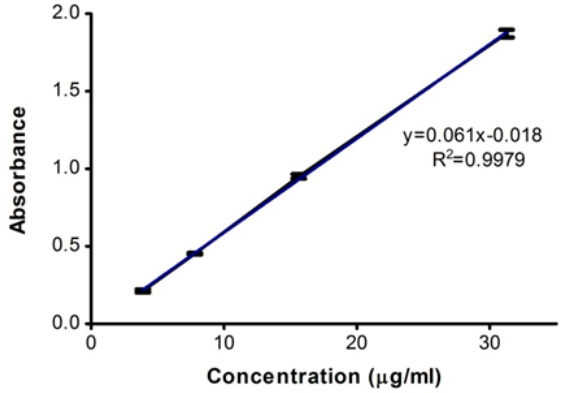

Figure 4.10 Calibration curve plotted for iron content determination.

Data represented in Figure 4.11a and b revealed that no significant decrease was observed in vascular cell viability after the administration of K-PA and SPION/K-PA compared to the non-treated group. Cells treated with SPION/K-PA exhibited more than 90% viability, suggesting that these nanoparticles could be employed safely in magnetic resonance imaging. Selected concentration (75 µg/mL) was used as administered dosage in MR, which was calculated based on the total circulating blood volume of a rat (64 mL/kg of body weight).[262] In the literature, higher cytotoxicities on HUVECs were reported at even nanomolar concentrations after 24 h of exposure when treated with dextran or citric acid coated nanoparticles.[263] Compared to those nanoparticles, SPION/K-PA system can be considered as safer alternative for bioimaging at the tested concentration.

Endothelial cells were stained with Prussian blue to visualize the accumulated nanoparticles in HUVECs. While clustered blue particles were observed on the surface and interior of HUVECs treated with SPION/K-PA, no blue dots were observed in non-treated group (Figure 4.11c). It was most likely due to the electrostatic interactions occurring between negatively charged phospholipid membrane of cells and positively charged nanoparticles.[264]

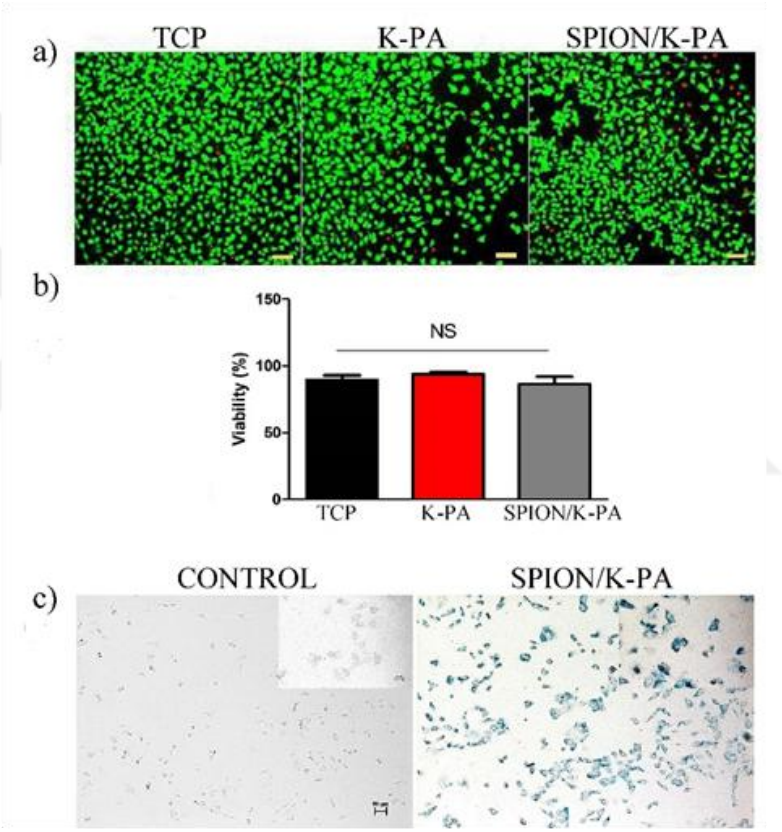

Figure 4.11 a) Live-dead assay for HUVECs treated with K-PA (855 µg/ml) and SPION/K-PA (75 µg/mL) for 24 h. scale bar = 100 µm, 10x magnification b) Quantification of live-dead assay c) Light microscopy of HUVECs after 6 h of incubation with and *w/o* SPION/K-PA. Insets are 40X magnified images.

4.3.3 *In vivo* Magnetic Resonance Imaging Studies

The usability of SPION/K-PA system as a negative contrast agent in MR imaging was investigated in a clinical 1.5 T MRI system with a T_2-weighted m-GRASE sequence by injecting the nanoparticle solution through the tail vein. MRI results pointed out that preferential accumulation of nanoparticles was observed in breast tumor rather than RES organs. After the administration of SPION/K-PA, gradual fade-out in tumor tissue was noticed in T_2-weighted images and it was remarkably attenuated at 4 h, which was not experienced in pre-injection group and non-injected control animals (Figure 4.12a). Contrast enhancement in dark signal was quantified by calculating the signal intensity changes associated with the uptake of nanoparticle into tumor and other organs from the ROIs of the T_2-weighted m-GRASE images (Figure 4.12b). Reduction in signal intensity was observed in the liver, kidney and spleen of both healthy and tumor-bearing animals immediately after PA functionalized nanoparticle administration, which is most likely due to the fast blood flow rate in these abdominal organs.[265] After an hour, the signal intensity of magnetic nanoparticles in RES organs started increasing to the pre-injection value and no T_2 shortening was observed after 15 d in any organ, indicating the removal of nanoparticles from the organs within two weeks (Figure 4.12b). The most crucial issue in designing an efficient nanomaterial for diagnostic applications is that while the material's residence time in the organ of interest should be long enough to provide sufficient time for effective imaging, it should also be degraded and cleared from the body after the imaging without any accumulation.[266] Our results revealed that SPION/K-PA was removed from the body after localizing in the tumor site and allowing enhanced MRI imaging.

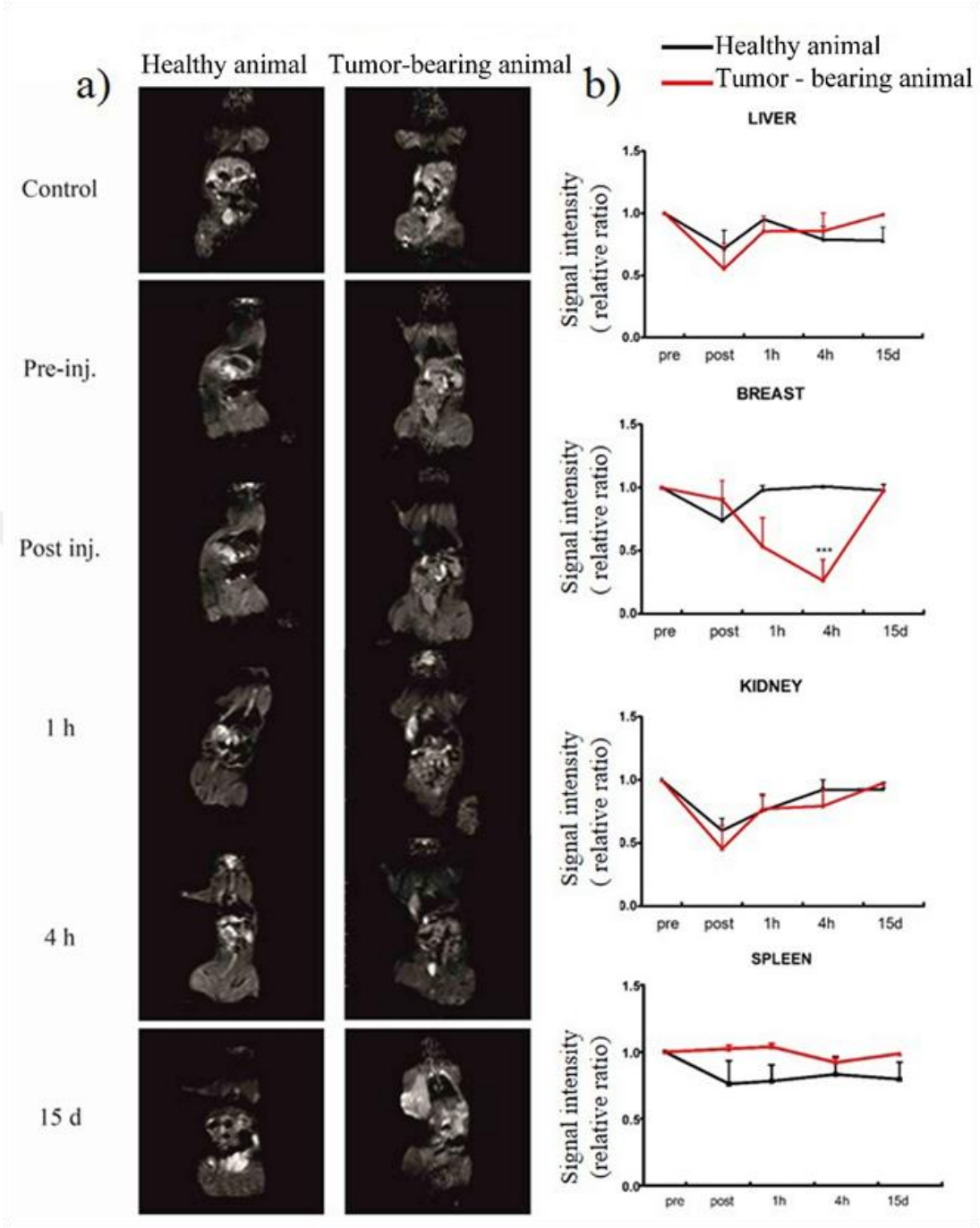

Figure 4.12 a) *In vivo* MRI of rats treated with and *w/o* SPION/K-PA b) Signal intensity changes in T_2 relaxations at pre-, immediately after injection (post), 1 h, 4 h and 15 d post administration in breast, liver, spleen, kidney and breast tumor of rats.

Although SPION/PA system does not bear any targeting moiety on its surface, it was observed that they markedly accumulated in tumors most likely due to the leaky vascular structure of tumor tissue. This phenomenon is commonly known as the enhanced permeation and retention (EPR) effect. The fact that SPIONs functionalized with non-bioactive ligands have been exploited for *in vivo* cancer imaging and the effectiveness of contrast agent conjugated PAs have been shown in the literature using *in vitro* assays stress the potential of new developed system as negative contrast agent for MR imaging.[267-271]

4.4 CONCLUSION

In summary, it was demonstrated that proline-rich peptide amphiphiles are suitable molecules for transferring hydrophobic iron oxide nanoparticles into aqueous environments through noncovalent interactions. The peptide functionalization was well analyzed and hydrodynamic size of peptide coated nanoparticles was found in the range of optimal values for *in vivo* applications. Cellular viability and uptake of amphiphilic peptide coated SPIONs (SPION/K-PA) were evaluated with HUVECs. The efficiency of SPION/K-PA as MRI contrast agents was analyzed in Sprague-Dawley rats with mammary gland tumors. A significant enhancement was observed in the MRI signal of breast tumor tissue after the administration of SPION/K-PA, suggesting that the nanocomposite system is promising as a MRI negative contrast agent. The enhanced permeability and retention (EPR) effect appears to be responsible for the passive targeting of these nanoparticles. Studies regarding the *in vivo* fate of SPION/K-PA suggest that the co-assembled system is biocompatible and biodegradable, as confirmed by the long-term consistency of the MRI signal and the material's lack of accumulation in RES organs. Due to the ease of functionalization

of nanoparticles, the practical utility of PA functionalized SPIONs can be further extended by appending bioactive epitopes into the PA construct to selectively target a specific type of receptor or cell.

CHAPTER 5

SUPRAMOLECULAR GAG-LIKE SELF-ASSEMBLED GLYCOPEPTIDE NANOFIBERS INDUCE CHONDROGENESIS AND CARTILAGE REGENERATION

Part of this thesis is published in the following article[272]; Reprinted from "Supramolecular GAG-like self-assembled glycopeptides nanofibers induce chondrogenesis and cartilage regeneration"; Sardan Ekiz, M., Ustun Yaylaci, S., Arslan, E., Can, N., Kilic, E., Ozkan, H., Orujalipoor, I., Ide, S., Tekinay, A.B., and Guler, M.O., *Biomacromolecules*, 2016, 17(2), 679-689, with permission from American Chemical Society (equal contribution)

5.1 INTRODUCTION

Carbohydrates, consisting of sugar chains, are one of the most abundant biomolecules present in nature, and in particular on the surface of cells.[273] Unlike amino acids and nucleotides, carbohydrates dictate highly specific interactions due to the variance in their anomeric status, tethering position, ring size and branching. In spite of the developed chemical tools, the diversity in its structure obstructs both synthesizing and characterizing such complex structures. Therefore, significant effort is directed toward developing alternative structures to carbohydrates such as glycoconjugates, not only mimicking their structures but also imparting multivalency to afford enhanced specificity and selectivity.[274] In last few decades, scientists have employed a variety of approaches to the synthesis of these glycoconjugates; however, there is still demanding need for further improvement of the presented strategies.

Glycosaminoglycans (GAG) and proteoglycans are the main glycoconjugates existing on the surface of cell membranes and in the extracellular matrix.[275-276] GAGs are long, linear and highly charged heterogeneous polysaccharides that are located in various forms in the body. They have roles in many biological processes such as organogenesis and growth control, cell adhesion, signaling, inflammation, tumorigenesis, and interactions with pathogens.[277-280] While the density of the sugar units in the structure affects the avidity of the interactions and selectivity of the recognition sites, abovementioned biological processes can be controlled by changing the type and degree of glycosylation.[281-283] Therefore, producibility of these structures synthetically is of great importance for the diagnosis and treatment of

many diseases. This is one of the most important reasons for the birth of the science of glycobiology.

The structure and function of GAG molecules can be mimicked by exploiting different synthetic approaches.[284] In addition to the structural mimicking, functional mimicry can even be provided by utilizing chemistries with no relation to biological structures.[285] GAG-mimetic molecules can be synthesized by the polymerization of oligosaccharides, by the functionalization of natural carbohydrates, or by the functionalization of synthetic polymers with sugar moieties.[286] [287-290] Apart from the carbohydrate bearing mimics, there are also several nonsaccharide GAG mimetic examples in the literature presenting only functional chemical groups in the structure such as poly (sodium-4-styrenesulfonate) (PSS),[291-292] sulfated aromatic scaffolds,[293] polymerized 2-acrylamido, 2-methylpropane sulfonic acid (NaAMPS) and 3-sulfopropyl acrylate (SPA),[294] and sulphonated peptide amphiphile.[122]

Glycopeptides are peptide bearing carbohydrate moities (glycans) covalently bound to the amino acid side chains. Despite the fact that carbohydrate chemistry has several complications in terms of structural branching, varied stereochemistry found in large oligosaccharides, and required strictly anhydrous conditions during glycosidic bond formation, wide range of carbohydrate units from monosaccharides to large glycans can be anchored to amino acid residues through chemical synthesis, chemoenzymatic synthesis, and chemical ligation.[295] The critical step in the chemical synthesis of glycopeptides is the conjugation of the sugar unit to the peptide. To overcome this, preformed glycosylated amino acid residues can be used for stepwise synthesis of the peptide skeleton (building block approach), or a properly protected full-length peptide can be directly glycosylated (convergent synthesis).[296] In the

convergent synthesis, unprotected hydroxyl or carboxylic acid units of saccharides are incorporated into protected peptide by glycosylation for the synthesis of *O*-glycopeptides and *N*-glycopeptides, respectively. An advantage of this approach is rapid formation of glycopeptides with different glycan structures.[296] For instance, an HBTU mediated coupling of GlcNAc glycosamine with the side chain aspartate carboxylate in a pentapeptide was performed by Lansbury and coworkers in 1990 resulted in the formation of an Asn-N-linked GlcNAc-unit bearing glycopeptide.[297] Also, Danishefsky and coworkers used the improved version of the same approach to synthesize gp120 glycopeptide fragments chemically.[298] On the other hand, the convergent method brings about low yields due to the low reactivity of the side chains of hydroxyls and low solubility of the peptides for the *O*-glycosylation case.[296] Moreover, intramolecular aspartimides can form during the condensation of a glycosylamine and an aspartic acid-containing peptide in the case of *N*-glycosylation.[299] In addition to these disadvantages, glycosylation results in less than perfect α/β ratios.[275] Therefore, building block approach is often preferred. The glycoamino acid is formed in solution and then incorporated into the peptide based on the standard solid phase peptide synthesis (SPPS) techniques. In the case of having fully acylated carbohydrates, glycosidic linkages can show resistance to short treatment of TFA during the removal of side-chain protecting groups of amino acids. Furthermore, β-elimination occured in *O*-linked serine and threonine glycosides is generally hindered by relatively weak base usage such as morpholine and piperidine. Hence, it is suitable to apply the Fmoc SPPS chemistry to the synthesis of glycopeptides.[300] However, this strategy has also some limitations such as the need of both carbohydrate and amino acid protection and acid-base lability of glycosylated

amino acid residues.[301] Selection of proper protecting groups are rather limited: *O*-glycosidic bond and particularly the α-fucosidic linkage show acid labile property, and β-elimination can take place in the *O*-linked glycopeptide upon treatment with strong bases. Racemization of the stereogenic centers of peptides can be seen in the presence of strong bases.[296] Additionally, glycopeptides up to 50 residues can be synthesized *via* SPPS technique.[302]

There are attempts to develop supramolecular glycopeptide nanostructures and use them as biocompatible materials in biological applications. Until now, different kind of glycosyl units was anchored to Fmoc- or naphthalene conjugated amphiphilic di- or tripeptides to create self-supportive glycopeptide gels through noncovalent interactions. Nevertheless, the anchorage of saccharide units to peptide skeleton was achieved by using different chemical approaches, all of which had lack of glycosylation bonds found in native systems.[303-306] Previously, glycopolypeptides as polymeric mimics of natural glycoproteins were devised and the resulting hydrogels were also exploited as synthetic scaffolds for cartilage tissue engineering.[307-308]

For cartilage tissue regeneration, hyaluronic acid molecule in different formulations has been used as a bioactive scaffold due to its inherent feature of cellular recognition, regulatory role in condensation and high abundance in native cartilage extracellular matrix.[309-311] Apart from their high cost and batch-to-batch variations in the extraction process, polysaccharides derived from animals may cause chronic immunogenic responses when introduced to the body.[312-314] The proposed reagents used in crosslinking reactions to obtain modified hyaluronic acid derivatives have also exhibited cytotoxicity.[315] Alternative to natural one, many polymer-based hydrogels could not pass the toxicity and degradability barriers due to the non-

natural building blocks existing in their structure, impeding their use in *in vivo*. Moreover, in protein-glycosaminoglycan conjugates, improved scaffold properties are provided in cartilage; however, bioactivity pertaining to the core protein is often lost.[316] These setbacks can be overcome by using glycopeptide-based materials.

In this chapter, a self-assembled glycopeptide nanofiber system was presented, which has been devised to serve as an analog of hyaluronic acid. The co-assembled system composed of a Ser-linked β-D-glucose containing amphiphilic glycopeptide and a carboxylic acid-bearing PA formed a synthetic hyaluronic acid emulating system. As a result of the self-assembly of glycopeptide amphiphile molecules, multiple glucose residues organized in close proximity on a nanoscale supramoleculer polymeric system. These high aspect ratio glycopeptide nanostructures communicated with MSCs through CD44 receptors and the interaction led to the induction of chondrogenic differentiation in a manner similar to native hyaluronic acid. Additionally, to further support the *in vitro* experiments, an *in vivo* microfracture-treated osteochondral defect model was utilized to examine the effect of glycopeptide nanofiber hydrogels in promoting hyaline-like cartilage formation.

5.2 EXPERIMENTAL SECTION

5.2.1 Materials

9-Fluorenylmethoxycarbonyl (Fmoc), tert-Butyloxycarbonyl (Boc) protected amino acids, Wang resin and MBHA Rink Amide resin were purchased from NovaBiochem. HBTU (2-(1H-Benzotriazol-1-yl)-1,1,3,3-tetramethyluronium hexafluorophosphate) and Fmoc-Ser[β-*D*-Glc(OAc)$_4$]-OH were purchased from

ABCR and Aapptec, respectively. The other chemicals were purchased from Alfa Aesar and Sigma-Aldrich and used as provided.

5.2.2 Synthesis of acetylated β-*D*-Glucose linked serine glyco amino acid

5.2.2.1 Protection of the Carboxylic Acid of Fmoc-Ser-OH to Yield Fmoc-Ser-OAllyl

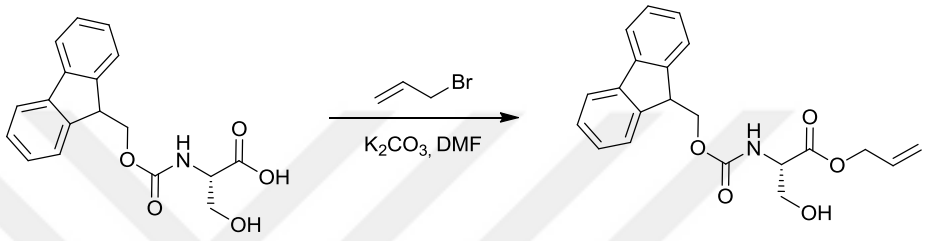

Fmoc-Ser-OH (1.5 g, 4.5 mmol) was dissolved in DMF and mixed with allyl bromide (2.14 ml, 5.4 mmol) in the presence of K_2CO_3 (0.93 g, 6.75 mmol). The reaction was allowed to stay for 24 h at room temperature. After diethylether addition, the mixture was extracted with water and brine solution. Aqueous phase was discarded and Na_2SO_4 was added into organic phase. The solution was concentrated with rotary evaporator and purified using flash column chromatography (1:1 nHex/EtOAc). ^{1}H NMR (400 MHz, $CDCl_3$) δ ppm 7.80 (dd, J = 1.6, 7.1 Hz, 2H), 7.64 (d, J = 6.3 Hz, 2H), 7.43 (m, 2H), 7.39-7.31 (m, 2H), 7.31-7.27 (m, 1H), 5.95 (m, 1H), 5.75 (s, 1H), 5.45-5.25 (m, 1H), 4.77-4.68 (m, 2H), 4.55-4.47 (m, 1H), 4.47-4.40 (m, 2H), 4.32-4.22 (m, 1H), 4.02 (dd, J= 11.1, 22.5 Hz, 2H), 2.12 (s, 1H); ^{13}C NMR (100 MHz, $CDCl_3$) δ170.12, 143.82, 143.69, 141.37, 141.33, 127.92, 127.10, 125.06, 120.32, 120.01, 119.99, 119.04, 67.22, 66.36, 63.34, 56.13, 47.19. ESI-TOF-HRMS m/z: calculated for $C_{21}H_{21}NO_5$ $[M+Na]^+$ *m/z*= 390.1420, experimental *m/z*= 390.1363, $[2M+Na]^+$ *m/z* =757.281.

5.2.2.2 *D*-Glucose Pentaacetate Coupling to Fmoc-Ser-OAllyl to Yield Fmoc-Ser[β-D-Glc(OAc_4)]-OAllyl

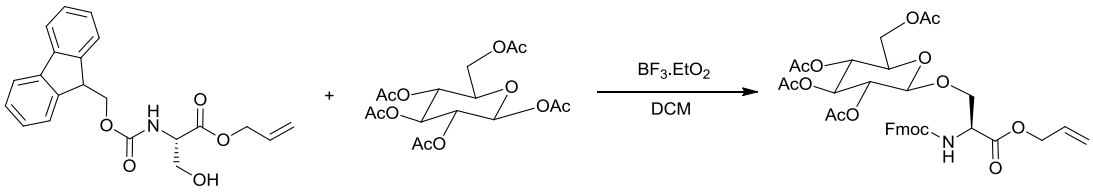

The Lewis acid, $BF_3.Et_2O$ (8 mL, 0.3 mmol) was added to the glucose pentaacetate (0.3 eq., 4g) and the N-α-Fmoc-Ser-OAllyl (1 eq., 2.9 g) in dry CH_2Cl_2 under argon atmosphere. The reaction was cooled to 0°C for Lewis acid addition, after 5-10 min reaction was allowed to stay at room temperature for 12 h. The progress of the glycosylation reaction was monitored by TLC (2:3 nHex/EtOAc). The solution was diluted with DCM and extraction was done with water (3 times). Na_2SO_4 was added to remove trace amount of water and concentrated in rotary evaporator. Compound was purified with column chromatography (2:3 nHex/EtOAc). ^{1}H NMR (400 MHz, $CDCl_3$) δ ppm 7.80 (d, J = 7.5 Hz, 2H), 7.64 (d, J = 7.3 Hz, 2H), 7.43 (m, 2H), 7.37-7.33 (m, 2H), 5.96-5.86 (m, 1H), 5.61 (d, J = 8 Hz, 1H), 5.35 (d, J = 17.2 Hz, 1H), 5.28 (dd, J =1.1, 10.5 Hz, 1H), 5.22 (t, J = 9, 1H), 5.11-5.06 (m, 1H), 5.0-4.9 (m, 1H), 4.68 (d, J= 5.4 Hz, 2H), 4.52-4.48 (m, 2H), 4.46-4.41 (m, 1H), 4.31 (dd, J = 2.9, 10.5 Hz, 1H), 4.28-4.21 (m, 2H), 4.14 (dd, J = 2.2, 12.3 Hz, 1H), 3.89 (dd, J = 3.1, 10.5 Hz, 1H), 3.70-3.66 (m, 1H), 2.11-2.01 (m, 12H); ^{13}C NMR (100 MHz, CDCl3) δ170.59, 170.19, 169.36, 169.24, 169.13, 155.84, 143.78, 143.66, 141.37, 141.33, 131.36, 125.00, 120.33, 120.05, 118.80, 101.10, 68.25, 66.40, 61.81, 54.40, 47.16, 20.67, 20.59, 20.56, 20.51. ESI-TOF-HRMS m/z: calculated for $C_{35}H_{39}NO_{14}$ $[M+Na]^+$ *m/z*= 720.2371, experimental *m/z*= 720.2218, $[M+K]^+$ *m/z*= 736.08717

5.2.2.3 Deprotection of Allyl Group to Yield Fmoc- Ser[β-D-Glc(OAc$_4$)]-OH

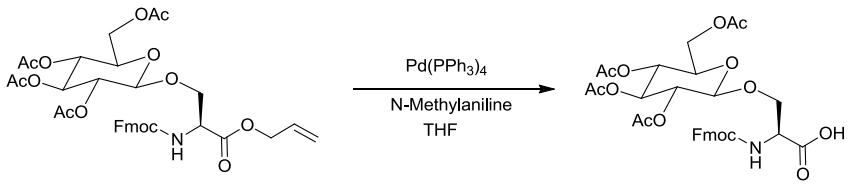

Glycosylated amino acid (4.02 mmol, 2.8 g), N-Methylaniline (40.68 mmol, 4.40 ml) and $Pd(PPh_3)_4$ (0.048 mmol, 55 mg) were dissolved in THF. The reaction took place at room temperature overnight and monitored with TLC (98:2, DCM:AcOH). The compound was concentrated with rotary evaporator and the product was purified with column chromatography (1:1 nHex/EtOAc). ^{1}H NMR (400 MHz, $CDCl_3$) δ ppm 7.79 (d, J = 7.5 Hz, 2H), 7.63 (d, J = 7.2 Hz, 2H), 7.43 (t, J=7.4 Hz, 2H), 7.34 (td, J= 1.1, 7.5 Hz, 2H), 6.44 (bs, 1H), 5.71 (d, J=7.8 Hz, 1H), 5.24-5.20 (m, 1H), 5.11 (t, J = 9.7 Hz, 1H), 5.02-4.97 (m, 1H), 4.56-4.50 (m, 2H), 4.49-4.42 (m, 1H), 4.31 (dd, J =2.1, 10.6 Hz, 1H), 4.28-4.23 (m, 1H), 4.14 (q, J = 7.2 Hz, 1H), 3.96 (dd, J = 3.3, 10.6 Hz, 1H), 3.73-3.67 (m, 1H), 2.10-2.01 (m, 12H); ^{13}C NMR (100 MHz, CDCl3) δ172.28, 171.33, 171.4, 170.27, 169.62, 169.47, 143.74, 143.74, 141.64, 141.34, 127.79, 127.13, 125.06, 120.03, 101.14, 72.63, 67.19, 61.81, 60.46, 54.09, 47.14, 21.03, 20.75, 20.58, 20.56. ESI-TOF-HRMS m/z: calculated for $C_{32}H_{35}NO_{14}$ $[M-H]^-$ *m/z*= 656.2058, experimental *m/z*= 656.1897, $[2M-H]^+$ *m/z*= 1313.3849.

5.2.3 Synthesis and Characterization of Glycopeptide and Peptide Amphiphiles

Protected glycopeptide was constructed on MHBA Rink Amide resin. All amino acid couplings were performed with 2 equivalents of Fmoc protected amino acid, 1.95 equivalents of HBTU and 3 equivalents of N,N-diisopropylethylamine (DIEA) in DMF for 3 h. Fmoc deprotections were performed with 20% piperidine/ dimethyl

formamide (DMF) solution for 20 min. Cleavage of the peptides from the resin and deprotection of acid labile protected amino acids were carried out with a mixture of trifluoroacetic acid (TFA) : triisoproplysilane (TIS) : water in the ratio of 95 : 2.5 : 2.5 for 2 h. Excess TFA was removed by rotary evaporation. The remaining residue was triturated with ice-cold diethyl ether and the resulting white pellet was freeze-dried. The protected glycopeptide was identified and analyzed by reverse phase HPLC on an Agilent 6530 accurate-Mass Q-TOF LC/MS equipped with an Agilent 1200 HPLC. An phenomenex Luna Luna 3µ C8 100A (50 x 3.00 mm) column as stationary phase and water/acetonitrile gradient with 0.1% volume of formic acid as mobile phase were used to identify protected amphiphilic glycopeptide. In solution deacetylation was schematically demonstrated in Figure 5.1. For the cleavage of acetyl groups, 210 mg of protected glycopeptide (1 eq.) was dissolved in 105 ml of anhydrous methanol. 2M of NaOMe (4.4 eq.) was dissolved in methanol and poured into the solution. After adjusting pH to 8-8.5, the reaction was carried out at room temperature for 2-3 h. To stop the reaction, the solution was neutralized with a few drops of acetic acid. The solvent was removed by vacuo. After water addition, it was frozen at -80°C and freeze-dried. The deprotected glycopeptide was identified and analyzed by reverse phase HPLC on an Agilent 6530 accurate-Mass Q-TOF LC/MS equipped with an Agilent 1200 HPLC. An phenomenex Luna 3µ C8 100A (50 x 3.00 mm) column as stationary phase and water/acetonitrile gradient with 0.1% volume of formic acid as mobile phase were used to identify peptide amphiphile. It was purified on Agilent 1200 by using a Zorbax prepHT 300CB-C8 column with a water–acetonitrile (0.1% TFA) gradient. K-PA was synthesized and purified as indicated above. For E-PA synthesis, 1.1 mmol/g loaded Wang resin was preloaded with

Fmoc-Glu(OtBu)-OH and resultant resin had 0.72 mmol/g loading. The rest of the procedure was also repeated for E-PA. Due to its acidic character, an Agilent 6530 accurate-Mass Q-TOF LC/MS was operated by eluting it from an Agilent Zorbax Extend-C18 (50 x 2.1 mm) column with a water/acetonitrile mixture (0.1% NH_4OH) for the elucidation of the molecule. The purification was performed on a Zorbax Extend C18 prep-HT with a water/acetonitrile (0.1% NH_4OH) gradient.

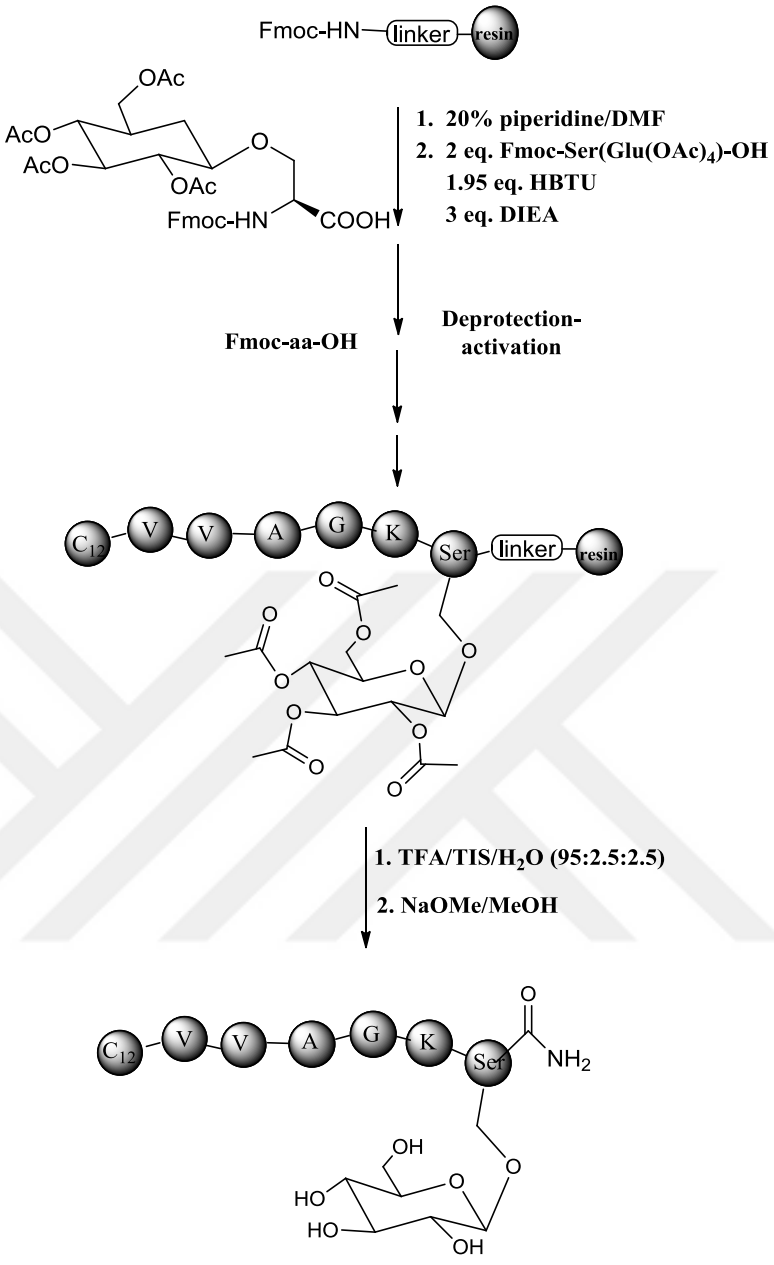

Figure 5.1 Schematic representation of the sequential synthesis of amphiphilic glycopeptide

5.2.4 Hydrogel Preparation

Oppositely charged glyco/peptide amphiphiles (10 mM) were mixed at a specified ratio (1:1 or 2:1) to obtain neutral or negatively charged supramolecular gels. While Glc-PA and K-PA are positively charged at physiological pH, E-PA exhibited

negative charge due to acidic character of molecule. When they are mixed, they formed three dimensional network as a result of different combination of interactions such as hydrogen bonding, van der Waals and electrostatic interactions.

5.2.5 Chemical, Physical and Mechanical Characterization of Self-Assembled Nanofiber Network

5.2.5.1 Circular Dichroism

Secondary structure of PA nanofibers were investigated with circular dichroism (CD). A Jasco J-815 CD spectrophotometer was used for CD analysis. All samples were measured at physiological pH at 0.25 mM. Prior to the nanofiber formation, PAs were sonicated one by one. For each measurements, 300 uL of the sample was transfered into a 1 mm quartz cuvette which was inverted gently for mixing without damaging any assembled structures and spectra was obtained at room temperature from 300 nm to 190 nm with 1 nm data interval and 100 nm/min scanning speed. The results were expressed as mean residue ellipticity and converted the unit of $deg.cm^2.dmol^{-1}$.

Temperature dependent circular dichroism experiments were also performed with the same instrument and the effect of temperature on the secondary structures of Glyco/E-PA (1:1, v/v%) and K/E-PA (2:1, v/v%) nanofibers were investigated. All samples were prepared at pH 7 having 250 and 633 uM of concentration, respectively. Spectra was obtained between 25-70°C from 300 nm to 190 nm with 0.1 nm data interval and 100 nm/min scanning speed. Data points were recorded at each 5°C difference.

5.2.5.2 Determination of Zeta Potential of Nanofiber Systems at Dilute Concentration

Samples were prepared by dissolving each component in water at a concentration of 0.250 mM separately and mixed at specific ratios: Glc-PA/E-PA and HA/K-PA (1:1 v/v %) and E-PA/K-PA (1:2 v/v %). Zeta potential of the particles were measured with Malvern Nanosizer/Zetasizer nano-ZS ZEN 3600 (Malvern Instruments, USA) instrument. Measurements were performed in glass cuvettes and repeated at least three times.

5.2.5.3 Transmission Electron Microscopy Imaging

TEM images were obtained with FEI Tecnai G2 F30 TEM at 200 kV. For the images taken in STEM mode, a high angle annular dark field (HAADF) detector was used. 1 mM of Glc-PA/E-PA, K-PA/E-PA and HA/K-PA nanofiber systems were firstly diluted 50 times and then dropped on a 200-mesh copper TEM grid. It was allowed to stay for 5 min followed by 2 wt% uranyl-acetate staining for 5 min and air dried.

5.2.5.4 Scanning Electron Microscopy Imaging

For SEM imaging, samples were prepared on cleaned silicon wafer by mixing 10 mM Glc-PA and E-PA at 1:1 ratio, 10 mM K-PA and E-PA at 2:1 ratio and 10 mM HA and K-PA at 1:1 ratio. They were allowed to stay for 20 min for gelation. To preserve its initial network structure, dehyration of samples were employed by immersing silicon wafers into gradually increasing concentration of ethanol solutions. After solvent exchange, the samples were dried using a Tourismis Autosamdri-815B critical point drier. SEM imaging was performed with FEI Quanta

200 FEG, using the GSED detector at ESEM mode with 3-10 keV beam energy for 5 nm Au-Pd coated Glc-PA/E-PA, K-PA/E-PA and HA/K-PA systems.

5.2.5.5 Small Angle X-Ray Scattering (SAXS)

SAXS measurements were performed with a Kratky compact HECUS (Hecus X-ray systems, Graz, Austria) system for 1 mM Glc-PA/E-PA (1:1) and K-PA/E-PA (2:1) nanofiber systems. Solutions were directly loaded to quartz capillary cell. SAXS system is equipped with a linear collimation system, a linear-position sensitive detector (PSD), X-ray tube Cu target (λ=1.54 Å) and a generator which was operated at a power of 2 kW (50 kV and 40 mA). Distances between 1024 channels (in PSD) and the sample-detector are 54 μm and 28.1 cm, respectively. Scattering curves were monitored in q ranges of 0.002-0.55 Å-1 for SAXS. The SAXS measurements were carried out at room temperature (23 °C) and the data collection time was 900 s for each sample.

For data analysis, the flexible cylinder-polydisperse length, shortly defined by flexible rod, model was used for both Glc-PA/E-PA and K-PA/E-PA assemblies and it was determined as the best fitted model for the scattering profiles of the samples.[317-318] Inter-cylinder interactions were neglected during the calculations. The form factor normalized by the particle volume is shown below,

$$P(q) = \frac{scale < f^2 >}{Vol} + Bkg$$

where < > is an average over all possible orientations of the flexible cylinder. The illustration of a flexible rod is presented below:

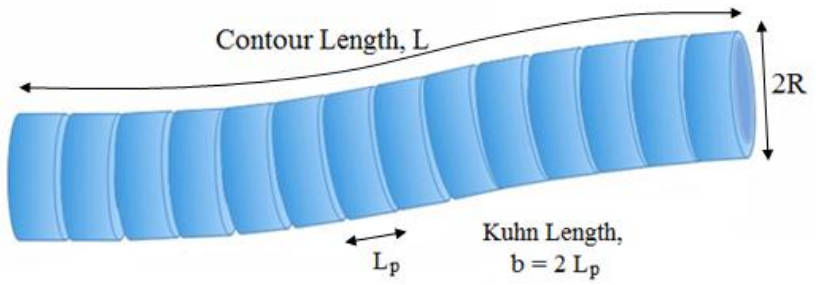

The chain of contour length, L, (the total length) can be described as a chain of some number of locally stiff segments of length Lp. The persistence length, Lp, is the length along the cylinder over which the flexible cylinder can be considered a rigid rod. The Kuhn length (b) used in the model is also used to describe the stiffness of a chain, which is equal to $2L_p$.

Fractal dimensions (d_i) as a widely measured index in nanoscopic analysis were obtained by using Porod region ($q \rightarrow \infty$) data to characterize inner surface morphology (3). There are three types of surface morphologies for inner surfaces determined according to the value.

$1 < d_i < 3$, mass fractals (surface has 3D globular formation)

$3 < d_i < 4$, surface fractals (surface has 2D plate like formation)

$d_i = 4$ smooth surface

Boucle term may be useful to explain the hydrogen bonded regions and intersections between the fibers. The mean number of the fibers in a boucle means that there are more than two fibers connected to each other in the same intersection region. The number of the fibers in a boucle was obtained by using the number of the appeared

humps while the diameter of a boucle was determined by the ratio of maximum distance range per the number of humps in PDDs.

5.2.5.6 Investigation of Viscoelastic Behavior of Nanofiber Systems by Oscillatory Rheology

Viscoelastic properties of the PA systems were analyzed with an Anton Paar Physica RM301 Rheometer operating with a 25 mm parallel plate configuration. Samples of 10 mM K-PA, E-PA and Glc-PA were mixed for the desired gel systems. While 10 mM of K-PA and E-PA were mixed with 2:1 ratio to form neutral hydrogel system, Glc-PA and E-PA were mixed with 1:1 ratio to form negatively charged (overall -1 charge) gels. Rheological analyses were also performed in biological media. While Glc-PA and K-PA were dissolved in 0.25 M sucrose, E-PA was dissolved in DMEM. The ratios used for the analysis performed in water were kept same for the experiments conducted in biological media. A gap distance of 0.5 mm was used with 10 rad/s angular frequency and 0.1% shear strain and performed at room temperature. Measurement were performed with three replicates.

5.2.6 *In Vitro* Studies

mMSCs expanded to passage 3 in maintenance medium (DMEM with 10% (v/v) FBS, 1% (v/v) GlutaMAX and 1% penicilin-streptomycin) was used for *in vitro* studies. Maintenance of cells was carried out in humidified incubators at 5% CO_2 at 37 °C. Tissue culture plate or surfaces coated with Glc-PA/E-PA, K-PA/E-PA or HA/K-PA were used to culture mMSCs. Wells were coated with oppositely charged 1 mM PA solutions or hyaluronic acid solution prepared from sodium salt.

Biocompatibility was evaluated by colorimetric MTT assay. Cells seeded at a density of 250 cells/ cm^2 were cultured for 24 h, 48 h and 72 h at parallel plates. Quantification of the cellular viability was conducted by measuring the absorbance at 590 nm and results were normalized to the tissue culture plate.

The amount of produced sulfated GAG was quantified by dimethylmethylene blue (DMMB) assay.[31] After measuring total DNA per well, it was normalized to the sulfated GAG content. Standard curves for the DMMB assay were plotted from serially diluted chondroitin sulfate solutions (0-35 $\mu g\ mL^{-1}$) prepared from standards. Optical densities (ODs) of the solutions were measured using a 595 nm filter on a microplate reader. The absorbance of the cell-free control groups was read as blank and subtracted from that of the experimental groups.

Gene expression of cells was analyzed by the quantitative real time PCR (qRT-PCR) to investigate the chondrogenic differentiation. Prior to qRT-PCR experiments, extraction of RNA from each sample with TRIazol was followed with the determination of the yield and purity of extracted RNA by Nanodrop 2000. SuperScript III Platinum SYBR Green One-Step qRT-PCR Kit was utilized both to synthesize cDNA from RNA and to conduct qRT-PCR. Each run was internally normalized to GAPDH, and each group was normalized to the expression levels of mesenchymal stem cells cultured in maintenance medium. While an expression ratio of greater than 1 corresponds to the upregulation, a ratio less than 1 indicates the downregulation of the gene of interest.

Primers used for qRT-PCR expression analysis are listed below:

Sox-9; F: 5'-AGGAAGCTGGCAGA CCAGTA-3', R: 5'CGTTCTTCACCGACT

TCCTC-3', Hyal-1: F: 5'-ATGCCCTTTACCCC AGTATT-3', R: 5'TGGGGGTC TCTGGAAACTAT-3'

5.2.7 *In Vivo* Study

In vivo experiments were conducted by using 12 white male New Zealand rabbits (mean weight 2500±400 g, age 12 weeks). Gulhane Military Medical Academy (GATA) Animal Ethics Committee approved all procedures applied to animals. Prior to surgery, 30–40 mg/kg ketamine and 5–7 mg/kg xylazine were injected to anasthesize animals. Osteochondral defect model was generated in the shaved and aseptically prepared region. All debris, as well as articular cartilage, was discarded with a micro curette. Three holes within each defect were generated to mobilize bone marrow blood for microfracture treatment. Defects were started to be filled with either physiological saline (saline-treated), 100 μL of Glc-PA/E-PA or a clinically approved formulation of hyaluronic acid (Hyalgan ®), as blood flow from holes was observed and then, the wound was closed. IM antibiotics were given to each rabbit during 3 days. After 12 weeks, the rabbits were euthanized with overdose sodium pentobarbital while they were under sedation and only one defect was generated for each trochlea.

For tissue sectioning, fixation and decalcification were carried out with 4% paraformaldeyde for 48 h at 4 °C and in 5% formic acid, respectively, followed by the dehydration of samples in a graded series of ethanol and replacement with xylene. The samples were embedded in paraffin and sectioned at 5 μm thickness by microtome. Sections were deparaffinized and rehydrated by treating with a series of graded alcohol solutions for histological and immunohistochemical examinations.

For GAG imaging, sections were sequentially stained with Safranin-O and Fast Green for 5 min. After the dehydration and replacement with xylene, slides were mounted by Histomount® mounting medium and imaged by light microscopy. For immunohistochemical stainings, slides were treated with an antigen retriever to present epitopes for 15 min at 37 °C after rehydration steps. After blocking at room temperature and incubation with primary Collagen II antibody at 4 °C overnight, sections were rinsed extensively with TBS w/Triton-X (0.01% v/v) and treated with 500 times diluted Goat anti-Mouse IgG-HRP for 1 h at room temperature to detect bound primary antibodies. While secondary antibody binding was visualized with diaminobenzidine (DAB), nuclei were stained with hematoxylin.

5.2.8 Statistical Analysis

All data were presented as means ± standard error of means (SEM). The significance of observed differences between the study groups was determined either by one way ANOVA or two way- ANOVA with post tests Tukey's/Bonferroni. A p value lower than 0.05 was considered to be statistically significant, except where noted.

5.3 RESULTS AND DISCUSSION

5.3.1 Synthesis and Characterization of Glucose Linked Serine Amino Acid

In order to develop a hyaluronic acid mimetic scaffold composed of glycopeptides, we initially started from the synthesis of sugar linked amino acid. It is known that hyaluronic acid is composed of *D*-glucuronic acid and *D*-N-acetylglucosamine disaccharide units. Since this polysaccharide is rich in glucose backbone, glucose was chosen as the sugar component to be conjugated to serine amino acid, yielding natural *O*-glycosidic bond.

It was synthesized in three steps (Figure 4.2). Starting material was selected as Fmoc-Ser-OH whose side chain was unprotected. In the first step, Fmoc-Ser-OH was converted to allyl ester derivative (compound **1**, Fmoc-Ser-OAllyl) by the addition of allyl bromide in the presence of potassium carbonate.[319] In the second step, Fmoc and allyl ester protected β-*O*-glycosylated serine, compound **2**, was synthesized by reacting with *D*-glucose pentaacetate and boron trifluoride diethyl etherate ($BF_3.Et_2O$).[320-321] In the last step, allyl ester protection was removed by palladium(0)-catalyzed allyl transfer to nucleophile N-methylaniline.[322-323] Chemical identification of all compounds (**1**-**3**) were carried out by NMR and mass spectroscopy (Figure 4.3-4.10).

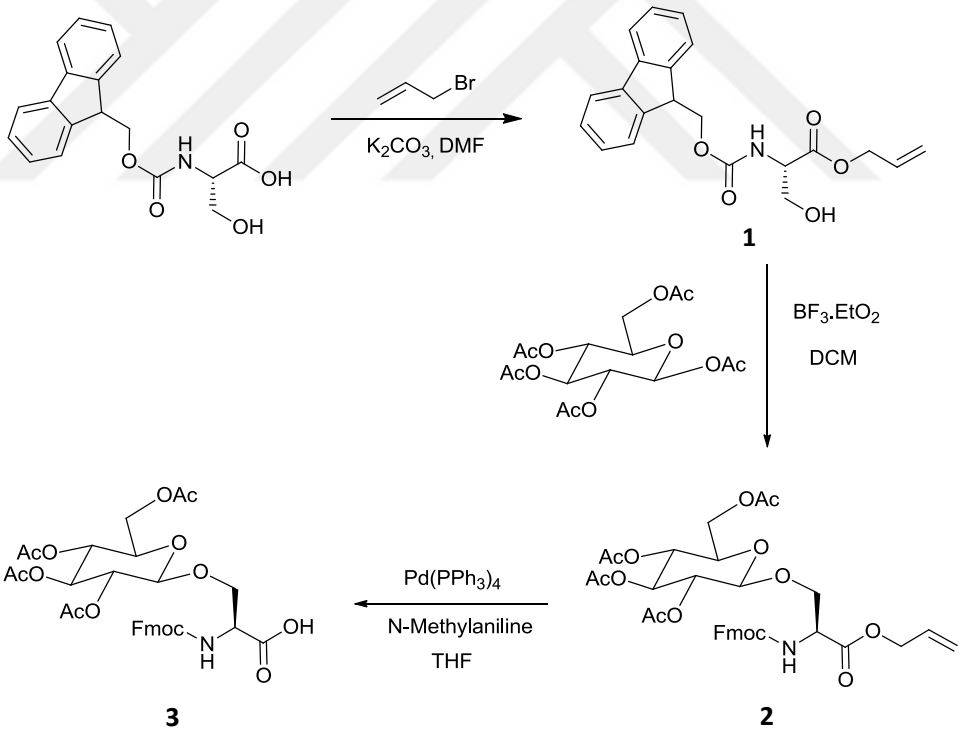

Figure 5.2 Synthesis of compound **3**, Fmoc-Ser [β-*D*-Glc$(OAc)_4$]-OH.

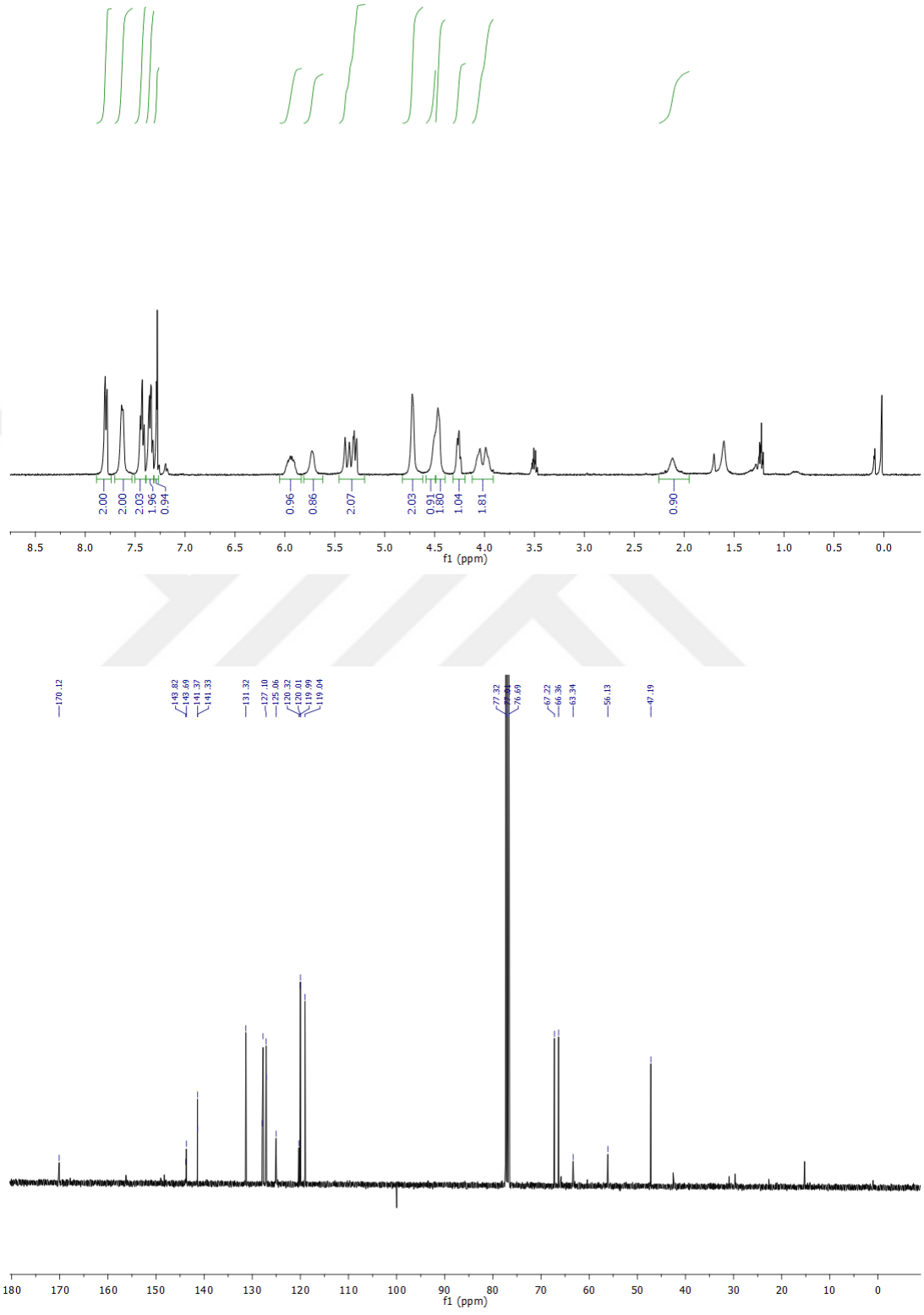

Figure 5.3 ^{1}H- and ^{13}C-NMR spectra of compound **1**.

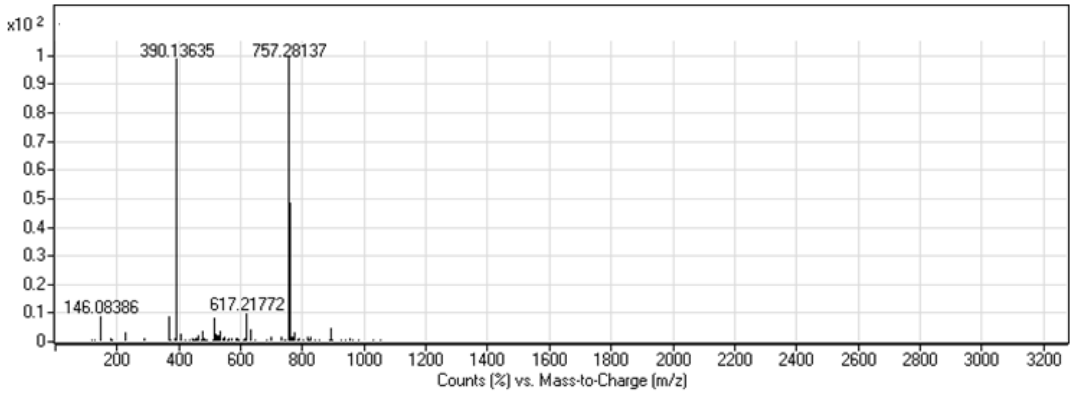

Figure 5.4 Mass spectrum of compound **1**. Calculated $[M+Na]^+$ *m/z*= 390.1420, experimental *m/z* = 390.1363, $[2M+Na]^+$ *m/z* =757.281.

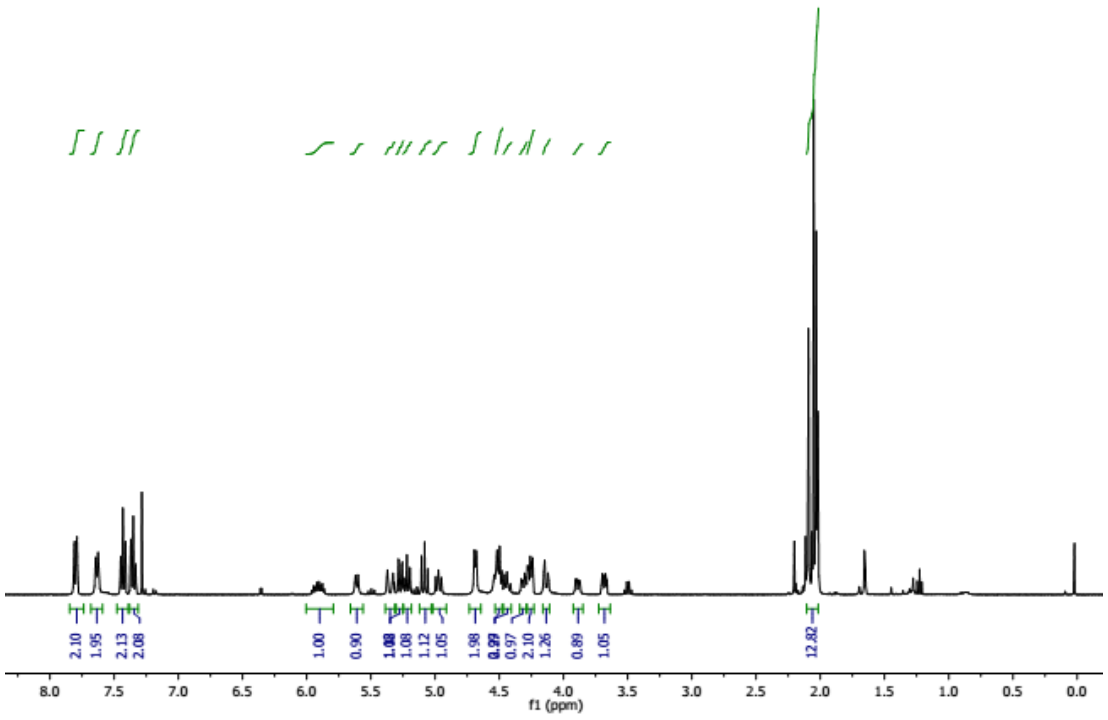

Figure 5.5 ^{1}H-NMR spectrum of compound **2**

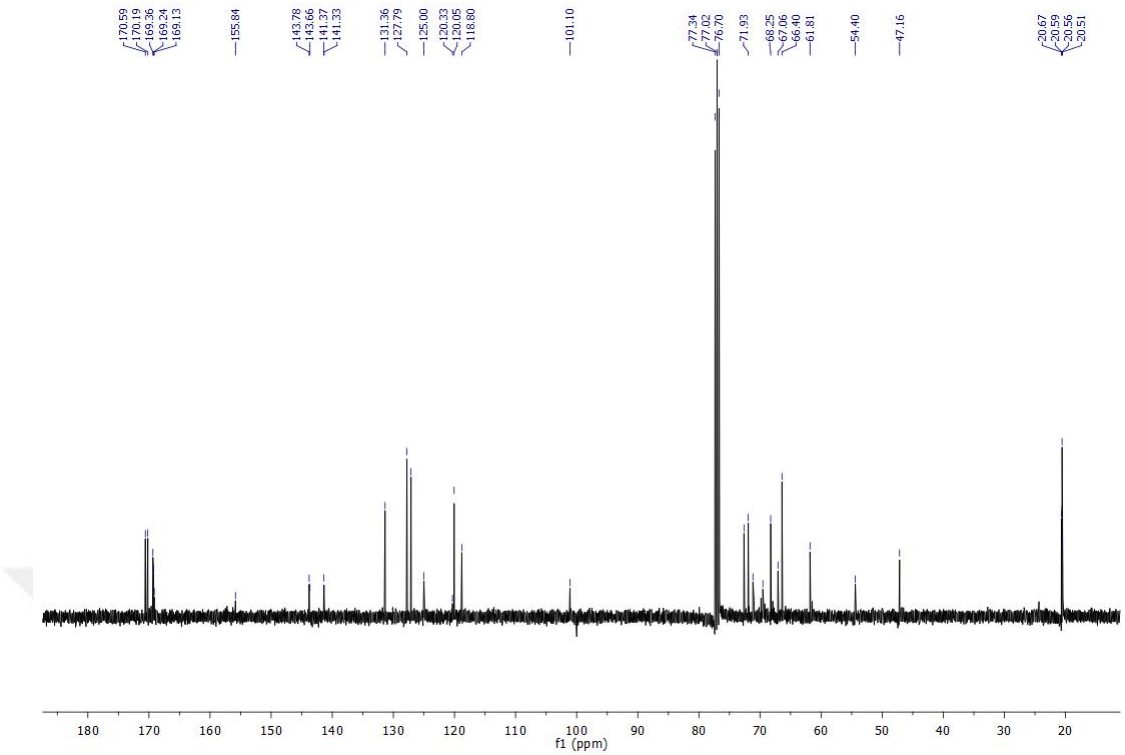

Figure 5.6 ^{13}C-NMR spectrum of compound **2**.

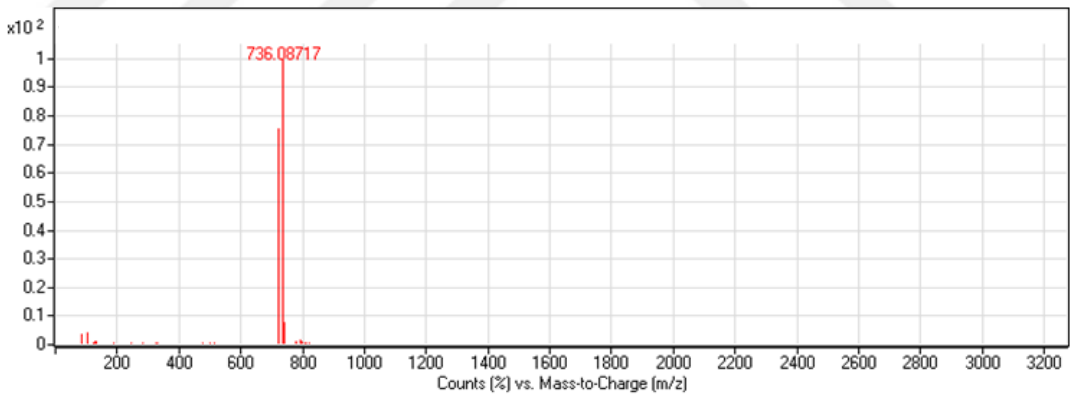

Figure 5.7 Mass spectrum of compound **2**. Calculated $[M+Na]^+$ *m/z*= 720.2371, experimental *m/z*= 720.2218, $[M+K]^+$ *m/z*= 736.08717.

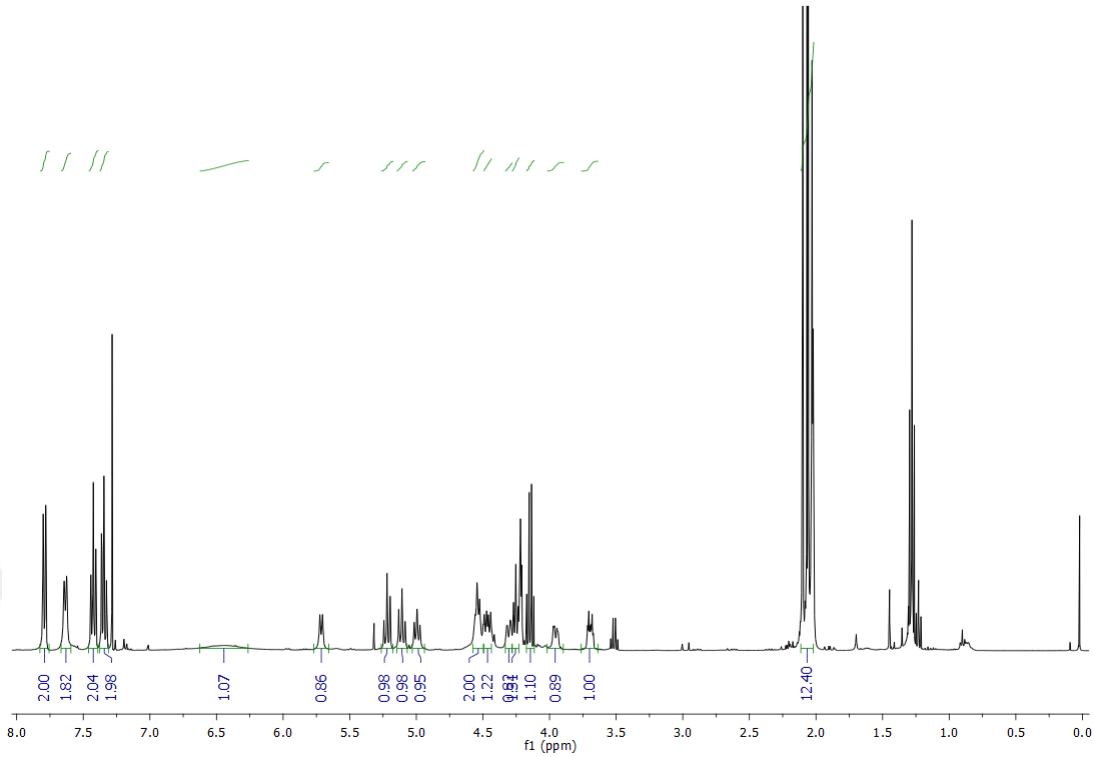

Figure 5.8 ^{1}H-NMR spectrum of compound **3**.

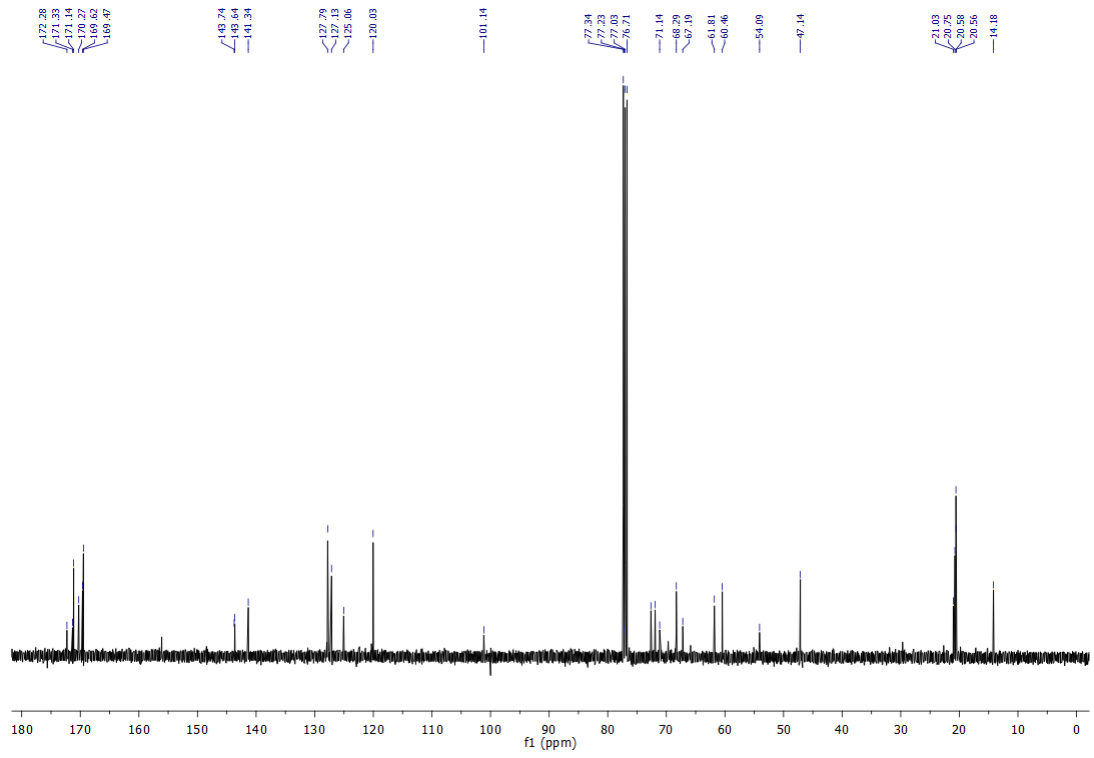

Figure 5.9 ^{13}C-NMR spectrum of compound **3**.

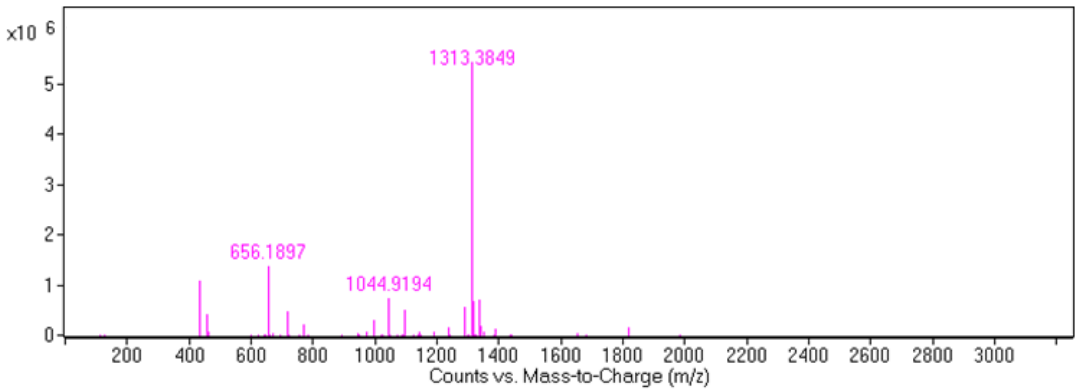

Figure 5.10 Mass spectrum of compound **3**. Calculated $[M-H]^-$ *m/z*= 656.2058, experimental *m/z*= 656.1897, $[2M-H]^+$ *m/z*= 1313.3849.

5.3.2 Design, Synthesis and Characterization of Glycopeptide Nanofibers

Synthesized Fmoc-Ser[β-*D*-Glc(OAc_4)]-OH was used as the first amino acid residue of the sequence during the elongation of the peptide on the solid support. After resin cleavage, amphiphilic glycopeptide was obtained in the protected form due to the acetylated sugar hydroxyl groups. Its chemical structure was elucidated by LC-MS (Figure 4.11). While the glucose amino acid residue existed at the C-terminus of the peptide segment, amphiphilic character was gained by the conjugation of hydrocarbon tail to the N-terminus of the peptide moiety (Figure 5.1).

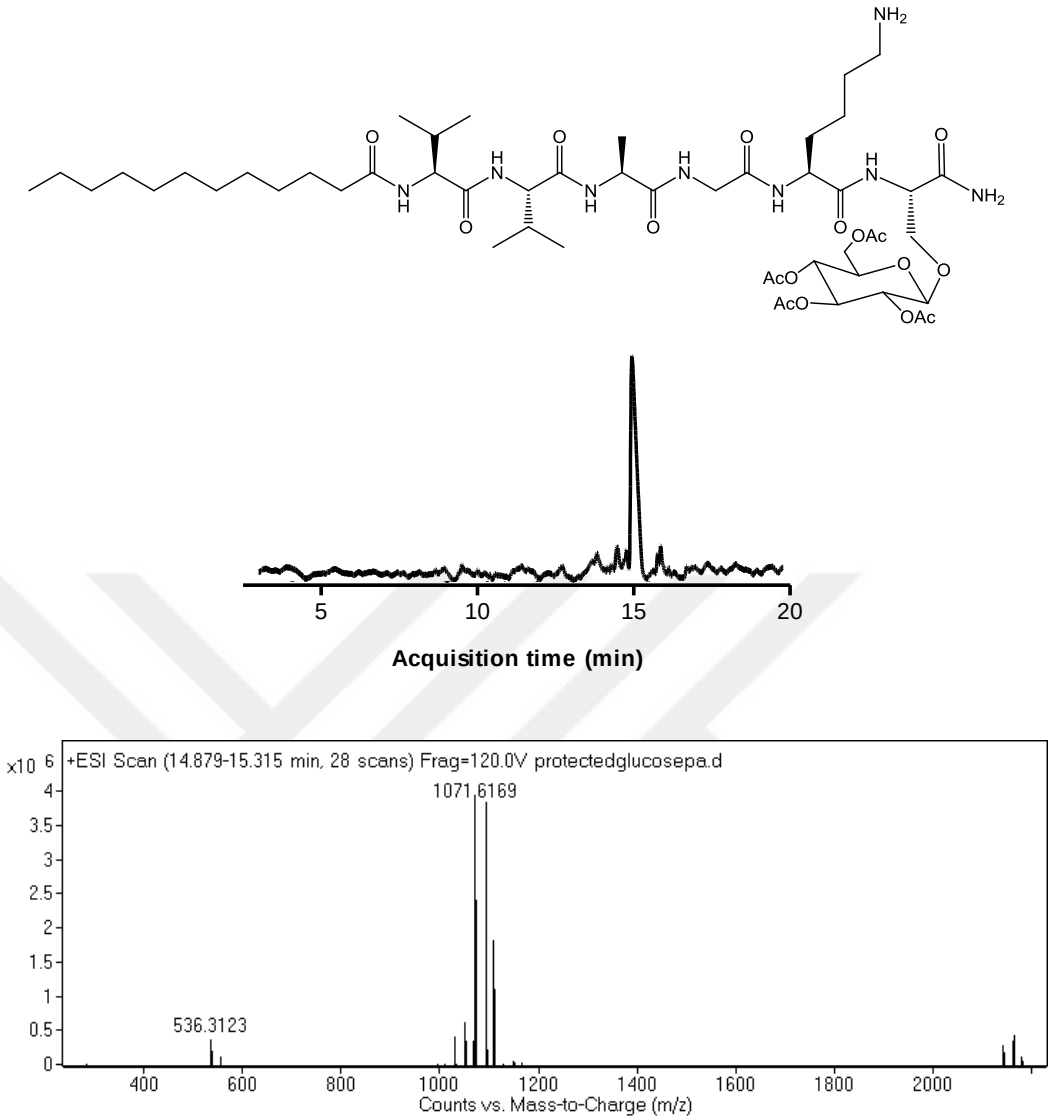

Figure 5.11 Liquid chromatograms and mass spectra of protected amphiphilic glycopeptide. $[M+H]^+$ (calculated) = 1071.6111, $[M+H]^+$ (observed) = 1071.6169 (observed $[M+2H]^{+2}$ = 536.3123)

Deacetylation of hydroxyl groups was carried out after resin cleavage in solution phase in the presence of methanolic sodium methoxide to prevent *O*-glycosidic bond cleavage during acid treatment in SPPS.[324] The other two PAs, E-PA and K-PA, were also prepared by Fmoc solid-phase peptide techniques. While the former one

serves as a charge neutralizer with its glutamic acid residue during self assembly process with lysine bearing Glc-PA, the latter one was used as oppositely charged counterpart of E-PA to form a coassembled control system. The chemical structures of all three PAs were confirmed with electrospray mass spectrometry (Figures 5.12 and 5.13). Designed glycopeptide molecule is unique in term of its amphiphilic nature and its capability to self assemble into nanofibers when oppositely charged PA molecule is introduced. Driving force promoting the self assembly process and enabling the formation of three dimensional network is the cohesive interactions between PA molecules, such as hydrogen bonding, van der Waals, hydrophobic and electrostatic interactions.[7, 325]

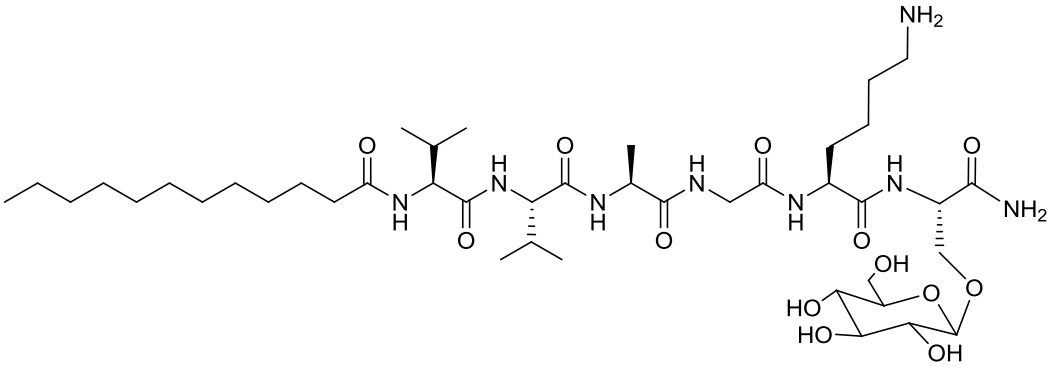

Lauryl-VVAGKS(β-Glc)-Am (**Glc-PA**)

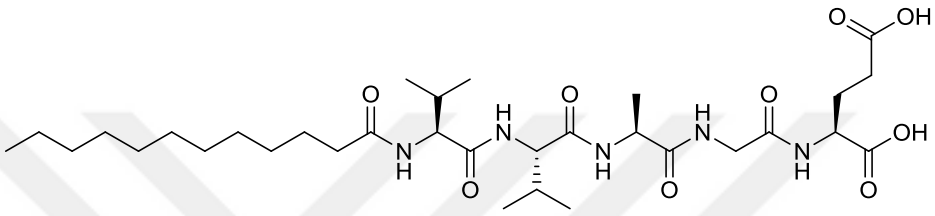

Lauryl-VVAGE (**E-PA**)

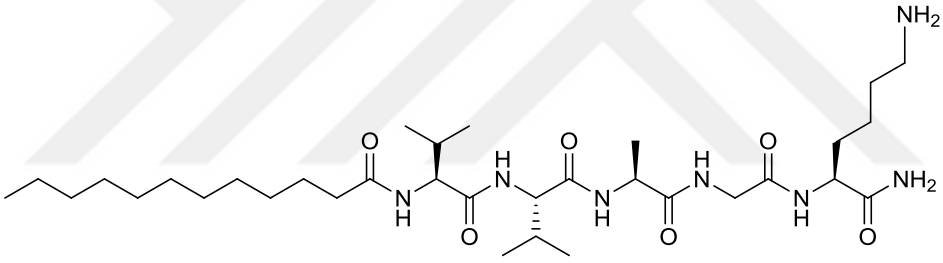

Lauryl-VVAGK-Am (**K-PA**)

Figure 5.12 Chemical structures of amphiphilic glycopeptide (Glc-PA) and two peptide amphiphiles (E-PA and K-PA)

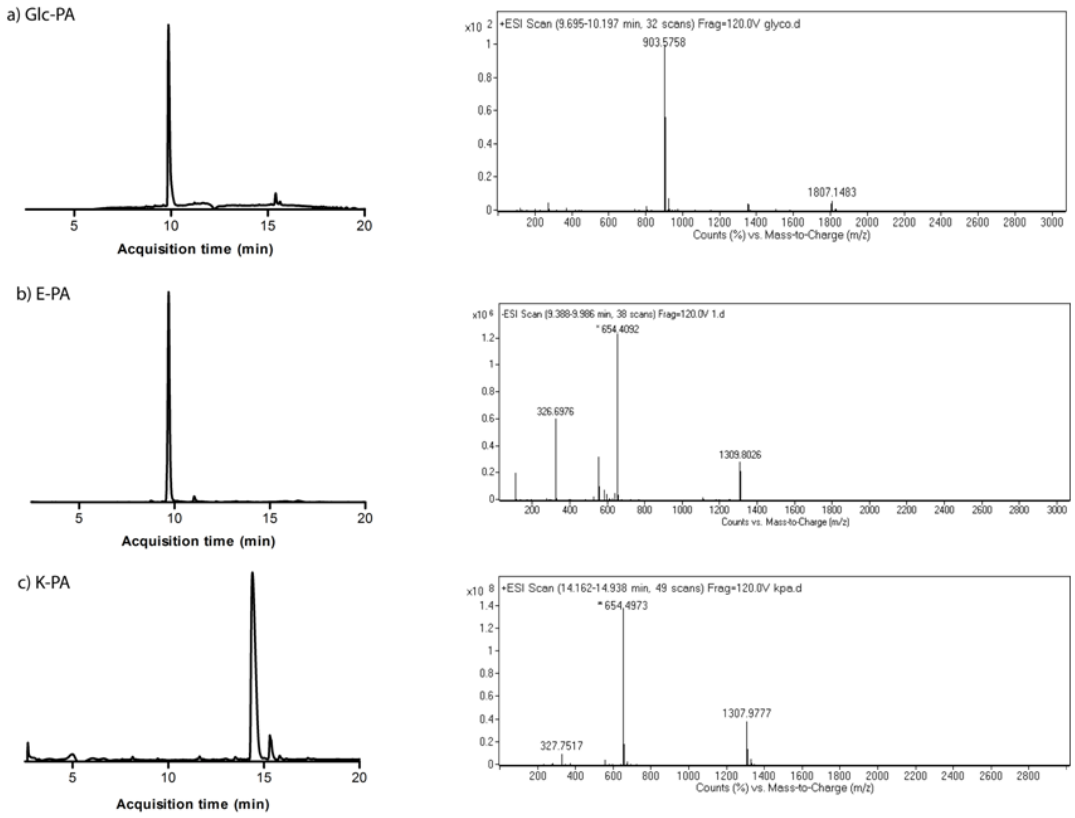

Figure 5.13 Liquid chromatograms and mass spectra of PAs. a) Glc-PA, $[M+H]^+$ (calculated) = 903.5688, $[M+H]^+$ (observed) = 903.5758 (observed $2[M+H]^+$ = 1807.1483). b) E-PA, $[M-H]^-$ (calculated) = 654.4156, $[M-H]^-$ (observed) = 654.4092 (observed $[M-2H]^{-2}$ *m/z* = 326,6976, $[2M-H]^-$ *m/z* = 1309,8026). c) K-PA, $[M+H]^+$ (calculated) = 654.4840, $[M+H]^+$ (observed) = 654.4973 (observed $[M+2H]^{+2}$ *m/z* = 327.7517, $[2M+H]^+$ = 1307.9777).

Secondary structure analysis of pure and co-assembled PAs were employed by circular dichroism spectroscopy. The results revealed that co-assembled systems oriented in β-sheet conformation displaying a negative minimum at 220 nm and positive ellipticity at 202 nm. In case of pure PAs, while Glc-PA and E-PA showed

disordered conformation, K-PA exhibited β-sheet structure, possibly due to the lack of sufficient charge repulsion at physiological pH (Figure 5.14).

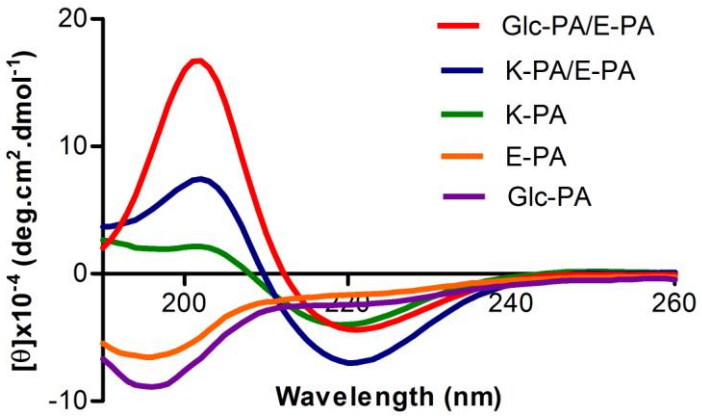

Figure 5.14 CD spectra of peptide amphiphile solutions and nanofiber systems

The thermal stability of nanofibers was further investigated by monitoring the change of dichroism intensity at peaks corresponding to beta sheet signals as a function of temperature (Figure 5.15). The results revealed that as the temperature increased, gradual change was observed for both nanofiber systems. While positive peak at 202 nm decreased in Glc-PA/E-PA nanofibers, negative peak at 222 nm slightly increased in K-PA/E-PA system. Although it was previously reported that a change in the ellipticity at 218 nm gave information about the beta-sheet content of the structure, in our case, obtained signal intensities slightly decreased and they still exhibited beta-sheet signature in CD, indicating their stabilities against high temperature.[326]

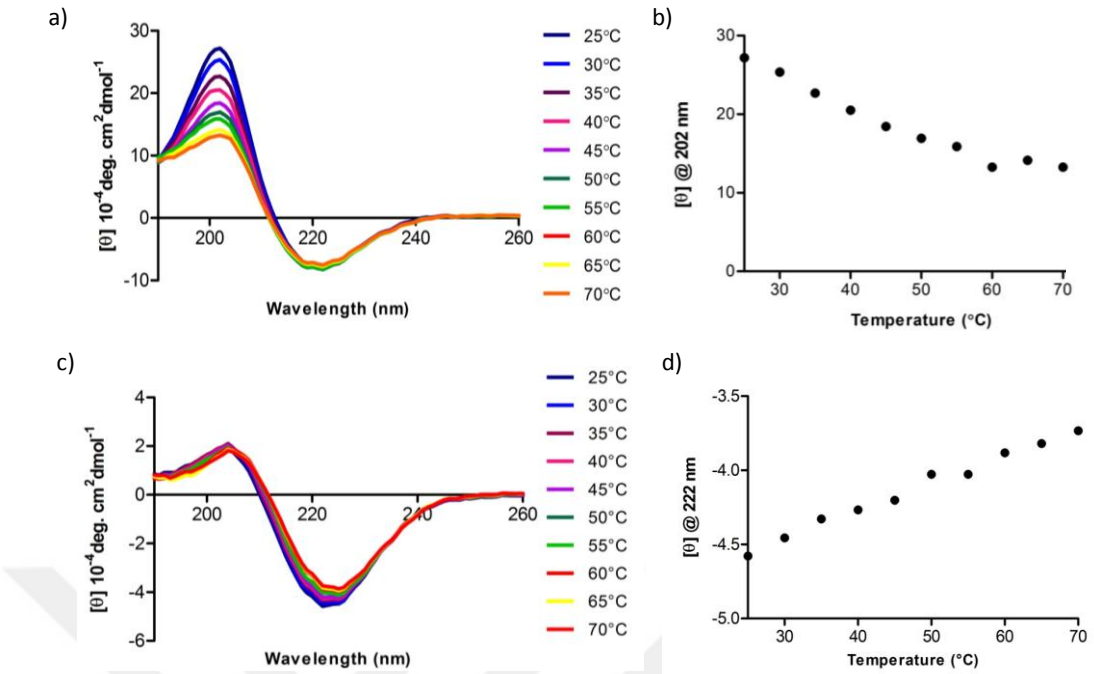

Figure 5.15 Temperature dependent CD spectra of a) Glc-PA/E-PA and c) K-A/E-PA nanofibers. Change in molar ellipticity at certain wavelengths with respect to temperature b) Glc-PA/E-PA at 202 nm and d) K-PA/E-PA at 222 nm.

Coassembled PA nanofibers were visualized by scanning transmission electron microscopy (STEM). STEM of negatively stained diluted hydrogels revealed that high aspect ratio nanofibers were formed with a size of about 8-10 nm in diameter and micrometers in length. (Figure 5.16) Small-angle X-ray scattering (SAXS) analysis was also conducted to gain further insight into the structural characteristics of PA systems in aqueous environment. 1 mM of Glc-PA/E-PA and K-PA/E-PA assemblies prepared at physiological pH were inserted into quartz capillaries for the analysis. Their SAXS analyses were conducted in low q regions (0.002-0.5 $Å^{-1}$) and flexible cylinder-polydisperse length model was found as the best fitted model with a

radius of 9.2±0.1 nm and 8.9±0.1 nm for Glc-PA/E-PA and K-PA/E-PA, respectively (Figure 5.17a and Table 5.1).[317-318]

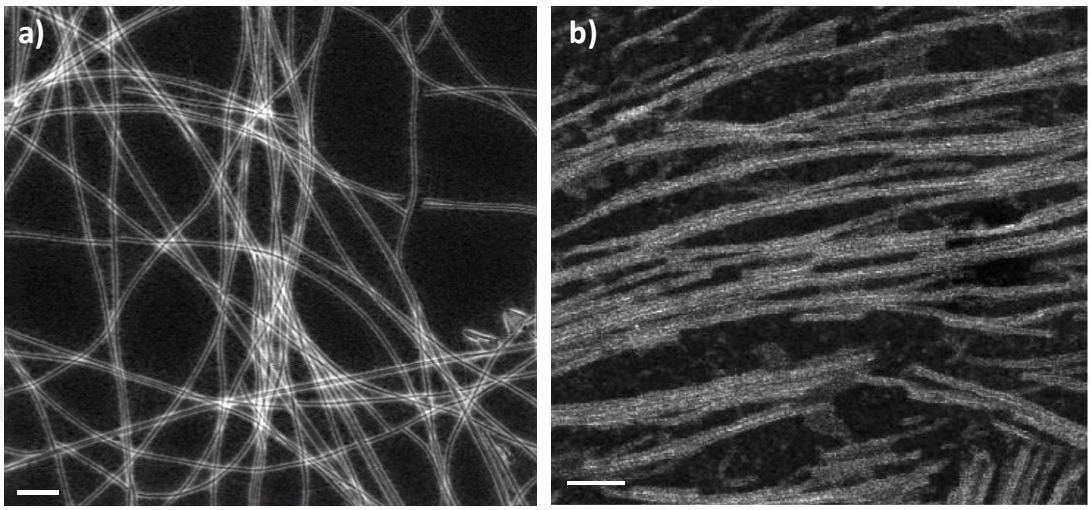

Figure 5.16 STEM images of a) Glc-PA/E-PA and b) K-PA/E-PA nanofibers, scale bar = 100 nm.

It was also utilized from pair distance distributions (PDDs) of corresponding SAXS analyses to investigate the difference in electron densities of Glc-PA/E-PA and K-PA/E-PA nanofibers. (Figure 5.17b) Although symmetrical humps were observed in the PDDs of both PA systems, sharper humps were obtained arising from the existence of glucose units in the case of Glc-PA/E-PA, which are also evidence of more numbers of the scattered nanoscale aggregations and indirectly more electron-dense regions. In light of the results acquired from TEM and SAXS analysis, it was observed that both systems self-assembled into micrometer-length nanofibers and their diameters were close to each other. The difference in the diameter of two nanofiber systems can be attributed to the additional serine linked glucose moiety.

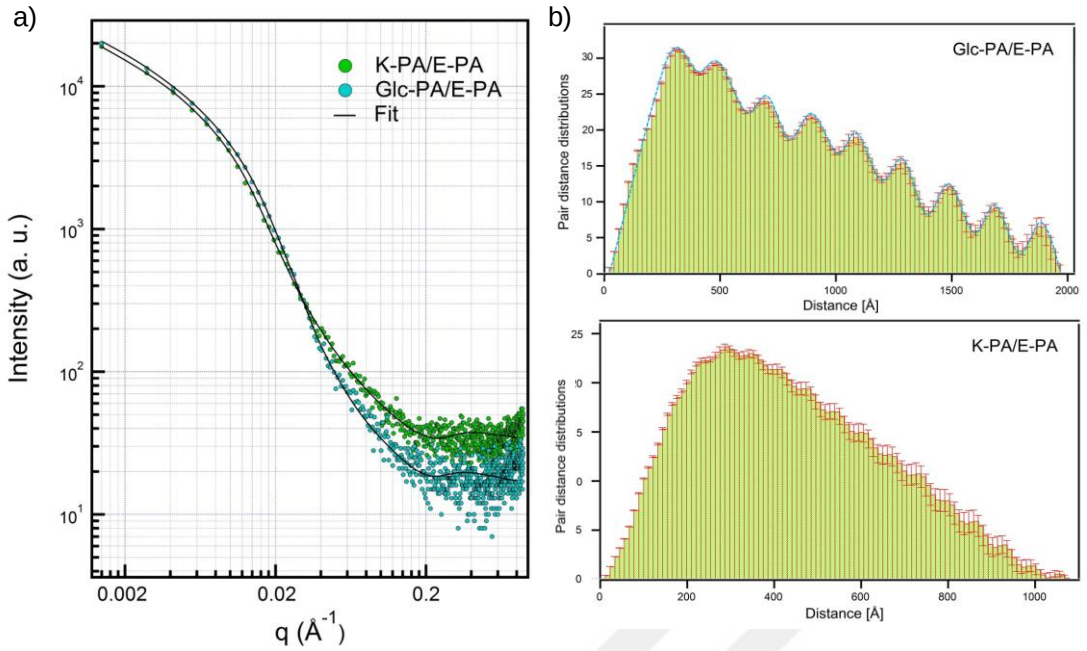

Figure 5.17 a) SAXS profile and fit curve for the scattering data of Glc-PA/E-PA and K-PA/E-PA nanofibers, b) Pair distance distributions of Glc-PA/E-PA and K-PA/E-PA nanofiber systems.

Table 5.1 Results obtained from the fitting process of Glc-PA/E-PA and K-PA/E-PA scattering data using flexible cylinder-polydisperse length model

Fitting results	**Glc-PA/E-PA**	**K-PA/E-PA**
2R (nm)	9.2±0.1	8.9±0.1
Contour Length (nm)	1010.3±0.3	905.2±0.2
Kuhn Length (nm)	51.3±0.1	50.2±0.1
Mean number of the fibers in a boucle	10	17
Mean diameter of a boucle (nm)	196.4	138.2
Fractal dimension	2.45	2.17
Polydispersity	0.2	0.2

In the self-assembly mechanism of peptide amphiphiles, they are organized in such a way that hydrophobic alkyl tail and hydrophobic amino acid residues are buried inside and hydrophilic residues are exposed to aqueous environment resulting in the formation of nanofibers with high aspect ratio. It was previously shown that oppositely charged PAs were coassembled within the same nanofiber.[106] It was also reported that enantiomeric amphiphatic peptides underwent coassembly to form hybrid fibrils.[327] These findings confirmed the presentation of glucose conjugated PA and glutamic acid containing PA within the same nanofiber.

Three dimensional fiber network of Glc-PA/E-PA and K-PA/E-PA hydrogels was assessed under a scanning electron microcope. Structural organization of the nanofibers resembles native extracellular matrix and provides a favorable milieu conducive to cells for gathering chemical, physical and biological cues (Figure 5.18). Mechanical properties of the nanofibrous hydrogels were examined by using oscillatory rheology to understand whether the prepared peptide hydrogels are relevant for tissue engineering applications as a synthetic scaffold. It is known that oscillatory rheology is a proper technique to examine the viscoelastic behavior of the hydrogels. In time sweep test, storage (G') and loss (G'') moduli were recorded for an hour at constant shear strain and angular frequency to determine viscoelastic behavior of PA hydrogels (Figure 5.19 a,b). Equilibrium modulus values showed that storage modulus values are greater than loss modulus values for Glc-PA/E-PA and K-PA/E-PA nanofibers prepared both in water at physiological pH and in sucrose/DMEM medium, indicating elastic solid behavior of resulting networks. (Figure 5.19 c,d) These self-supporting hydrogels are suitable candidates for *in vivo* applications.[119]

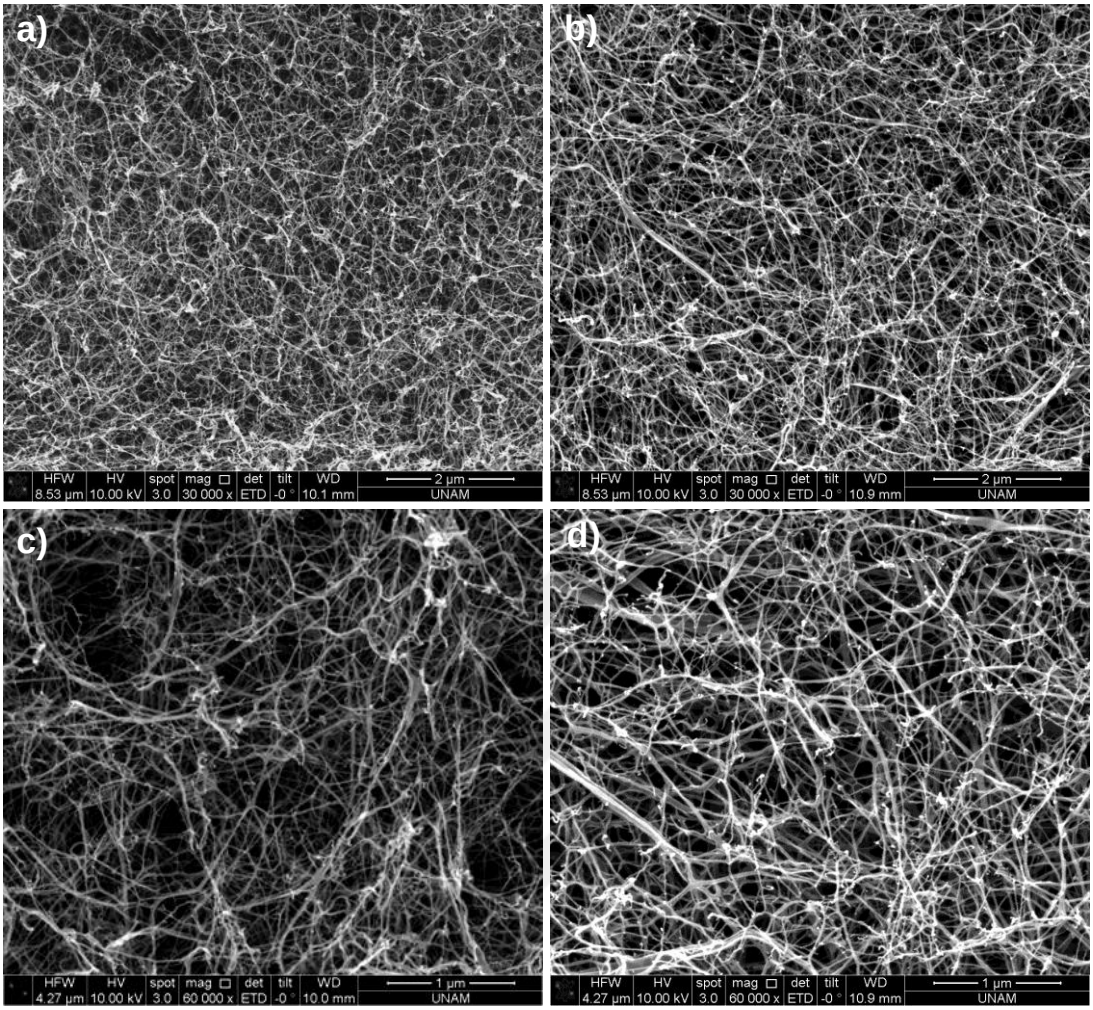

Figure 5.18 SEM micrograph of Glc-PA/E-PA nanofibers (a, c), and K-PA/E-PA nanofibers (b, d). scale bar = 2 µm (a, b) and 1 µm (c, d).

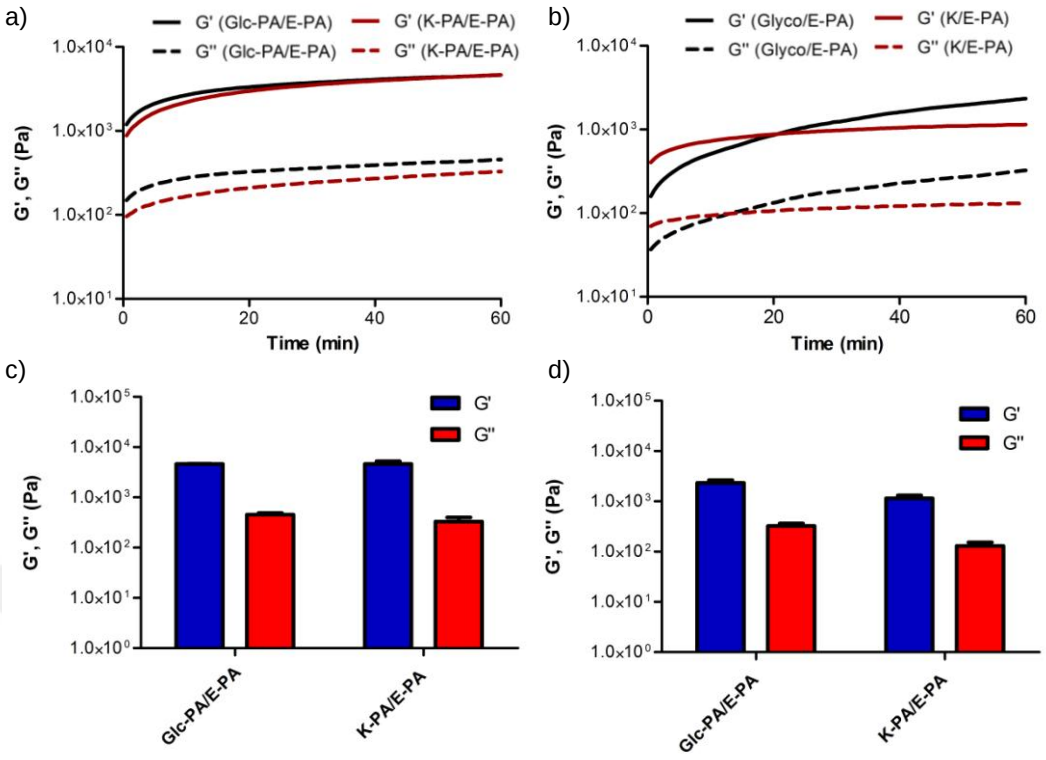

Figure 5.19 Time sweep test for Glc-PA/E-PA and K-PA/E-PA nanofibers prepared a) in water at pH 7 and b) in 0.25 M sucrose/DMEM medium. Equilibrium storage and loss moduli of Glc-PA/E-PA and K-PA/E-PA nanofibers prepared c) in water at pH 7 and d) in 0.25 M sucrose/DMEM medium.

5.3.3 Characterization of HA/K-PA Assembly

During the evaluation of the hyaluronic acid mimetic character of Glc-PA/E-PA nanofibers, HA/K-PA group was used as a biological positive control. Similar to previously demonstrated analyses conducted for Glc-PA/E-PA nanofibers, HA/K-PA system was also analyzed in terms of secondary structure and morphological properties before starting biological experiments. CD results revealed that HA alone exhibited a very weak signal, while the HA/K-PA mixture forms a β-sheet composition with a negative signal at around 220 nm and a positive signal below 200 nm (Figure 5.20c). The assembly of HA and K-PA was also inspected by TEM and

SEM imaging. HA/K-PA assemblies were found to form bundles with micrometer-scale lengths, and their nanoporous structure presumably allows the mimicking of the native ECM environment (Figure 5.20b and d).

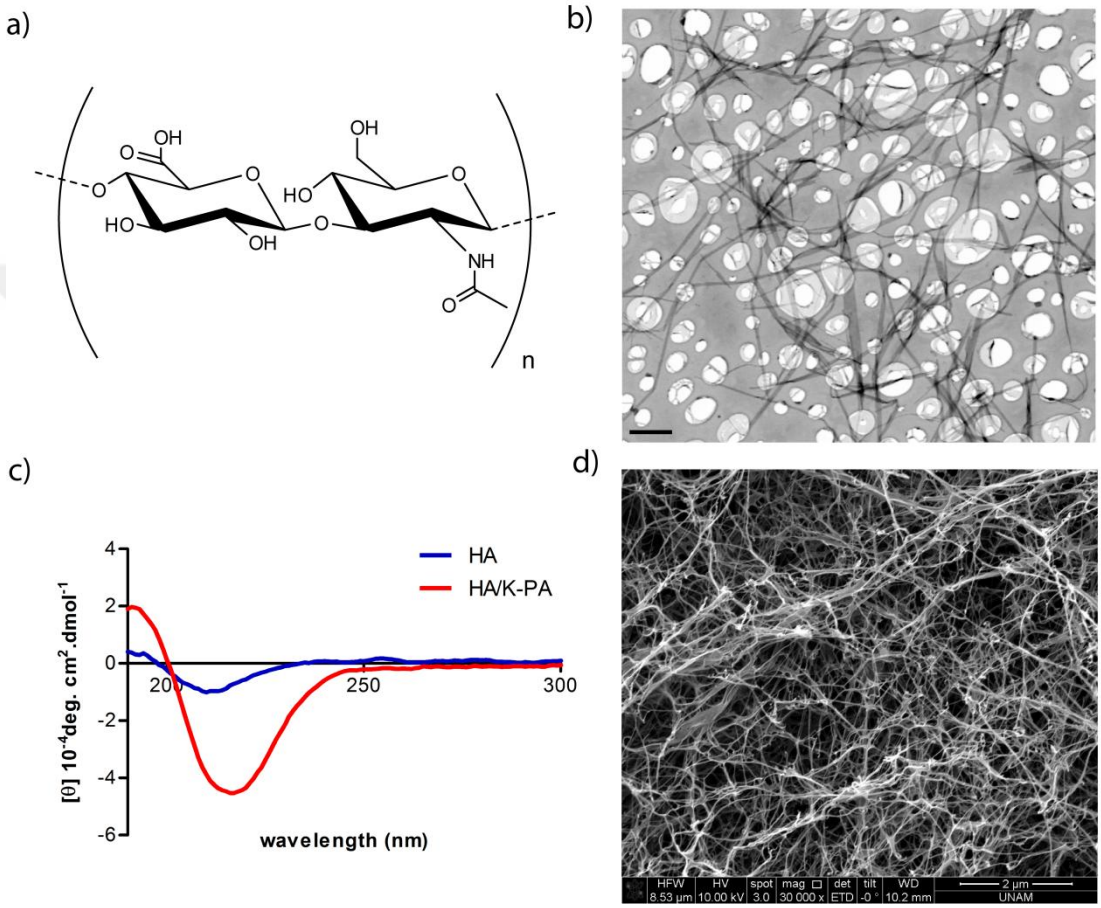

Figure 5.20 Hyaluronic acid (HA) and its self-assembly with K-PA molecule. a) Chemical structure of HA. b) TEM image of self-assembled HA/K-PA nanostructures, scale bar = 1 µm. c) Circular dichroism spectra of HA and HA/K-PA. d) SEM micrograph of HA/K-PA assembly, scale bar = 2 µm.

Zeta potential of HA/K-PA, in addition to that of Glc-PA/E-PA and K-PA/E-PA nanofibers, was also monitored prior to biological experiments. Results revealed that all three of the nanosystems displayed similar zeta potentials (Figure 5.21).

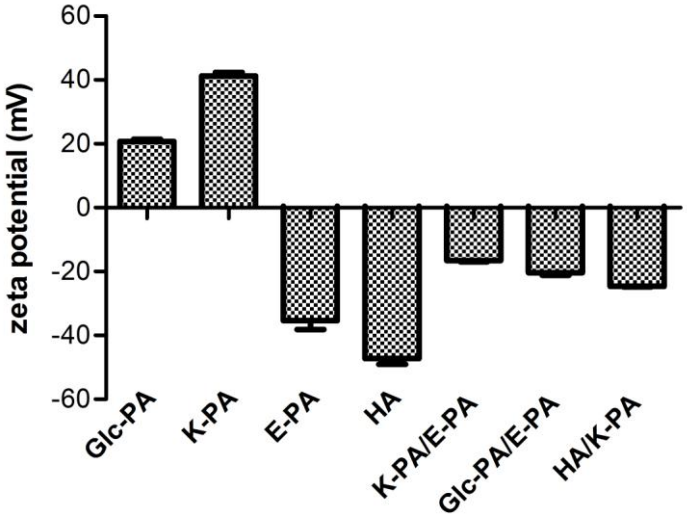

Figure 5.21 Zeta potentials of glycopeptide and peptide nanofiber systems

5.3.4 *In Vitro* Studies

Mouse MSCs were used during *in vitro* analyses and they were cultured on Glc-PA/E-PA, HA/K-PA, E-PA/K-PA and standard polystyrene culture plate. Viability of mMSCs was evaluated and results revealed that no significant difference was observed among hydrogel groups at day 1, 2 and 3, indicating the biocompatibility of nanofibrous networks on cells (Figure 5.22a).

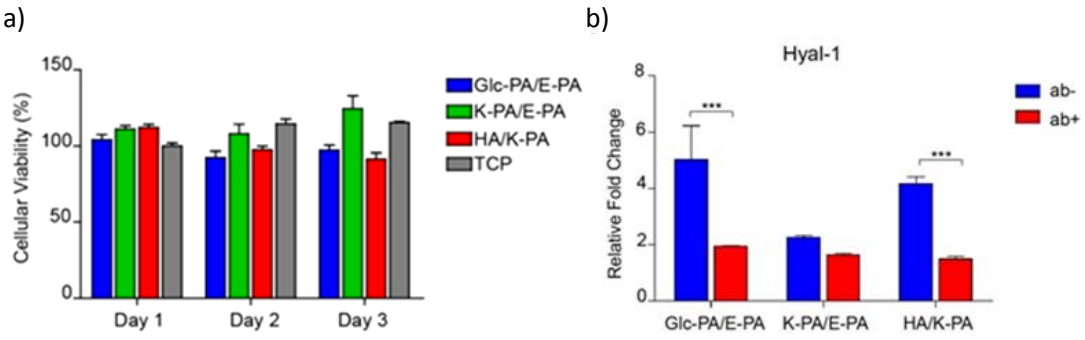

Figure 5.22 a) Cellular viability of mMSC cultured on Glc-PA/E-PA, K-PA/E-PA, HA/K-PA and TCP at days 1, 2 and 3. b) Hyal-1 gene expression after 36 h of anti-CD44 incubation. Results were normalized to GAPDH and calibrated to cultured cells on TCP. Error bars indicate SEM, n = 3, **p<0.05.

After ensuring the biocompatibility of hydrogels cultured with mMSC, mimicking of native HA by Glc-PA/E-PA nanofibers was examined by analyzing hyaluronidase-1 (Hyal-1) expression. Hyal-1 is one of the main enzymes that cleaves HA chains and leads to the upregulation in response to the binding of CD44 to HA.[328-329] Therefore, its expression was monitored on the second day of culture to understand whether the recognition of the Glc-PA/E-PA matrix by mMSCs is in a similar manner to the CD44-HA binding process. Unlike the mRNA expression of Hyal-1 in cells cultured on K-PA/E-PA nanofibers, mMSCs coated on Glc-PA/E-PA and HA/K-PA exhibited enhanced Hyal-1 mRNA expressions and blocking of CD44 receptor by anti-CD44 antibody resulted in the downregulation of Hyal-1 expression of cells seeded on Glc-PA/E-PA and HA/K-PA (Figure 5.22b). The results indicated that mMSCs recognize the bioactive fibrous structure through CD44 interactions.

Sulfated GAG deposition is one of the major characteristics of the cartilage ECM and Safranin-O staining is a qualitative assay used to visualize sulfated GAG accumulation. Since the dye is cationic, it binds to GAGs stochiometrically. Localization and distribution of GAGs on or around cellular aggregation was analyzed by Safranin-O staining at day 3, 7 and 14 (Figure 5.23a). It was observed that the staining intensity was gradually increased parallel to the increased aggregate size during 14 days, indicating ongoing differentiation process. In addition to Safranin-O staining, DMMB assay was also performed to gather more reliable quantitative results (Figure 5.23b). The GAG deposition was significantly higher on day 3 when mMSCs were cultivated in Glc-PA/E-PA compared to those cultured on HA/K-PA, K-PA/E-PA and culture plate.

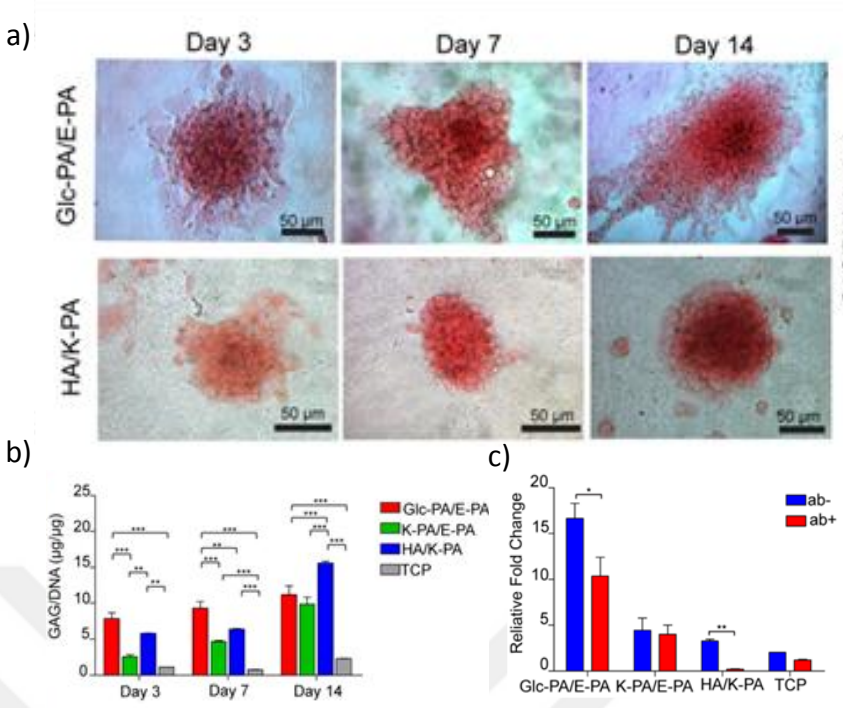

Figure 5.23 a) Safranin-O stainings and b) DMMB assay for quantification of GAGs (normalized to DNA amount) produced by mMSCs cultured on Glc-PA/E-PA and HA/K-PA on days 3, 7 and 14 in chondrogenic medium. c) Sox 9 expression analysis performed at day 1 using mMSCs cultured in chondrogenic medium.

In addition to the analyses of GAG deposition on mMSCs treating with different scaffolds, chondrogenic commitment was also tested through the evaluation of Sox9 expression in the presence and absence of anti-CD44. HA is reported to enhance chondrogenic differentiation of mesenchymal stem cells and CD 44 is the most pronounced receptor type for HA, which plays a significant role in the differentiation commitment.[309, 311] On the other hand, Sox 9 is a transcription factor responsible for boosting chondrogenesis related pathways. To understand whether enhanced chondrogenic differentiation is due to CD 44 mediated interaction, Sox 9 expression was analyzed in the presence of anti-CD 44 (Figure 5.23c). The expression of Sox 9 was downregulated in mMSCs cultivated on Glc-PA/E-PA following CD44

blocking, while no difference in expression was observed in K-PA/E-PA control. These results clearly demonstrated the interactions between CD44 and hyaluronate and its role in chondregenic differentiation.

5.3.5 *In Vivo* Study

The effect of hyaluronic acid mimetic hydrogels on cartilage tissue regeneration was investigated in full thickness chondral defect treated with microfracture model. In microfracture model, regeneration process was triggered through the transportation of bone marrow derived stem cells to defect site by blood due to the bleeding of subchondral bone. It made possible to answer how differentiation potential of transported mesenchymal stem cells was induced by glycopeptide hydrogel in comparison with clinically used HA (Hyalgan®) and sham group.

Regenerated tissue characeristics were qualitatively analyzed by Safranin-O stainings in combination with Fast Green/Haemotoxylin counterstaining. Samples treated with Hyalgan® and saline mostly demonstrated weak Safranin-O stainings and loose arrangement (Figure 5.24a). On the contrary, Glc-PA/E-PA exhibited proper complete integration to surrounding tissue at two lateral sites and basal integration to subchondral bone. Collagen II immunostainings revealed that lower amount of collagen was accumulated in saline-treated groups, especially at the uppermost part of the tissue of interest (Figure 5.24b). Overall, the intense and uniformly distributed staining of both collagen II and Safranin-O in Glc-PA/E-PA treated groups pointed out that hyaline-like cartilage formation was observed in the regenerated tissue and its morphology and composition firmly complied with the surrounding tissue.

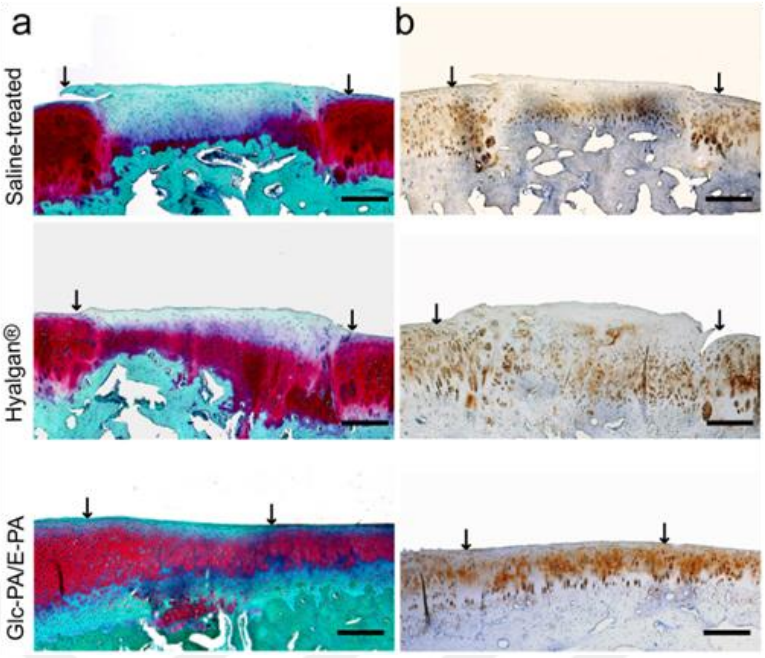

Figure 5.24 Staining of tissue sections with a) Safranin-O and b) Collagen II immunostain.

5.4 CONCLUSION

In conclusion, amphiphilic glycopeptide molecule (Glc-PA) was synthesized after the synthesis of glyco amino acid residue (Fmoc-Ser [β-D-Glc(OAc_4)]. As a result of self-assembly process, we envisaged that supramolecular glycopeptide nanofibers present multiple glucose residues in close proximity, which could mimic chemical structure of hyaluronic acid macromolecule. The morphological, mechanical and biophysical properties of the self-assembled nanofibers were investigated by different techniques. Glucose moieties of both glucuronic acid and N-acetylglucosamine found in HA and carboxylic acid functionality in the glucuronic acid molecule are main elements for designing a hyaluronic acid inspired material. Its function concerning the CD44 receptor interactions can induce chondrogenic differentiation. Therefore, functional mimicry was investigated by tracking the Hyal-

1 expression of cells following the blocking of CD44 receptors with an anti-CD44 antibody, which is indicative sign for the cellular recognition of bioactive fibrous structures by CD44. The changes in Sox 9 expression, which is a transcription factor that activates chondrogenesis-related pathways, were further analyzed after CD44 blockage. Both findings are consistent with each other and suggest that the mMSCs can recognize functional units of Glc-PA/E-PA nanofibers in a similar way to Hyaluronate. Naturally-derived HA can be replaced by the current design to avoid the potential health hazards associated with natural scaffolds. Our *in vivo* results also demonstrated that glycopeptide nanofibers can be exploited as less invasive and cell-free *in situ* cartilage regeneration approach by committing mesenchymal stem cells released from bone marrow toward chondrogenic lineage.

CHAPTER 6

CONCLUSION and FUTURE PROSPECTS

Nature as an important inspirational source for scientists presents complex and elegant examples for adaptive and intelligent systems created by self-assembly. Significant effort has been devoted to understanding these sophisticated systems. Self assembly aids us to generate supramolecular nanostructures with high order and complexity. One of the reason behind the rapid growth of self-assembly is that it allows synthesizing larger structures that cannot be feasible with covalent bonds due to poor stability. Therefore, peptide based self assembling building blocks are considered as proper platforms to construct supramolecular nanostructures showing diverse features and applications. The resulting morphology, as well as its function, can be manipulated at the molecular level by altering the number, type and sequence of amino acids and also by inducing external stimuli such as pH, temperature, electric field, magnetic field, light, sound etc.

This thesis describes the design and synthesis of different peptide-based materials used for potential applications in different fields of biomedicine. Here, the driving forces triggering the formation of the defined nanostructures (nanofibers, micelles, vesicles, nanosheets) is mainly noncovalent interactions such as electrostatic interactions between charged amino acids, hydrogen bonding, π-π stacking and hydrophobic interactions. Although a change in the hydrophilic segment of the peptide can lead to the morphological alterations, the contribution of intermolecular hydrogen bonds was mainly considered in our designs to generate structurally different PA systems. It was known that while high content of hydrogen bonding between peptide blocks favored the formation of cylindrical nanofibers, intermolecular hydrogen bonding deficient PA systems self-assembled into micellar structures.

In the first study, arginine rich cell penetrating PA molecules were designed and synthesized to prepare PA integrated unilamellar liposomes with high encapsulation efficiencies and improved cellular uptake profiles. Vesicular structures were obtained as a result of noncovalent interactions occurring between amphiphilic peptide and phospholipid molecules. Liposomes have been studied for almost 50 years for different purposes. Despite of their drug loading abilities and biocompatibility properties, stability, short circulation time and storage of the prepared formulations are the major obstacles needed to be overcome for further progress in the development of such products. By using arginine-rich sequence, we aimed to improve the cellular uptake of the delivery agent. It is known that guanidinium group of arginine residues interacts with phosphates of lipid parts residing in cell membrane through hydrogen bonding and electrostatic interactions, leading to improved cellular internalization of the molecule of interest. The employed functionalization strategy enables preparation of varied liposomal formulations decorated with bioactive epitope bearing peptides for the delivery of cargos to target site.

In the second study, similar functionalization strategy was utilized to develop peptide functionalized fluorescent MSNs. In previously reported studies, peptides were covalently attached to the silica surface via additional cross-linking agents to be used in drug delivery and theranostic applications due to their functional tunibility, biodegradability and targeting ability. Our study demonstrated that peptide modified nanoparticles exhibited marked increase in cellular uptake compared to bare MSNs in HUVECs and A10 cell line. Same as the previous study, biorecognition can be gained through the integration of bioactive signal presenting peptides into MSNs.

In the third study, PAs were used for MR imaging after functionalized with superparamagnetic iron oxide nanoparticles. Similar to previous two studies, PAs were noncovalently interacted with hydrophobic SPION surface. While functionalization did not affect the crystal structure of SPIONs, they were transfered into aqueous medium from organic phase. They were shown to enhance MRI signal in breast tumor tissue when administrated into mammary gland tumor bearing rats. The signal enhancement in tumor site via passive targeting of nanoparticles might be attributed to the EPR effect.

The last study reported in this thesis is related to the synthesis of amphiphilic glycopeptide molecule and its co-assembly with oppositely charged PA molecule to afford one-dimensional nanofibrous structures mimicking chemical structure of native hyaluronic acid found in cartilage. Hyaluronic acid abundantly found in native extracellular matrix was known to enhance cartilage repair by providing inductive microenvironment to the cells. However, cost of production, batch to batch variations encountered during the extraction process and immunogenic effect of the animal derived product limit its usage in tissue engineering. Our results acquired from the biological experiments revealed that designed glycopeptide gel can be used instead of naturally-derived hyaluronic acid to hinder the potential health hazards associated with natural scaffolds. Our *in vivo* results also indicated that the HA mimetic glycopeptide gel can be considered as less invasive and cell-free in situ cartilage regeneration approach.

Consequently, beta sheet breaker proline rich domain was exploited in the peptide designs for the first three studies to develop hybrid peptide systems used in drug delivery and bioimaging studies. On the other hand, in the last study, beta-sheet

forming segment (-VVA) was incorporated into backbone to obtain fibrillar structure as well as self-supportive gels at concentrated conditions. The peptide nanostructure can be tailored depending on the function of material. While creating new materials applicable in biomedical field, working in an interdisciplinary research environment is very crucial to improve the idea by looking from different scientific perspectives. Development of novel nanomaterials with new properties using supramolecular interactions is an exciting research field and designing controllable materials with precise length, composition and complex shapes will be the ultimate goal for the next generation supramolecular materials.

Bibliography

1. Ozin, G. A.; Hou, K.; Lotsch, B. V.; Cademartiri, L.; Puzzo, D. P.; Scotognella, F.; Ghadimi, A.; Thomson, J., Nanofabrication by self-assembly. *Materials Today* **2009,** 12, (5), 12-23.
2. Stephanopoulos, N.; Ortony, J. H.; Stupp, S. I., Self-assembly for the synthesis of functional biomaterials. *Acta materialia* **2013,** 61, (3), 912-930.
3. Whitesides, G. M.; Grzybowski, B., Self-assembly at all scales. *Science* **2002,** 295, (5564), 2418-2421.
4. Fialkowski, M.; Bishop, K. J.; Klajn, R.; Smoukov, S. K.; Campbell, C. J.; Grzybowski, B. A., Principles and implementations of dissipative (dynamic) self-assembly. *The Journal of Physical Chemistry B* **2006,** 110, (6), 2482-2496.
5. Fairman, R.; Åkerfeldt, K. S., Peptides as novel smart materials. *Current opinion in structural biology* **2005,** 15, (4), 453-463.
6. Zhao, X.; Pan, F.; Xu, H.; Yaseen, M.; Shan, H.; Hauser, C. A.; Zhang, S.; Lu, J. R., Molecular self-assembly and applications of designer peptide amphiphiles. *Chemical Society Reviews* **2010,** 39, (9), 3480-3498.
7. Toksoz, S.; Acar, H.; Guler, M. O., Self-assembled one-dimensional soft nanostructures. *Soft Matter* **2010,** 6, (23), 5839-5849.
8. Steed, J. W.; Atwood, J. L., *Supramolecular chemistry*. John Wiley & Sons: 2013.
9. Moreira Leite, D.; Barbu, E.; Pilkington, G. J.; Lalatsa, A., Peptide self-assemblies in drug delivery. *Current topics in medicinal chemistry* **2015**.
10. Castillo, J.; Sasso, L.; Svendsen, W. E., *Self-assembled peptide nanostructures: Advances and applications in nanobiotechnology*. CRC Press: 2012.
11. Dasgupta, A.; Mondal, J. H.; Das, D., Peptide hydrogels. *RSC Advances* **2013,** 3, (24), 9117-9149.
12. Brack, A.; Orgel, L. E., β structures of alternating polypeptides and their possible prebiotic significance. **1975**.
13. Berg, J. M.; Tymoczko, J. L.; Stryer, L., Secondary Structure: Polypeptide Chains Can Fold Into Regular Structures Such as the Alpha Helix, the Beta Sheet, and Turns and Loops. **2002**.
14. Apostolovic, B.; Danial, M.; Klok, H.-A., Coiled coils: attractive protein folding motifs for the fabrication of self-assembled, responsive and bioactive materials. *Chemical Society Reviews* **2010,** 39, (9), 3541-3575.
15. Mart, R. J.; Osborne, R. D.; Stevens, M. M.; Ulijn, R. V., Peptide-based stimuli-responsive biomaterials. *Soft matter* **2006,** 2, (10), 822-835.
16. Dehsorkhi, A.; Castelletto, V.; Hamley, I. W.; Adamcik, J.; Mezzenga, R., The effect of pH on the self-assembly of a collagen derived peptide amphiphile. *Soft matter* **2013,** 9, (26), 6033-6036.

17. Hartgerink, J. D.; Beniash, E.; Stupp, S. I., Peptide-amphiphile nanofibers: a versatile scaffold for the preparation of self-assembling materials. *Proceedings of the National Academy of Sciences* **2002,** 99, (8), 5133-5138.
18. Lin, B. F.; Megley, K. A.; Viswanathan, N.; Krogstad, D. V.; Drews, L. B.; Kade, M. J.; Qian, Y.; Tirrell, M. V., pH-responsive branched peptide amphiphile hydrogel designed for applications in regenerative medicine with potential as injectable tissue scaffolds. *Journal of Materials Chemistry* **2012,** 22, (37), 19447-19454.
19. Tang, C.; Smith, A. M.; Collins, R. F.; Ulijn, R. V.; Saiani, A., Fmoc-Diphenylalanine Self-Assembly Mechanism Induces Apparent p K a Shifts. *Langmuir* **2009,** 25, (16), 9447-9453.
20. Moyer, T. J.; Finbloom, J. A.; Chen, F.; Toft, D. J.; Cryns, V. L.; Stupp, S. I., pH and Amphiphilic Structure Direct Supramolecular Behavior in Biofunctional Assemblies. *Journal of the American Chemical Society* **2014,** 136, (42), 14746-14752.
21. Lowik, D.; Meijer, J. T.; Minten, I. J.; Van Kalkeren, H.; Heckenmuller, L.; Schulten, I.; Sliepen, K.; Smittenaar, P.; van Hest, J., Controlled disassembly of peptide amphiphile fibres. *Journal of Peptide Science* **2008,** 14, (2), 127.
22. Muraoka, T.; Cui, H.; Stupp, S. I., Quadruple helix formation of a photoresponsive peptide amphiphile and its light-triggered dissociation into single fibers. *Journal of the American Chemical Society* **2008,** 130, (10), 2946-2947.
23. Muraoka, T.; Koh, C. Y.; Cui, H.; Stupp, S. I., Light-Triggered Bioactivity in Three Dimensions. *Angewandte Chemie* **2009,** 121, (32), 6060-6063.
24. Diegelmann, S. R.; Hartman, N.; Markovic, N.; Tovar, J. D., Synthesis and alignment of discrete polydiacetylene-peptide nanostructures. *Journal of the American Chemical Society* **2012,** 134, (4), 2028-2031.
25. Altman, M.; Lee, P.; Rich, A.; Zhang, S., Conformational behavior of ionic self-complementary peptides. *Protein Science* **2000,** 9, (6), 1095-1105.
26. Hamley, I. W.; Dehsorkhi, A.; Castelletto, V.; Furzeland, S.; Atkins, D.; Seitsonen, J.; Ruokolainen, J., Reversible helical unwinding transition of a self-assembling peptide amphiphile. *Soft matter* **2013,** 9, (39), 9290-9293.
27. Miravet, J. F.; Escuder, B.; Segarra-Maset, M. D.; Tena-Solsona, M.; Hamley, I. W.; Dehsorkhi, A.; Castelletto, V., Self-assembly of a peptide amphiphile: transition from nanotape fibrils to micelles. *Soft matter* **2013,** 9, (13), 3558-3564.
28. Pochan, D. J.; Schneider, J. P.; Kretsinger, J.; Ozbas, B.; Rajagopal, K.; Haines, L., Thermally reversible hydrogels via intramolecular folding and consequent self-assembly of a de novo designed peptide. *Journal of the American Chemical Society* **2003,** 125, (39), 11802-11803.
29. Nuhn, H.; Klok, H.-A., Secondary structure formation and LCST behavior of short elastin-like peptides. *Biomacromolecules* **2008,** 9, (10), 2755-2763.

30. Lock, L. L.; Reyes, C.; Zhang, P.; Cui, H., Tuning Cellular Uptake of Molecular Probes by Rational Design of Their Assembly into Supramolecular Nanoprobes. *Journal of the American Chemical Society* **2016**.
31. Pim, W., Transient supramolecular reconfiguration of peptide nanostructures using ultrasound. *Materials Horizons* **2015,** 2, (2), 198-202.
32. Hong, Y.; Pritzker, M. D.; Legge, R. L.; Chen, P., Effect of NaCl and peptide concentration on the self-assembly of an ionic-complementary peptide EAK16-II. *Colloids and Surfaces B: Biointerfaces* **2005,** 46, (3), 152-161.
33. Ozbas, B.; Kretsinger, J.; Rajagopal, K.; Schneider, J. P.; Pochan, D. J., Salt-triggered peptide folding and consequent self-assembly into hydrogels with tunable modulus. *Macromolecules* **2004,** 37, (19), 7331-7337.
34. Mishra, A.; Chan, K.-H.; Reithofer, M. R.; Hauser, C. A., Influence of metal salts on the hydrogelation properties of ultrashort aliphatic peptides. *RSC Advances* **2013,** 3, (25), 9985-9993.
35. Toksoz, S.; Mammadov, R.; Tekinay, A. B.; Guler, M. O., Electrostatic effects on nanofiber formation of self-assembling peptide amphiphiles. *Journal of colloid and interface science* **2011,** 356, (1), 131-137.
36. Stendahl, J. C.; Rao, M. S.; Guler, M. O.; Stupp, S. I., Intermolecular forces in the self-assembly of peptide amphiphile nanofibers. *Advanced Functional Materials* **2006,** 16, (4), 499-508.
37. Beyer, R. L.; Hoang, H. N.; Appleton, T. G.; Fairlie, D. P., Metal clips induce folding of a short unstructured peptide into an α-helix via turn conformations in water. Kinetic versus thermodynamic products. *Journal of the American Chemical Society* **2004,** 126, (46), 15096-15105.
38. Dublin, S. N.; Conticello, V. P., Design of a selective metal ion switch for self-assembly of peptide-based fibrils. *Journal of the American Chemical Society* **2008,** 130, (1), 49-51.
39. Pires, M. M.; Chmielewski, J., Self-assembly of collagen peptides into microflorettes via metal coordination. *Journal of the American Chemical Society* **2009,** 131, (7), 2706-2712.
40. Pagel, K.; Seri, T.; von Berlepsch, H.; Griebel, J.; Kirmse, R.; Böttcher, C.; Koksch, B., How Metal Ions Affect Amyloid Formation: Cu2+-and Zn2+-Sensitive Peptides. *ChemBioChem* **2008,** 9, (4), 531-536.
41. Kar, T.; Mandal, S. K.; Das, P. K., Organogel–Hydrogel Transformation by Simple Removal or Inclusion of N-Boc-Protection. *Chemistry-A European Journal* **2011,** 17, (52), 14952-14961.
42. Koley, P.; Gayen, A.; Drew, M. G.; Mukhopadhyay, C.; Pramanik, A., Design and Self-Assembly of a Leucine-Enkephalin Analogue in Different Nanostructures: Application of Nanovesicles. *Small* **2012,** 8, (7), 984-990.
43. Zhao, Y.; Deng, L.; Wang, J.; Xu, H.; Lu, J. R., Solvent Controlled Structural Transition of KI4K Self-Assemblies: from Nanotubes to Nanofibrils. *Langmuir* **2015,** 31, (47), 12975-12983.

44. Madine, J.; Davies, H. A.; Shaw, C.; Hamley, I. W.; Middleton, D. A., Fibrils and nanotubes assembled from a modified amyloid-β peptide fragment differ in the packing of the same β-sheet building blocks. *Chemical Communications* **2012,** 48, (24), 2976-2978.
45. Webber, M. J.; Newcomb, C. J.; Bitton, R.; Stupp, S. I., Switching of self-assembly in a peptide nanostructure with a specific enzyme. *Soft matter* **2011,** 7, (20), 9665-9672.
46. Castelletto, V.; McKendrick, J.; Hamley, I.; Olsson, U.; Cenker, C., PEGylated amyloid peptide nanocontainer delivery and release system. *Langmuir* **2010,** 26, (14), 11624-11627.
47. Hirst, A. R.; Roy, S.; Arora, M.; Das, A. K.; Hodson, N.; Murray, P.; Marshall, S.; Javid, N.; Sefcik, J.; Boekhoven, J., Biocatalytic induction of supramolecular order. *Nature chemistry* **2010,** 2, (12), 1089-1094.
48. Hughes, M.; Birchall, L. S.; Zuberi, K.; Aitken, L. A.; Debnath, S.; Javid, N.; Ulijn, R. V., Differential supramolecular organisation of Fmoc-dipeptides with hydrophilic terminal amino acid residues by biocatalytic self-assembly. *Soft matter* **2012,** 8, (45), 11565-11574.
49. Dehsorkhi, A.; Hamley, I. W.; Seitsonen, J.; Ruokolainen, J., Tuning self-assembled nanostructures through enzymatic degradation of a peptide amphiphile. *Langmuir* **2013,** 29, (22), 6665-6672.
50. Klok, H. A., Protein-Inspired Materials: Synthetic Concepts and Potential Applications. *Angewandte Chemie International Edition* **2002,** 41, (9), 1509-1513.
51. Cavalli, S.; Albericio, F.; Kros, A., Amphiphilic peptides and their cross-disciplinary role as building blocks for nanoscience. *Chemical Society Reviews* **2010,** 39, (1), 241-263.
52. Merrifield, R. B., Solid phase peptide synthesis. I. The synthesis of a tetrapeptide. *Journal of the American Chemical Society* **1963,** 85, (14), 2149-2154.
53. Isidro-Llobet, A.; Alvarez, M.; Albericio, F., Amino acid-protecting groups. *Chemical reviews* **2009,** 109, (6), 2455-2504.
54. El-Faham, A.; Albericio, F., Peptide coupling reagents, more than a letter soup. *Chemical reviews* **2011,** 111, (11), 6557-6602.
55. Pedersen, S. L.; Tofteng, A. P.; Malik, L.; Jensen, K. J., Microwave heating in solid-phase peptide synthesis. *Chemical Society Reviews* **2012,** 41, (5), 1826-1844.
56. Maude, S.; Tai, L.; Davies, R.; Liu, B.; Harris, S.; Kocienski, P.; Aggeli, A., Peptide synthesis and self-assembly. In *Peptide-Based Materials*, Springer: 2012; pp 27-69.
57. Hamley, I., Self-assembly of amphiphilic peptides. *Soft matter* **2011,** 7, (9), 4122-4138.
58. Chapman, R.; Danial, M.; Koh, M. L.; Jolliffe, K. A.; Perrier, S., Design and properties of functional nanotubes from the self-assembly of cyclic peptide templates. *Chemical Society Reviews* **2012,** 41, (18), 6023-6041.

59. Ramakers, B.; van Hest, J.; Löwik, D., Molecular tools for the construction of peptide-based materials. *Chemical Society Reviews* **2014,** 43, (8), 2743-2756.
60. Garanger, E.; Lecommandoux, S., Towards bioactive nanovehicles based on protein polymers. *Angewandte Chemie International Edition* **2012,** 51, (13), 3060-3062.
61. ávan Hest, J. C., Protein-based materials, toward a new level of structural control. *Chemical Communications* **2001**, (19), 1897-1904.
62. Dougherty, D. A., Unnatural amino acids as probes of protein structure and function. *Current opinion in chemical biology* **2000,** 4, (6), 645-652.
63. Hadjichristidis, N.; Iatrou, H.; Pitsikalis, M.; Sakellariou, G., Synthesis of well-defined polypeptide-based materials via the ring-opening polymerization of α-amino acid N-carboxyanhydrides. *Chemical reviews* **2009,** 109, (11), 5528-5578.
64. Huang, J.; Heise, A., Stimuli responsive synthetic polypeptides derived from N-carboxyanhydride (NCA) polymerisation. *Chemical Society Reviews* **2013,** 42, (17), 7373-7390.
65. Cheng, J.; Deming, T. J., Synthesis of polypeptides by ring-opening polymerization of α-amino acid N-carboxyanhydrides. In *Peptide-based materials*, Springer: 2012; pp 1-26.
66. Pattabiraman, V. R.; Bode, J. W., Rethinking amide bond synthesis. *Nature* **2011,** 480, (7378), 471-479.
67. Tam, J. P.; Xu, J.; Eom, K. D., Methods and strategies of peptide ligation*. *Peptide Science* **2001,** 60, (3), 194-205.
68. Li, S.-C.; Deber, C. M., Glycine and β-branched residues support and modulate peptide helicity in membrane environments. *FEBS letters* **1992,** 311, (3), 217-220.
69. Ulijn, R. V.; Smith, A. M., Designing peptide based nanomaterials. *Chemical Society Reviews* **2008,** 37, (4), 664-675.
70. Ackbarow, T.; Buehler, M. J., Alpha-helical protein domains unify strength and robustness through hierarchical nanostructures. *Nanotechnology* **2009,** 20, (7), 075103.
71. Smeenk, J. M.; Otten, M. B.; Thies, J.; Tirrell, D. A.; Stunnenberg, H. G.; van Hest, J., Controlled Assembly of Macromolecular β-Sheet Fibrils. *Angewandte Chemie International Edition* **2005,** 44, (13), 1968-1971.
72. Alemán, C.; Bianco, A.; Venanzi, M., *Peptide Materials: From Nanostuctures to Applications*. John Wiley & Sons: 2013.
73. Smith, K. H.; Tejeda-Montes, E.; Poch, M.; Mata, A., Integrating top-down and self-assembly in the fabrication of peptide and protein-based biomedical materials. *Chemical Society Reviews* **2011,** 40, (9), 4563-4577.
74. Hinterding, K.; Alonso-Díaz, D.; Waldmann, H., Organic synthesis and biological signal transduction. *Angewandte Chemie International Edition* **1998,** 37, (6), 688-749.

75. Löwik, D. W.; van Hest, J. C., Peptide based amphiphiles. *Chemical Society Reviews* **2004,** 33, (4), 234-245.
76. Hamley, I. W.; Dehsorkhi, A.; Jauregi, P.; Seitsonen, J.; Ruokolainen, J.; Coutte, F.; Chataigné, G.; Jacques, P., Self-assembly of three bacterially-derived bioactive lipopeptides. *Soft matter* **2013,** 9, (40), 9572-9578.
77. Israelachvili, J. N., *Intermolecular and surface forces: revised third edition*. Academic press: 2011.
78. Lalatsa, A.; Schätzlein, A. G.; Mazza, M.; Le, T. B. H.; Uchegbu, I. F., Amphiphilic poly (l-amino acids)—new materials for drug delivery. *Journal of Controlled Release* **2012,** 161, (2), 523-536.
79. Shrestha, L. K.; Strzelczyk, K. M.; Shrestha, R. G.; Ichikawa, K.; Aramaki, K.; Hill, J. P.; Ariga, K., Nonionic amphiphile nanoarchitectonics: self-assembly into micelles and lyotropic liquid crystals. *Nanotechnology* **2015,** 26, (20), 204002.
80. M Leite, D.; Barbu, E.; J Pilkington, G.; Lalatsa, A., Peptide Self-Assemblies for Drug Delivery. *Current topics in medicinal chemistry* **2015,** 15, (22), 2277-2289.
81. Velichko, Y. S.; Stupp, S. I.; de la Cruz, M. O., Molecular simulation study of peptide amphiphile self-assembly. *The Journal of Physical Chemistry B* **2008,** 112, (8), 2326-2334.
82. Paramonov, S. E.; Jun, H.-W.; Hartgerink, J. D., Self-assembly of peptide-amphiphile nanofibers: the roles of hydrogen bonding and amphiphilic packing. *Journal of the American Chemical Society* **2006,** 128, (22), 7291-7298.
83. Cui, H.; Webber, M. J.; Stupp, S. I., Self-assembly of peptide amphiphiles: From molecules to nanostructures to biomaterials. *Peptide Science* **2010,** 94, (1), 1-18.
84. Tsonchev, S.; Schatz, G. C.; Ratner, M. A., Electrostatically-directed self-assembly of cylindrical peptide amphiphile nanostructures. *The Journal of Physical Chemistry B* **2004,** 108, (26), 8817-8822.
85. Lee, O.-S.; Stupp, S. I.; Schatz, G. C., Atomistic molecular dynamics simulations of peptide amphiphile self-assembly into cylindrical nanofibers. *Journal of the American Chemical Society* **2011,** 133, (10), 3677-3683.
86. Fu, I. W.; Markegard, C. B.; Chu, B. K.; Nguyen, H. D., The Role of Electrostatics and Temperature on Morphological Transitions of Hydrogel Nanostructures Self-Assembled by Peptide Amphiphiles Via Molecular Dynamics Simulations. *Advanced healthcare materials* **2013,** 2, (10), 1388-1400.
87. Greenfield, M. A.; Hoffman, J. R.; Olvera de la Cruz, M.; Stupp, S. I., Tunable mechanics of peptide nanofiber gels. *Langmuir* **2009,** 26, (5), 3641-3647.
88. Zhang, S.; Greenfield, M. A.; Mata, A.; Palmer, L. C.; Bitton, R.; Mantei, J. R.; Aparicio, C.; de La Cruz, M. O.; Stupp, S. I., A self-assembly pathway to aligned monodomain gels. *Nature materials* **2010,** 9, (7), 594-601.
89. Pashuck, E. T.; Stupp, S. I., Direct observation of morphological tranformation from twisted ribbons into helical ribbons. *Journal of the American Chemical Society* **2010,** 132, (26), 8819-8821.

90. Cui, H.; Cheetham, A. G.; Pashuck, E. T.; Stupp, S. I., Amino acid sequence in constitutionally isomeric tetrapeptide amphiphiles dictates architecture of one-dimensional nanostructures. *Journal of the American Chemical Society* **2014,** 136, (35), 12461-12468.
91. Moyer, T. J.; Cui, H.; Stupp, S. I., Tuning nanostructure dimensions with supramolecular twisting. *The Journal of Physical Chemistry B* **2012,** 117, (16), 4604-4610.
92. Shimada, T.; Lee, S.; Bates, F. S.; Hotta, A.; Tirrell, M., Wormlike Micelle Formation in Peptide-Lipid Conjugates Driven by Secondary Structure Transformation of the Headgroups†. *The Journal of Physical Chemistry B* **2009,** 113, (42), 13711-13714.
93. Missirlis, D.; Chworos, A.; Fu, C. J.; Khant, H. A.; Krogstad, D. V.; Tirrell, M., Effect of the peptide secondary structure on the peptide amphiphile supramolecular structure and interactions. *Langmuir* **2011,** 27, (10), 6163-6170.
94. Zhang, J.; Hao, R.; Huang, L.; Yao, J.; Chen, X.; Shao, Z., Self-assembly of a peptide amphiphile based on hydrolysed Bombyx mori silk fibroin. *Chemical Communications* **2011,** 47, (37), 10296-10298.
95. Ghosh, A.; Dobson, E. T.; Buettner, C. J.; Nicholl, M. J.; Goldberger, J. E., Programming pH-Triggered Self-Assembly Transitions via Isomerization of Peptide Sequence. *Langmuir* **2014,** 30, (51), 15383-15387.
96. Sever, M.; Mammadov, B.; Guler, M. O.; Tekinay, A. B., Tenascin-C mimetic peptide nanofibers direct stem cell differentiation to osteogenic lineage. *Biomacromolecules* **2014,** 15, (12), 4480-4487.
97. Mumcuoglu, D.; Sardan, M.; Tekinay, T.; Guler, M. O.; Tekinay, A. B., Oligonucleotide Delivery with Cell Surface Binding and Cell Penetrating Peptide Amphiphile Nanospheres. *Molecular pharmaceutics* **2015,** 12, (5), 1584-1591.
98. Moyer, T. J.; Kassam, H. A.; Bahnson, E. S.; Morgan, C. E.; Tantakitti, F.; Chew, T. L.; Kibbe, M. R.; Stupp, S. I., Shape-Dependent Targeting of Injured Blood Vessels by Peptide Amphiphile Supramolecular Nanostructures. *Small* **2015**.
99. Xu, X.-D.; Jin, Y.; Liu, Y.; Zhang, X.-Z.; Zhuo, R.-X., Self-assembly behavior of peptide amphiphiles (PAs) with different length of hydrophobic alkyl tails. *Colloids and Surfaces B: Biointerfaces* **2010,** 81, (1), 329-335.
100. van den Heuvel, M.; Löwik, D. W.; van Hest, J. C., Effect of the diacetylene position on the chromatic properties of polydiacetylenes from self-assembled peptide amphiphiles. *Biomacromolecules* **2010,** 11, (6), 1676-1683.
101. Black, M.; Trent, A.; Kostenko, Y.; Lee, J. S.; Olive, C.; Tirrell, M., Self-Assembled Peptide Amphiphile Micelles Containing a Cytotoxic T-Cell Epitope Promote a Protective Immune Response In Vivo. *Advanced Materials* **2012,** 24, (28), 3845-3849.
102. Zhang, P.; Cheetham, A. G.; Lin, Y.-a.; Cui, H., Self-assembled Tat nanofibers as effective drug carrier and transporter. *ACS nano* **2013,** 7, (7), 5965-5977.

103. Cui, H.; Muraoka, T.; Cheetham, A. G.; Stupp, S. I., Self-assembly of giant peptide nanobelts. *Nano letters* **2009,** 9, (3), 945-951.
104. Castelletto, V.; Hamley, I. W.; Perez, J.; Abezgauz, L.; Danino, D., Fibrillar superstructure from extended nanotapes formed by a collagen-stimulating peptide. *Chemical Communications* **2010,** 46, (48), 9185-9187.
105. Niece, K. L.; Hartgerink, J. D.; Donners, J. J.; Stupp, S. I., Self-assembly combining two bioactive peptide-amphiphile molecules into nanofibers by electrostatic attraction. *Journal of the American Chemical Society* **2003,** 125, (24), 7146-7147.
106. Behanna, H. A.; Donners, J. J.; Gordon, A. C.; Stupp, S. I., Coassembly of amphiphiles with opposite peptide polarities into nanofibers. *Journal of the American Chemical Society* **2005,** 127, (4), 1193-1200.
107. Mammadov, B.; Mammadov, R.; Guler, M. O.; Tekinay, A. B., Cooperative effect of heparan sulfate and laminin mimetic peptide nanofibers on the promotion of neurite outgrowth. *Acta biomaterialia* **2012,** 8, (6), 2077-2086.
108. Ceylan, H.; Kocabey, S.; Tekinay, A. B.; Guler, M. O., Surface-adhesive and osteogenic self-assembled peptide nanofibers for bioinspired functionalization of titanium surfaces. *Soft matter* **2012,** 8, (14), 3929-3937.
109. Hamley, I.; Dehsorkhi, A.; Castelletto, V., Coassembly in binary mixtures of peptide amphiphiles containing oppositely charged residues. *Langmuir* **2013,** 29, (16), 5050-5059.
110. Guler, M. O.; Claussen, R. C.; Stupp, S. I., Encapsulation of pyrene within self-assembled peptide amphiphile nanofibers. *Journal of Materials Chemistry* **2005,** 15, (42), 4507-4512.
111. Mammadov, R.; Cinar, G.; Gunduz, N.; Goktas, M.; Kayhan, H.; Tohumeken, S.; Topal, A. E.; Orujalipoor, I.; Delibasi, T.; Dana, A., Virus-like nanostructures for tuning immune response. *Scientific reports* **2015,** 5.
112. Löwik, D. W.; Garcia-Hartjes, J.; Meijer, J. T.; van Hest, J. C., Tuning secondary structure and self-assembly of amphiphilic peptides. *Langmuir* **2005,** 21, (2), 524-526.
113. Meijer, J. T.; Roeters, M.; Viola, V.; Löwik, D. W.; Vriend, G.; van Hest, J. C., Stabilization of peptide fibrils by hydrophobic interaction. *Langmuir* **2007,** 23, (4), 2058-2063.
114. He, C.; Han, Y.; Fan, Y.; Deng, M.; Wang, Y., Self-assembly of Aβ-based peptide amphiphiles with double hydrophobic chains. *Langmuir* **2012,** 28, (7), 3391-3396.
115. Berndt, P.; Fields, G. B.; Tirrell, M., Synthetic lipidation of peptides and amino acids: monolayer structure and properties. *Journal of the American Chemical Society* **1995,** 117, (37), 9515-9522.
116. Yu, Y.-C.; Berndt, P.; Tirrell, M.; Fields, G. B., Self-assembling amphiphiles for construction of protein molecular architecture. *Journal of the American Chemical Society* **1996,** 118, (50), 12515-12520.

117. Gore, T.; Dori, Y.; Talmon, Y.; Tirrell, M.; Bianco-Peled, H., Self-assembly of model collagen peptide amphiphiles. *Langmuir* **2001,** 17, (17), 5352-5360.
118. Hartgerink, J. D.; Beniash, E.; Stupp, S. I., Self-assembly and mineralization of peptide-amphiphile nanofibers. *Science* **2001,** 294, (5547), 1684-1688.
119. Arslan, E.; Garip, I. C.; Gulseren, G.; Tekinay, A. B.; Guler, M. O., Bioactive supramolecular peptide nanofibers for regenerative medicine. *Advanced healthcare materials* **2014,** 3, (9), 1357-1376.
120. Shah, R. N.; Shah, N. A.; Lim, M. M. D. R.; Hsieh, C.; Nuber, G.; Stupp, S. I., Supramolecular design of self-assembling nanofibers for cartilage regeneration. *Proceedings of the National Academy of Sciences* **2010,** 107, (8), 3293-3298.
121. Ustun, S.; Tombuloglu, A.; Kilinc, M.; Guler, M. O.; Tekinay, A. B., Growth and differentiation of prechondrogenic cells on bioactive self-assembled peptide nanofibers. *Biomacromolecules* **2012,** 14, (1), 17-26.
122. Mammadov, R.; Mammadov, B.; Toksoz, S.; Aydin, B.; Yagci, R.; Tekinay, A. B.; Guler, M. O., Heparin mimetic peptide nanofibers promote angiogenesis. *Biomacromolecules* **2011,** 12, (10), 3508-3519.
123. Boekhoven, J.; Stupp, S. I., 25th anniversary article: supramolecular materials for regenerative medicine. *Advanced Materials* **2014,** 26, (11), 1642-1659.
124. Busseron, E.; Ruff, Y.; Moulin, E.; Giuseppone, N., Supramolecular self-assemblies as functional nanomaterials. *Nanoscale* **2013,** 5, (16), 7098-7140.
125. Accardo, A.; Tesauro, D.; Mangiapia, G.; Pedone, C.; Morelli, G., Nanostructures by self-assembling peptide amphiphile as potential selective drug carriers. *Peptide Science* **2007,** 88, (2), 115-121.
126. Cheetham, A. G.; Zhang, P.; Lin, Y.-a.; Lock, L. L.; Cui, H., Supramolecular nanostructures formed by anticancer drug assembly. *Journal of the American Chemical Society* **2013,** 135, (8), 2907-2910.
127. Soukasene, S.; Toft, D. J.; Moyer, T. J.; Lu, H.; Lee, H.-K.; Standley, S. M.; Cryns, V. L.; Stupp, S. I., Antitumor activity of peptide amphiphile nanofiber-encapsulated camptothecin. *ACS nano* **2011,** 5, (11), 9113-9121.
128. Kim, J.-K.; Anderson, J.; Jun, H.-W.; Repka, M. A.; Jo, S., Self-assembling peptide amphiphile-based nanofiber gel for bioresponsive cisplatin delivery. *Molecular pharmaceutics* **2009,** 6, (3), 978-985.
129. Webber, M. J.; Matson, J. B.; Tamboli, V. K.; Stupp, S. I., Controlled release of dexamethasone from peptide nanofiber gels to modulate inflammatory response. *Biomaterials* **2012,** 33, (28), 6823-6832.
130. Bulut, S.; Erkal, T. S.; Toksoz, S.; Tekinay, A. B.; Tekinay, T.; Guler, M. O., Slow release and delivery of antisense oligonucleotide drug by self-assembled peptide amphiphile nanofibers. *Biomacromolecules* **2011,** 12, (8), 3007-3014.
131. Chu-Kung, A. F.; Bozzelli, K. N.; Lockwood, N. A.; Haseman, J. R.; Mayo, K. H.; Tirrell, M. V., Promotion of peptide antimicrobial activity by fatty acid conjugation. *Bioconjugate chemistry* **2004,** 15, (3), 530-535.

132. Laverty, G.; McLaughlin, M.; Shaw, C.; Gorman, S. P.; Gilmore, B. F., Antimicrobial activity of short, synthetic cationic lipopeptides. *Chemical biology & drug design* **2010,** 75, (6), 563-569.
133. Makovitzki, A.; Baram, J.; Shai, Y., Antimicrobial Lipopolypeptides Composed of Palmitoyl Di-and Tricationic Peptides: In Vitro and in Vivo Activities, Self-Assembly to Nanostructures, and a Plausible Mode of Action†. *Biochemistry* **2008,** 47, (40), 10630-10636.
134. Webber, M. J.; Tongers, J.; Newcomb, C. J.; Marquardt, K.-T.; Bauersachs, J.; Losordo, D. W.; Stupp, S. I., Supramolecular nanostructures that mimic VEGF as a strategy for ischemic tissue repair. *Proceedings of the National Academy of Sciences* **2011,** 108, (33), 13438-13443.
135. Lee, S. S.; Huang, B. J.; Kaltz, S. R.; Sur, S.; Newcomb, C. J.; Stock, S. R.; Shah, R. N.; Stupp, S. I., Bone regeneration with low dose BMP-2 amplified by biomimetic supramolecular nanofibers within collagen scaffolds. *Biomaterials* **2013,** 34, (2), 452-459.
136. Berns, E. J.; Sur, S.; Pan, L.; Goldberger, J. E.; Suresh, S.; Zhang, S.; Kessler, J. A.; Stupp, S. I., Aligned neurite outgrowth and directed cell migration in self-assembled monodomain gels. *Biomaterials* **2014,** 35, (1), 185-195.
137. Harrington, D. A.; Cheng, E. Y.; Guler, M. O.; Lee, L. K.; Donovan, J. L.; Claussen, R. C.; Stupp, S. I., Branched peptide-amphiphiles as self-assembling coatings for tissue engineering scaffolds. *Journal of biomedical materials research Part A* **2006,** 78, (1), 157-167.
138. Bull, S. R.; Guler, M. O.; Bras, R. E.; Meade, T. J.; Stupp, S. I., Self-assembled peptide amphiphile nanofibers conjugated to MRI contrast agents. *Nano letters* **2005,** 5, (1), 1-4.
139. Sulek, S.; Mammadov, B.; Mahcicek, D. I.; Sozeri, H.; Atalar, E.; Tekinay, A. B.; Guler, M. O., Peptide functionalized superparamagnetic iron oxide nanoparticles as MRI contrast agents. *Journal of Materials Chemistry* **2011,** 21, (39), 15157-15162.
140. Sardan, M.; Kilinc, M.; Genc, R.; Tekinay, A. B.; Guler, M. O., Cell penetrating peptide amphiphile integrated liposomal systems for enhanced delivery of anticancer drugs to tumor cells. *Faraday discussions* **2013,** 166, 269-283.
141. Lee, R. J., Liposomal delivery as a mechanism to enhance synergism between anticancer drugs. *Mol. Cancer Ther.* **2006,** 5, (7), 1639-1640.
142. Woodle, M. C., Sterically stabilized liposome therapeutics. *Adv. Drug Deliv. Rev.* **1995,** 16, (2), 249-265.
143. Walde, P., Preparation of vesicles (liposomes). In *Encyclopedia of nanoscience and nanotechnology*, American Scientific Publishers: 2004; Vol. 8, pp 43-79.
144. Rezler, E. M.; Khan, D. R.; Lauer-Fields, J.; Cudic, M.; Baronas-Lowell, D.; Fields, G. B., Targeted drug delivery utilizing protein-like molecular architecture. *J. Am. Chem. Soc.* **2007,** 129, (16), 4961-4972.

145. Sihorkar, V.; Vyas, S., Potential of polysaccharide anchored liposomes in drug delivery, targeting and immunization. *J. Pharm. Pharm. Sci* **2001,** 4, (2), 138-158.
146. Kale, A. A.; Torchilin, V. P., Design, synthesis, and characterization of pH-sensitive PEG-PE conjugates for stimuli-sensitive pharmaceutical nanocarriers: the effect of substitutes at the hydrazone linkage on the ph stability of PEG-PE conjugates. *Bioconjugate Chem.* **2007,** 18, (2), 363-370.
147. Yoshina-Ishii, C.; Miller, G. P.; Kraft, M. L.; Kool, E. T.; Boxer, S. G., General method for modification of liposomes for encoded assembly on supported bilayers. *J. Am. Chem. Soc.* **2005,** 127, (5), 1356-1357.
148. Löwik, D. W.; Linhardt, J. G.; Adams, P. H. M.; van Hest, J. C., Non-covalent stabilization of a β-hairpin peptide into liposomes. *Org. Biomol. Chem* **2003,** 1, (11), 1827-1829.
149. Lasic, D. D.; Papahadjopoulos, D., *Medical applications of liposomes*. Elsevier: 1998.
150. Agrawal, A. K.; Gupta, C., Tuftsin-bearing liposomes in treatment of macrophage-based infections. *Advanced drug delivery reviews* **2000,** 41, (2), 135-146.
151. Crommelin, D.; Nässander, U.; Peeters, P.; Steerenberg, P.; De Jong, W.; Eling, W.; Storm, G., Drug-laden liposomes in antitumor therapy and in the treatment of parasitic diseases. *Journal of Controlled Release* **1990,** 11, (1-3), 233-243.
152. Cosco, D.; Paolino, D.; Cilurzo, F.; Casale, F.; Fresta, M., Gemcitabine and tamoxifen-loaded liposomes as multidrug carriers for the treatment of breast cancer diseases. *International journal of pharmaceutics* **2012,** 422, (1), 229-237.
153. Zhi, D.; Zhang, S.; Cui, S.; Zhao, Y.; Wang, Y.; Zhao, D., The headgroup evolution of cationic lipids for gene delivery. *Bioconjugate chemistry* **2013,** 24, (4), 487-519.
154. Gregoriadis, G.; Bacon, A.; Caparros-Wanderley, W.; McCormack, B., A role for liposomes in genetic vaccination. *Vaccine* **2002,** 20, B1-B9.
155. Allen, T. M.; Cullis, P. R., Liposomal drug delivery systems: from concept to clinical applications. *Advanced drug delivery reviews* **2013,** 65, (1), 36-48.
156. Tu, R.; Mohanty, K.; Tirrell, M., Liposomal targeting through peptide-amphiphile functionalization. *American Pharmaceutical Review* **2004,** 7, 36-48.
157. Yu, Y.-C.; Roontga, V.; Daragan, V. A.; Mayo, K. H.; Tirrell, M.; Gregg, B., Structure and dynamics of peptide-amphiphiles incorporating triple-helical proteinlike molecular architecture. *Biochemistry* **1999,** 38, (5), 1659-1668.
158. Garg, A.; Tisdale, A. W.; Haidari, E.; Kokkoli, E., Targeting colon cancer cells using PEGylated liposomes modified with a fibronectin-mimetic peptide. *International journal of pharmaceutics* **2009,** 366, (1), 201-210.

159. D'Errico, G.; D'Ursi, A. M.; Marsh, D., Interaction of a peptide derived from glycoprotein gp36 of feline immunodeficiency virus and its lipoylated analogue with phospholipid membranes. *Biochemistry* **2008,** 47, (19), 5317-5327.
160. Rezler, E. M.; Khan, D. R.; Tu, R.; Tirrell, M.; Fields, G. B., Peptide-mediated targeting of liposomes to tumor cells. *Methods In Molecular Biology* **2007,** 386, 269-298.
161. Kokkoli, E. In *Engineering Biomimetic Peptides for Targeted Drug Delivery*, Frontiers of Engineering: Reports on Leading-Edge Engineering from the 2010 Symposium, 2011; National Academy Press: 2011.
162. Magzoub, M.; Graslund, A., Cell-penetrating peptides: smallfrom inception to application. *Q .Rev. Biophys.* **2004,** 37, (2), 147-95.
163. Suzuki, T.; Futaki, S.; Niwa, M.; Tanaka, S.; Ueda, K.; Sugiura, Y., Possible existence of common internalization mechanisms among arginine-rich peptides. *Journal of Biological Chemistry* **2002,** 277, (4), 2437-2443.
164. Pham, W.; Kircher, M. F.; Weissleder, R.; Tung, C. H., Enhancing membrane permeability by fatty acylation of oligoarginine peptides. *ChemBiochem* **2004,** 5, (8), 1148-1151.
165. Genç, R. k.; Ortiz, M.; O′ Sullivan, C. K., Curvature-Tuned Preparation of Nanoliposomes. *Langmuir* **2009,** 25, (21), 12604-12613.
166. Wang, F.; Chen, Y.; Zhang, D.; Zhang, Q.; Zheng, D.; Hao, L.; Liu, Y.; Duan, C.; Jia, L.; Liu, G., Folate-mediated targeted and intracellular delivery of paclitaxel using a novel deoxycholic acid-O-carboxymethylated chitosan–folic acid micelles. *Int. J. Nanomed.* **2012,** 7, 325-337.
167. Yanasarn, N.; Sloat, B. R.; Cui, Z., Negatively Charged Liposomes Show Potent Adjuvant Activity When Simply Admixed with Protein Antigens. *Mol. Pharm.* **2011,** 8, (4), 1174-1185.
168. Genç, R. k.; Clergeaud, G.; Ortiz, M.; O'Sullivan, C. K., Green Synthesis of Gold Nanoparticles Using Glycerol-Incorporated Nanosized Liposomes. *Langmuir* **2011,** 27, (17), 10894-10900.
169. De Meyer, F.; Smit, B., Effect of cholesterol on the structure of a phospholipid bilayer. *Proceedings of the National Academy of Sciences* **2009,** 106, (10), 3654-3658.
170. García, M.; Alsina, M.; Reig, F.; Haro, I., Liposomes as vehicles for the presentation of a synthetic peptide containing an epitope of hepatitis A virus. *Vaccine* **1999,** 18, (3), 276-283.
171. Deshayes, S.; Konate, K.; Aldrian, G.; Crombez, L.; Heitz, F.; Divita, G., Structural polymorphism of non-covalent peptide-based delivery systems: highway to cellular uptake. *BBA-Biomembranes* **2010,** 1798, (12), 2304-2314.
172. Boato, F.; Thomas, R. M.; Ghasparian, A.; Freund-Renard, A.; Moehle, K.; Robinson, J. A., Synthetic Virus-Like Particles from Self-Assembling Coiled-Coil Lipopeptides and Their Use in Antigen Display to the Immune System. *Angew. Chem. Int. Edit.* **2007,** 119, (47), 9173-9176.

173. Torchilin, V. P., Cell penetrating peptide-modified pharmaceutical nanocarriers for intracellular drug and gene delivery. *Peptide Science* **2008,** 90, (5), 604-610.
174. Güven, A.; Ortiz, M.; Constanti, M.; O'Sullivan, C. K., Rapid and efficient method for the size separation of homogeneous fluorescein-encapsulating liposomes. *J. Lipos. Res.* **2009,** 19, (2), 148-154.
175. Brzozowska, I.; Figaszewski, Z. A., The equilibrium of phosphatidylcholine–cholesterol in monolayers at the air/water interface. *Colloid Surface B* **2002,** 23, (1), 51-58.
176. Pan, J.; Heberle, F. A.; Tristram-Nagle, S.; Szymanski, M.; Koepfinger, M.; Katsaras, J.; Kučerka, N., Molecular structures of fluid phase phosphatidylglycerol bilayers as determined by small angle neutron and X-ray scattering. *BBA-Biomembranes* **2012,** 1818, (9), 2135-2148.
177. Feitosa, E.; Alves, F. R.; Niemiec, A.; Oliveira, M. E. C. R.; Castanheira, E. M.; Baptista, A. L., Cationic Liposomes in mixed didodecyldimethylammonium bromide and dioctadecyldimethylammonium bromide aqueous dispersions studied by differential scanning calorimetry, nile red fluorescence, and turbidity. *Langmuir* **2006,** 22, (8), 3579-3585.
178. Duzgunes, N., *Liposomes*. Academic Press: 2004.
179. Tardi, P. G.; Boman, N. L.; Cullis, P. R., Liposomal doxorubicin. *J. Drug Target.* **1996,** 4, (3), 129-140.
180. Chung, S.-J.; Shim, C.-K.; Kim, D.-D., Enhanced solubility and stability of PEGylated liposomal paclitaxel: in vitro and in vivo evaluation. *Int. J. Pharm.* **2007,** 338, 317-326.
181. Huth, U. S.; Schubert, R.; Peschka-Süss, R., Investigating the uptake and intracellular fate of pH-sensitive liposomes by flow cytometry and spectral bio-imaging. *J. Control. Release* **2006,** 110, (3), 490-504.
182. Kikkeri, R.; Maglinao, M.; Laurino, P.; Collot, M.; Hong, S. Y.; Lepenies, B.; Seeberger, P. H., Design, synthesis and biological evaluation of carbohydrate-functionalized cyclodextrins and liposomes for hepatocyte-specific targeting. *Org. Biomol. Chem.* **2010,** 8, (21), 4987-4996.
183. Machy, P.; Leserman, L. D., Small liposomes are better than large liposomes for specific drug delivery in vitro. *BBA-Biomembranes* **1983,** 730, (2), 313-320.
184. Lee, J. S.; Tung, C.-H., Lipo-oligoarginines as effective delivery vectors to promote cellular uptake. *Mol. Biosyst.* **2010,** 6, (10), 2049-2055.
185. Pan, L.; He, Q.; Liu, J.; Chen, Y.; Ma, M.; Zhang, L.; Shi, J., Nuclear-targeted drug delivery of TAT peptide-conjugated monodisperse mesoporous silica nanoparticles. *J. Am. Chem. Soc.* **2012,** 134, (13), 5722-5725.
186. Zhang, S.; Zhang, Q.-C.; Jiang, S.-J., Effect of trichostatin A and paclitaxel on the proliferation and apoptosis of lung adenocarcinoma cells. *Chinese Med.* **2013,** 126, (1), 129-134.

187. Hussain, S.; Plückthun, A.; Allen, T. M.; Zangemeister-Wittke, U., Antitumor activity of an epithelial cell adhesion molecule–targeted nanovesicular drug delivery system. *Mol.Cancer Ther.* **2007,** 6, (11), 3019-3027.
188. Sutherland, R. L.; Hall, R. E.; Taylor, I. W., Cell proliferation kinetics of MCF-7 human mammary carcinoma cells in culture and effects of tamoxifen on exponentially growing and plateau-phase cells. *Cancer Res.* **1983,** 43, (9), 3998-4006.
189. Sardan, M.; Yildirim, A.; Mumcuoglu, D.; Tekinay, A. B.; Guler, M. O., Noncovalent functionalization of mesoporous silica nanoparticles with amphiphilic peptides. *Journal of Materials Chemistry B* **2014,** 2, (15), 2168-2174.
190. Mody, K. T.; Popat, A.; Mahony, D.; Cavallaro, A. S.; Yu, C.; Mitter, N., Mesoporous silica nanoparticles as antigen carriers and adjuvants for vaccine delivery. *Nanoscale* **2013,** 5, 5167-5179.
191. Lee, J. E.; Lee, N.; Kim, T.; Kim, J.; Hyeon, T., Multifunctional mesoporous silica nanocomposite nanoparticles for theranostic applications. *Accounts. Chem. Res.* **2011,** 44, (10), 893-902.
192. Wu, S.-H.; Hung, Y.; Mou, C.-Y., Mesoporous silica nanoparticles as nanocarriers. *Chem. Commun.* **2011,** 47, (36), 9972-9985.
193. Lu, J.; Liong, M.; Zink, J. I.; Tamanoi, F., Mesoporous silica nanoparticles as a delivery system for hydrophobic anticancer drugs. *Small* **2007,** 3, (8), 1341-1346.
194. Liu, C.; Guo, J.; Yang, W.; Hu, J.; Wang, C.; Fu, S., Magnetic mesoporous silica microspheres with thermo-sensitive polymer shell for controlled drug release. *J. Mater. Chem.* **2009,** 19, (27), 4764-4770.
195. Lin, Y.-S.; Tsai, C.-P.; Huang, H.-Y.; Kuo, C.-T.; Hung, Y.; Huang, D.-M.; Chen, Y.-C.; Mou, C.-Y., Well-ordered mesoporous silica nanoparticles as cell markers. *Chem. Mater.* **2005,** 17, (18), 4570-4573.
196. Tang, F.; Li, L.; Chen, D., Mesoporous silica nanoparticles: synthesis, biocompatibility and drug delivery. *Advanced Materials* **2012,** 24, (12), 1504-1534.
197. Sharifi, S.; Behzadi, S.; Laurent, S.; Forrest, M. L.; Stroeve, P.; Mahmoudi, M., Toxicity of nanomaterials. *Chem. Soc. Rev.* **2012,** 41, (6), 2323-2343.
198. Hudson, S. P.; Padera, R. F.; Langer, R.; Kohane, D. S., The biocompatibility of mesoporous silicates. *Biomaterials* **2008,** 29, (30), 4045-4055.
199. Zhao, Y.; Sun, X.; Zhang, G.; Trewyn, B. G.; Slowing, I. I.; Lin, V. S.-Y., Interaction of mesoporous silica nanoparticles with human red blood cell membranes: size and surface effects. *ACS Nano* **2011,** 5, (2), 1366-1375.
200. Yildirim, A.; Ozgur, E.; Bayindir, M., Impact of mesoporous silica nanoparticle surface functionality on hemolytic activity, thrombogenicity and non-specific protein adsorption. *J. Mater. Chem. B* **2013,** 1, (14), 1909-1920.
201. Wang, L.-S.; Wu, L.-C.; Lu, S.-Y.; Chang, L.-L.; Teng, I.-T.; Yang, C.-M.; Ho, J.-a. A., Biofunctionalized phospholipid-capped mesoporous silica nanoshuttles for targeted drug delivery: improved water suspensibility and decreased nonspecific protein binding. *ACS Nano* **2010,** 4, (8), 4371-4379.

202. He, Q.; Zhang, J.; Shi, J.; Zhu, Z.; Zhang, L.; Bu, W.; Guo, L.; Chen, Y., The effect of PEGylation of mesoporous silica nanoparticles on nonspecific binding of serum proteins and cellular responses. *Biomaterials* **2010,** 31, (6), 1085-1092.
203. Yildirim, A.; Demirel, G. B.; Erdem, R.; Senturk, B.; Tekinay, T.; Bayindir, M., Pluronic polymer capped biocompatible mesoporous silica nanocarriers. *Chem. Commun.* **2013,** 49, (84), 9782-9784.
204. Sun, J. T.; Yu, Z. Q.; Hong, C. Y.; Pan, C. Y., Biocompatible Zwitterionic Sulfobetaine Copolymer-Coated Mesoporous Silica Nanoparticles for Temperature-Responsive Drug Release. *Macromol. Rapid Comm.* **2012,** 33, (9), 811-818.
205. Ma, M.; Chen, H.; Chen, Y.; Zhang, K.; Wang, X.; Cui, X.; Shi, J., Hyaluronic acid-conjugated mesoporous silica nanoparticles: excellent colloidal dispersity in physiological fluids and targeting efficacy. *J. Mater. Chem.* **2012,** 22, (12), 5615-5621.
206. Liong, M.; Lu, J.; Kovochich, M.; Xia, T.; Ruehm, S. G.; Nel, A. E.; Tamanoi, F.; Zink, J. I., Multifunctional inorganic nanoparticles for imaging, targeting, and drug delivery. *ACS nano* **2008,** 2, (5), 889-896.
207. Erathodiyil, N.; Ying, J. Y., Functionalization of inorganic nanoparticles for bioimaging applications. *Accounts. Chem. Res.* **2011,** 44, (10), 925-935.
208. van Schooneveld, M. M.; Vucic, E.; Koole, R.; Zhou, Y.; Stocks, J.; Cormode, D. P.; Tang, C. Y.; Gordon, R. E.; Nicolay, K.; Meijerink, A., Improved biocompatibility and pharmacokinetics of silica nanoparticles by means of a lipid coating: a multimodality investigation. *Nano letters* **2008,** 8, (8), 2517-2525.
209. Ashley, C. E.; Carnes, E. C.; Phillips, G. K.; Padilla, D.; Durfee, P. N.; Brown, P. A.; Hanna, T. N.; Liu, J.; Phillips, B.; Carter, M. B., The targeted delivery of multicomponent cargos to cancer cells by nanoporous particle-supported lipid bilayers. *Nat. Mater.* **2011,** 10, (5), 389-397.
210. Sulek, S.; Mammadov, B.; Mahcicek, D. I.; Sozeri, H.; Atalar, E.; Tekinay, A. B.; Guler, M. O., Peptide functionalized superparamagnetic iron oxide nanoparticles as MRI contrast agents. *J. Mater. Chem.* **2011,** 21, (39), 15157-15162.
211. Levine, R. M.; Scott, C. M.; Kokkoli, E., Peptide functionalized nanoparticles for nonviral gene delivery. *Soft Matter* **2013,** 9, (4), 985-1004.
212. Ferris, D. P.; Lu, J.; Gothard, C.; Yanes, R.; Thomas, C. R.; Olsen, J. C.; Stoddart, J. F.; Tamanoi, F.; Zink, J. I., Synthesis of biomolecule-modified mesoporous silica nanoparticles for targeted hydrophobic drug delivery to cancer cells. *Small* **2011,** 7, (13), 1816-1826.
213. Epler, K.; Padilla, D.; Phillips, G.; Crowder, P.; Castillo, R.; Wilkinson, D.; Wilkinson, B.; Burgard, C.; Kalinich, R.; Townson, J., Delivery of Ricin Toxin A-Chain by Peptide-Targeted Mesoporous Silica Nanoparticle-Supported Lipid Bilayers. *Adv. Healthcare Mater.* **2012,** 1, (3), 348-353.
214. Cheng, S.-H.; Lee, C.-H.; Chen, M.-C.; Souris, J. S.; Tseng, F.-G.; Yang, C.-S.; Mou, C.-Y.; Chen, C.-T.; Lo, L.-W., Tri-functionalization of mesoporous silica

nanoparticles for comprehensive cancer theranostics—the trio of imaging, targeting and therapy. *J. Mater. Chem.* **2010,** 20, (29), 6149-6157.
215. Wang, Y.; Shi, W.; Song, W.; Wang, L.; Liu, X.; Chen, J.; Huang, R., Tumor cell targeted delivery by specific peptide-modified mesoporous silica nanoparticles. *J. Mater. Chem.* **2012,** 22, (29), 14608-14616.
216. Li, X.; Chen, Y.; Wang, M.; Ma, Y.; Xia, W.; Gu, H., A mesoporous silica nanoparticle–PEI–Fusogenic peptide system for siRNA delivery in cancer therapy. *Biomaterials* **2013,** 34, 1391-1401.
217. Medintz, I. L.; Pons, T.; Delehanty, J. B.; Susumu, K.; Brunel, F. M.; Dawson, P. E.; Mattoussi, H., Intracellular delivery of quantum dot− protein cargos mediated by cell penetrating peptides. *Bioconjugate Chem.* **2008,** 19, (9), 1785-1795.
218. Ye, S.-f.; Tian, M.-m.; Wang, T.-x.; Ren, L.; Wang, D.; Shen, L.-h.; Shang, T., Synergistic effects of cell-penetrating peptide Tat and fusogenic peptide HA2-enhanced cellular internalization and gene transduction of organosilica nanoparticles. *Nanomed-Nanotechnol.* **2012,** 8, (6), 833-841.
219. Coll, C.; Mondragón, L.; Martínez-Máñez, R.; Sancenón, F.; Marcos, M. D.; Soto, J.; Amorós, P.; Pérez-Payá, E., Enzyme-Mediated Controlled Release Systems by Anchoring Peptide Sequences on Mesoporous Silica Supports. *Angew. Chem. Int. Edit.* **2011, 50**, (9), 2138-2140.
220. Luo, G.-F.; Chen, W.-H.; Liu, Y.; Zhang, J.; Cheng, S.-X.; Zhuo, R.-X.; Zhang, X.-Z., Charge-reversal plug gate nanovalves on peptide-functionalized mesoporous silica nanoparticles for targeted drug delivery. *J. Mater. Chem. B* **2013,** 1, (41), 5723-5732.
221. Oishi, M.; Tamura, A.; Nakamura, T.; Nagasaki, Y., A Smart Nanoprobe Based On Fluorescence-Quenching PEGylated Nanogels Containing Gold Nanoparticles for Monitoring the Response to Cancer Therapy. *Adv. Funct. Mater.* **2009,** 19, (6), 827-834.
222. Choi, Y.; Cho, Y.; Kim, M.; Grailhe, R.; Song, R., Fluorogenic Quantum Dot-Gold Nanoparticle Assembly for Beta Secretase Inhibitor Screening in Live Cell. *Anal. Chem.* **2012,** 84, (20), 8595-8601.
223. Deng, D.; Zhang, D.; Li, Y.; Achilefu, S.; Gu, Y., Gold nanoparticles based molecular beacons for< i> in vitro</i> and< i> in vivo</i> detection of the matriptase expression on tumor. *Biosens. Bioelectron.* **2013, 49**, 216-221.
224. Rio-Echevarria, I. M.; Tavano, R.; Causin, V.; Papini, E.; Mancin, F.; Moretto, A., Water-soluble peptide-coated nanoparticles: control of the helix structure and enhanced differential binding to immune cells. *J. Am. Chem. Soc.* **2010,** 133, (1), 8-11.
225. Baudin, B.; Bruneel, A.; Bosselut, N.; Vaubourdolle, M., A protocol for isolation and culture of human umbilical vein endothelial cells. *Nature protocols* **2007,** 2, (3), 481-485.
226. Yildirim, A.; Budunoglu, H.; Daglar, B.; Deniz, H.; Bayindir, M., One-pot preparation of fluorinated mesoporous silica nanoparticles for liquid marble

formation and superhydrophobic surfaces. *ACS Appl. Mater. Interfaces* **2011,** 3, (6), 1804-1808.
227. Cauda, V.; Schlossbauer, A.; Kecht, J.; Zürner, A.; Bein, T., Multiple Core−Shell Functionalized Colloidal Mesoporous Silica Nanoparticles. *J. Am. Chem. Soc.* **2009,** 131, (32), 11361-11370.
228. Zhuravlev, L., Concentration of hydroxyl groups on the surface of amorphous silicas. *Langmuir* **1987,** 3, (3), 316-318.
229. Kar, M.; Vijayakumar, P.; Prasad, B.; Gupta, S. S., Synthesis and characterization of poly-L-lysine-grafted silica nanoparticles synthesized via NCA polymerization and click chemistry. *Langmuir* **2010,** 26, (8), 5772-5781.
230. Kim, D.; Finkenstaedt-Quinn, S.; Hurley, K. R.; Buchman, J. T.; Haynes, C. L., On-chip evaluation of platelet adhesion and aggregation upon exposure to mesoporous silica nanoparticles. *Analyst* **2014**.
231. Chen, L.; Mccrate, J. M.; Lee, J. C.; Li, H., The role of surface charge on the uptake and biocompatibility of hydroxyapatite nanoparticles with osteoblast cells. *Nanotechnology* **2011,** 22, (10), 105708.
232. Sardan, M.; Ozkan, A. D.; Zengin, A.; Tekinay, A. B.; Guler, M. O., Advances In Nanoparticle--Based Medical Diagnostic And Therapeutictechniques. *Therapeutic Nanomaterials* **2016**, 197.
233. Selvan, S. T.; Tan, T. T. Y.; Yi, D. K.; Jana, N. R., Functional and multifunctional nanoparticles for bioimaging and biosensing. *Langmuir* **2009,** 26, (14), 11631-11641.
234. Ammari, H., *An introduction to mathematics of emerging biomedical imaging*. Springer: 2008.
235. Mulder, W.; Strijkers, G. J.; Van Tilborg, G.; Griffioen, A. W.; Nicolay, K., Lipid-based nanoparticles for contrast-enhanced MRI and molecular imaging. *NMR in Biomedicine* **2006,** 19, (1), 142-164.
236. Wang, H.; Chen, X., Applications for site-directed molecular imaging agents coupled with drug delivery potential. **2009**.
237. Bertin, A.; Steibel, J.; Michou-Gallani, A.-I.; Gallani, J.-L.; Felder-Flesch, D., Development of a dendritic manganese-enhanced magnetic resonance imaging (MEMRI) contrast agent: synthesis, toxicity (in vitro) and relaxivity (in vitro, in vivo) studies. *Bioconjugate chemistry* **2009,** 20, (4), 760-767.
238. Yu, M. K.; Jeong, Y. Y.; Park, J.; Park, S.; Kim, J. W.; Min, J. J.; Kim, K.; Jon, S., Drug-loaded superparamagnetic iron oxide nanoparticles for combined cancer imaging and therapy in vivo. *Angewandte Chemie International Edition* **2008,** 47, (29), 5362-5365.
239. Gupta, A. K.; Gupta, M., Synthesis and surface engineering of iron oxide nanoparticles for biomedical applications. *Biomaterials* **2005,** 26, (18), 3995-4021.
240. Jun, Y. w.; Lee, J. H.; Cheon, J., Chemical Design of Nanoparticle Probes for High-Performance Magnetic Resonance Imaging. *Angewandte Chemie International Edition* **2008,** 47, (28), 5122-5135.

241. Caravan, P., Protein-targeted gadolinium-based magnetic resonance imaging (MRI) contrast agents: design and mechanism of action. *Accounts of chemical research* **2009,** 42, (7), 851-862.
242. Cole, A. J.; Yang, V. C.; David, A. E., Cancer theranostics: the rise of targeted magnetic nanoparticles. *Trends in biotechnology* **2011,** 29, (7), 323-332.
243. Ling, D.; Hyeon, T., Chemical design of biocompatible iron oxide nanoparticles for medical applications. *Small* **2013,** 9, (9-10), 1450-1466.
244. Cavalli, S.; Carbajo, D.; Acosta, M.; Lope-Piedrafita, S.; Candiota, A. P.; Arús, C.; Royo, M.; Albericio, F., Efficient γ-amino-proline-derived cell penetrating peptide–superparamagnetic iron oxide nanoparticle conjugates via aniline-catalyzed oxime chemistry as bimodal imaging nanoagents. *Chemical Communications* **2012,** 48, (43), 5322-5324.
245. Xie, J.; Chen, K.; Lee, H.-Y.; Xu, C.; Hsu, A. R.; Peng, S.; Chen, X.; Sun, S., Ultrasmall c (RGDyK)-coated Fe3O4 nanoparticles and their specific targeting to integrin αvβ3-rich tumor cells. *Journal of the American Chemical Society* **2008,** 130, (24), 7542-7543.
246. Hadjipanayis, C. G.; Machaidze, R.; Kaluzova, M.; Wang, L.; Schuette, A. J.; Chen, H.; Wu, X.; Mao, H., EGFRvIII antibody–conjugated iron oxide nanoparticles for magnetic resonance imaging–guided convection-enhanced delivery and targeted therapy of glioblastoma. *Cancer research* **2010,** 70, (15), 6303-6312.
247. Landmark, K. J.; DiMaggio, S.; Ward, J.; Kelly, C.; Vogt, S.; Hong, S.; Kotlyar, A.; Myc, A.; Thomas, T. P.; Penner-Hahn, J. E., Synthesis, characterization, and in vitro testing of superparamagnetic iron oxide nanoparticles targeted using folic acid-conjugated dendrimers. *ACS nano* **2008,** 2, (4), 773-783.
248. Lee, C. M.; Jeong, H. J.; Kim, E. M.; Kim, D. W.; Lim, S. T.; Kim, H. T.; Park, I. K.; Jeong, Y. Y.; Kim, J. W.; Sohn, M. H., Superparamagnetic iron oxide nanoparticles as a dual imaging probe for targeting hepatocytes in vivo. *Magnetic Resonance in Medicine* **2009,** 62, (6), 1440-1446.
249. Sun, S.; Zeng, H., Size-controlled synthesis of magnetite nanoparticles. *Journal of the American Chemical Society* **2002,** 124, (28), 8204-8205.
250. Scopes, R., Measurement of protein by spectrophotometry at 205 nm. *Analytical biochemistry* **1974,** 59, (1), 277-282.
251. Simonian, M. H., Spectrophotometric determination of protein concentration. *Current Protocols in Toxicology* **2004**, A. 3G. 1-A. 3G. 7.
252. Obenauf, A. C.; Zou, Y.; Ji, A. L.; Vanharanta, S.; Shu, W.; Shi, H.; Kong, X.; Bosenberg, M. C.; Wiesner, T.; Rosen, N.; Lo, R. S.; Massague, J., Therapy-induced tumour secretomes promote resistance and tumour progression. *Nature* **2015,** 520, (7547), 368-372.
253. Premkumar, A.; Marincola, F.; Taubenberger, J.; Chow, C.; Venzon, D.; Schwartzentruber, D., Metastatic melanoma: Correlation of MRI characteristics and histopathology. *Journal of Magnetic Resonance Imaging* **1996,** 6, (1), 190-194.

254. Laurent, S.; Forge, D.; Port, M.; Roch, A.; Robic, C.; Vander Elst, L.; Muller, R. N., Magnetic iron oxide nanoparticles: synthesis, stabilization, vectorization, physicochemical characterizations, and biological applications. *Chemical reviews* **2008,** 108, (6), 2064-2110.
255. Sun, S.; Zeng, H.; Robinson, D. B.; Raoux, S.; Rice, P. M.; Wang, S. X.; Li, G., Monodisperse MFe2O4 (M= Fe, Co, Mn) nanoparticles. *Journal of the American Chemical Society* **2004,** 126, (1), 273-279.
256. Cornell, R.; Schwertmann, U., Dissolution. *The Iron Oxides: Structure, Properties, Reactions, Occurences and Uses, Second Edition* **1996**, 297-344.
257. Li, Z.; Wei, L.; Gao, M.; Lei, H., One-pot reaction to synthesize biocompatible magnetite nanoparticles. *Advanced Materials* **2005,** 17, (8), 1001-1005.
258. Muthiah, M.; Park, I.-K.; Cho, C.-S., Surface modification of iron oxide nanoparticles by biocompatible polymers for tissue imaging and targeting. *Biotechnology advances* **2013,** 31, (8), 1224-1236.
259. Ma, M.; Zhang, Y.; Yu, W.; Shen, H.-y.; Zhang, H.-q.; Gu, N., Preparation and characterization of magnetite nanoparticles coated by amino silane. *Colloids and Surfaces A: Physicochemical and Engineering Aspects* **2003,** 212, (2), 219-226.
260. Mahdavi, M.; Ahmad, M. B.; Haron, M. J.; Namvar, F.; Nadi, B.; Rahman, M. Z. A.; Amin, J., Synthesis, surface modification and characterisation of biocompatible magnetic iron oxide nanoparticles for biomedical applications. *Molecules* **2013,** 18, (7), 7533-7548.
261. Boyer, C.; Whittaker, M. R.; Bulmus, V.; Liu, J.; Davis, T. P., The design and utility of polymer-stabilized iron-oxide nanoparticles for nanomedicine applications. *NPG Asia Materials* **2010,** 2, (1), 23-30.
262. Diehl, K. H.; Hull, R.; Morton, D.; Pfister, R.; Rabemampianina, Y.; Smith, D.; Vidal, J. M.; van de Vorstenbosch, C.; Methods, E. F. o. P. I. A. a. E. C. f. t. V. o. A., A good practice guide to the administration of substances and removal of blood, including routes and volumes. *J Appl Toxicol* **2001,** 21, (1), 15-23.
263. Wu, X.; Tan, Y.; Mao, H.; Zhang, M., Toxic effects of iron oxide nanoparticles on human umbilical vein endothelial cells. *Int J Nanomedicine* **2010,** 5, 385-99.
264. Yang, C.; Uertz, J.; Yohan, D.; Chithrani, B. D., Peptide modified gold nanoparticles for improved cellular uptake, nuclear transport, and intracellular retention. *Nanoscale* **2014,** 6, (20), 12026-33.
265. Myer, K., *Standard Handbook of Biomedical Engineering & Design*. McGRAW-HILL: New York, Chicago, San Francisco, Lisbon, London, Madrid, Mexico City, Milan, New Delhi, San Juan, Seoul, Singapore, Sydney, Toronto, 2003.
266. Meerasa, A.; G. Huang, J.; X. Gu, F., CH50: A Revisited Hemolytic Complement Consumption Assay for Evaluation of Nanoparticles and Blood Plasma Protein Interaction. *Current Drug Delivery* **2011,** 8, (3), 290-298.

267. Yu, M. K.; Jeong, Y. Y.; Park, J.; Park, S.; Kim, J. W.; Min, J. J.; Kim, K.; Jon, S., Drug-loaded superparamagnetic iron oxide nanoparticles for combined cancer imaging and therapy in vivo. *Angew Chem Int Ed Engl* **2008,** 47, (29), 5362-5.
268. Lee, N.; Choi, Y.; Lee, Y.; Park, M.; Moon, W. K.; Choi, S. H.; Hyeon, T., Water-Dispersible Ferrimagnetic Iron Oxide Nanocubes with Extremely High r2 Relaxivity for Highly Sensitive in Vivo MRI of Tumors. *Nano Letters* **2012,** 12, (6), 3127-3131.
269. Bull, S. R.; Guler, M. O.; Bras, R. E.; Venkatasubramanian, P. N.; Stupp, S. I.; Meade, T. J., Magnetic resonance imaging of self-assembled biomaterial scaffolds. *Bioconjug Chem* **2005,** 16, (6), 1343-8.
270. Bull, S. R.; Guler, M. O.; Bras, R. E.; Meade, T. J.; Stupp, S. I., Self-assembled peptide amphiphile nanofibers conjugated to MRI contrast agents. *Nano Lett* **2005,** 5, (1), 1-4.
271. Preslar, A. T.; Parigi, G.; McClendon, M. T.; Sefick, S. S.; Moyer, T. J.; Haney, C. R.; Waters, E. A.; MacRenaris, K. W.; Luchinat, C.; Stupp, S. I.; Meade, T. J., Gd(III)-labeled peptide nanofibers for reporting on biomaterial localization in vivo. *ACS Nano* **2014,** 8, (7), 7325-32.
272. Ustun Yaylaci, S.; Sardan Ekiz, M.; Arslan, E.; Can, N.; Kilic, E.; Ozkan, H.; Orujalipoor, I.; İde, S.; Tekinay, A. B.; Guler, M. O., Supramolecular GAG-like Self-Assembled Glycopeptide Nanofibers Induce Chondrogenesis and Cartilage Regeneration. *Biomacromolecules* **2015**.
273. Oyelaran, O.; Gildersleeve, J. C., Glycan arrays: recent advances and future challenges. *Current opinion in chemical biology* **2009,** 13, (4), 406-413.
274. Simon, P. M., Pharmaceutical oligosaccharides. *Drug Discovery Today* **1996,** 1, (12), 522-528.
275. Jensen, K. J.; Brask, J., Carbohydrates in peptide and protein design. *Peptide Science* **2005,** 80, (6), 747-761.
276. Varki, A.; Cummings, R.; Esko, J.; Freeze, H.; Hart, G.; Marth, J., Essentials of glycobiology, 1999. *Cold Spring Harber Laboratory Press, New York* **1998**.
277. Hsieh-Wilson, L. C., Bioorganic chemistry: A sweet synthesis. *Nature* **2007,** 445, (7123), 31-33.
278. Artner, L. M.; Merkel, L.; Bohlke, N.; Beceren-Braun, F.; Weise, C.; Dernedde, J.; Budisa, N.; Hackenberger, C. P., Site-selective modification of proteins for the synthesis of structurally defined multivalent scaffolds. *Chemical Communications* **2012,** 48, (4), 522-524.
279. Dwek, R. A., Glycobiology: toward understanding the function of sugars. *Chemical reviews* **1996,** 96, (2), 683-720.
280. Roth, J., Protein N-glycosylation along the secretory pathway: relationship to organelle topography and function, protein quality control, and cell interactions. *Chemical reviews* **2002,** 102, (2), 285-304.

281. Mammen, M.; Choi, S.-K.; Whitesides, G. M., Polyvalent interactions in biological systems: implications for design and use of multivalent ligands and inhibitors. *Angewandte Chemie International Edition* **1998,** 37, (20), 2754-2794.
282. Watanabe, I.; Zhu, J.; Recio-Pinto, E.; Thornhill, W. B., Glycosylation Affects the Protein Stability and Cell Surface Expression of Kv1. 4 but Not Kv1. 1 Potassium Channels A Pore Region Determinant Dictates The Effect Of Glycosylation On Trafficking. *Journal of Biological Chemistry* **2004,** 279, (10), 8879-8885.
283. Gong, Q.; Anderson, C. L.; January, C. T.; Zhou, Z., Role of glycosylation in cell surface expression and stability of HERG potassium channels. *American Journal of Physiology-Heart and Circulatory Physiology* **2002,** 283, (1), H77-H84.
284. Griffin, M. E.; Hsieh-Wilson, L. C., Synthetic probes of glycosaminoglycan function. *Current opinion in chemical biology* **2013,** 17, (6), 1014-1022.
285. Place, E. S.; Evans, N. D.; Stevens, M. M., Complexity in biomaterials for tissue engineering. *Nature materials* **2009,** 8, (6), 457-470.
286. Rawat, M.; Gama, C. I.; Matson, J. B.; Hsieh-Wilson, L. C., Neuroactive chondroitin sulfate glycomimetics. *Journal of the American Chemical Society* **2008,** 130, (10), 2959-2961.
287. Barbucci, R.; Magnani, A.; Chiumiento, A.; Pasqui, D.; Cangioli, I.; Lamponi, S., Fibroblast cell behavior on bound and adsorbed fibronectin onto hyaluronan and sulfated hyaluronan substrates. *Biomacromolecules* **2005,** 6, (2), 638-645.
288. Freeman, I.; Kedem, A.; Cohen, S., The effect of sulfation of alginate hydrogels on the specific binding and controlled release of heparin-binding proteins. *Biomaterials* **2008,** 29, (22), 3260-3268.
289. Rouet, V.; Hamma-Kourbali, Y.; Petit, E.; Panagopoulou, P.; Katsoris, P.; Barritault, D.; Caruelle, J.-P.; Courty, J., A synthetic glycosaminoglycan mimetic binds vascular endothelial growth factor and modulates angiogenesis. *Journal of Biological Chemistry* **2005,** 280, (38), 32792-32800.
290. de Paz, J. L.; Noti, C.; Böhm, F.; Werner, S.; Seeberger, P. H., Potentiation of fibroblast growth factor activity by synthetic heparin oligosaccharide glycodendrimers. *Chemistry & biology* **2007,** 14, (8), 879-887.
291. Sangaj, N.; Kyriakakis, P.; Yang, D.; Chang, C.-W.; Arya, G.; Varghese, S., Heparin mimicking polymer promotes myogenic differentiation of muscle progenitor cells. *Biomacromolecules* **2010,** 11, (12), 3294-3300.
292. Nguyen, T. H.; Kim, S.-H.; Decker, C. G.; Wong, D. Y.; Loo, J. A.; Maynard, H. D., A heparin-mimicking polymer conjugate stabilizes basic fibroblast growth factor. *Nature chemistry* **2013,** 5, (3), 221-227.
293. Patel, N. J.; Karuturi, R.; Al-Horani, R. A.; Baranwal, S.; Patel, J.; Desai, U. R.; Patel, B. B., Synthetic, non-saccharide, glycosaminoglycan mimetics selectively target colon cancer stem cells. *ACS chemical biology* **2014,** 9, (8), 1826-1833.

294. Sivan, S.; Roberts, S.; Urban, J.; Menage, J.; Bramhill, J.; Campbell, D.; Franklin, V.; Lydon, F.; Merkher, Y.; Maroudas, A., Injectable hydrogels with high fixed charge density and swelling pressure for nucleus pulposus repair: Biomimetic glycosaminoglycan analogues. *Acta biomaterialia* **2014,** 10, (3), 1124-1133.
295. Pratt, M. R.; Bertozzi, C. R., Synthetic glycopeptides and glycoproteins as tools for biology. *Chemical Society Reviews* **2005,** 34, (1), 58-68.
296. Buskas, T.; Ingale, S.; Boons, G.-J., Glycopeptides as versatile tools for glycobiology. *Glycobiology* **2006,** 16, (8), 113R-136R.
297. Anisfeld, S. T.; Lansbury Jr, P. T., A convergent approach to the chemical synthesis of asparagine-linked glycopeptides. *The Journal of Organic Chemistry* **1990,** 55, (21), 5560-5562.
298. Mandal, M.; Dudkin, V. Y.; Geng, X.; Danishefsky, S. J., In Pursuit of Carbohydrate-Based HIV Vaccines, Part 1: The Total Synthesis of Hybrid-Type gp120 Fragments. *Angewandte Chemie International Edition* **2004,** 43, (19), 2557-2561.
299. Böttcher, C.; Spengler, J.; Essawy, S. A.; Burger, K., Hexafluoroacetone as protecting and activating reagent. A new approach to N-glycosides. *Monatshefte für Chemie/Chemical Monthly* **2004,** 135, (7), 853-863.
300. Liu, L.; Bennett, C. S.; Wong, C.-H., Advances in glycoprotein synthesis. *Chemical Communications* **2006**, (1), 21-33.
301. Davis, B. G., Synthesis of glycoproteins. *Chemical reviews* **2002,** 102, (2), 579-602.
302. Kiessling, L. L.; Splain, R. A., Chemical approaches to glycobiology. *Annual review of biochemistry* **2010,** 79, 619-653.
303. Xu, X.-D.; Liang, L.; Cheng, H.; Wang, X.-H.; Jiang, F.-G.; Zhuo, R.-X.; Zhang, X.-Z., Construction of therapeutic glycopeptide hydrogel as a new substitute for antiproliferative drugs to inhibit postoperative scarring formation. *Journal of Materials Chemistry* **2012,** 22, (35), 18164-18171.
304. Zhao, F.; Weitzel, C. S.; Gao, Y.; Browdy, H. M.; Shi, J.; Lin, H.-C.; Lovett, S. T.; Xu, B., β-Galactosidase-instructed formation of molecular nanofibers and a hydrogel. *Nanoscale* **2011,** 3, (7), 2859-2861.
305. Zhao, F.; Heesters, B. A.; Chiu, I.; Gao, Y.; Shi, J.; Zhou, N.; Carroll, M. C.; Xu, B., L-Rhamnose-containing supramolecular nanofibrils as potential immunosuppressive materials. *Organic & biomolecular chemistry* **2014,** 12, (35), 6816-6819.
306. Roytman, R.; Adler-Abramovich, L.; Kumar, K. A.; Kuan, T.-C.; Lin, C.-C.; Gazit, E.; Brik, A., Exploring the self-assembly of glycopeptides using a diphenylalanine scaffold. *Organic & biomolecular chemistry* **2011,** 9, (16), 5755-5761.
307. Bonduelle, C.; Lecommandoux, S. b., Synthetic Glycopolypeptides as Biomimetic Analogues of Natural Glycoproteins. *Biomacromolecules* **2013,** 14, (9), 2973-2983.

308. Ren, K.; He, C.; Xiao, C.; Li, G.; Chen, X., Injectable glycopolypeptide hydrogels as biomimetic scaffolds for cartilage tissue engineering. *Biomaterials* **2015,** 51, 238-249.
309. Bian, L.; Guvendiren, M.; Mauck, R. L.; Burdick, J. A., Hydrogels that mimic developmentally relevant matrix and N-cadherin interactions enhance MSC chondrogenesis. *Proceedings of the National Academy of Sciences* **2013,** 110, (25), 10117-10122.
310. Toh, W. S.; Lim, T. C.; Kurisawa, M.; Spector, M., Modulation of mesenchymal stem cell chondrogenesis in a tunable hyaluronic acid hydrogel microenvironment. *Biomaterials* **2012,** 33, (15), 3835-3845.
311. Kim, I. L.; Mauck, R. L.; Burdick, J. A., Hydrogel design for cartilage tissue engineering: a case study with hyaluronic acid. *Biomaterials* **2011,** 32, (34), 8771-8782.
312. Drury, J. L.; Mooney, D. J., Hydrogels for tissue engineering: scaffold design variables and applications. *Biomaterials* **2003,** 24, (24), 4337-4351.
313. Lee, K. Y.; Mooney, D. J., Hydrogels for tissue engineering. *Chemical reviews* **2001,** 101, (7), 1869-1880.
314. Lutolf, M.; Hubbell, J., Synthetic biomaterials as instructive extracellular microenvironments for morphogenesis in tissue engineering. *Nature biotechnology* **2005,** 23, (1), 47-55.
315. Fakhari, A.; Berkland, C., Applications and emerging trends of hyaluronic acid in tissue engineering, as a dermal filler and in osteoarthritis treatment. *Acta biomaterialia* **2013,** 9, (7), 7081-7092.
316. Weyers, A.; Linhardt, R. J., Neoproteoglycans in tissue engineering. *FEBS Journal* **2013,** 280, (10), 2511-2522.
317. Chen, W.-R.; Butler, P. D.; Magid, L. J., Incorporating intermicellar interactions in the fitting of SANS data from cationic wormlike micelles. *Langmuir* **2006,** 22, (15), 6539-6548.
318. Pedersen, J. S.; Schurtenberger, P., Scattering functions of semiflexible polymers with and without excluded volume effects. *Macromolecules* **1996,** 29, (23), 7602-7612.
319. Xiang, Y.; He, B.; Li, X.; Zhu, Q., The design and synthesis of novel "turn-on" fluorescent probes to visualize monoamine oxidase-B in living cells. *RSC Advances* **2013,** 3, (15), 4876-4879.
320. Cudic, M.; Ertl, H. C.; Otvos, L., Synthesis, conformation and T-helper cell stimulation of an O-linked glycopeptide epitope containing extended carbohydrate side-chains. *Bioorganic & medicinal chemistry* **2002,** 10, (12), 3859-3870.
321. Motiei, L.; Rahimipour, S.; Thayer, D. A.; Wong, C.-H.; Ghadiri, M. R., Antibacterial cyclic d, l-α-glycopeptides. *Chemical Communications* **2009**, (25), 3693-3695.

322. Friedrich-Bochnitschek, S.; Waldmann, H.; Kunz, H., Allyl esters as carboxy protecting groups in the synthesis of O-glycopeptides. *The Journal of Organic Chemistry* **1989,** 54, (4), 751-756.
323. Stolze, S. C.; Kaiser, M., Case studies of the synthesis of bioactive cyclodepsipeptide natural products. *Molecules* **2013,** 18, (2), 1337-1367.
324. Liu, M.; Barany, G.; Live, D., Parallel solid-phase synthesis of mucin-like glycopeptides. *Carbohydrate research* **2005,** 340, (13), 2111-2122.
325. Dehsorkhi, A.; Castelletto, V.; Hamley, I. W., Self-assembling amphiphilic peptides. *Journal of Peptide Science* **2014,** 20, (7), 453-467.
326. Zhang, S.; Rich, A., Direct conversion of an oligopeptide from a β-sheet to an α-helix: a model for amyloid formation. *Proceedings of the National Academy of Sciences* **1997,** 94, (1), 23-28.
327. Swanekamp, R. J.; DiMaio, J. T.; Bowerman, C. J.; Nilsson, B. L., Coassembly of enantiomeric amphipathic peptides into amyloid-inspired rippled β-sheet fibrils. *Journal of the American Chemical Society* **2012,** 134, (12), 5556-5559.
328. Nicoll, S. B.; Barak, O.; Csóka, A. B.; Bhatnagar, R. S.; Stern, R., Hyaluronidases and CD44 undergo differential modulation during chondrogenesis. *Biochemical and biophysical research communications* **2002,** 292, (4), 819-825.
329. Harada, H.; Takahashi, M., CD44-dependent intracellular and extracellular catabolism of hyaluronic acid by hyaluronidase-1 and-2. *Journal of Biological Chemistry* **2007,** 282, (8), 5597-5607.

APPENDIX

Copyright Clearance Aggrements*

Reference Number	Licence Supplier	Licence Number
4	American Chemical Society	Not required
11	Royal Society of Chemistry	3852970051594
15	Royal Society of Chemistry	3852970500022
73	Royal Society of Chemistry	3852970757771
124	Royal Society of Chemistry	Not required
140	Royal Society of Chemistry	Not required
189	Royal Society of Chemistry	Not required
232	John Wiley and Sons	3858231381410
272	American Chemical Society	Not required

* All licence agreements between Melis Sardan Ekiz and the Licence Suppliers are made by means of Copyright Clearance Center (CCC).